

T  
4-73  
GUP

# MODELS IN APPLIED GEOELECTROMAGNETICS

THESIS  
FOR  
THE DEGREE OF DOCTOR OF PHILOSOPHY  
IN  
APPLIED GEOPHYSICS  
BY  
CHANDRA P. GUPTA



26/5/75  
1.10.80



Forwarded

*M. Mittal*

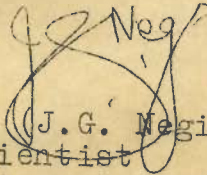
Professor & Head 24.7.73  
Department of Geology & Geophysics  
University of Roorkee,  
Roorkee.

DEPARTMENT OF GEOLOGY & GEOPHYSICS  
UNIVERSITY OF ROORKEE  
ROORKEE, INDIA

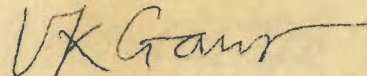
APRIL 1973

CERTIFICATE

The thesis presented by Shri C.P. Gupta embodies the results of investigations carried out by him since May, 1970 under our supervision and guidance. We certify that this work has not been submitted for the award of any other degree or diploma.



(J.G. Negi)  
Scientist  
National Geophysical  
Research Institute  
Hyderabad, India



(V.K. Gaur)  
Professor of Geophysics  
Department of Geology and  
Geophysics  
University of Roorkee  
Roorkee, India

## FOREWORD

The faculties of perception and expression encompass the entire ocean of human knowledge. They distinguish the human beings from the rest of the biological kingdom. Their evolution and sophistication is a never ending activity of all scientific endeavours. The perceived information coupled with the intelligent knowledge furthers the comprehension and exposition of the Nature. The present work comprises the observation and understanding of the electromagnetic induction processes in some models employed in geoelectromagnetics. This has also led to the quantitative identification and discussion of some inherent ambiguities in the induction prospecting data.

I find it much more difficult to depict my feelings towards the elite who contributed in several ways towards the completion of the work. However, I wish to express my deepest gratitude to Dr. J.G. Negi and Prof. V.K. Gaur for their inspiring guidance, motivation and a critical examination of the manuscript. I am greatly indebted to Dr. Hari Narain for his continued interest and encouragement for the work. To Prof. R.S. Mithal, who provided the necessary facilities and unstinted support conducive to the completion of the thesis, I owe a deep sense of gratitude.

Enlightening discussions with Dr. D.S. Parasnis have been extremely valuable and I gratefully acknowledge them. I record my grateful thanks to Mr. D. Gupta Sarma for his help in instrumentation and for many thought-provoking discussions.

I realize the inadequacy of even my fondest appreciation of the many-faceted and dedicated co-operation by my colleagues and co-Zodiac sign-holders Mr. U. Raval and Mr. Y.M. Ramachandra during the entire course of the work. I am sincerely thankful to Dr. O.P. Verma for many a meaningful interactions from time to time, to Mr. M.R.K. Sarma for precise plotting of data, and to Mr. K.N.N. Rao for the invaluable assistance in computation.

I am also thankful to Messrs M.V. Nandakumar, P.N. Sarma, S. Jamaluddin, Md. Jafer Ali, M. Jaya Rama Rao, P. Krishnaswamy, R. Acharya, Chandra Pal, P.T. Varghese, M. Devanandam, V. Krishnan, B.S. Rathor, and other colleagues who most willingly rendered their help in different ways in the preparation of the manuscript.

- C.P. Gupta

## CONTENTS

FOREWORD	ii
ABSTRACT	1
CHAPTER I: INTRODUCTION	
1.1 Electromagnetic Exploration - A Preview	6
1.2 Electromagnetic Exploration Systems	7
1.2.1 Interpretation techniques	8
1.2.1.1 Direct interpretation	9
1.2.1.2 Indirect interpretation	11
1.3 Analytical Investigations	15
1.4 Simulation Technique and Scale-Model Experiments	17
1.5 Motivation and Scope of the Present Work	19
CHAPTER II: THEORETICAL INVESTIGATIONS ON MODELS OF SPHERICAL AND PLANAR BOUNDARIES	
2.1 Introduction	24
2.2 Induced Current Distribution in a Conducting Two-Layer Spherical Body	26
2.2.1 Formulation	26
2.2.2 Solutions	29
2.2.3 Constants of integration	31
2.2.4 Discussion	36
2.2.4.1 Amplitude variation	37
2.2.4.2 Phase rotation	38
2.2.4.3 Resonance effect	40
2.2.4.4 Variation of the conductivity of the sphere	42
2.2.4.5 Variation of the conductivity and the thickness of the cover	45
2.2.5 Concluding remarks on current distribution in a covered sphere	46

4.2	Slichter's Experiment	117
4.2.1	Copper wires	118
4.2.2	Horizontal graphite cylinders	122
4.2.3	Physical explanation	128
4.2.3.1	Relative enhancement of the in-phase and quadrature components	129
4.3	Isometric Conductors	131
4.3.1	Spherical models	132
4.3.1.1	Variation of the conductivity of the surrounding medium and the frequency of energisation	136
4.3.2	Thick short cylinders	139
4.4	Tabular Sheet Type Bodies	146
4.4.1	Steeply dipping graphite sheet	146
4.4.1.1	Variation of the conductivity of the surrounding medium	147
4.4.1.2	Variation of the frequency of energisation	151
4.4.1.3	Variation of the depth of burial	155
4.4.2	Thin sheets	158
4.4.3	Horizontal graphite sheets	174
4.4.3.1	Variation of the depth of burial and the conductivity of the surrounding medium	175
4.5	Concluding Remarks	179

CHAPTER V: INDUCTIVE INTERACTION OF THE TARGET WITH SURROUNDING MEDIUM AND NEIGHBOURING BODIES

5.1	Introduction	187
5.2	Effect of Conducting Surrounding Medium and/or Overburden Insulated from the Target	187
5.2.1	Spherical models	188

2.3	Scattered Field due to a Two-Layer Permeable Conducting Sphere in a Dipolar Field	47
2.3.1	Formulation and solution	47
2.3.2	Discussion	54
2.3.2.1	Variation of the conductivity of the shell	55
2.3.2.2	Variation of the frequency of energisation	56
2.4	Profiles of the Electromagnetic Response over a Covered Conducting Sphere	58
2.5	Electromagnetic Response of a Horizontal Perfectly Conducting Half-Plane to a Line Current Source	67
2.5.1	Introduction	67
2.5.2	Formulation	70
2.5.3	Contribution of the conducting vein	76
2.5.4	Solution of the integral equation	79
CHAPTER III: EXPERIMENTAL SIMULATION - PRINCIPLE AND TECHNIQUES		
3.1	Introduction	85
3.2	Principle of Simulation	87
3.2.1	Geometrically dissimilar models	91
3.2.2	Variation of response parameter	92
3.3	Experimental Set-Up	93
3.3.1	Transmitter section	93
3.3.2	Receiver section	98
3.3.3	Operational procedure	101
3.3.4	Mechanical system	102
3.3.5	Model tank	107
3.4	Mode of Measurement and Reckoning of Anomalies	108
CHAPTER IV: RESPONSE OF TARGETS IN CONDUCTIVE CONTACT WITH THE SURROUNDING MEDIUM		
4.1	Introduction	114

5.2.2	Tabular sheet type bodies	190
5.2.2.1	Effect of the overburden when the hostrock is highly resistive	192
5.2.2.2	Effect of the overburden when the hostrock is finitely conducting	195
5.3	Closely Spaced Ore Bodies	200
5.3.1	Equal sheets	201
5.3.2	Unequal sheets	206
5.3.3	Models of other shapes	209
CHAPTER VI: CONCLUSIONS AND PLANS FOR FURTHER STUDY		
6.1	Main Results and Inferences	214
6.1.1	Analytical studies	215
6.1.2	Scale-model experiments	219
6.2	Limitations and Extensions of the Present Study	221
REFERENCES		224
CAPTIONS FOR FIGURES		240



## MODELS IN APPLIED GEOELECTROMAGNETICS

### ABSTRACT

Theoretical analysis of the electromagnetic induction in conducting models of simple geometry and scale-model experimental investigation over relatively more realistic and analytically intractable models have been carried out. Whilst the former is useful in elucidating the physical principles, the latter additionally provides a quantitative basis for the interpretation in Exploration Geoelectromagnetics. At the outset, the principles of induction prospecting and procedures of data interpretation are briefly stated. Some problems which provided incitement for the present work are also mentioned.

In order to gain a useful physical insight into the induction processes in extended objects, an analysis of quasi-static induced currents in a two-layer spherical model has been made. The numerical computation of their spatial distribution shows that the amplitude of the current density in the core decreases due to the presence of a conducting cover. An apparent enhancement of the in-phase component is, however, caused because of the phase rotation of the current vector by the cover. Current density maxima in the core and the cover are found

to occur for some characteristic frequencies. A reduction of the current density in the less conducting cover with increase in the conductivity of the core is also noticed. This apparent redistribution of the induced currents within the composite system is of greater significance in the case of elongated conductors as evinced by the results of scale-model experiments. Effect of the inhomogeneity in the conductivity has also been examined in some cases.

The maximum value as well as the variation of the vertical component of the scattered field along a profile over a similar spherical model has also been calculated. Besides conforming to the analysis of the induced currents, investigations on the scattered field bring out an apparently paradoxical phenomenon that for certain induction number of the cover the in-phase component of the response reduces with the increase of the core conductivity. The anomaly profiles also reveal that for a frequency band, whose value is governed by the conductivity values of the system, the electromagnetic response of a homogeneous sphere may be greater than that of a layered one of same size but enclosing a concentric core of higher conductivity. A multi-frequency response analysis is found to help delineate the layering of the spherical system. Analytical expressions for the response of a highly conducting vein embedded in a partially

conducting half-space and overlain by a conducting overburden have been obtained using the Wiener-Hopf technique.

The responses of more realistic and complex model set-ups have been investigated through experimental simulation. The principle of physical simulation is discussed in brief. A possibility of simulating anisotropic media is also outlined. Salient features of the experimental set-up including the transmitting and receiving equipment have been described. A fast and continuous measurement of the anomaly along a profile over a conducting target has been achieved through the method of sampling the signal induced in the receiving coil.

Investigations of the multi-frequency electromagnetic response of targets of various shapes, sizes and conductivities have been done. The effect of conductive as well as nonconductive contact between the target and the surrounding medium on the response of the former has been studied.

The response of a target is appreciably modified due to its conductive contact with the solution. In the case of elongated targets a pronounced enhancement of the response is observed when the target is immersed in a conducting solution. The effect may be ascribed to the

collection of more current lines by the better conducting target. However under similar conditions, the response of symmetrical bodies like spheres do not change significantly.

In the case of horizontal sheet-type models even the shape of the anomaly is changed due to conductive contact with the surrounding medium making it appear thinner and of greater depth extent. The existence of maxima in the curves which depict the variation of the enhancement ratio with the conductivity contrast between the target and the surrounding medium indicates the zones of greater effect of the surrounding medium. In cases when the conducting overburden is insulated from the target, a reduction of the response vector and its rotation in time-phase is obtained.

The dependence of the variation of response on the shape of the target and the type of contact with the surrounding medium and/or the overburden introduces an ambiguity in the interpretation. Furthermore, because of the phase-change in the anomaly vector, the in-phase and quadrature components of the response are modified in different proportions causing a substantial change in their ratio i.e. the induction index. The induction index is found to vary with change in depth of burial also. A first order classification of anomalies which is usually

done on the basis of induction indices will, therefore, no more be valid in such cases.

Finally, the response of closely spaced conductors which are known to occur in nature frequently, has also been investigated. A minimum distance between neighbouring bodies has been identified for which their composite response is almost a geometrical superposition of the individual responses. At closer distances between them the anomaly profiles appear like that of a single body owing to the mutual inductive interaction which precludes their resolution. At such a close spacing of the bodies as this, their combined response may even be less than the response of the either and hence the estimated conductivities in such cases will be on the lower side.

The anomaly profiles and the anomaly index diagrams presented in the thesis are expected to provide a quantitative basis for the interpretation of the induction prospecting data over some pertinent geological situations.

## CHAPTER I

### INTRODUCTION

#### 1.1 Electromagnetic Exploration - A Preview

The quest of mankind to know its environment is greatly based upon the process of 'seeing'. In a wider sense, the faculty of sight utilizes not only the visible light but the entire electromagnetic spectrum aided by sophisticated detection instruments and interpretational techniques. Depending upon the physical properties of the target and its environment, a suitable band from the wide electromagnetic spectrum is chosen to 'see' it. The selected band should be such as to have the maximum favourable interaction with the target and should not be unduly affected by the environment. For example, infra-red radiations and colour imagery are used in remote-sensing the surface features of the earth. But strong attenuation of these frequency bands during propagation inside the earth renders them unsuitable for exploration of the subterranean structures. The low frequency electromagnetic fields which have better penetration into the earth are needed for exploration of the conducting subsurface regions.

The present work deals mainly with the problems connected with electromagnetic exploration of

shallow conducting structures (depth range  $\approx$  300m) such as massive sulfide ore-deposits and strata of interest for the occurrence of groundwater etc. The ensuing analysis, however, could as well be extended to deeper conductivity-discontinuities in the crust and the mantle.

## 1.2 Electromagnetic Exploration Systems

Several systems for electromagnetic prospecting of shallow conducting bodies are in vogue based on the principle of induction. The energising electromagnetic field, generated either artificially or through some natural process, induces electric currents in conductors occurring within the zone of its influence. These currents manifest themselves, in the observation space, as secondary electromagnetic field which is commonly termed as the response or the anomaly due to the target. Study on the characteristics of the anomaly vector viz its magnitude and variation thereof in space and time comprises, as in other geophysical methods, the basis of electromagnetic exploration. The anomaly characteristics are suitably interpreted in terms of the physical properties and geometrical disposition of the causative body viz the target. Usually, the electromagnetic data is coupled with the findings of other geophysical methods particularly resistivity, gravity, magnetic, and radioactivity measurements for an integrated interpretation and for extracting maximum information.

The electromagnetic exploration systems can be classified on the basis of the nature of the energising source, the orientation of the transmitting and the detecting devices relative to the target and with each other, and the mode of measurement. Though some of the C.W. prospecting systems still utilize the tilt-angle method, most of them measure either (a) the amplitude and phase of the anomaly or (b) the in-phase and the quadrature ( $90^{\circ}$  out of phase) components of the anomaly vector resolved in time phase with respect to the primary field. In either case the quantities are measured as ratios normalised in terms of the primary field. The operational details are well described by Grant and West (1965), Parasnis (1966 and 1970a), Keller and Frischknecht (1966), Ward (1967), Bosschart (1967), and Hood and Ward (1969).

#### 1.2.1 Interpretation techniques

The interpretation of electromagnetic data is more involved than those of other geophysical methods which use static potential fields. The complication arises primarily due to an additional parameter of time-dependence. Owing to much longer experience and relative ease of operation in the static methods, the techniques of processing the data for the maximisation of information content and its interpretation are fairly advanced. Even the method of seismic prospecting, which also involves a dynamic process, is comparatively more developed



because of its extensive use in petroleum exploration which constitutes the most important activity of geophysical exploration. The state of art in Exploration Geoelectromagnetics has remained relatively underdeveloped in spite of many valuable contributions from physicists and electrical engineers and one still looks for the rules-of-thumb in this field.

Similar to other geophysical methods, the interpretational procedure of the electromagnetic data also, consists of two stages viz direct and indirect. A judicious combination of both is resorted to in an attempt of interpreting the available data.

#### 1.2.1.1 Direct interpretation

The direct interpretation consists, as the term implies, in inferring the characteristics of the causative body directly from the observational data. A preliminary examination of the anomaly components and their spatial variations constitutes the initial stage of direct interpretation. The ratio of the in-phase ( $I_p$ ) and quadrature ( $Q_r$ ) components of the anomaly, particularly for moving source methods, is also determined. Because of the predominance of the  $I_p$  component over the  $Q_r$  component for good conductors, the  $I_p/Q_r$  ratio termed as the induction index ( $I_i$ ) offers a useful criterion to obtain a rough estimate of the electrical conductivity

of the targets.  $I_i$  is approximately unity for average conductors (Parasnis, 1970a) and its higher values indicate proportionately better conductors. A gradational classification of anomalies is done on the basis of  $I_i$  values. The analysis during the present work will reveal that the inferences drawn from  $I_i$  values are not always reliable and may sometimes lead to quite erroneous conclusions. Still, in a large number of cases encountered in electromagnetic prospecting this criterion has successfully been used as a first order filter.

The shape of the anomaly profile may indicate the orientation of the conductor. For example, the anomaly profile due to a steeply dipping lenticular or tabular conductor as recorded by a horizontal coplanar-coil prospecting system has a sharp negative peak flanked by two symmetrical positive shoulders. If the conductor has a larger extent so that it could be represented by a horizontal sheet, an additional positive hump appears in the middle of the anomaly profile. The flanking positive shoulders are unequal if the dip of the conductor lies between  $0^\circ$  and  $90^\circ$  and the ratio of their magnitudes gives an approximate estimate of the dip (Strangway, 1966a).

Advanced techniques are being developed using fast computers for direct interpretation. The anomaly is attempted to be synthesized with the help of linear

electric network. Bödvarsson (1966) has discussed the interpretation of magnetotelluric data through such a method.

#### 1.2.1.2 Indirect interpretation

The indirect interpretation is based on the comparison of the data with predetermined electromagnetic response ( $R$ ) of some heuristic models. The function  $R$ , which depends on the various electric and geometric parameters, can be written, neglecting the displacement currents for quasi-static excitation (Grant and West, 1965), as:

$$R = F(x, \sigma_1, \sigma_2, \dots, \mu_1, \mu_2, \dots, \omega, L_1, L_2, \dots, \varphi_1, \varphi_2, \dots). \quad (1.1)$$

Here  $x$  defines the position of the prospecting system relative to the target;  $\sigma_1, \sigma_2, \dots$  etc. and  $\mu_1, \mu_2, \dots$  etc. are the electrical conductivities and magnetic permeabilities of the target and those of the neighbouring bodies including the surrounding medium;  $\omega$  is the angular frequency of the energising field;  $L_1, L_2, \dots$  etc. are the linear dimensions of target and the prospecting system; and  $\varphi_1, \varphi_2, \dots$  are the dimensionless quantities describing the relative dispositions and orientations of the target and the prospecting system. The function  $R$  is determined for the various parametric

values of the quantities in the parenthesis of equation (1.1). The anomaly profiles over known models are obtained by varying  $x$ . These standard profiles are known as type curves. The plots between the peak-to-peak values of the  $I_p$  and  $Q_r$  components (cf. Sec. 3.4) obtained from different type curves (Grant and West, 1965) are known as anomaly index diagrams.

Figure 1.1 illustrates an anomaly index diagram for a vertical thin sheet which approximates a half plane placed in air. The diagram may be prepared by varying the height of the prospecting system and the frequency of the energising field and/or sheet-thickness. If an anomaly profile gives an indication of the presence of a thin vertical tabular body, the present diagram can be used to evaluate the response parameter ( $\sigma\omega\mu tL$ ) of the body. The frequency of the field and the dimension  $L$  which is the separation between the transmitting and receiving coils are known quantities. Unless there is an association of magnetic minerals such as magnetite etc., the permeability  $\mu$  of the target may be regarded to be the same as that of free space. From the response parameter one can thus find the surface conductivity ( $\sigma t$ ) of the target.

It is interesting to note that in several cases described by Grant and West (1965), Strangway (1966b),

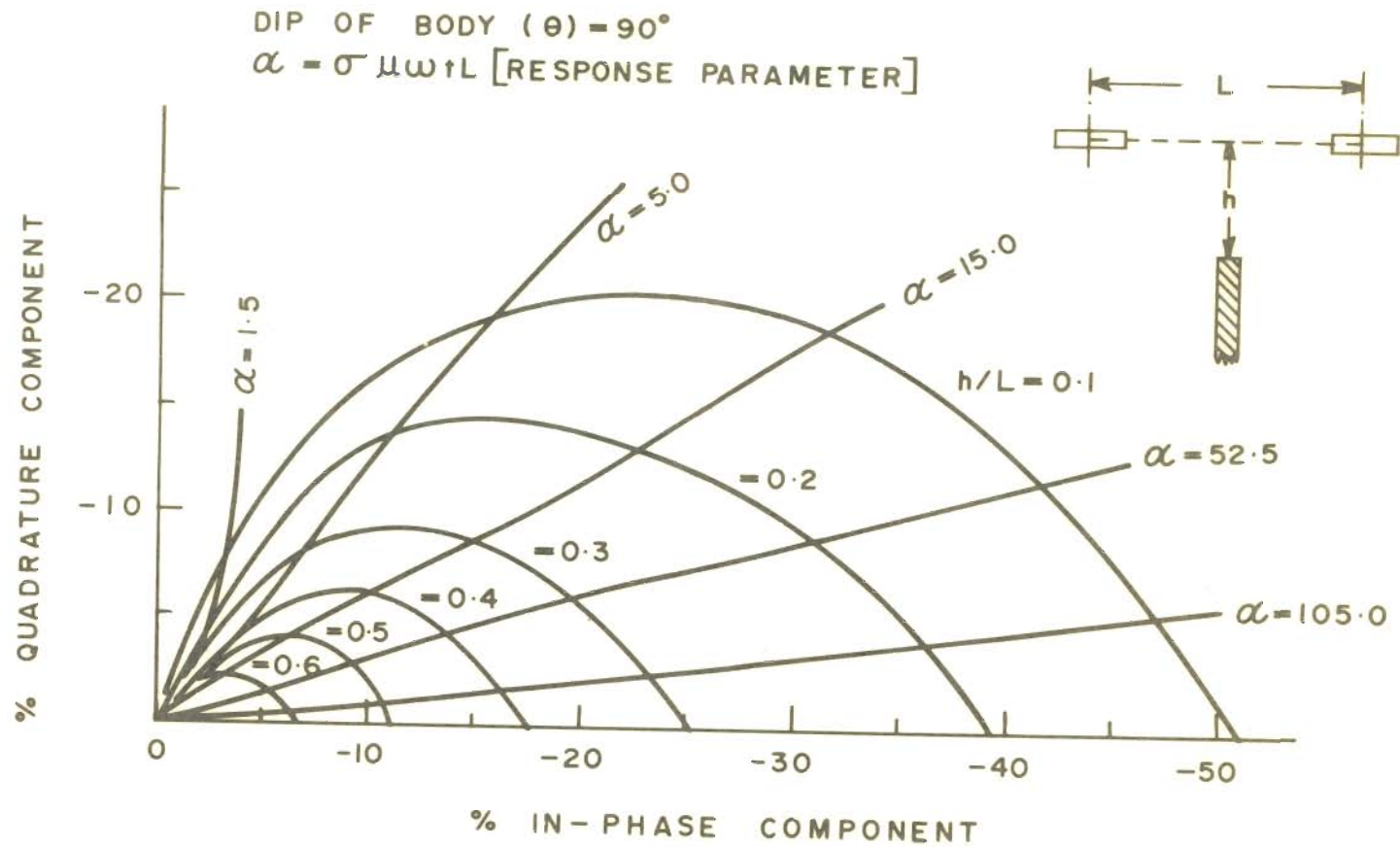


Fig.1-1 ANOMALY INDEX DIAGRAM FOR A VERTICAL THIN SHEET IN AIR (After Strangway, 1966 b)

Parasnis (1970a), Bosschart (1967), Ward (1967) and Paterson (1967), the use of anomaly index diagrams prepared from relatively idealised models, disregarding the environmental conditions as are usually found associated with conducting mineralised zones, have aided the interpretation of electromagnetic prospecting data leading to discoveries of many economic ore-deposits.

The electromagnetic response of a representative model is determined either experimentally or analytically. In both the cases, however, the models chosen are usually of simple geometry and are abstracted representations of realistic complicated geological situations. This is particularly true of analytical investigations. Recently, however, there has been a growing realisation of this shortcoming (Ward, 1971). The analytical techniques aided by approximation-iterative methods and numerical techniques using high speed and large memory computers are being increasingly used to solve problems intractable heretofore. The sophistication in instrumentation and realisability of complex physical models have led to the advance of model experiments too. Broadly speaking, the theoretical and experimental techniques, which are of complementary nature, have progressed significantly during the last decade.

### 1.3 Analytical Investigations

Because of the simplicity of formulation and derivation of the solution, a large number of analytical investigations have been carried out on such conducting models as have regular spherical, circular-cylindrical or planar boundaries. The problems, in general, have been formulated in the form of partial differential equations solvable through method of separation of variables. Bouwkamp (1954) has given a detailed review of investigations on electromagnetic diffraction theory. Some of the notable earlier contributions to geoelectromagnetics have been by Slichter (1951), Wait (1951, 1952, 1953a and b, 1959, 1960, and 1962), March (1953), Ward (1952 and 1959), Belluigi (1956), Tikhonov and Shakhshvarov (1956, 1959, and 1961), Nikitina (1956 and 1960), Dyakonov (1957 and 1959), Wesley (1958a and b) Slichter and Knopoff (1959), Dmitriev (1959 and 1960), Tikhonov et al (1959), Kertz (1960), Brekhovskikh (1960), Negi (1962a, b, and c), Meyer (1963), Schaub (1963 and 1965), Vanyan (1963a and b), and Pris (1965). Though the results obtained on these simple models had restrictive utility as an interpretational tool in electromagnetic prospecting, they have met the desired objective of elucidating the principles of induction processes in conducting structures. A detailed review of these investigations is given by Raval (1972).

The investigations on conducting bodies of more complicated geometries have been quite scanty. Some of the earlier studies on elliptical cylinders, spheroids, and ellipsoids etc. have been carried out by Schultz (1950), Rauch (1953), Seigel et al (1953), Clemmow and Weston (1961), Barakat (1963), Germey (1964), and Ashour (1965). These investigations pertain mainly to the realm of physics and radio-communication and their applicability in geophysical exploration has not been widely recognised.

Chetaev (1966), Praus (1966), Negi (1967), Davydov (1969), Negi and Raval (1969), Wait (1969), Dmitriev (1969), Zakharov and Ilin (1970), Raval and Gupta (1971a and b), Fuller (1971), Parry and Ward (1971), Vozoff (1971), Coggon (1971), Hohmann (1971), Swift (1971), Jones and Price (1971), Lamontagne and West (1971), Hill and Wait (1972), Negi et al (1972a and b, and 1973), and Negi and Saraf (1973) made some of the recent contributions incorporating influences of (i) conductivity of the surrounding medium, (ii) inhomogeneity and anisotropy in the conductivity of the target, and (iii) variation from the simple geometry etc. The models studied by these workers were usually nearer to the realistic situations.

Though an application of both theoretical and experimental findings is recommended to extract maximum information from the available data, the



technique of simulation experiments has proved to be more versatile as regards the applicability.

#### 1.4 Simulation Technique and Scale Model Experiments

The representation of the essential physical characteristics of a large scale system (prototype) by a model on a conveniently reduced scale is based on the principle of similitude. It primarily consists in the recognition of certain vital nondimensional parameters describing the behavior of the prototype and maintaining their invariance in the model.

The geophysical application of electromagnetic scale model experiments dates back to the works of Slichter (1932) on spherical models and Bruckshaw (1936) on laminar bodies. Ever since then, the general methodology of e.m. model experiments has hardly undergone any major change. But the multiplicity and variety of associated problems have given enough scope for carrying out different types of model experiments by numerous investigators using sophisticated physical modeling equipment.

Stratton (1941) has discussed the principle of electrodynamic similitude. Sinclair (1948) presented a detailed treatment for geometrical as well as absolute modeling. The latter simulates the power levels of the

electrical and magnetic field vectors besides the geometrical and electrical properties of the prototype. As has however been mentioned above, measurements of the anomaly vector in electromagnetic exploration are made in terms of the primary field and hence the absolute power levels of the field vectors do not come into the picture.

Amongst the pioneering studies whose results have found application in induction prospecting are those of Hedström and Parasnis (1958), Gaur (1959), and West (1960). All these investigations were made on thin sheets. Strangway (1966a) and Negi and Gupta (1968) have reviewed some of the important studies in the field. Ward (1967) has given a catalogue of some model results based on his own work and those of West (1960), Frischknecht and Mangan (1960), and some Exploration Companies of North America.

The work of Clark and Mungal (1951) has been of great value for conceptual understanding in geoelectromagnetics. The contributions of Tornqvist (1958), Dolan (1960), Svetov (1960), Boyd and Roberts (1961), Douloff (1961), Zakharov (1963), Gaur (1963), Faldus et al (1963), Lowrie and West (1965), Poddar and Bhattacharya (1966), Dosso (1966a, b, and c), Nair et al (1968), Gupta Sarma and Maru (1971), Gaur et al (1972) etc.

are the noted few in the field of electromagnetic scale-model experiments. Besides, a number of Ph.D. and M.A. theses including those of Tesche (1951), Ward (1952), Gaur (1959), West (1960), Douloff (1960), Bosschart (1964), Fraser (1966), and Verma (1972); and Burrows (1957), Martin (1960), Ranasinghe (1962), Parry (1965), and Lamontagne (1970) etc. have also been devoted partly or wholly to electromagnetic model experiments.

#### 1.5 Motivation and Scope of the Present Work

Ward (1967 and 1971) described the geological situations usually encountered in induction prospecting. The system to be explored consists of a target of irregular shape and inhomogeneous electric properties, surrounded by a zone of disseminated mineralisation, embedded in a comparatively less conducting hostrock and overlain by a conducting overburden of a rough topography (figure 1.2). A physical modeling should take into account as many of the above factors as possible. But a majority of investigations reported in geophysical literature have been confined to idealised models. An attempt has been made in the present thesis to study relatively more realistic physical models theoretically as well as experimentally.

Gaur (1963) investigated the effect of conducting surrounding medium, represented by a common

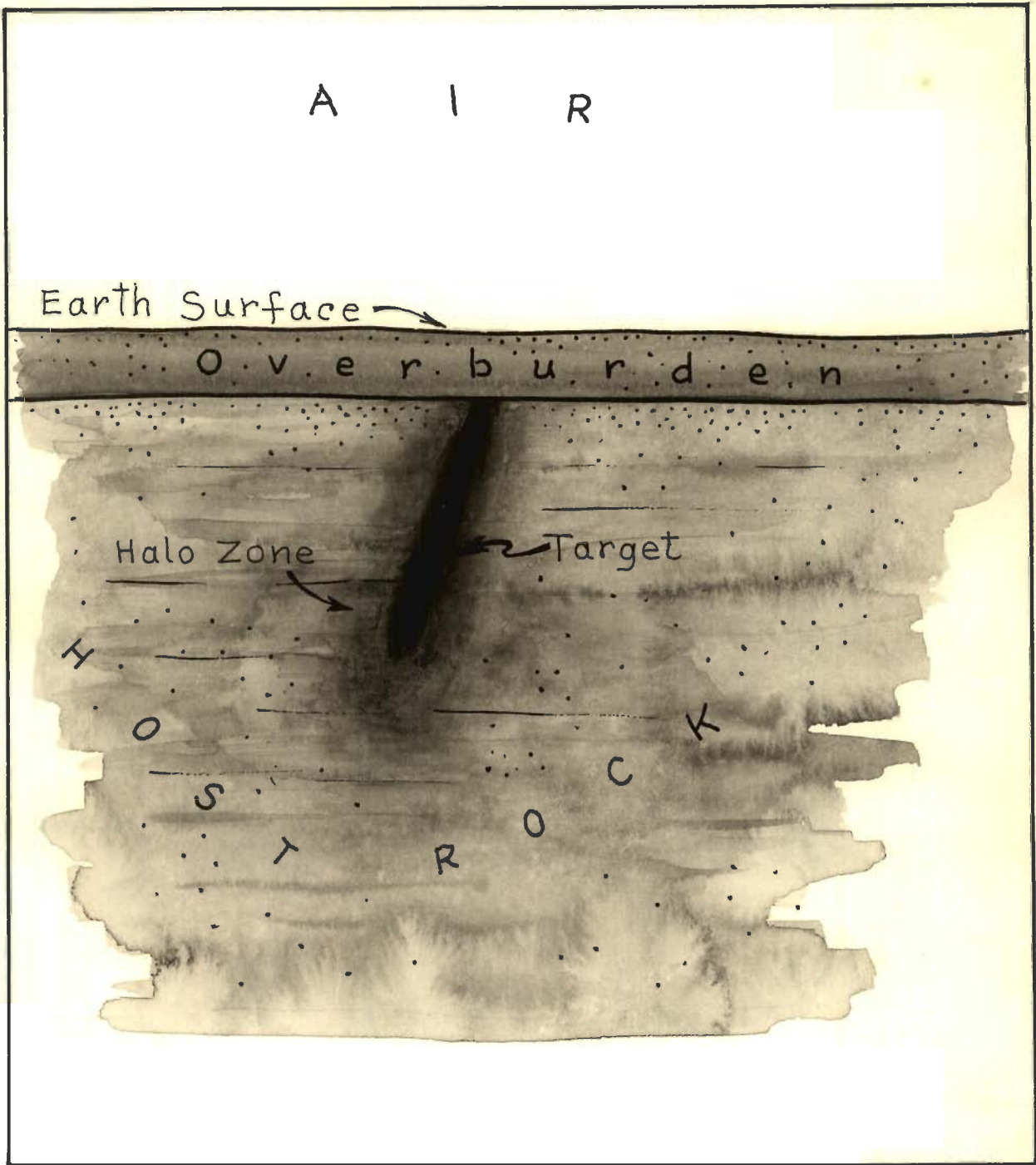


Fig. 1-2 A Generalised Geological Situation of Occurrence of an Ore-body

salt solution, on the electromagnetic response of conducting sheets. The use of a salt solution to simulate conducting surroundings had also been recommended by Molotschnow and Janovsky (1959). Lowrie and West (1965) studied the effect of conducting overburden by simulating it with a thin metallic foil. Theoretical investigations by Negi (1967), Negi and Raval (1969), and Wait (1969) aroused much interest in the problems of conducting surroundings. The review of Roy (1970), theoretical results of Fuller (1971), model investigations of Gupta Sarma and Maru (1971) and Gaur et al (1972), and field reports of Parasnis (1971) have stimulated further investigation of this problem. Ward (1971) summarised some general aspects of the influence of conducting halo-zone, hostrock and overburden. A detailed examination of the influence of the conducting surrounding on the electromagnetic response of embedded and underlying targets comprises a major part of the present study.

Theoretical investigations of induced currents in a two-layer spherical conductor have been made in order to gain a useful physical insight into the problem of induction. The influence of the conducting cover of different thicknesses and conductivities on the response of the core for different frequencies of energising field has been analysed. The scattered field for the

same spherical model has also been computed and the maximum anomaly as well as the spatial profile of the anomaly components have been plotted. An illustration of the integral equation formulation and use of the Wiener-Hopf technique has been made through calculating the response of an ideally conducting horizontal half plane embedded in a conducting half space and overlain by a conducting overburden (Chapter II).

The limitations of theoretical methods have led to resorting to model experiments for studying the electromagnetic problems in greater complexity and variety. The principle of simulation, experimental set-up for model studies, necessary details of instruments used, and mode of measurements and analysis of anomaly profiles have been described (Chapter III).

Some representative results on the influence of conducting surrounding in conductive contact with the targets of different shapes, sizes, and conductivities have been presented. In the majority of cases, a substantial enhancement of the response of the target is found to be caused by the surrounding medium. Some basic experiments have been made to analyse and hypothesise this phenomenon. The varied and puzzling nature of results appear to indicate the inherent difficulties in evolving some rules-of-thumb for

interpretation of the geoelectromagnetic data (Chapter IV).

As distinct from the conductive effects of the surrounding medium on the target response, the inductive interaction between the target and the hostrock/overburden insulated from the target has also been studied. The inductive coupling between closely spaced bodies has been found which adds further complications in the data interpretation (Chapter V).

While summarising the main results of the present study, some more problems of applied importance have also been delineated which need to be investigated in further detail (Chapter VI).

## CHAPTER II

### THEORETICAL INVESTIGATIONS ON MODELS OF SPHERICAL AND PLANAR BOUNDARIES

#### 2.1 Introduction

Conducting spherical structures have probably been the most extensively studied models in applied geoelectromagnetics employing analytical methods. These may represent isometric massive sulfide ore bodies. Although their occurrence is not reported to be very common, the analytical simplicity in their study and usefulness thereof in examining the physical principles involved have greatly encouraged their investigations.

Raval (1972) presented a historical perspective of the studies carried out on scattering of light and radio-frequency waves by spherical objects. The response of a conducting sphere to a low frequency time-harmonic uniform magnetic field was determined by Wait (1951). March (1953) and Wait (1953a) further extended this study for a magnetic dipolar field. Later, Ward (1959) presented numerically computed response of a permeable conducting sphere surrounded by a non-conducting medium and proposed a method for the unique determination of both its electrical properties and its geometry. Negi (1962c) investigated an inhomogeneous conducting sphere considering a radial



conductivity variation similar to that assumed by Lahiri and Price (1939) in their studies related to Geomagnetism. Bhattacharya and Sinha (1965) computed the response profiles over a sphere for different configurations of a dipole - dipole prospecting system.

The influence of a halo of disseminated mineralized zone, represented by a conducting concentric cover, on the electromagnetic response of a sphere was calculated by Negi (1967). His theoretical analysis indicated that under certain conditions the  $I_p$  component of the response of a sphere is enhanced by a conducting cover. Wait (1969) made a similar study assuming the cover to be in the form of a thin shell insulated from the sphere. A similar model as that of Wait was examined by Fuller (1971) who considered the shell to be of finite thickness. Although, the differences in models studied by these workers prevented a direct comparison of their results, the findings and more so their contentions did not qualitatively conform with one another. It was, therefore, considered desirable to examine the problem in greater detail.

As the electromagnetic response of a conductor is an integrated effect of the currents induced in its entire volume, a study has been made both of the induced currents and the scattered field so as to gain a comprehensive physical insight of the problem.

Furthermore, anomaly profiles over a covered sphere have also been calculated.

## 2.2 Induced Currents Distribution in a Conducting Two-Layer Spherical Body

Price (1949) calculated induced currents in conducting sheets and shells and Ashour (1950) in a circular disk. These results have been useful in geomagnetic studies. Consbruch (1963) investigated the current distribution in an inhomogeneous cylinder, Koefoed and Kegge (1968) in a plate, and Satpathy (1971) in an uncovered sphere. The present work analyses characteristics of induced currents in a two-layer spherical model for different parameters of the conducting system at different frequencies (Gupta et al, 1973).

### 2.2.1 Formulation

The geometry of the system under investigation is shown in figure 2.1. A sphere of radius  $r_1$  is covered by a concentric shell of thickness  $d_b = r_2 - r_1$  and is in conductive contact with it. The conductivity, permeability and permittivity of the sphere are denoted by  $\sigma_1$ ,  $\mu_1$  and  $\epsilon_1$  respectively and the corresponding parameters for the shell and the surrounding outermost medium by  $\sigma_2$ ,  $\mu_2$ ,  $\epsilon_2$  and  $\sigma_3$ ,  $\mu_3$ ,  $\epsilon_3$ . The outermost medium (region 3) is considered to be homogeneous and of infinite extent. The conductivities of both the sphere and the shell are assumed to be inhomogeneous

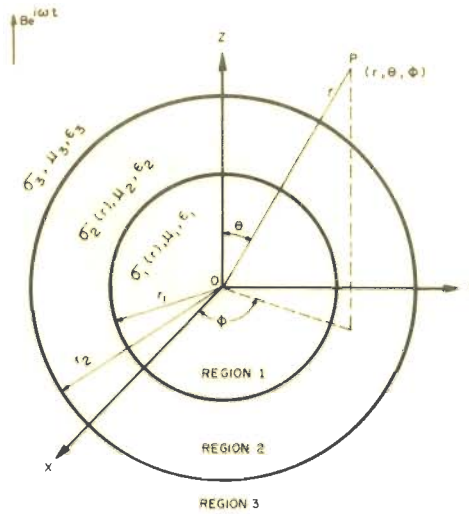


Fig.2-1 AN INHOMOGENEOUS COVERED SPHERE IN A UNIFORM ALTERNATING MAGNETIC FIELD

$\sigma_{01}$	= 10.0 mho/m	$\sigma_{02}$	= 1.0 mho/m
$r_1$	= 10.0 m	$r_2$	= 12.5 m
$\rho_1$	= 0	$\rho_2$	= 0

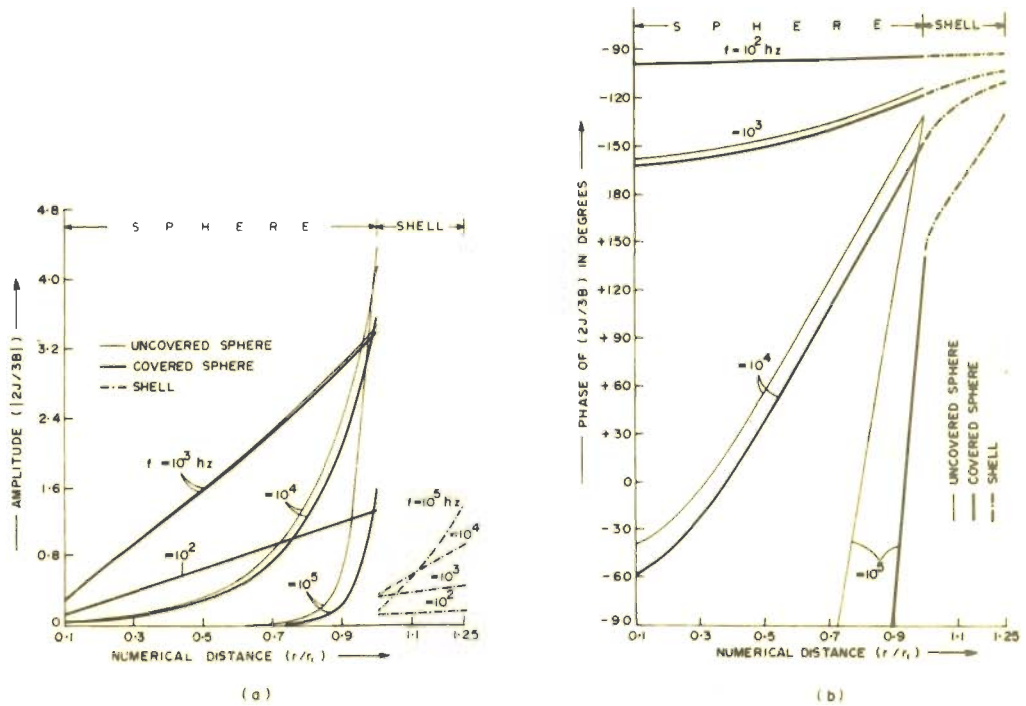


Fig.2-2 THE (a) AMPLITUDE AND (b) PHASE OF THE NORMALISED INDUCED CURRENT DENSITY IN THE SPHERE AND THE SHELL VARYING WITH THE DISTANCE FROM THE CENTRE FOR DIFFERENT FREQUENCIES

having a radial variation of the type,

$$\sigma_j = \sigma_{oj} \left( \frac{r}{r_j} \right)^{-p_j}, \quad j = 1 \text{ or } 2. \quad (2.1)$$

A spherical polar coordinate system  $(r, \theta, \varphi)$ , whose origin  $O$  coincides with the centre of the spherical system, is employed. The exciting field is assumed, for analytical simplicity, to be uniform and of the form  $B e^{i\omega t}$ . As is known (Wait, 1953a), the uniform field assumption is equivalent to considering only the first term of the multipolar response of the sphere to a dipolar energising field.

The propagation constants for various regions (figure 2.1) are given by

$$\gamma_j^2 = i\omega\mu_j\sigma_j - \epsilon_j\mu_j\omega^2, \quad j = 1, 2 \text{ or } 3. \quad (2.2)$$

The electric (E) and magnetic (H) field vectors are derivable from a magnetic vector potential as

$$E = -i\omega A \quad (2.3a)$$

$$\text{and } H = \frac{1}{\mu} \text{Curl } A. \quad (2.3b)$$

The vector  $A$  satisfies the following dissipative wave equation in the various regions:

$$\nabla^2 A_j = \gamma_j^2 A_j. \quad (2.4)$$

### 2.2.2 Solutions

The vector potentials in the three regions may be written, following Lahiri and Price (1939), as follows:

#### 1. Region 3 i.e. in the outermost medium

$$A_3 = A_0 + \sqrt{\frac{2r}{\pi\gamma_3}} \sum_{n=0}^{\infty} D_n K_{n+\frac{1}{2}}(\gamma_3 r) P_n^1(\cos \theta). \quad (2.5)$$

If the frequency of the exciting field is quite low, as is true in induction prospecting, and the conductivity of the surrounding medium may be regarded as negligible i.e.  $|\gamma_3 r| \ll 1$ , the expression for  $A_3$  reduces to

$$A_3 = A_0 + \sum_{n=0}^{\infty} D_n r^{-n-1} P_n^1(\cos \theta), \quad (2.6)$$

where  $A_0$  is the potential of the primary field expressible as (Smythe, 1968, p. 375),

$$A_0 = \frac{1}{2} B r P_1^1(\cos \theta), \quad (2.6a)$$

where  $I_n(\alpha)$  and  $K_n(\alpha)$  are the modified Bessel functions of first and second kind respectively and  $P_n^1(\cos \theta)$  is the associated Legendre polynomial.

The quasi-static limit, as referred above, will be assumed to be valid in all the cases hereafter and equation (2.6) will be adopted in all the subsequent derivations.

2. Region 2 i.e. in the shell

$$A_2 = \sum_{n=0}^{\infty} \left[ \sqrt{\frac{\pi}{2 \gamma_{02} r}} E_n I \frac{2n+1}{|2-p_2|} \left\{ \frac{2\gamma_{02}}{r_2} \frac{r^{(2-p_2)/2}}{|2-p_2|} \right\} \right. \\ \left. + \sqrt{\frac{2}{\pi \gamma_{02} r}} F_n K \frac{2n+1}{|2-p_2|} \left\{ \frac{2\gamma_{02}}{r_2} \frac{r^{(2-p_2)/2}}{|2-p_2|} \right\} \right] P_n^1(\cos \theta),$$

for  $p_2 \neq 2$  (2.7a)

or

$$A_2 = \sum_{n=0}^{\infty} \left[ \tilde{E}_n r^{\sqrt{(n+\frac{1}{2})^2 + \gamma_{02}^2 r^2}} + \tilde{F}_n r^{-\sqrt{(n+\frac{1}{2})^2 + \gamma_{02}^2 r^2}} \right] P_n^1(\cos \theta),$$

for  $p_2 = 2$ . (2.7b)

3. Region 1 i.e. in the sphere

$$A_1 = \sum_{n=0}^{\infty} \sqrt{\frac{\pi}{2 \gamma_{01} r}} G_n I \frac{2n+1}{|2-p_1|} \left\{ \frac{2\gamma_{01}}{r} \frac{r^{(2-p_1)/2}}{|2-p_1|} \right\} P_n^1(\cos \theta),$$

for  $p_1 < 2$  (2.8a)

or

$$A_1 = \sum_{n=0}^{\infty} G'_n \sqrt{\frac{2}{\pi \gamma_{01} r}} K \frac{2n+1}{|2-p_1|} \left\{ \frac{2\gamma_{01}}{r_1} \frac{r^{(2-p_1)/2}}{|2-p_1|} \right\}$$

$P_n^1(\cos \theta)$ , for  $p_1 > 2$  (2.8b)

or

$$A_1 = \sum_{n=0}^{\infty} G_n'' r \frac{\sqrt{(n+\frac{1}{2})^2 + \gamma_{01}^2 r_1^2}}{r_1} P_n^1(\cos\theta),$$

for  $p_1 = 2$ . (2.8c)

### 2.2.3 Constants of integration

The constants  $E_n$ ,  $F_n$ ,  $G_n$  etc. determining the field inside the spherical system for different values of  $p_1$  and  $p_2$  may be obtained from the boundary conditions at the surfaces  $r = r_1$  and  $r_2$  employing appropriate expressions of the vector potentials. Because of the orthogonality property of the Legendre polynomials, all other constants except for  $n = 1$  will be zero. We assume here  $\mu_1 = \mu_2 = \mu_3$  i.e. both the sphere and the shell are magnetically nonpermeable.

The expressions for  $E_1$ ,  $F_1$ , and  $G_1$  for  $p_2 \neq 2$  and  $p_1 < 2$ , using equations (2.6), (2.7a) and (2.8a) may be written after the necessary algebraic calculations as

$$G_1 = \frac{\left[ R \sqrt{\frac{\pi}{2\gamma_{02} r_1}} I \frac{3}{|2-p_2|} \left\{ \delta_2 r_1^{(2-p_2)/2} \right\} + \sqrt{\frac{2}{\pi\gamma_{02} r_1}} K \frac{3}{|2-p_2|} \left\{ \delta_2 r_1^{(2-p_2)/2} \right\} \right]}{\left[ R \sqrt{\frac{\pi\gamma_{02} r_2}{2}} I \frac{3}{|2-p_2|} - 1 \left\{ \delta_2 r_2^{(2-p_2)/2} \right\} - \sqrt{\frac{2\gamma_{02} r_2}{\pi}} K \frac{3}{|2-p_2|} - 1 \left\{ \delta_2 r_2^{(2-p_2)/2} \right\} \right]}$$

$$\frac{\frac{3}{2} Br_2}{\sqrt{\frac{\pi}{2\gamma_{01} r_1} I \frac{3}{|2-p_1|} \left\{ \delta_1 r_1^{(2-p_1)/2} \right\}}}, \quad (2.9a)$$

where

$$R = \frac{\left[ Q \sqrt{\frac{2\gamma_{02} r_1}{\pi}} \left(\frac{r_1}{r_2}\right)^{-p_2/2} K \frac{3}{|2-p_2|} - 1 \left\{ \delta_2 r_1^{(2-p_2)/2} \right\} + \sqrt{\frac{2}{\pi\gamma_{02} r_1}} K \frac{3}{|2-p_2|} \left\{ \delta_2 r_1^{(2-p_2)/2} \right\} \right]}{\quad}, \quad (2.10)$$

$$Q = \frac{\left[ Q \sqrt{\frac{\pi\gamma_{02} r_1}{2}} \left(\frac{r_1}{r_2}\right)^{-p_2/2} I \frac{3}{|2-p_2|} - 1 \left\{ \delta_2 r_1^{(2-p_2)/2} \right\} + \sqrt{\frac{\pi}{2\gamma_{02} r_1}} I \frac{3}{|2-p_2|} \left\{ \delta_2 r_1^{(2-p_2)/2} \right\} \right]}{\gamma_{01} r_1 I \frac{3}{|2-p_1|} - 1 \left\{ \delta_1 r_1^{(2-p_1)/2} \right\}}, \quad (2.11)$$

and

$$\delta_j = \frac{2\gamma_{0j}}{r_j^{-p_j/2} |2-p_j|}, \quad j = 1, 2. \quad (2.12)$$



Also,

$$F_1 = \frac{\frac{3}{2} Br_2}{R \sqrt{\frac{\pi \gamma_{O_2} r_2}{2}} I \frac{3}{|2-p_2|} - 1 \left\{ \delta_2 r_2^{(2-p_2)/2} \right\}} \quad (2.13)$$

$$- \sqrt{\frac{2 \gamma_{O_2} r_2}{\pi}} K \frac{3}{|2-p_2|} - 1 \left\{ \delta_2 r_2^{(2-p_2)/2} \right\}$$

and  $E_1 = F_1 R.$  (2.14)

Similarly, the constants for  $p_2 \neq 2$  and  $p_1 > 2$  can be written as follows:

$$G_1' = \frac{\left[ R' \sqrt{\frac{\pi}{2 \gamma_{O_2} r_1}} I \frac{3}{|2-p_2|} \left\{ \delta_2 r_1^{(2-p_2)/2} \right\} + \sqrt{\frac{2}{\pi \gamma_{O_2} r_1}} K \frac{3}{|2-p_2|} \left\{ \delta_2 r_1^{(2-p_2)/2} \right\} \right]}{\left[ R' \sqrt{\frac{\pi \gamma_{O_2} r_2}{2}} I \frac{3}{|2-p_2|} - 1 \left\{ \delta_2 r_2^{(2-p_2)/2} \right\} - \sqrt{\frac{2 \gamma_{O_2} r_2}{\pi}} K \frac{3}{|2-p_2|} - 1 \left\{ \delta_2 r_2^{(2-p_2)/2} \right\} \right]}$$

$$\frac{\frac{3}{2} Br_2}{\sqrt{\frac{2}{\pi \gamma_{01} r_1} K \frac{3}{|2-p_1|} \left\{ \delta_1 r_1^{(2-p_1)/2} \right\}}}, \quad (2.9b)$$

where  $R'$  may be obtained from equation (2.10) on replacing  $Q$  by  $Q'$ , which is given as

$$Q' = \frac{K \frac{3}{|2-p_1|} \left\{ \delta_1 r_1^{(2-p_1)/2} \right\}}{\gamma_{01} r_1 K \frac{3}{|2-p_1|} - 1 \left\{ \delta_1 r_1^{(2-p_1)/2} \right\}}. \quad (2.11b)$$

The constants  $F_1'$  and  $E_1'$  may be obtained from equations (2.13) and (2.14) respectively, on replacing  $R$  by  $R'$ .

The constants for  $p_2 \neq 2$  and  $p_1 = 2$  may be written as

$$G'' = \frac{\left[ R'' \sqrt{\frac{\pi}{2\gamma_{02} r_1}} I \frac{3}{|2-p_2|} \left\{ \delta_2 r_1^{(2-p_2)/2} \right\} + \sqrt{\frac{2}{\pi \gamma_{02} r_2}} K \frac{3}{|2-p_2|} \left\{ \delta_2 r_1^{(2-p_2)/2} \right\} \right] \frac{3}{2} Br_2}{\left[ R'' \sqrt{\frac{\pi \gamma_{02} r_2}{2}} I \frac{3}{|2-p_2|} - 1 \left\{ \delta_2 r_2^{(2-p_2)/2} \right\} \right] r_1 \eta_1 - \left[ \frac{2\gamma_{02} r_2}{\pi} K \frac{3}{|2-p_2|} - 1 \left\{ \delta_2 r_2^{(2-p_2)/2} \right\} \right]}, \quad (2.9c)$$

$$\text{where } \eta_j = \sqrt{\frac{9}{4} + \gamma_{0j}^2 r_j^2}, \quad j = 1 \text{ or } 2 \quad (2.15)$$

and  $R''$  is obtained from equation (2.10) on replacing  $Q$  by  $Q''$  which is expressed as

$$Q'' = \frac{1}{2 + \eta_1}. \quad (2.11c)$$

The constants  $F_1''$  and  $E_1''$  are also obtained as above from equations (2.13) and (2.14), on replacing  $R$  by  $R''$ . Similarly, the corresponding constants for  $p_2 = 2$  and different values of  $p_1$  may be written if we employ equation (2.7b) in place of (2.7a). Thus, for example, the equations corresponding to (2.9a), (2.10), (2.13) and (2.14) for  $p_1 < 2$  and  $p_2 = 2$  may be written as

$$\tilde{G}_1 = \underbrace{\frac{\tilde{R} r_1^{\eta_2} + r_1^{-\eta_2}}{\tilde{R}(2+\eta_2)r_2^{\eta_2} + (2-\eta_2)r_2^{-\eta_2}}}_{\text{[I]}} \underbrace{\frac{\frac{3}{2} Br_2}{\sqrt{\frac{\pi}{2\gamma_{01} r_1}} I \frac{3}{|2-p_1|} \left\{ \delta_1 r_1^{(2-p_1)/2} \right\}}}_{\text{[II]}} \quad (2.16)$$

$$\tilde{R} = r_1^{-2\eta_2} \left[ \frac{Q(\eta_2-2) + 1}{Q(\eta_2+2) - 1} \right], \quad (2.17)$$

$$\tilde{F}_1 = \frac{\frac{3}{2} Br_2}{\tilde{R} (2+\eta_2) r_2^{\eta_2} + (2-\eta_2) r_2^{-\eta_2}}, \quad (2.18)$$

$$\text{and } \tilde{E}_1 = \tilde{F}_1 \tilde{R}.$$

Here  $Q$  is given by equation (2.11). The value of constants for  $p_2 = 2$  and  $p_1 > 2$  may be obtained through replacing  $Q$  by  $Q'$  from equation (2.11b), and for  $p_2 = 2$  and  $p_1 = 2$  through replacing  $Q$  by  $Q''$  from equation (2.11c) in the equations (2.16) to (2.19). The denominator of factor [II] in equation (2.16) will change according to equations (2.9b) and (2.9c), respectively.

#### 2.2.4 Discussion

The values of the magnetic vector potential  $A_1$  and  $A_2$  are, thus, determined completely for different conductivity variations of the core and the shell. The electric field may be determined using equation (2.3a). The current density inside the conducting system may be expressed as

$$J_j = -i\omega \sigma_{oj} \left( \frac{r}{r_j} \right)^{-p_j} A_j, \quad j = 1, 2. \quad (2.20)$$

Numerical computations of the amplitude and phase (also the in-phase and quadrature components) of the complex quantity  $2J/3B$  at various distances from the centre, at an azimuth of 90 degrees, have been made to find the

effect of varying

- i) the frequency of energisation
- and ii) the conductivity contrast between the sphere and the shell.

The effect of inhomogeneity in the conductivity of the core on the current density distribution in the system has also been studied. The current density in the sphere will be denoted by  $J_c$  and that in the shell by  $J_s$ . The numerical values of the various parameters are indicated in the corresponding diagrams.

#### 2.2.4.1 Amplitude variation

It is observed that for all frequencies upto  $10^5$  hz, within which the quasi-static limit holds, the amplitude of the current density  $J_c$  in a covered sphere is less than that in an uncovered one (figure 2.2a, p.27). At low frequencies such as  $10^2$  hz, the cover is almost transparent and does not influence  $J_c$ . At  $10^3$  hz, the amplitude of  $J_c$  is greater, at all the depths given here, than that at  $10^2$  hz.

For a frequency of  $10^4$  hz,  $J_c$  further increases in the peripheral region on account of increased induction at higher frequencies. But at greater depths, it is reduced due to increased inductive shielding effect of the outer layers. At  $10^5$  hz the shielding due to the cover itself becomes so predominant

that  $J_c$  is reduced even at the surface ( $r = r_1$ ) of the sphere.

#### 2.2.4.2 Phase rotation

The phase of the current density vector, at various depths, in the shell and the sphere is shown in figure 2.2b. A parallelism (except for the central region of the sphere) between the curves for the covered and uncovered spheres at a particular frequency suggests that the downward shift of the curve is a measure of the phase rotation of the current density vector introduced by the cover. This phase rotation is also demonstrated in figure 2.3 (a, b) which shows argand-diagrams of the current density at  $5 \times 10^2$  Hz,  $5 \times 10^3$  Hz, and  $5 \times 10^4$  Hz for (a) an uncovered and (b) a covered sphere respectively.

Owing to the phase rotation, the in-phase component of the current density vector gets apparently enhanced by the cover in some cases in spite of a decrease in its amplitude. For the present combination of the conductivities and radii of the sphere and the shell, the in-phase component of  $J_c$  inside a covered sphere has a greater value than that in an uncovered one at  $10^3$  Hz as shown in figure 2.4.

It is also noteworthy that at this frequency, the maximum value of the in-phase component of  $J_c$  does not occur at the surface of the sphere but is at a depth

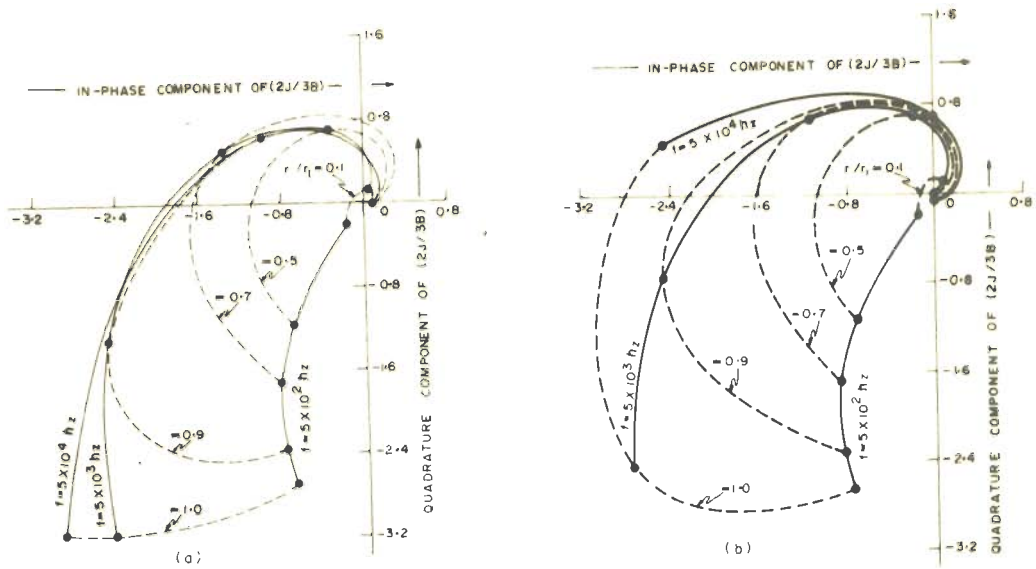


Fig.2-3 THE ARGAND DIAGRAMS OF THE NORMALISED CURRENT DENSITY AT DIFFERENT DEPTHS FOR (a) UNCOVERED SPHERE AND (b) COVERED SPHERE FOR DIFFERENT FREQUENCIES

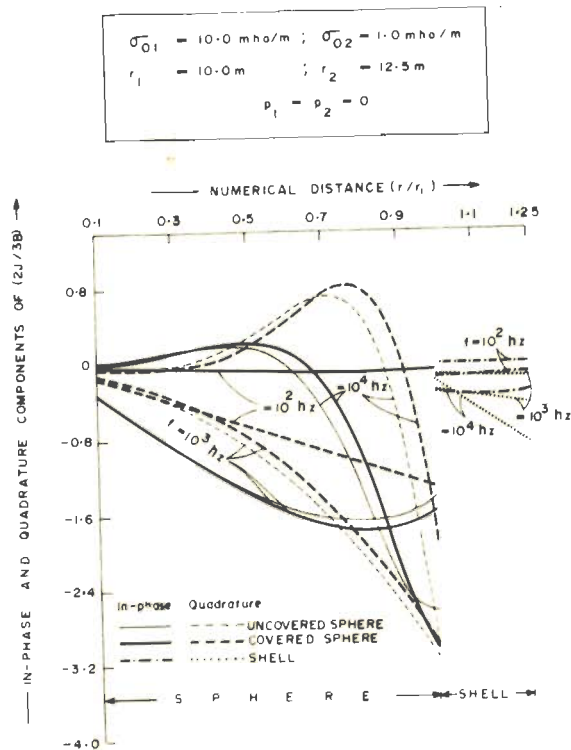


Fig.2-4 THE IN-PHASE AND QUADRATURE COMPONENTS OF THE NORMALISED CURRENT DENSITY FOR DIFFERENT FREQUENCIES

of about  $0.2r_1$  from the surface ( $r = r_1$ ). This maximum may be attributed to the mutually opposing influences, brought about by peripheral layers, of (i) the skin-effect which reduces the current density with depth and hence the in-phase component and (ii) the rotation of the current density vector towards the in-phase axis which increases the in-phase component. It also explains the appearance of a maximum in the in-phase component of  $J_c$ , for the uncovered case, inside the sphere. At higher frequencies, viz  $10^4$  hz and more, the in-phase component of  $J_c$  at the surface is greater than at  $10^3$  hz but decays steeply towards the centre of the sphere. The positive peak for the quadrature component of  $J_c$  at a particular depth ( $\approx 0.25r_1$  from the sphere surface) for  $10^4$  hz in figure 2.4 may also be explained in a similar way as the negative peak of the in-phase component at  $10^3$  hz.

#### 2.2.4.3 Resonance effect

Figure 2.5 shows a plot of amplitude, at various depths, against frequency of the field on a logarithmic scale. For an uncovered sphere the value of  $J_c$  at the surface ( $r = r_1$ ) increases continuously with increase in frequency to settle at a limiting value. For the internal layers, however, the current density attains a maximum at a frequency characterised by the induction numbers of the core and shell. The peaks shift towards the lower frequency side with increasing depth.



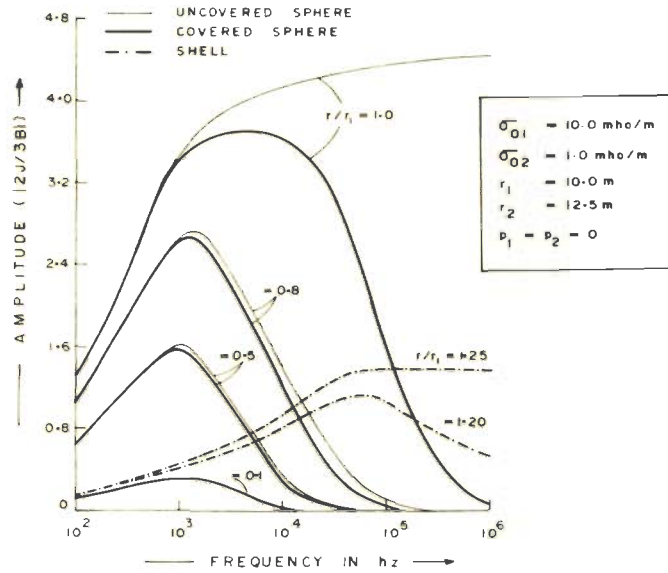


Fig. 2-5 THE AMPLITUDE OF THE NORMALISED CURRENT DENSITY IN THE SPHERE AND THE SHELL VERSUS FREQUENCY

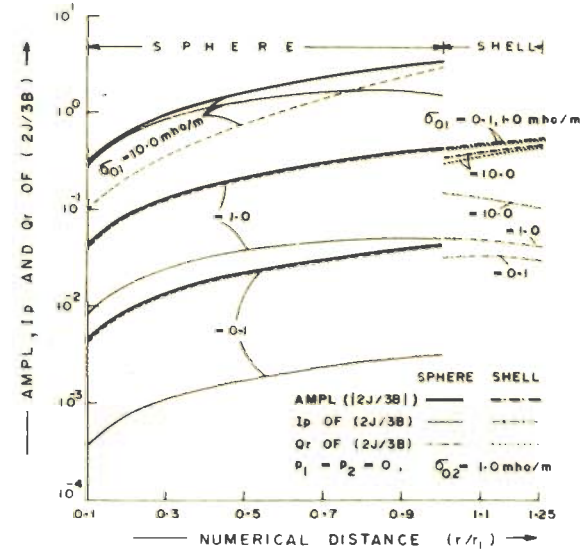


Fig. 2-6 THE INFLUENCE OF CHANGING THE CONDUCTIVITY OF THE SPHERE ON THE INDUCED CURRENT DENSITY FOR  $10^3$  hz. THE AMPLITUDE AS WELL AS THE IN-PHASE AND QUADRATURE COMPONENTS HAVE BEEN PLOTTED

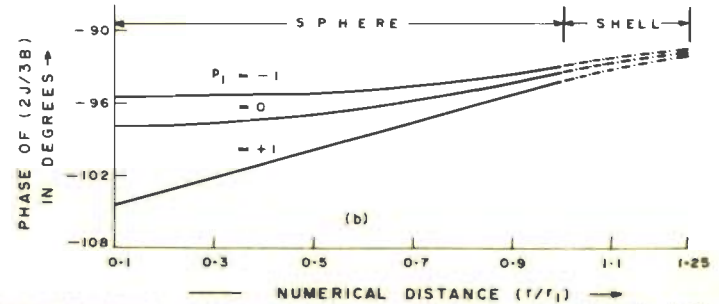
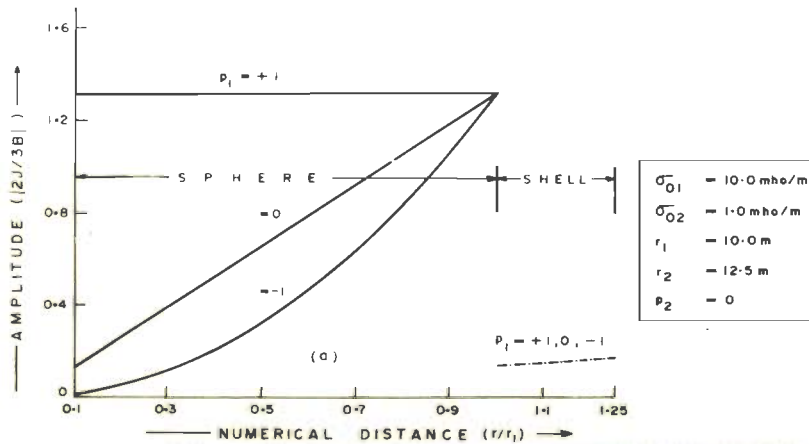


Fig. 2-7 THE EFFECT OF INHOMOGENEITY IN THE CONDUCTIVITY OF THE SPHERE ON THE (a) AMPLITUDE AND (b) PHASE OF THE CURRENT DENSITY FOR  $10^2$  hz

For a covered sphere the value of  $J_c$  at the surface ( $r = r_1$ ) also becomes maximum at nearly  $5 \times 10^3$  Hz. The resonance effect explains why the amplitude of  $J_c$  at  $10^3$  Hz, as shown in figure 2.2a, is greater than those at  $10^2$  Hz and  $10^4$  Hz (except in the peripheral region for the latter). The existence of the resonance phenomenon signifies the importance of multifrequency prospecting for an improved detection of an ore-body. Of course, to choose an appropriate range of frequencies may be a complicated prospecting problem unless there exists some general information about the conductivity of the target body.

A similar resonance phenomenon is observed for the less conducting shell at a higher frequency ( $\approx 10^5$  Hz) for which the shielding effect of the shell is likely to be maximum. The resonance effects have also been observed in the scattered field (Fuller, 1971 and Negi et al, 1973).

#### 2.2.4.4 Variation of the conductivity of the sphere

It is interesting to note that the amplitude of  $J_s$  decreases as the conductivity of the sphere is increased at  $10^3$  Hz (figure 2.6). However, the in-phase component of  $J_s$  shows a normal increase under these conditions and exhibits a peak value inside the shell (and not on its surface).

The effect of inhomogeneity in the conductivity of the sphere is presented only for two cases viz when  $\sigma_{01}$  (i) increases ( $p_1 = +1$ ) or (ii) decreases ( $p_1 = -1$ ), linearly from the peripheral region towards the centre. Figure 2.7 (a, b) shows the amplitude and phase of the current density at  $10^2$  Hz for  $p_1 = -1, 0$  and  $+1$ . At this frequency the amplitude of  $J_c$  decreases towards the centre if  $p_1 = -1$  as compared to that in a homogeneous sphere ( $p_1 = 0$ ). An interesting case arises for  $p_1 = +1$ , when the current density  $J_c$  remains almost unaltered with depth. In this case i.e.  $p_1 = 1$ , the decrease in the amplitude due to the shielding effect appears to be fully compensated by the increase in the conductivity towards the centre. If the inhomogeneity factor is further increased, the amplitude will vary depending upon the relative contributions of these two opposing factors. These observations have a direct bearing on the shielding process in media of inhomogeneous conductivities.

At  $10^3$  Hz, the value of  $J_c$  decreases in the peripheral region and increases in the central region with increase in  $p_1$  (figure 2.8a). A similar trend is visible at  $10^4$  Hz also, even though because of the increased induction effect, the influence of a linear inhomogeneity is not appreciable (figure 2.8b).

The decrease of  $J_s$  for both homogeneous and

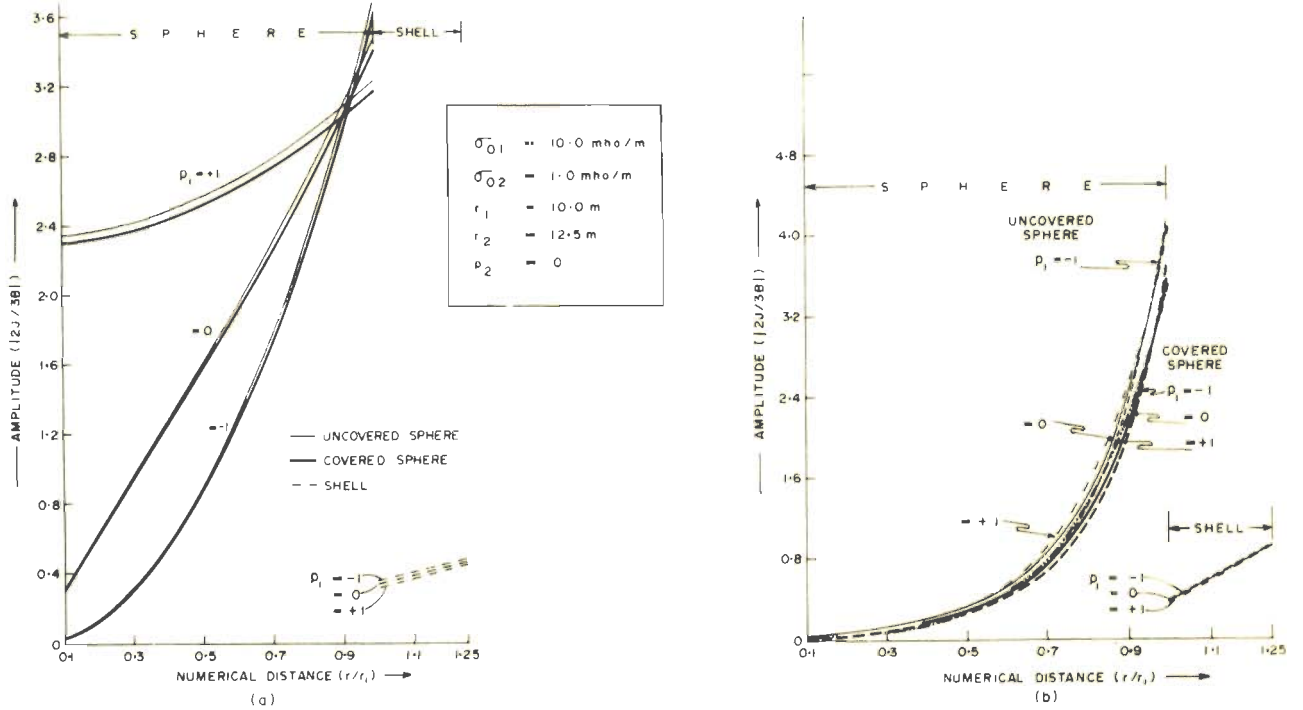


Fig 2-8 THE EFFECT OF INHOMOGENEITY IN THE CONDUCTIVITY OF THE SPHERE ON THE AMPLITUDE OF THE CURRENT DENSITY FOR (a)  $10^3 \text{ Hz}$  AND (b)  $10^4 \text{ Hz}$

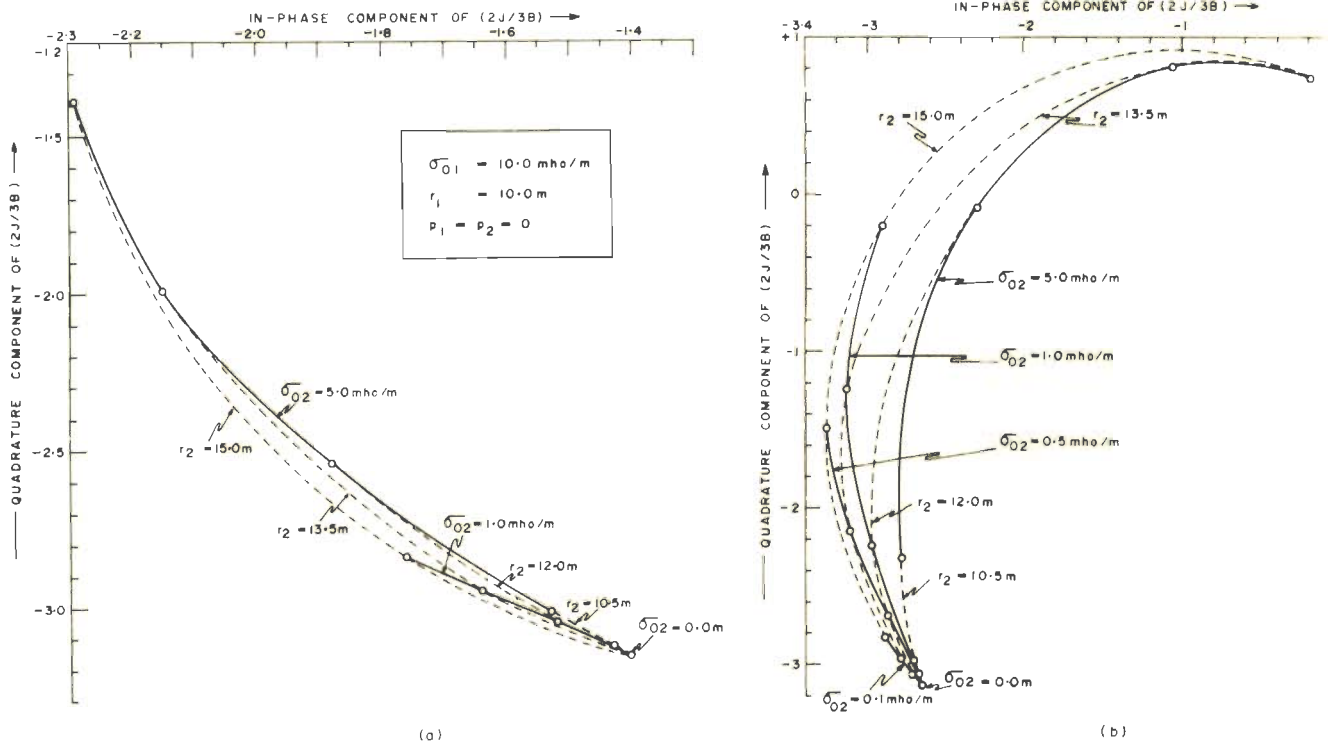


Fig 2-9 THE ARGAND DIAGRAMS OF THE NORMALISED CURRENT DENSITY ON THE SURFACE OF THE SPHERE SHOWING EFFECTS OF VARYING THE CONDUCTIVITY AND THICKNESS OF THE SHELL FOR (a)  $10^3 \text{ Hz}$  AND (b)  $10^4 \text{ Hz}$

inhomogeneous cores may, possibly, be attributed to the availability of more conducting region in deeper layers. This also explains the decrease in the current density  $J_c$  in the peripheral layers of an inhomogeneous sphere with increase in value of  $p_1$ .

#### 2.2.4.5 Variation of the conductivity and the thickness of the cover

Figure 2.9 (a, b) shows the variation of the in-phase and quadrature components of  $J_c$  at the surface of the sphere as both the conductivity ( $\sigma_{O_2}$ ) and the thickness ( $d_b$ ) of the shell increase from zero values to 5 mho/m and 5 m, respectively. Within these limits, the in-phase component of  $J_c$  increases and the quadrature component decreases monotonically with increase in either the conductivity or the thickness of the shell at a frequency of  $10^3$  hz (figure 2.9a). At this frequency the in-phase component of  $J_c$  for a covered sphere is greater than that in an uncovered one for all the  $\sigma_{O_2}$  and  $d_b$  values studied here. However, at  $10^4$  hz, the quadrature component shows a monotonic decrease, whilst the in-phase component shows a maximum for certain combinations of  $\sigma_{O_2}$  and  $d_b$  (figure 2.9b). Thus, for a combination ( $\sigma_{O_2} = 1$  mho/m,  $d_b = 3.5$ m) or ( $\sigma_{O_2} = 5$  mho/m,  $d_b = 0.75$ m) the in-phase component of  $J_c$  is found to be maximum. In all the cases, the amplitude decreases with increase of either the conductivity or the thickness, or both, of the shell.

### 2.2.5 Concluding remarks on current distribution in a covered sphere

The effect of increasing the frequency of the energising field on the induced current distribution is observed to be two fold viz

- a) enhancement of the current density towards the peripheral region, and
- b) increased inductive shielding of the interior due to the induced currents in the outer layers of the sphere and/or the shell which causes a diminution in the amplitude of the current density vector and its rotation in time phase.

A conducting cover of any thickness and conductivity has been found to decrease the amplitude of the currents in the sphere at all the frequencies. However, in some cases an enhancement of the in-phase component due to the cover is seen. This observation is explicable considering the second of the above factors. Further, since there is a direct correspondence between the electromagnetic response of a target and the currents induced in it, an increase in the in-phase component of the latter would cause an increase of the in-phase component of the former.

The reduction of the current density in the shell with increase in the core-conductivity may increase the current in the core and possibly explain the

enhancement of anomalies observed in scale-model experiments over conducting bodies placed in a partially conducting medium.

The above findings on induced currents are expected to help in evolving a better understanding of the behavior of the scattered field by conductors particularly when surrounded by a conducting medium.

### 2.3 Scattered Field Due to a Two-Layer Permeable Conducting Sphere in a Dipolar Field

#### 2.3.1 Formulation and solution

Employing a similar spherical model, as used above for investigations on the induced currents, the scattered field outside the sphere has also been calculated. The energising field is obtained from an oscillating magnetic dipole (figure 2.10). The electromagnetic field at any point  $P (r, \theta, \phi)$  due to a dipolar source is, in general, made up of two partial fields  $E_u$ ,  $H_u$  and  $E_v$ ,  $H_v$  which, in turn, are derivable from two scalar potentials  $U$  and  $V$ . The two fields may be described as transverse magnetic (TM) and transverse electric (TE), respectively (Debye, 1909 and March, 1953).

If the magnetic dipole is assumed to be radial, only TE modes of electric and magnetic fields exist. The field vectors for this case may be expressed as

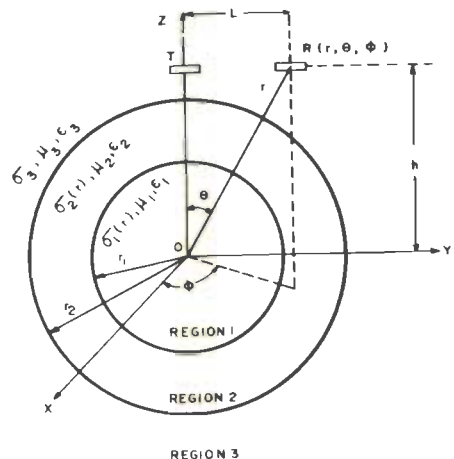


Fig.2-10 A COVERED SPHERE IN A RADIAL DIPOLAR FIELD

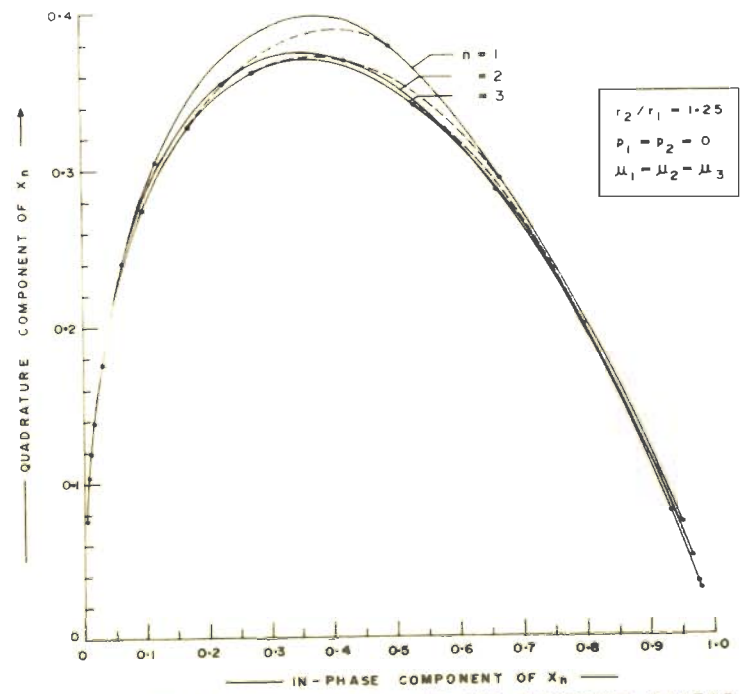


Fig.2-11 ANOMALY INDEX DIAGRAM OF THE RESPONSE FACTOR  $X_n$  FOR  $n=1,2, \text{ AND } 3$

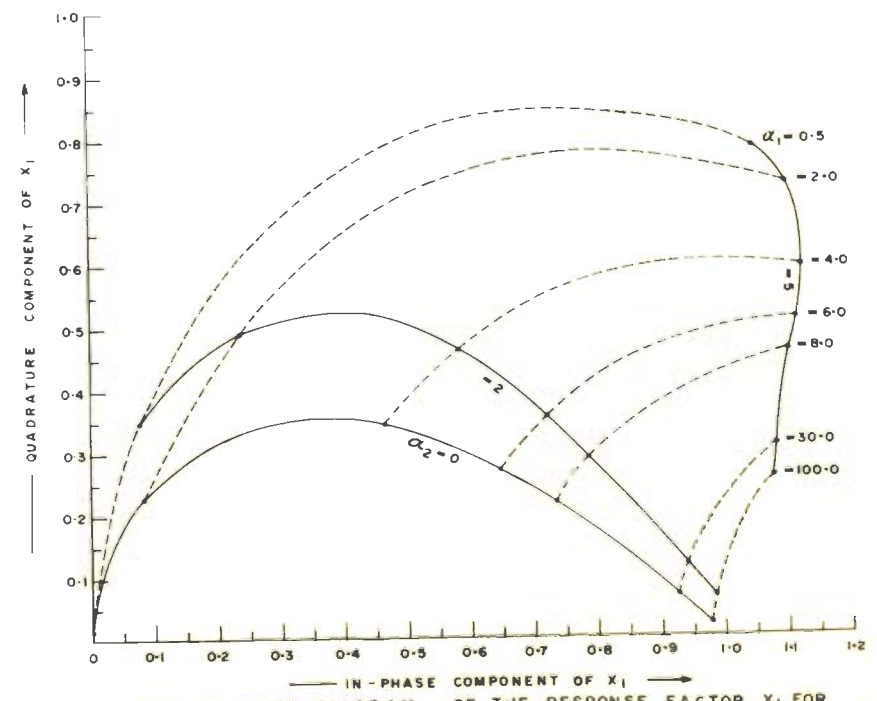


Fig.2-12 ANOMALY INDEX DIAGRAM OF THE RESPONSE FACTOR  $X_1$  FOR DIFFERENT CONDUCTIVITIES OF THE SHELL OVER A NON-PERMEABLE SPHERE



$$E_v = \left[ -\frac{i\mu_j \omega}{r \sin \theta} \frac{\partial(rV_j)}{\partial \phi} \right] e_\theta + \left[ \frac{i\mu_j \omega}{r} \frac{\partial(rV_j)}{\partial \theta} \right] e_\phi \quad (2.21)$$

and

$$H_v = \left[ \frac{\partial^2(rV_j)}{\partial r^2} - \gamma_j^2 (rV_j) \right] e_r + \left[ \frac{1}{r} \frac{\partial^2(rV_j)}{\partial r \partial \theta} \right] e_\theta + \left[ \frac{1}{r \sin \theta} \frac{\partial^2(rV_j)}{\partial r \partial \phi} \right] e_\phi \quad (2.22)$$

Here  $j = 1, 2$  or  $3$  denote the three different regions as shown in figure 2.10 and  $e_r, e_\theta,$  and  $e_\phi$  denote unit vectors along  $r, \theta,$  and  $\phi$  directions respectively. The scalar potential  $V_j$  satisfies the following equation

$$\frac{\partial}{\partial r} \left( r^2 \frac{\partial V_j}{\partial r} \right) + \frac{1}{\sin \theta} \frac{\partial}{\partial \theta} \left( \sin \theta \frac{\partial V_j}{\partial \theta} \right) + \frac{1}{\sin^2 \theta} \frac{\partial^2 V_j}{\partial \phi^2} - \gamma_j^2 r^2 V_j = 0. \quad (2.23)$$

The potential  $V_j$  as a solution of equation (2.23) may be written in the three regions as follows:

(1) Region 3

$$V_3 = V_p + \sum_{n=0}^{\infty} a_n \frac{\xi_n(\gamma_3 r)}{r} P_n(\cos \theta) \quad (2.24)$$

where  $V_p$ , the potential of the primary field is given as (March, 1953):

$$V_p = \frac{1}{h} \sum_{n=0}^{\infty} a_{pn} \frac{\psi_n(\gamma_3 r)}{r} P_n(\cos \theta), \quad (2.25)$$

$$a_{pn} = \frac{(2n+1) \xi'_n(\gamma_3 h)}{\gamma_3 h}, \quad (2.25a)$$

$$\psi_n(\gamma_3 r) = \sqrt{\frac{\pi \gamma_3 r}{2}} I_{n+\frac{1}{2}}(\gamma_3 r), \quad (2.25b)$$

and

$$\xi_n(\gamma_3 r) = \sqrt{\frac{2 \gamma_3 r}{\pi}} K_{n+\frac{1}{2}}(\gamma_3 r). \quad (2.25c)$$

The second term on the right hand side of equation (2.24) is the secondary potential which may be termed as  $V_{3s}$ .

(2) Region 2

$$V_2 = \sum_{n=0}^{\infty} \left[ b_n \frac{M_n(\gamma_2 r)}{r} + c_n \frac{N_n(\gamma_2 r)}{r} \right] P_n(\cos \theta) \quad (2.26)$$

where the functions  $M_n$  and  $N_n$  are defined in general as

$$M_n(\gamma_j r) = \sqrt{\frac{\pi \gamma_{0j} r}{2}} I_{\frac{2n+1}{|2-p_j|}} \left\{ \delta_j r^{(2-p_j)/2} \right\}, \quad (2.27a)$$

or

$$M_n(\gamma_j r) = r^{\frac{1}{2} + \sqrt{(n+\frac{1}{2})^2 + \gamma_{0j}^2}} r_j^2, \quad (2.27b)$$

for  $p_j = 2$ ,

and

$$N_n(\gamma_j r) = \sqrt{\frac{2\gamma_{0j} r}{\pi}} K_{\frac{2n+1}{|2-p_j|}} \left\{ \delta_j r^{(2-p_j)/2} \right\}, \quad (2.28a)$$

for  $p_j \neq 2$

or

$$N_n(\gamma_j r) = r^{\frac{1}{2} - \sqrt{(n+\frac{1}{2})^2 + \gamma_{0j}^2}} r_j^2, \quad (2.28b)$$

for  $p_j = 2$ .

The value of  $\delta_j$  is given by equation (2.12).

### (3) Region 1

$$V_1 = \sum_{n=0}^{\infty} d_n \frac{M_n(\gamma_1 r)}{r} P_n(\cos \theta), \text{ for } p_1 \leq 2 \quad (2.29)$$

or

$$V_1 = \sum_{n=0}^{\infty} d_n \frac{N_n(\gamma_1 r)}{r} P_n(\cos \theta), \text{ for } p_1 > 2. \quad (2.29a)$$

The constants can be determined by applying the boundary conditions at  $r = r_1$  and  $r_2$  as in the case of induced currents. After the necessary algebra we obtain,

$$a_n = a_{pn} \frac{\Psi_n(\gamma_3 r_2)}{\xi_n(\gamma_3 r_2)} R_n, \quad (2.30)$$

where,

$$R_n = \frac{\left[ \left\{ M_n(\gamma_2 r_2) - \beta_n N_n(\gamma_2 r_2) \right\} - \frac{\mu_2}{\mu_3} \frac{\gamma_3 \Psi'_n(\gamma_3 r_2)}{\Psi_n(\gamma_3 r_2)} \left\{ M_n(\gamma_2 r_2) - \beta_n N_n(\gamma_2 r_2) \right\} \right]}{\left[ \frac{\mu_2}{\mu_3} \gamma_3 \frac{\xi'_n(\gamma_3 r_2)}{\xi_n(\gamma_3 r_2)} \left\{ M_n(\gamma_2 r_2) - \beta_n N_n(\gamma_2 r_2) \right\} - \left\{ M'_n(\gamma_2 r_2) - \beta_n N'_n(\gamma_2 r_2) \right\} \right]} \quad (2.31)$$

with

$$\beta_n = \frac{\frac{\mu_1}{\mu_2} M_n(\gamma_1 r_1) M'_n(\gamma_2 r_1) - M'_n(\gamma_1 r_1) M_n(\gamma_2 r_1)}{\frac{\mu_1}{\mu_2} M_n(\gamma_1 r_1) N'_n(\gamma_2 r_1) - M'_n(\gamma_1 r_1) N_n(\gamma_2 r_1)}, \quad (2.32a)$$

for  $p_1 \leq 2$ ,

or

$$\beta_n = \frac{\frac{\mu_1}{\mu_2} N_n(\gamma_1 r_1) M_n'(\gamma_2 r_1) - N_n'(\gamma_1 r_1) M_n(\gamma_2 r_1)}{\frac{\mu_1}{\mu_2} N_n(\gamma_1 r_1) N_n'(\gamma_2 r_1) - N_n'(\gamma_1 r_1) N_n(\gamma_2 r_1)}, \quad (2.32b)$$

for  $p_1 > 2$ .

The expression for  $V_{3S}$  can be further simplified if the frequency of the energising field is assumed to be so low that  $|\gamma_3| r \ll 1$ . It may then be written

$$V_{3S} = \sum_{n=1}^{\infty} \frac{r_1^{2n+1}}{h^{n+1} r^{n+1}} X_n P_n(\cos \theta) \quad (2.23)$$

where

$$X_n = \left( \frac{r_2}{r_1} \right)^{2n+1} R_n. \quad (2.23a)$$

The complex quantity  $X_n$ , termed as the response factor, is proportional to the moments of the multipoles excited in the sphere-shell system. The generalised expression for  $X_n$  can be reduced to the particular cases studied by Wait (1951 and 1953a), March (1953), Ward (1959) and Negi (1962c and 1967) under appropriate simplifying assumptions. The in-phase and quadrature components of  $X_n$  for different values of  $n$  have been computed. The case  $n = 1$  corresponds to

excitation by a uniform field. It can be seen that for a particular value of the induction number  $\alpha_1 (= \sqrt{\sigma_{01} \mu_1 \omega r_1^2})$ , the value of  $X_n$  decreases rapidly with increasing  $n$  (figure 2.11). Even for large values of  $\alpha_1$  say 50,  $[V_s]_{n=4}$  is about 1.56 percent of  $[V_s]_{n=1}$  (Negi et al, 1973) when the other parameters are  $h/r_1 = 2.0$ ,  $r/r_1 = 1.95$ ,  $r_2/r_1 = 1.25$ , and  $\alpha_2 (= \sqrt{\sigma_{02} \mu_2 \omega r_2^2}) = 1$ .

Further, the general qualitative behavior of the various terms for different values of  $n$  is the same. The curves showing the effect of the cover on the response of the sphere have, therefore, been presented here only for  $n=1$ .

### 2.3.2 Discussion

In contrast to the study of the induced currents, there is an inherent difficulty here in reckoning the quantity which may effectively represent the response of the target in presence of a cover. In the field, it is the total anomaly caused by the target and its surrounding medium which is measured. This quantity corresponds to  $X_1$ . However, Negi (1967) and Gupta Sarma and Maru (1971) indicated that the effective contribution of the target may correspond to a quantity  $X_1 - X_1^{r_2}$  where  $X_1^{r_2}$  is the response factor of a sphere of radius  $r_2$  and a conductivity equal to that of the shell. A comparison of this factor with  $X_1^{r_1}$  which is the response factor of the core, gives the influence of the conducting cover on the

response of the core. Notwithstanding, presently the variation of  $X_1$  alone is studied and field corresponding to the factor  $X_1 - X_1^r$  is examined while studying the anomaly profiles in Section 2.4.

### 2.3.2.1 Variation of the conductivity of the shell

The influence of increasing the conductivity of the shell on the factor  $X_1$  which represents the total response of the sphere - shell system is shown in figure 2.12 for a non-permeable sphere and in figure 2.13 for a permeable one. The curve  $\alpha_2 = 0$  corresponds to an uncovered single sphere. As  $\alpha_2$  is increased, both the in-phase and the quadrature components of the response factor  $X_1$  are enhanced. The enhancement is more pronounced for low values of  $\alpha_1$ . For high values of  $\alpha_2$  (say 5) the behavior of the in-phase component of the response appears to be quite anomalous. It increases with increase in  $\alpha_1$ , attains a maximum value and then decreases with further increase in  $\alpha_1$ .

The decrease of the in-phase component with increase in  $\alpha_1$  (for  $\alpha_2 = 5$ ) implies that under these circumstances the in-phase response of a body of a given conductivity is smaller than that of a less conducting one when both are covered by similar shells. The phenomenon can be explained in terms of the phase rotation of the induced current vector in the sphere due

to the shell. For the present situation, the in-phase component of the response vectors due to the shell and the sphere are in opposition. Because of large  $\alpha_2$  value, the response due to the shell predominates over that due to the sphere for small values of  $\alpha_1$ . An increase in  $\alpha_1$  causes an increase in the in-phase component of the sphere response and consequent reduction in the total response of the composite system. Such a phenomenon will, thus, cause an ambiguity in the interpretation of the e.m. prospecting data.

#### 2.3.2.2 Variation of the frequency of energisation

The curves in figures 2.12 and 2.13 have been drawn assuming a fixed value of  $\alpha_2$  and the variation of the total response has been studied with change in  $\alpha_1$  alone. Figure 2.14(a, b) depicts the variation of the response with frequency which amounts to the variation of both  $\alpha_1$  and  $\alpha_2$ . The resonance effect observed for induced currents as described in Section 2.2.5.3 is noticeable from the scattered field also. Here two distinct peaks appear for the quadrature component. The first one at  $10^3$  hz corresponds to the situation when the shell is more or less transparent and the contribution to the total response is predominantly due to the core. As the frequency of the energising field is increased, the response of the shell as well as its masking influence increases due to increased induction. A



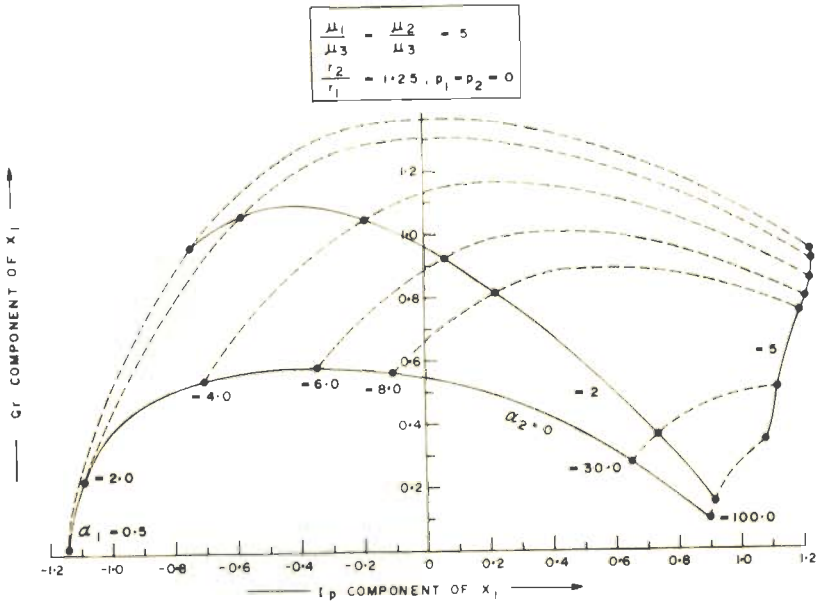


Fig. 2-13 ANOMALY INDEX DIAGRAMS OF THE RESPONSE FACTOR  $X_1$  FOR DIFFERENT CONDUCTIVITIES OF THE SHELL OVER A PERMEABLE SPHERE

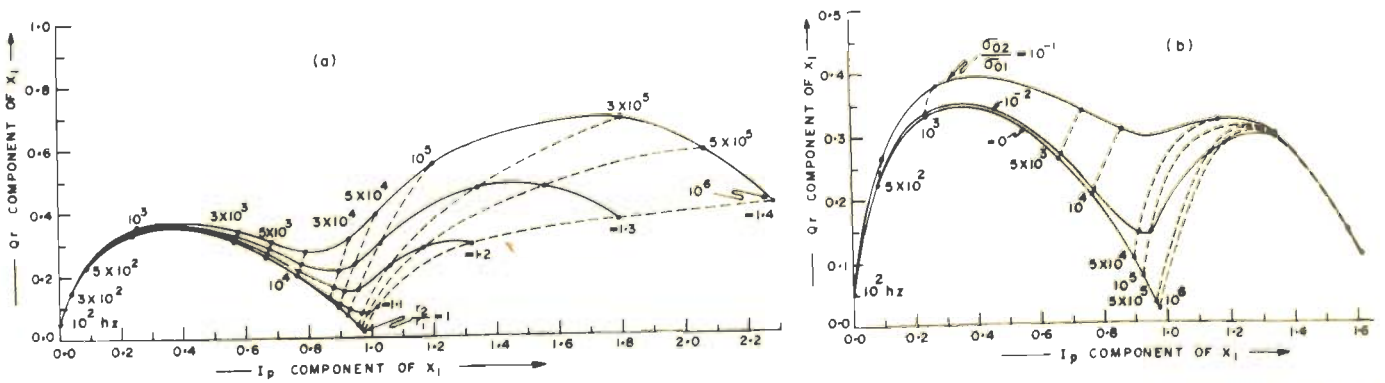


Fig. 2-14 MULTIFREQUENCY ANOMALY INDEX DIAGRAMS OF THE RESPONSE FACTOR  $X_1$  FOR DIFFERENT (a) THICKNESSES AND (b) CONDUCTIVITIES OF THE SHELL

second peak in the quadrature component is obtained at a frequency of about  $10^5$  hz which is mainly due to the shell. For small values of  $\frac{\sigma_{02}}{\sigma_{01}}$  and  $\frac{r^2}{r_1}$ , the second peak is smaller than the first peak. However, it increases with increase in either the conductivity or the thickness of the shell and surpasses even the first peak. A delineation of boundary between the sphere and shell can be made from the  $I_p$  component of the response also, as seen from an inflexion observed in the frequency characteristics of  $X_{1r}$ . Corresponding time-domain results have been reported both in experimental (Velikin and Bulgakov, 1967) and theoretical studies (Rao et al, 1973).

#### 2.4 Profiles of the E.M. Response Over A Covered Conducting Sphere

In order to have a direct correlation of the theoretical results with those of the experimental and field investigations, the response has also been computed along a profile for a T001 L100 R001 prospecting system. The magnetic field due to a z-directed dipole can be obtained by combining the fields of two dipoles of which one has a radial orientation and the other transverse (March, 1953).

As seen above from the results pertaining to the response factor  $X_n$ , the essential qualitative characteristics of the problem are brought out by

computing only the first term viz n=1 in equation (2.23). The response profiles have, therefore, been prepared corresponding to n=1 alone. Following Zakharov (1964) and Bhattacharya and Sinha (1965), the expression for the vertical component of the response field for the covered sphere may be written as

$$H_z = -\frac{1}{2}X_1 \left(\frac{r_1}{L}\right)^3 \frac{\left[2\frac{h^2}{L^2} - \left(\frac{x}{L} + \frac{1}{2}\right)^2\right] \left[2\frac{h^2}{L^2} - \left(\frac{x}{L} - \frac{1}{2}\right)^2\right] + 9\frac{h^2}{L^2} \left(\frac{x^2}{L^2} - \frac{1}{4}\right)}{\left[\frac{h^2}{L^2} + \left(\frac{x}{L} + \frac{1}{2}\right)^2\right]^{5/2} \left[\frac{h^2}{L^2} + \left(\frac{x}{L} - \frac{1}{2}\right)^2\right]^{5/2}}, \quad (2.33)$$

where,

$H_z$  is the vertical component of the magnetic field expressed in terms of the primary field,

$L$  is the distance between the transmitter (T) and the receiver (R),

$x$  is the horizontal distance between the centre of the sphere and the mid-point of the T-R system, and

$n$  is height of the T-R system from the centre of the spherical model.

All the distances have been normalised in terms of  $L$  (figure 2.10).

The computations of the in-phase and

quadrature components of both (i) the vertical component  $H_Z$  of total response field due to the composite system and (ii) the quantity  $H_Z - H_Z^{r2}$ , have been made, where  $H_Z^{r2}$  is the vertical component of response due to a sphere of radius  $r_2$  and conductivity  $\sigma_{O_2}$ . The second factor can be regarded as the vertical component of the effective response from the core in presence of the cover (cf. Section 2.3.2).

The profiles presented here pertain to two heights of the T-R system viz  $h/L = 0.3$  and  $h/L = 0.4$  and frequencies ranging from  $10^3$  hz to  $10^5$  hz. Figures 2.15 and 2.17 show the profiles of  $H_Z$  and  $H_Z^{r1}$  for  $\sigma_{O_2} = 1.0$  mho/m at  $h/L = 0.3$  and  $0.4$  respectively. Figures 2.20 and 2.22 depict the corresponding profiles for a less conducting shell, viz  $\sigma_{O_2} = 0.1$  mho/m. As expected, the Ip component of the total response  $H_Z$  increases and the Qr component decreases with increase in frequency. In all the cases  $H_Z$  is greater than that  $H_Z^{r1}$ .

The behavior of  $H_Z - H_Z^{r2}$  with change in frequency, however, shows some interesting features. The Ip component of  $H_Z^{r2}$  increases more rapidly than that of  $H_Z$ . Consequently, the Ip component of  $H_Z - H_Z^{r2}$  for  $10^4$  hz becomes less than that for  $10^3$  hz (figure 2.16 and 2.18). For  $f = 10^5$  hz, the Ip component of

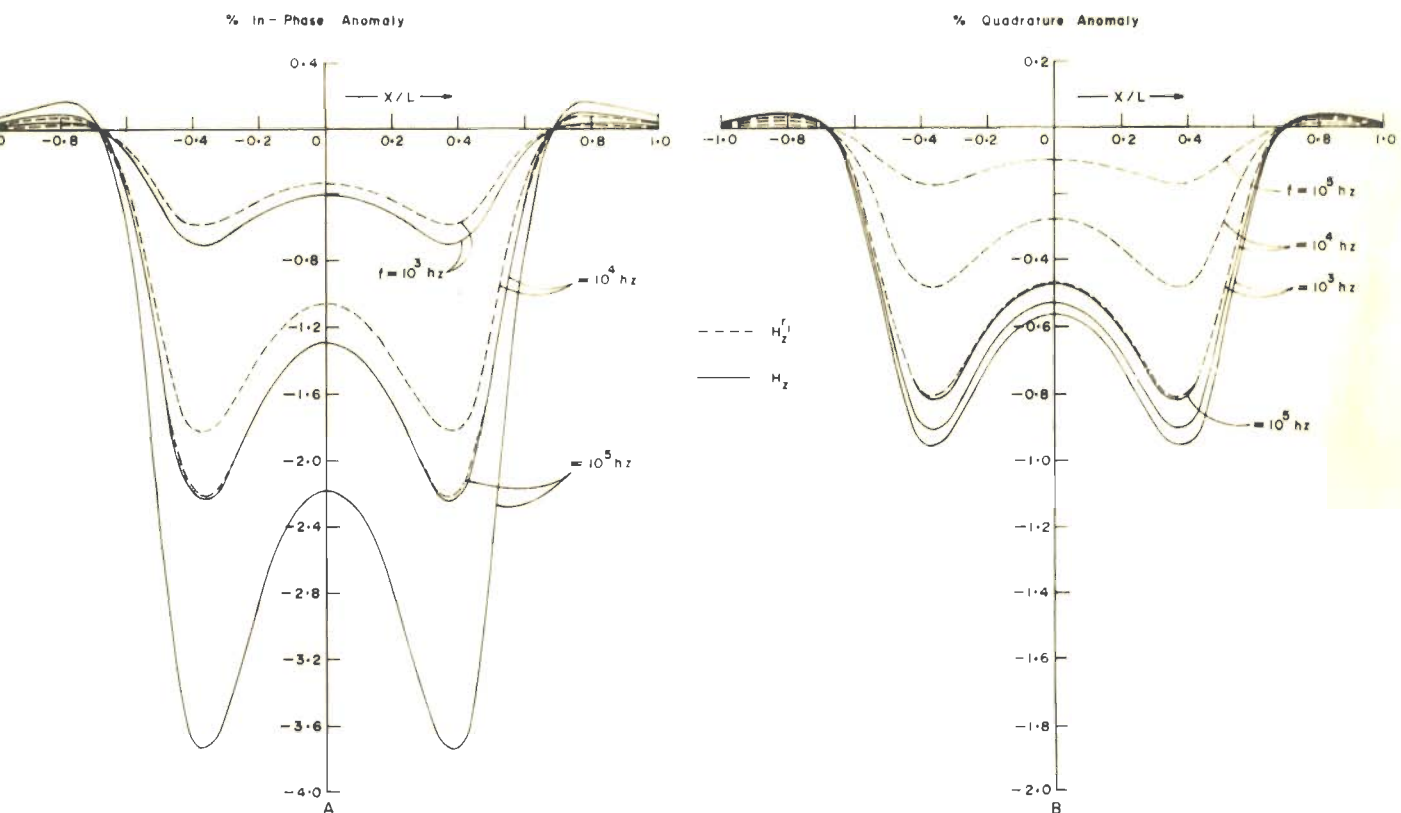


Fig. 2-15 PROFILES OF  $H_z^{r1}$  AND  $H_z$  OVER A COVERED SPHERE FOR DIFFERENT FREQUENCIES ( $h/L = 0.3$ ,  $\sigma_{02} = 1.0$  mho/m)

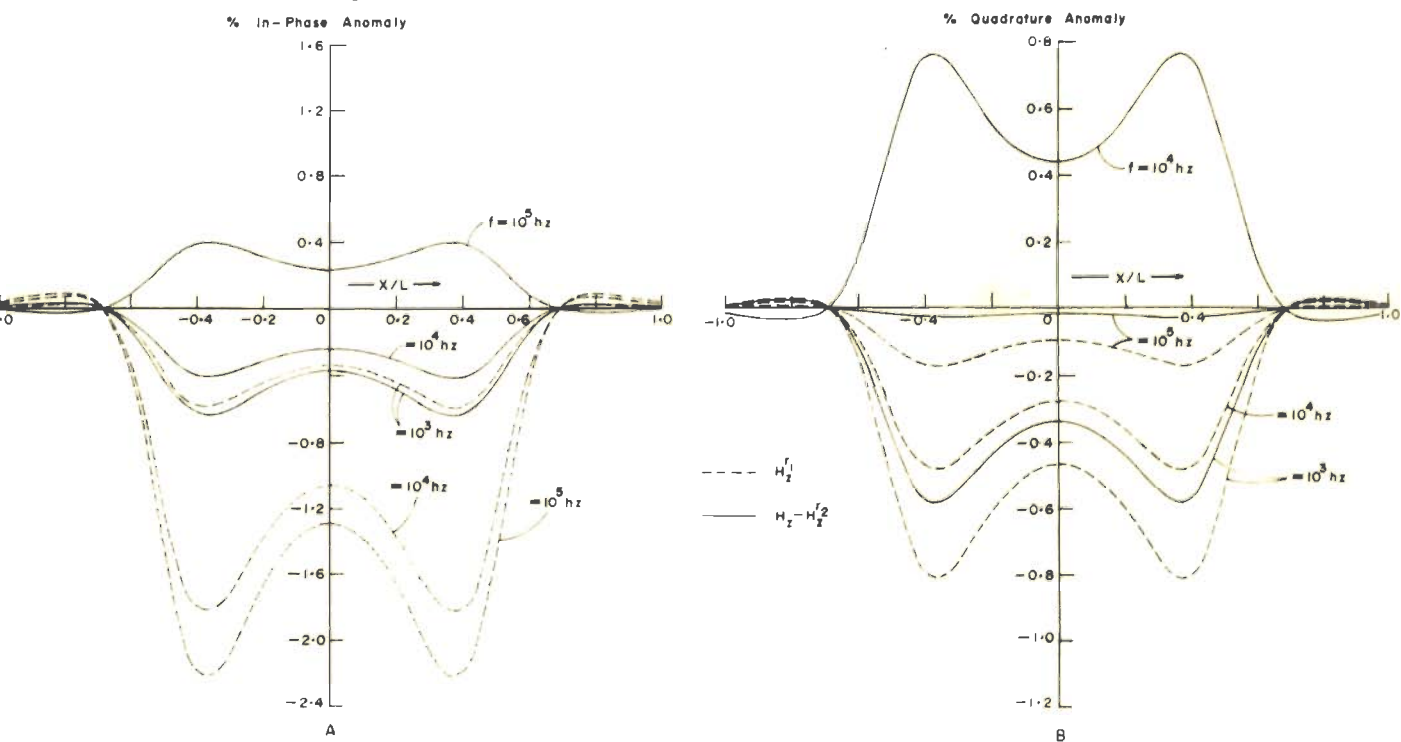


Fig. 2-16 PROFILES OF  $H_z^{r1}$  AND  $H_z - H_z^{r2}$  OVER A COVERED SPHERE FOR DIFFERENT FREQUENCIES ( $h/L = 0.3$ ,  $\sigma_{02} = 1.0$  mho/m)

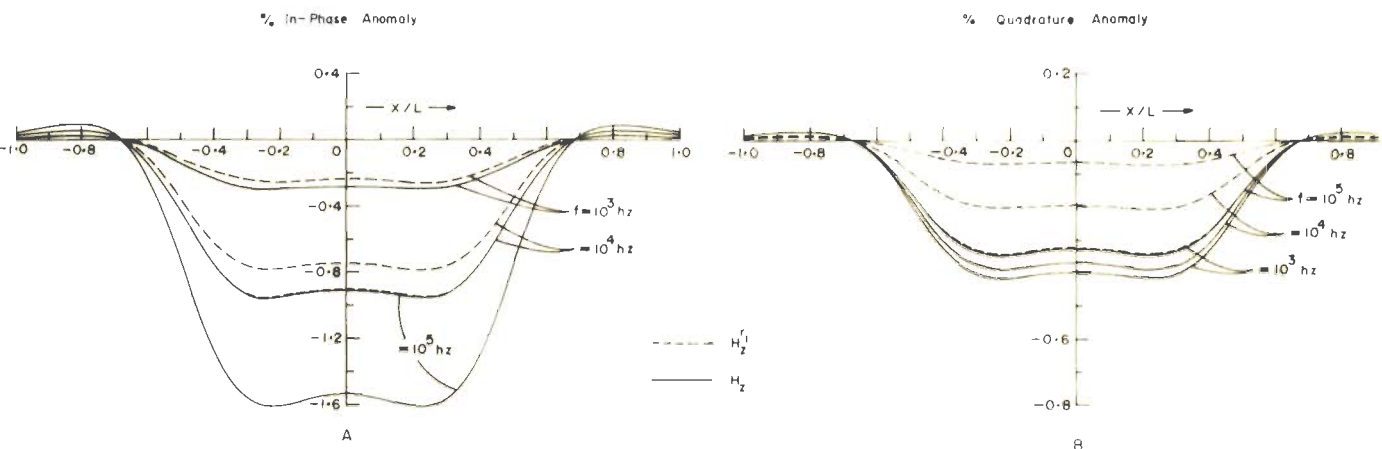


Fig. 2-17 PROFILES OF  $H_z^{r1}$  AND  $H_z$  OVER A COVERED SPHERE FOR DIFFERENT FREQUENCIES ( $h/L=0.4$ ,  $\sigma_{02}=1.0$  mho/m)

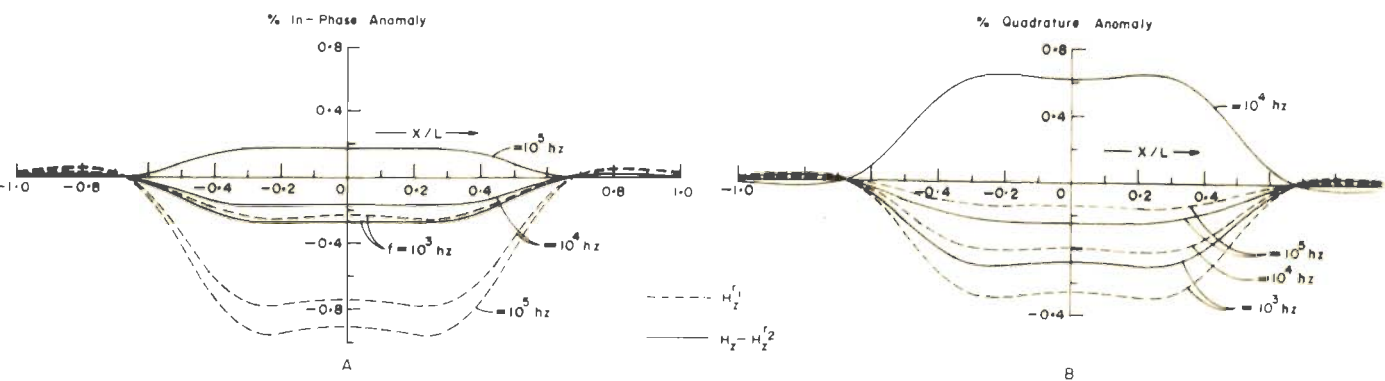


Fig. 2-18 PROFILES OF  $H_z^{r1}$  AND  $H_z - H_z^{r2}$  OVER A COVERED SPHERE FOR DIFFERENT FREQUENCIES ( $h/L=0.4$ ,  $\sigma_{02}=1.0$  mho/m)

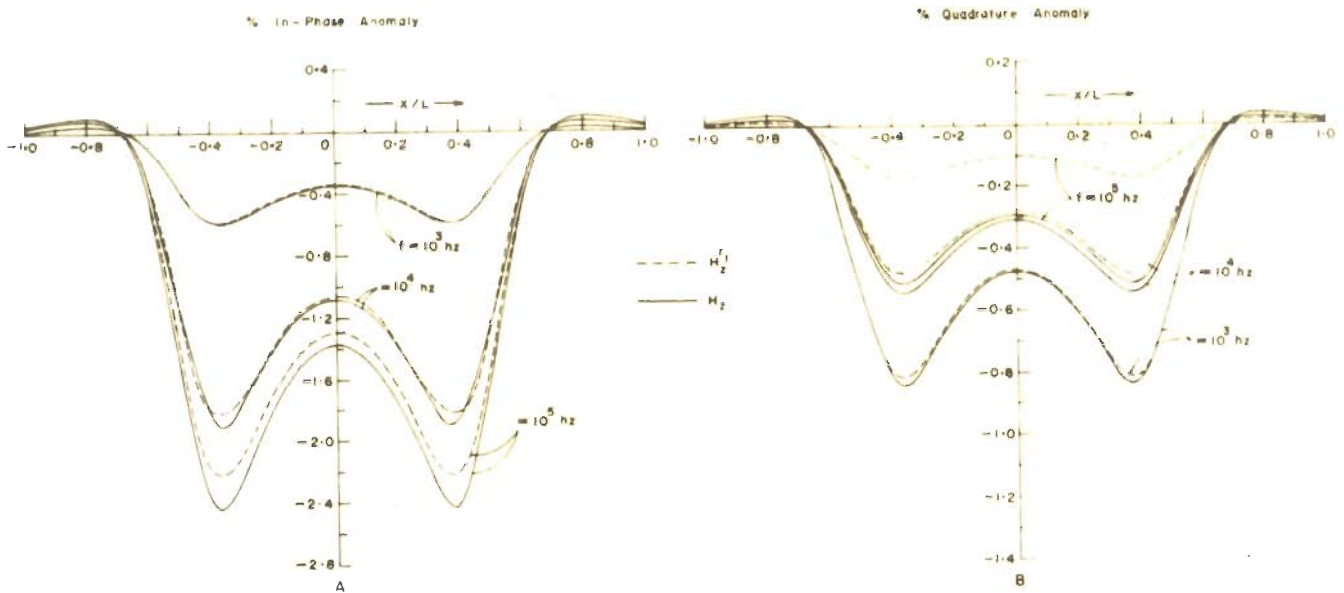


Fig. 2-20 PROFILES OF  $H_z^r$  AND  $H_z$  OVER A COVERED SPHERE FOR DIFFERENT FREQUENCIES ( $h/L = 0.3$ ,  $\bar{\sigma}_{02} = 0.1$  mho/m)

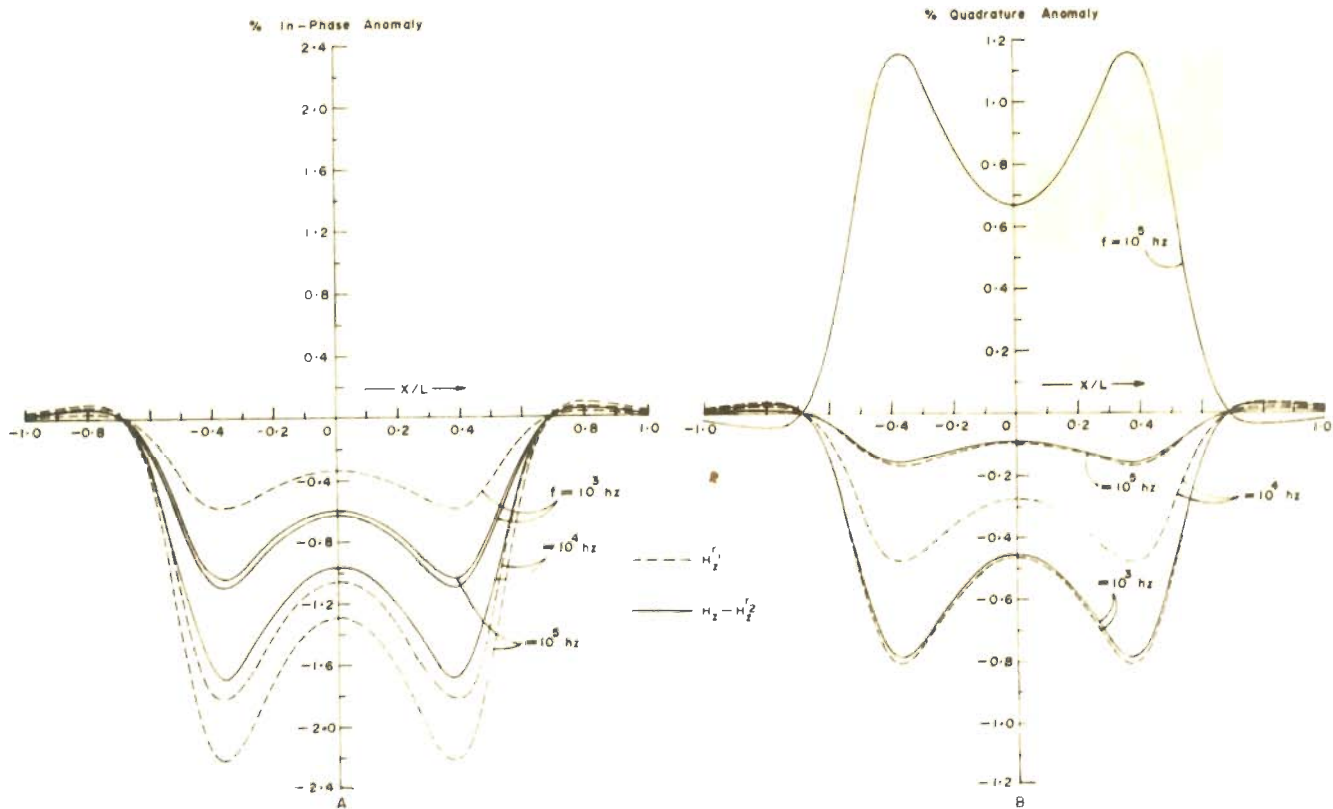
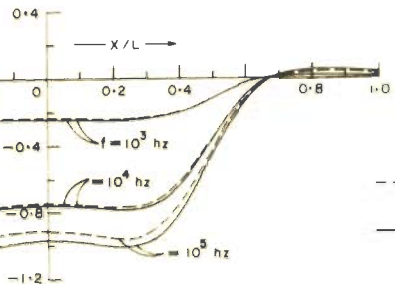
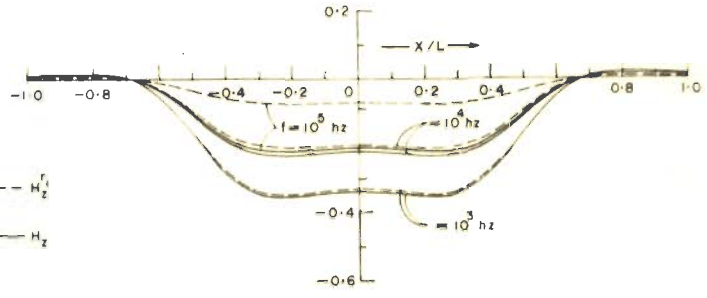


Fig. 2-21 PROFILES OF  $H_z^r$  AND  $H_z - H_z^r$  OVER A COVERED SPHERE FOR DIFFERENT FREQUENCIES ( $h/L = 0.3$ ,  $\bar{\sigma}_{02} = 0.1$  mho/m)

% In-Phase Anomaly



% Quadrature Anomaly

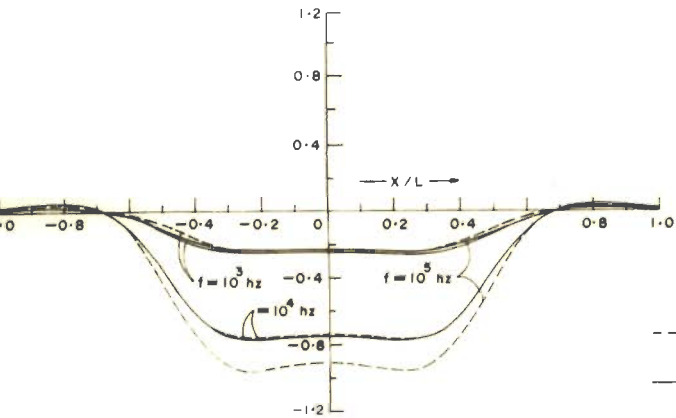


A

B

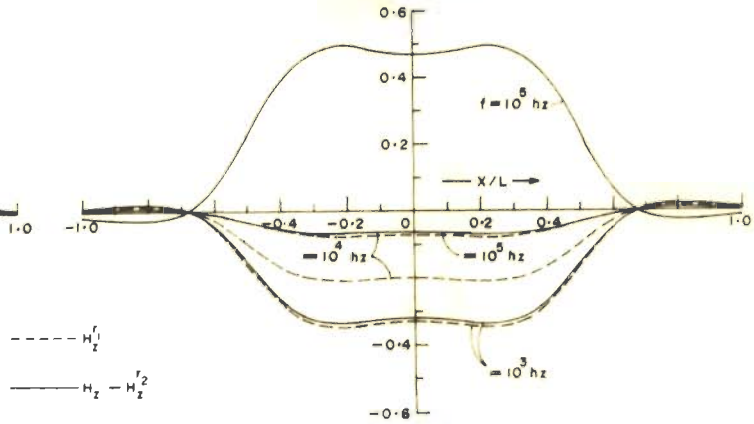
Fig. 2-22 PROFILES OF  $H_z^r_1$  AND  $H_z$  OVER A COVERED SPHERE FOR DIFFERENT FREQUENCIES ( $h/L = 0.4$ ,  $\sigma_{O_2} = 0.1$  mho/m)

% In-Phase Anomaly



A

% Quadrature Anomaly



B

Fig. 2-23 PROFILES OF  $H_z^r_1$  AND  $H_z - H_z^r_2$  OVER A COVERED SPHERE FOR DIFFERENT FREQUENCIES ( $h/L = 0.4$ ,  $\sigma_{O_2} = 0.1$  mho/m)



$H_z^r$  becomes even greater than that of  $H_z$  as shown by the inverted profile of the Ip component of  $H_z - H_z^r$ . The computation for some intermediate frequencies between  $5 \times 10^3$  hz and  $5 \times 10^4$  hz reveals a band of frequencies for which the Ip component of  $H_z^r$  is greater than that of  $H_z$ . This implies that the Ip response of a homogeneous sphere of radius  $r_2$  and conductivity  $\sigma_{O_2}$  is greater than that of a two-layer spherical model of the same dimension but enclosing a core of higher conductivity within it. The Qr component of  $H_z - H_z^r$  decreases with increase in frequency from  $10^3$  hz, becomes negative and acquires a peak negative value for about  $10^4$  hz, and again starts reducing with further increase in frequency. For  $\sigma_{O_2} = 0.1$  the phenomenon of reduction of the Ip component of  $H_z - H_z^r$  is, naturally, less pronounced. But still, as seen from figures 2.21 and 2.23, the Ip component of  $H_z - H_z^r$  for  $f = 10^5$  hz is less than at  $10^4$  hz.

The paradoxical behavior of the Ip component of  $H_z - H_z^r$  is similar to that observed in figure 2.12 when for a particular value of the induction number of the shell, the Ip component of the response is found to decrease with increase in the induction number of the core. The explanation is also, therefore, similar to that put forth in Section 2.3.2.1.

Tables 2.1 and 2.2 give the peak-to-peak excursions of the profiles for  $\sigma_{O_2} = 1.0$  mho/m and  $\sigma_{O_2} = 0.1$  mho/m at  $10^3$  Hz,  $10^4$  Hz, and  $10^5$  Hz.

The results obtained from the investigations of the induced current and of the scattered field conform with each other. The above general findings will help provide an integrated physical picture of the effect of a conducting surrounding on the electromagnetic response of an enclosed target.

## 2.5 Electromagnetic Response of a Horizontal Perfectly Conducting Half-Plane to a Line Current Source

### 2.5.1 Introduction

The spherical model investigated above is an idealised representation of actual geological situations chosen to illustrate the principles involved. A more realistic and representative model of frequently occurring mineralized structures is a tabular body. In cases where electric discontinuities occur in parallel planes, the method of Wiener and Hopf (1931) for solving the integral equations can be employed to study their electromagnetic response. This potential technique has been extensively used to solve problems in wave-propagation in several other fields. Noble (1958) and Weinstein (1969) have illustrated the applications of this

Table 2.1

peak-to-peak values for profiles (figures 2.15 to 2.18)  
 $\sigma_{01} = 10$  mho/m,  $r_1 = 10$  m,  $r_2 = 12.5$  m,  $\sigma_{02} = 1$  mho/m

-----  
 $h/L=0.3$   
 -----

In-phase Component

Quadrature Component

$H_z$	$H_z^{r_1}$	$H_z - H_z^{r_2}$	frequency	$H_z$	$H_z^{r_1}$	$H_z - H_z^{r_2}$
0.73,0.3	0.61,0.24	0.68,0.27	$10^3$	1.0,0.4	0.84,0.34	0.61,0.24
2.32,0.95	1.88,0.76	0.44,0.17	$10^4$	0.94,0.38	0.5,0.2	-0.79,0.32
3.89,1.55	2.3,0.93	-0.04,0.02	$10^5$	0.85,0.35	0.19,0.07	0.25,0.007

-----  
 $h/L=0.4$   
 -----

0.32,0.02	0.28,0.02	0.3,0.02	$10^3$	0.44,0.02	0.36,0.02	0.26,0.01
1.00,0.04	0.82,0.03	0.19,0.01	$10^4$	0.41,0.02	0.22,0.01	-0.34,0.01
1.71,0.07	1.01,0.05	-0.015	$10^5$	0.37,0.02	0.85,0.005	0.12

Table 2.2

Peak-to-peak values for profiles (figures 2.20 to 2.23)  
 $\sigma_{01} = 10 \text{ mho/m}$ ,  $r_1 = 10 \text{ m}$ ,  $r_2 = 12.5 \text{ m}$ ,  $\sigma_{02} = 0.1 \text{ mho/m}$

-----  
 $h/L=0.3$   
 -----

<u>In-phase Component</u>			frequency	<u>Quadrature Component</u>		
$H_z$	$H_z^{r_1}$	$H_z - H_z^{r_2}$		$H_z$	$H_z^{r_1}$	$H_z - H_z^{r_2}$
0.62,0.25	0.61,0.24	0.62,0.24	$10^3$	0.87,0.36	0.84,0.34	0.82,0.29
2.0,0.84	1.88,0.76	1.9,0.76	$10^4$	0.56,0.23	0.5,0.2	0.16,0.06
2.53,1.04	2.3,0.93	0.61,0.24	$10^5$	0.53,0.22	0.19,0.07	-1.19,0.48

-----  
 $h/L=0.4$   
 -----

0.28,0.02	0.28,0.02	0.27,0.015	$10^3$	0.37,0.015	0.36,0.02	0.35,0.015
0.84,0.04	0.82,0.03	0.82,0.03	$10^4$	0.24,0.01	0.22,0.01	0.75,0.005
1.07,0.05	1.01,0.05	0.25,0.01	$10^5$	0.23,0.01	0.85,0.05	-0.52,0.025

technique in detail. Some noted investigations wherein this technique has been used are due to Heins and Wiener (1946), Carlson and Heins (1947), Heins (1948), Levine and Schwinger (1948), Friedlander (1951), Senior (1952), Jones (1953), Koiter (1954), Williams (1954), Ament (1954), Heins (1956), Latter (1958), Lamb (1959), Clemmow (1959), Nikitina (1960), Wu and Wu (1963), Chu and Karp (1964) etc.

A brief outline of the application of this technique in obtaining an analytical expression of the electromagnetic response of a highly conducting vein embedded in a conducting half-space and overlain by a conducting overburden is presented here. The energising field is obtained by a line current source parallel to the vein. Because of the mixed boundaries, the usual method of partial differential equations is not applicable in this case as the variables are not separable. An integral equation formulation of the problem has, therefore, been done and the Wiener-Hopf technique applied to find the appropriate expressions which may be numerically evaluated to give the electromagnetic response of the body.

#### 2.5.2 Formulation

A mineralised vein having a large extent may be represented by a horizontal half-plane. One edge of the plane is assumed to be near the observation point

and it is likely to influence the electromagnetic field significantly. The electrical conductivity of the vein is assumed to be very high and hence the half-plane representing it has been considered to be perfectly conducting. The vein is embedded in a half-space (earth) whose electric parameters are denoted by  $\sigma_3$ ,  $\mu_3$  and  $\epsilon_3$  (figure 2.24). The corresponding parameters of an overburden of thickness  $d_b$  are denoted by  $\sigma_2$ ,  $\mu_2$ ,  $\epsilon_2$  and those of the external half-space (air) by  $\sigma_1$ ,  $\mu_1$ ,  $\epsilon_1$ . The depth of burial of the vein from the air-earth boundary is assumed to be  $d$ . A line-source carrying a current  $I_0 e^{i\omega t}$  at  $(y_0, z_0)$  produces the energising alternating magnetic field.

In view of the symmetry of the present problem the only non-zero component of a vector potential is  $A_x$  which does not vary with  $x$ . Thus,

$$A_y = A_z = 0 \quad \text{and} \quad \frac{\partial A}{\partial x} = 0.$$

Equation (2.4) may then be written in a rectangular coordinate system as

$$\frac{\partial^2 A_j}{\partial y^2} + \frac{\partial^2 A_j}{\partial z^2} + \gamma_j^2 A_j = 0, \quad j = 1, 2 \text{ or } 3. \quad (2.34)$$

The general solution of equation (2.34) may be written as

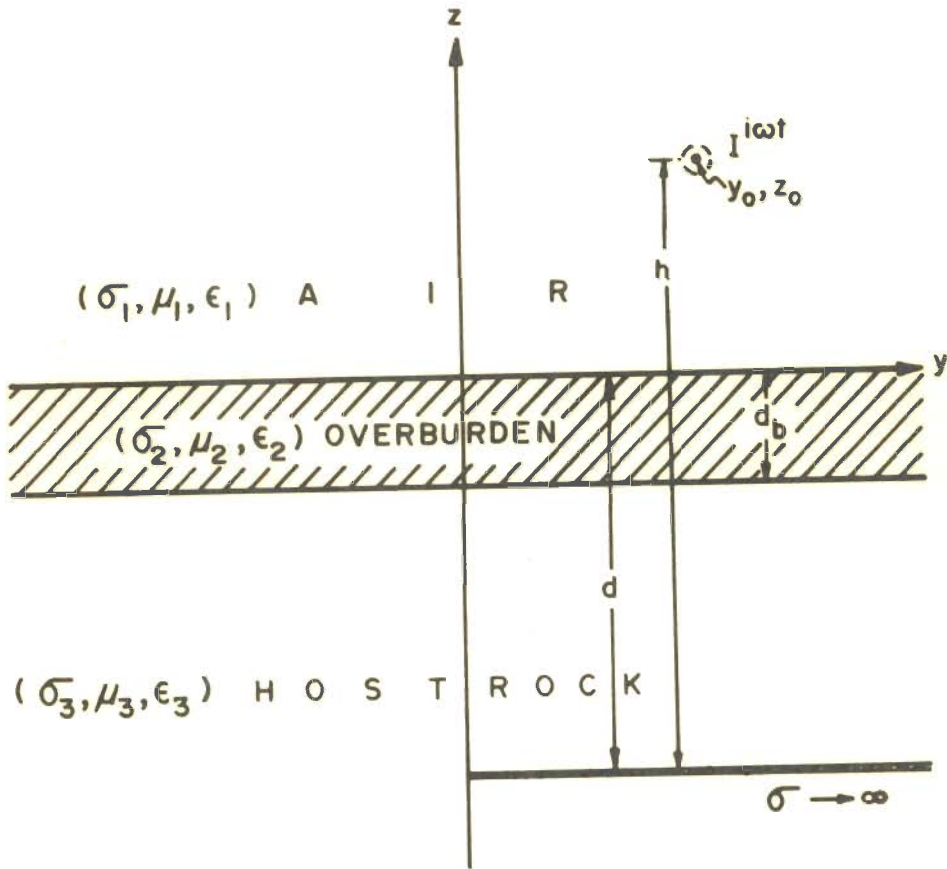


Fig. 2-24 AN IDEALLY CONDUCTING HORIZONTAL HALF-PLANE EMBEDDED IN A HALF-SPACE UNDERLYING AN OVERBURDEN

electrical discontinuities at  $z=0$  and underneath.

(2) Overburden layer i.e.  $0 > z > -d_b$  (2.37)

$$A_2 = \int_0^{\infty} \left[ a_2 e^{u_2 z} + b_2 e^{-u_2 z} \right] \cos \lambda (y-y_0) d\lambda. \quad (2.38)$$

(3) Lower half-space i.e.  $-d_b > z > -\infty$

$$A_3 = \int_0^{\infty} a_3 e^{u_3 z} \cos \lambda (y-y_0) d\lambda. \quad (2.39)$$

The primary potential due to the line current source situated at  $(y_0, z_0)$  is given by (Wait, 1962) as

$$A_{jp} = P_j K_0 \left[ -i\gamma_j \sqrt{(z-z_0)^2 + (y-y_0)^2} \right], \quad (2.40)$$

where  $P_j = \frac{1}{2\pi(\sigma_j - i\omega \epsilon_j)}$

and  $K_0$  is the McDonald function.

If  $K_0$  is expanded in terms of the eigen functions suitable for the problem one gets

$$A'_{lp} = P_1 \int_0^{\infty} e^{-u_1 (z-z_0)} \cos \lambda (y-y_0) d\lambda, \quad (2.40a)$$

for  $z > z_0$



$$A_j = \int_0^{\infty} \left[ a_j e^{u_j z} + b_j e^{-u_j z} \right] \cos \lambda (y - y_0) d\lambda, \quad (2.35)$$

where  $u_j = \sqrt{\lambda^2 + \gamma_j^2}$  and  $\lambda$  is a positive constant.

$a_j$  and  $b_j$  are the constants of integration to be determined from the boundary conditions at  $z = 0$  and  $z = -d_b$ . The terms containing  $\sin \lambda (y - y_0)$  have been left out because of the symmetry considerations.

Equation (2.35) holds irrespective of whether the vein is present or not. First, we shall write the vector potential in different regions disregarding the presence of the vein as:

(1) Upper half-space i.e.  $z > 0$

$$A_1' = \int_0^{\infty} b_1 e^{-u_1 z} \cos \lambda (y - y_0) d\lambda + \int_0^{\infty} R_{\lambda} e^{-u_1 z} \cos \lambda (y - y_0) d\lambda,$$

for  $z_0 < z < \infty$  (2.36a)

and

$$A_1'' = \int_0^{\infty} a_1 e^{u_1 z} \cos \lambda (y - y_0) d\lambda + \int_0^{\infty} R_{\lambda} e^{-u_1 z} \cos \lambda (y - y_0) d\lambda,$$

for  $0 < z < z_0$ . (2.36b)

Here  $R_{\lambda}$  is the reflection coefficient due to the

and

$$A_{1p}'' = P_1 \int_0^{\infty} e^{u_1(z-z_0)} \cos \lambda (y-y_0) d\lambda, \quad (2.40b)$$

for  $z < z_0$ .

The first terms of the R.H.S. of equations (2.36a) and (2.36b) may be identified with  $A_{1p}'$  and  $A_{1p}''$  respectively and hence

$$b_1 = \frac{P_1}{u_1} e^{u_1 z_0} \quad \text{and} \quad a_1 = \frac{P_1}{u_1} e^{-u_1 z_0}.$$

Also,  $A_{1p}'$  and  $A_{1p}''$  can be combined into a single expression as

$$A_{1p} = P_1 \int_0^{\infty} e^{-u_1 |z-z_0|} \cos \lambda (y-y_0) d\lambda. \quad (2.40c)$$

The expressions for  $A_1, A_2, A_3$  may, thus, be written as:

$$A_1 = P_1 \int_0^{\infty} \frac{d\lambda}{u_1} \cos \lambda (y-y_0) \left[ e^{-u_1 |z-z_0|} + f_1 e^{-u_1 (z+z_0)} \right], \quad (2.41)$$

$$A_2 = P_2 \int_0^{\infty} \frac{d\lambda}{u_2} \cos \lambda (y-y_0) \left[ f_2 e^{(u_2 z - u_1 z_0)} + g_2 e^{-(u_2 z + u_1 z_0)} \right], \quad (2.42)$$

and

$$A_3 = P_3 \int_0^{\infty} \frac{d\lambda}{u_3} \cos \lambda (y-y_0) \left[ f_3 e^{(u_3 z - u_1 z_0)} \right] . \quad (2.43)$$

Here  $f_1, f_2, g_2, f_3$  are the new constants of integration.

The boundary conditions at surfaces  $z=0$  and  $z=-d_b$  using equations (2.41), (2.42) and (2.43) yield after the usual algebra

$$f_1 = \frac{u_2 u_1 - u_2^2 \tanh u_2 d_b - u_2 u_3 + u_1 u_3 \tanh u_2 d_b}{u_2 u_1 + u_2^2 \tanh u_2 d_b + u_2 u_3 + u_1 u_3 \tanh u_2 d_b} \quad (2.44)$$

and

$$f_3 = \frac{\gamma_1^2 P_1}{\gamma_3^2 P_3} \left[ \left( \frac{u_2}{u_1} - 1 \right) + \left( \frac{u_2}{u_1} + 1 \right) f_1 \right] \left( \frac{u_2}{u_3} - 1 \right)^{-1} e^{(u_2 + u_3) d_b} . \quad (2.45)$$

### 2.5.3 Contribution of the conducting vein

The vein, which has been represented by a perfectly conducting half-plane, may be considered as an equivalent of a surface current (Horiuchi, 1957) comprised of a continuous distribution of line currents  $I(y_m)$  on the plane ( $z = -d, y > 0$ ) which may be determined from the boundary conditions at the half-plane. If

$\bar{A}_{jm}$  represents the vector potential at a point  $(y, z)$

due to a line-current at  $(y_m, -d)$  the total response vector due to the vein is

$$\bar{A}_j = \int_0^{\infty} \bar{A}_{jm}(y, z; y_m, -d) I(y_m) dy_m . \quad (2.46)$$

From the analogy of the physical situation, it can be easily seen that  $\bar{A}_{jm}$  may be written in the same form as equation (2.41) except for replacing  $u_1$  by  $u_3$  and vice versa. Also the signs of  $z$  and  $z_0$  should be taken as negative for  $\bar{A}_{3m}$ . Thus  $\bar{A}_{3m}(y, -d; y_m, -d)$  i.e. vector potential at any point  $(y, -d)$  on the vein due to the line current at  $(y_m, -d)$  may be expressed as

$$\bar{A}_{3m}(y, -d) = P_3 \int_0^{\infty} \frac{d\lambda}{u_3} \cos \lambda(y-y_m) \left[ 1 + \bar{F}_3 e^{2u_3 d} \right] \quad (2.47)$$

where

$$\bar{F}_3 = \frac{u_3 u_2 - u_2^2 \tanh u_2 d_b - u_2 u_1 + u_1 u_3 \tanh u_2 d_b}{u_3 u_2 + u_2^2 \tanh u_2 d_b + u_2 u_1 + u_1 u_3 \tanh u_2 d_b} . \quad (2.48)$$

The equation (2.47) does, in effect, gives the mutual interaction of the equivalent line currents on the surface of the half-plane. Substitution of equation (2.47) in equation (2.46) gives

$$A_3 = P_3 \int_0^{\infty} dy_m I(y_m) \int_0^{\infty} \frac{d\lambda}{u_3} \cos \lambda (y - y_m) \left[ 1 + \bar{f}_3 e^{2u_3 d} \right]. \quad (2.49)$$

The boundary condition at the surface of the half-plane warrants annulled electric field on its surface. This can be expressed in terms of the vector potential as

$$A_3 + \bar{A}_3 \left| \begin{array}{l} = 0 \\ y > 0 \\ z = -d \end{array} \right. \quad (2.50)$$

The values of  $A_3$  and  $\bar{A}_3$  may be put in equation (2.50) from equation (2.43) and (2.49) to obtain

$$\begin{aligned} & \int_0^{\infty} \frac{d\lambda}{u_3} \cos \lambda (y - y_0) f_3 e^{-u_3 d - u_1 z_0} \\ &= - \int_0^{\infty} dy_m I(y_m) \int_0^{\infty} \frac{d\lambda}{u_3} \cos \lambda (y - y_m) \left[ 1 + \bar{f}_3 e^{2u_3 d} \right]. \end{aligned} \quad (2.51)$$

Let

$$F(y) = - \int_0^{\infty} \frac{d\lambda}{u_3} \cos \lambda (y - y_0) f_3 e^{-u_3 d - u_1 z_0} \quad (2.52)$$

and

$$K(y - y_m) = \int_0^{\infty} \frac{d\lambda}{u_3} \cos \lambda (y - y_m) \left[ 1 + \bar{f}_3 e^{2u_3 d} \right] \quad (2.53)$$

be put in equation (2.51) which can then be written as

$$F(y) = \int_0^{\infty} I(y_m) K(y - y_m) dy_m \quad (2.54)$$

The equation (2.54) is the integral equation which gives the value of  $I(y_m)$  and hence the response of the vein. This equation may be solved through Wiener-Hopf technique.

#### 2.5.4 Solution of the integral equation

Equation (2.54) may be written as

$$\int_0^{\infty} I(y_m)K(y-y_m)dy_m = F(y)+G(y). \quad (2.55)$$

Here a new function  $G(y)$  ( $\equiv 0$ , for  $y > 0$ ) has been introduced. On taking the Fourier transform of both the sides of equation (2.55) and on applying the Faltung theorem, one obtains

$$\bar{F}(\alpha) + \bar{G}(\alpha) = \bar{I}(\alpha) \bar{K}(\alpha). \quad (2.56)$$

Here,  $\bar{F}(\alpha) = \int_{-\infty}^{\infty} F(y)e^{-i\alpha y} dy$ , and so on for  $\bar{G}(\alpha)$ ,  $\bar{I}(\alpha)$  and  $\bar{K}(\alpha)$ . Equation (2.56) holds in a common strip of regularity of functions  $\bar{G}(\alpha)$ ,  $\bar{F}(\alpha)$ ,  $\bar{I}(\alpha)$  and  $\bar{K}(\alpha)$ , considered as functions of  $\alpha$ . The common strip can be determined as below.

Since the incident field varies as  $e^{\frac{-i\gamma_3 y_m}{\sqrt{y_m}}}$  for large values of  $y_m$  (which can be verified by finding the limiting value of  $K_0$  at large values of  $r$ ) where  $\text{Im}(\gamma_3) > 0$  (where  $\text{Im}$  denotes the imaginary part), the

induced currents will also behave in a similar manner. It, therefore, follows from the relation

$$\bar{I}(\alpha) = \int_0^{\infty} I(y_m) e^{-i\alpha y_m} dy_m \quad (2.57)$$

that  $\bar{I}(\alpha)$  will be regular in the lower half of the  $\alpha$ -plane i.e. in the region  $\text{Im}(\alpha) < \text{Im}(\gamma_1)$  which starts above the real axis. By a similar argument  $\bar{G}(\alpha)$  will be regular in the upper half-plane starting below the real axis.

The region of regularity for  $\bar{K}(\alpha)$  and  $\bar{F}(\alpha)$  can be ascertained if these transforms are evaluated.

Now,

$$\bar{K}(\alpha) = \int_{-\infty}^{\infty} dt e^{-i\alpha t} \int_0^{\infty} \varphi(\lambda) \cos \lambda(t) d\lambda, \quad (2.58)$$

where  $\varphi(\lambda) = \frac{1}{u_3} [1 + \bar{F}_3 e^{2u_3 d}]$ .

As  $\varphi(\lambda)$  is an even function of  $\lambda$

$$\bar{K}(\alpha) = 2 \int_0^{\infty} dt \cos \alpha t \int_0^{\infty} \varphi(\lambda) \cos \lambda(t) d\lambda. \quad (2.59)$$

From the theory of Fourier transform (Erdelyi et al, 1954, V.1, p.117) it is evident

that

$$\bar{K}(\alpha) = 2 \frac{\pi}{2} \varphi(\alpha) = \pi \left[ \frac{1}{u_3(\alpha)} \left\{ 1 + \bar{f}_3(\alpha) e^{2u_3(\alpha)d} \right\} \right]. \quad (2.60)$$

Similarly

$$\bar{F}(\alpha) = -\pi \left[ \frac{1}{u_3(\alpha)} \left\{ f_3(\alpha) e^{-u_3(\alpha)d - u_1(\alpha)z_0} \right\} \right]. \quad (2.61)$$

From equation (2.60) and (2.61) it can be easily seen that  $\bar{K}(\alpha)$  and  $\bar{F}(\alpha)$  are both regular in the region  $\text{Im}(\gamma_1) > |\text{Im}(\alpha)|$ . It has, of course, been assumed that  $\text{Im}(\gamma_1) \leq \text{Im}(\gamma_2) \leq \text{Im}(\gamma_3)$ . Therefore, in a strip lying between  $\pm \text{Im}(\gamma_1)$

$$\bar{G}_+(\alpha) + \bar{F}(\alpha) = \bar{I}_-(\alpha) \bar{K}(\alpha), \quad (2.62)$$

where the subscripts + and - denote that the functions are regular in the upper and lower half-planes, respectively.

The equation (2.62) may be solved using the method of analytical continuation. For this, we have to factorise  $\bar{K}(\alpha)$  into  $\bar{K}_+(\alpha)$  and  $\bar{K}_-(\alpha)$  which are regular in the upper and lower half-planes of complex plane, respectively.



$$\text{Let } \tau(\alpha) = \left[ 1 + \bar{f}_3(\alpha) e^{2u_3(\alpha)d} \right] . \quad (2.63)$$

Applying Cauchy's integral formula, we get

$$\begin{aligned} \ln \tau(\alpha) &= \frac{1}{2\pi i} \oint_{(+)} \frac{\ln \tau(t)}{(t-\alpha)} dt - \frac{1}{2\pi i} \oint_{(-)} \frac{\ln \tau(t)}{(t-\alpha)} dt \\ &= \bar{X}_+(\alpha) - \bar{X}_-(\alpha) , \end{aligned} \quad (2.64)$$

where  $\bar{X}_+(\alpha)$  and  $\bar{X}_-(\alpha)$  are regular in the upper and lower half-planes and represent the values of contour integrations in equation (2.64).

The evaluation of  $\bar{X}_+(\alpha)$  and  $\bar{X}_-(\alpha)$  enables the factorisation of  $\bar{K}(\alpha)$  such that

$$\bar{K}(\alpha) = \frac{\bar{K}_+(\alpha)}{\bar{K}_-(\alpha)} = \frac{\pi e^{\frac{\bar{X}_+(\alpha)}{\sqrt{\alpha+\gamma_3}}}}{e^{\frac{\bar{X}_-(\alpha)}{\sqrt{\alpha-\gamma_3}}}} . \quad (2.65)$$

Substituting equation (2.65) in equation (2.62) we get

$$\frac{\bar{G}(\alpha)}{\bar{K}_+(\alpha)} - \frac{\bar{I}_-(\alpha)}{\bar{K}_-(\alpha)} = - \frac{\bar{F}(\alpha)}{\bar{K}_+(\alpha)} . \quad (2.66)$$

The inverse Fourier transform yields

$$\int_{-\infty}^{\infty} \frac{\bar{F}(\alpha)}{\bar{K}_+(\alpha)} e^{-i\alpha y} d\alpha = j(y) + g(y), \quad (2.67)$$

where

$$j(y) = 0, \quad \text{for } y < 0 \quad (2.68a)$$

$$= \int_{-\infty}^{\infty} \frac{\bar{I}_-(\alpha)}{\bar{K}_-(\alpha)} e^{i\alpha y} d\alpha, \quad \text{for } y > 0 \quad (2.68b)$$

and

$$g(y) = \int_{-\infty}^{\infty} \frac{\bar{G}_+(\alpha)}{\bar{K}_+(\alpha)} e^{i\alpha y} d\alpha, \quad \text{for } y < 0 \quad (2.69a)$$

$$= 0, \quad \text{for } y > 0. \quad (2.69b)$$

The equation (2.67) is multiplied by  $e^{-i\zeta y}$  and integrated over positive values of  $y$ , to obtain

$$\frac{\bar{I}_-(\zeta)}{\bar{K}_-(\zeta)} = \frac{1}{2\pi i} \int_{-\infty}^{\infty} \frac{\bar{F}(\alpha)}{(\alpha - \zeta)\bar{K}_+(\alpha)} d\alpha \quad (2.70)$$

which is regular for  $\text{Im}(\alpha) > \text{Im}(\zeta)$ .

The surface current distribution  $I(y)$  can finally be determined as

$$I(y) = \frac{1}{2\pi} \int_{-\infty}^{\infty} d\epsilon e^{i\epsilon y} \frac{\bar{K}_-(\epsilon)}{2\pi i} \int_{-\infty}^{\infty} \frac{\bar{F}(\alpha)}{(\alpha-\epsilon)\bar{K}_+(\alpha)} d\alpha, \quad (2.71)$$

where

$$|\operatorname{Im}(\alpha)| < \operatorname{Im}(\gamma), \quad \operatorname{Im}(\alpha) > \operatorname{Im}(\epsilon)$$

and  $y > 0$ .

Equation (2.71) thus gives the value of  $I(y)$  which in turn can be used to find  $\bar{A}_1$  employing equation (2.46). The response of the vein can then be determined. The crux of the present problem lies in the factorisation of the function  $\bar{K}(\alpha)$  into two components which are regular in the lower and upper half-planes, respectively. The numerical computation is in progress through evaluation of equations (2.63) and (2.72). But a rigorous calculation of the response of an imperfectly conducting vein in the disposition as shown in figure 2.24 is still theoretically intractable. It appears that for such situations experimental simulation technique is the only resort.

## CHAPTER III

### EXPERIMENTAL SIMULATION - PRINCIPLE AND TECHNIQUES

#### 3.1 Introduction

The technique of experimental simulation is inherently more potential than analytical methods in studying the electromagnetic response of conducting geological structures of arbitrary shapes, sizes, electrical properties and having conducting surroundings. While a mathematical description of a situation is almost always possible through a set of equations, it is not always possible to solve them so as to find the value of the electromagnetic field at all points in space and time. On the contrary, it is not always possible to make a physical model of any situation. But, once a model is realised its electromagnetic response can always be found. The only limitation of the scale-model experiments is set by the mechanical feasibility of the physical model. Mihram (1972) has given a very generalised discussion of the theory and classification of models. An appraisal of the potentiality and the extent of application of this powerful technique can be made from Table 3.1.

However, one doesn't simulate an infinity of situations occurring in nature as it is neither feasible nor useful to do so. Model experiments in geoelectro-

TABLE 3.1

Model		Material			Symbolic			
		Replication	Quasi-replica	Analogue	Descriptive	Similar	Formalization	
S T A T I C	Deterministic	Earthen Relief Map	Road Map	Statue of B. Franklin	Ten Commandments	Decision Logic Tables	Ohm's Law	↓ I N C R E A S I N G
	Stochastic	Critical Dosage Test	Weather Map	Die Toss for Russian Roulette	Weather Report	Non-Adaptive, Random, Chess Playing Program	Equilibrium Queue Length	
D Y N A M I C	Deterministic	Model Train Set	Planetarium Show	Analog Computer Circuitry for $\dot{y} = -y$	Constitution of U.S.A.	Critical Path Algorithm	Lanchester's Laws	G E N E R A L I T Y ↓
	Stochastic	Drosophila Genetic Experiment	CRT Display of Endurance Test	White Noise Generator	Text on Darwinian Evolution	Vehicle-By-Vehicle Transportation Model	Stochastic Differential Equation	

↘ ———— Increasing Abstraction ———— ↘  
 ↘ ———— Increasing Inferential Facility ———— ↘  
 ↘ ———— Decreasing Reality ———— ↘

Illustrations of the Wide Scope of Application of Modeling Process (After Mihram, 1972)

magnetics are designed so that they are useful in obtaining a physical insight through observations on some representative models and in providing standard interpretational curves. Their importance lies primarily in studying such systems as are not analytically tractable.

### 3.2 Principle of Simulation

The method of simulation calls for an establishment of certain criteria which should be satisfied to make the model have the same physical characteristics as those of the prototype. The criteria of similitude, in turn, involves the invariance of certain dimensionless parameters in the two similar systems. The number of the necessary parameters may be decided with the help of Buckingham's pi-theorem. This theorem enunciates, in principle, that the number of dimensional groups important for a particular process is equal to the total number of variables less the number of dimensions involved (Buckingham, 1914).

Thus, if a physical process is expressed by a functional relationship of the type

$$F(\eta_1, \eta_2, \eta_3, \dots, \eta_n) = 0$$

where  $(\eta_1, \eta_2, \eta_3, \dots, \eta_n)$  is the complete set of variables controlling the process, then this equation may be reduced to another of the form

$$\varphi(\pi_1, \pi_2, \pi_3 \dots \pi_{n-j}) = 0$$

where the  $\pi$ 's are the dimensionless parameters and  $j$  is the number of dimensions for the process. For a particular physical process, the values of  $\pi$ 's should be invariant in the two similar systems.

These dimensionless parameters, which define a particular process, may be determined by (a) utilising the property of invariance of equations governing the physical process, or (b) the method based on the principle of dimensional homogeneity in the mathematical description of the process. Stratton (1941) and Sinclair (1948) have discussed the criteria of similitude starting from Maxwell's equations which describe the electromagnetic field. For the sake of completeness, a preliminary treatment to derive the criteria of electromagnetic similitude is given below.

The equation (2.4) may be rewritten as

$$\nabla^2 A - i\omega\mu\sigma A + \epsilon\mu\omega^2 A = 0 \quad (3.1)$$

The form of equation (3.1) should remain invariant in systems which are electromagnetically similar. This condition may be expressed in the two systems designated by P (Prototype) and M (Model), as follows:

$$\nabla_P^2 A_P - i\omega_P \mu_P \sigma_P A_P + \epsilon_P \mu_P \omega_P^2 A_P = 0 \quad (3.1a)$$

and

$$\nabla_M^2 A_M - i\omega_M \mu_M \sigma_M A_M + \epsilon_M \mu_M \omega_M^2 A_M = 0 \quad (3.1b)$$

Since both the equations represent the same phenomenon in similar systems, equation (3.1a) should also be satisfied by  $A_M$ . Thus, if  $K_L$ ,  $K_\omega$ ,  $K_\sigma$ ,  $K_\epsilon$ , and  $K_\mu$  are the scale factors for transformations of the linear dimensions, the frequency of the electromagnetic field, the electrical conductivity, the permittivity and the magnetic permeability of the model to corresponding quantities of the prototype, equation (3.1a) may be rewritten as

$$\frac{\nabla_M^2}{K_L^2} A_M - ik_\omega k_\mu k_\sigma \omega_M \mu_M \sigma_M A_M + k_\epsilon k_\mu k_\omega^2 \epsilon_M \mu_M \omega_M^2 A_M = 0$$

or

$$\nabla_M^2 A_M - ik_L^2 k_\omega k_\mu k_\sigma \omega_M \mu_M \sigma_M A_M + k_L^2 k_\epsilon k_\mu k_\omega^2 \epsilon_M \mu_M \omega_M^2 A_M = 0 \quad (3.2)$$

The comparison of equations (3.1b) and (3.2) yields the following conditions of similitude:

$$k_L^2 k_\omega k_\mu k_\sigma = 1 \quad (3.3a)$$



and

$$k_L^2 k_\epsilon k_\mu k_\omega^2 = 1 . \quad (3.3b)$$

Equations (3.3a) and (3.3b) may be rewritten as

$$L_P^2 \omega \rho_P \mu_P \sigma_P = L_M^2 \omega \mu_M \sigma_M = \alpha \text{ (say)} \quad (3.4a)$$

and

$$L_P^2 \epsilon_P \mu_P \omega_P^2 = L_M^2 \epsilon_M \mu_M \omega_M^2 = \beta \text{ (say)}. \quad (3.4b)$$

The dimensionless parameters  $\alpha$  and  $\beta$  should remain invariant during linear modeling. There is, however, freedom of varying the constituent factors arbitrarily so long as their products viz  $\alpha$  and  $\beta$  do not change.

As mentioned above, the frequencies employed in induction prospecting are so low that displacement currents are negligibly small as compared to conduction currents and, therefore, the parameter  $\beta$  has little significance. Further, if the ferromagnetic materials are excluded, then both  $\mu_P$  and  $\mu_M$  may be regarded to be equal to that of free space. Thus, the only dimensionless parameter which need to be preserved is  $(L^2 \omega \sigma)$ .

### 3.2.1 Geometrically Dissimilar Models

From the above discussion, it is obvious that the lengths in various directions are normally scaled down in the same proportions and a geometrically similar model is obtained. An interesting case of a geometrically dissimilar yet physically similar modeling arises if we consider a transversely isotropic medium in a z-directed uniform time-varying electric field.

Let  $\sigma_{pp}$  denote the conductivity of the anisotropic medium along the x- and y- directions and  $\sigma_{nP}$  that along the z-direction at any point of the medium. This type of anisotropy is encountered quite frequently in nature. The electromagnetic wave equation for the prototype system may be written as (Negi and Gupta, 1968)

$$\frac{\partial^2 A_{zP}}{\partial x_P^2} + \frac{\partial^2 A_{zP}}{\partial y_P^2} + \frac{\sigma_{pP}}{\sigma_{nP}} \frac{\partial^2 A_{zP}}{\partial z_P^2} - i\omega \mu_P \sigma_{nP} A_{zP} = 0. \quad (3.5)$$

The Lorentz condition used in the derivation of equation (3.5) is given by

$$\text{div } A_P = -\sigma_{pP} \mu_P \phi_P \quad (3.6)$$

where  $\phi_P$  is the scalar magnetic potential. This system can be modelled by employing an isotropic medium of conductivity  $\sigma_{nM}$  provided the scale factor for lengths

in z-direction is  $\sigma_{nP}/\sigma_{pP}$  times that in x- or y-direction. The equation for the model corresponding to equation (3.5) would become

$$\frac{\partial^2 A_{zM}}{\partial x_M^2} + \frac{\partial^2 A_{zM}}{\partial y_M^2} + \frac{\partial^2 A_{zM}}{\partial z_M^2} - i\omega M^{\mu M} \sigma_{nM} A_{zM} = 0. \quad (3.5a)$$

Geometrically dissimilar models may thus be realised for certain specific studies. Such dissimilar geometrical models of anisotropic media have, however, not been commonly studied for want of available data on anisotropic structures.

### 3.2.2 Variations in response parameter

Svetov (1960), Grant and West (1965), Ward (1967) and others have discussed the variation of response parameters with the geometry of the model and the prospecting system. For example, in the case of a thin sheet investigated by a T001 L100 R001 prospecting system, the significant parameter is  $\sigma\mu\omega Lt$  where  $t$  is the thickness of the sheet and  $L$  is the separation between the transmitting and receiving coils. If the height  $h$  of the prospecting system from the target is much greater than  $L$ , the parameter  $\sigma\mu\omega ht$  becomes more significant and needs to be considered in simulation. In both the above examples, the thickness of the model need not be scaled correctly as it occurs in product with  $\sigma$ . In this sense the model of this system also is not

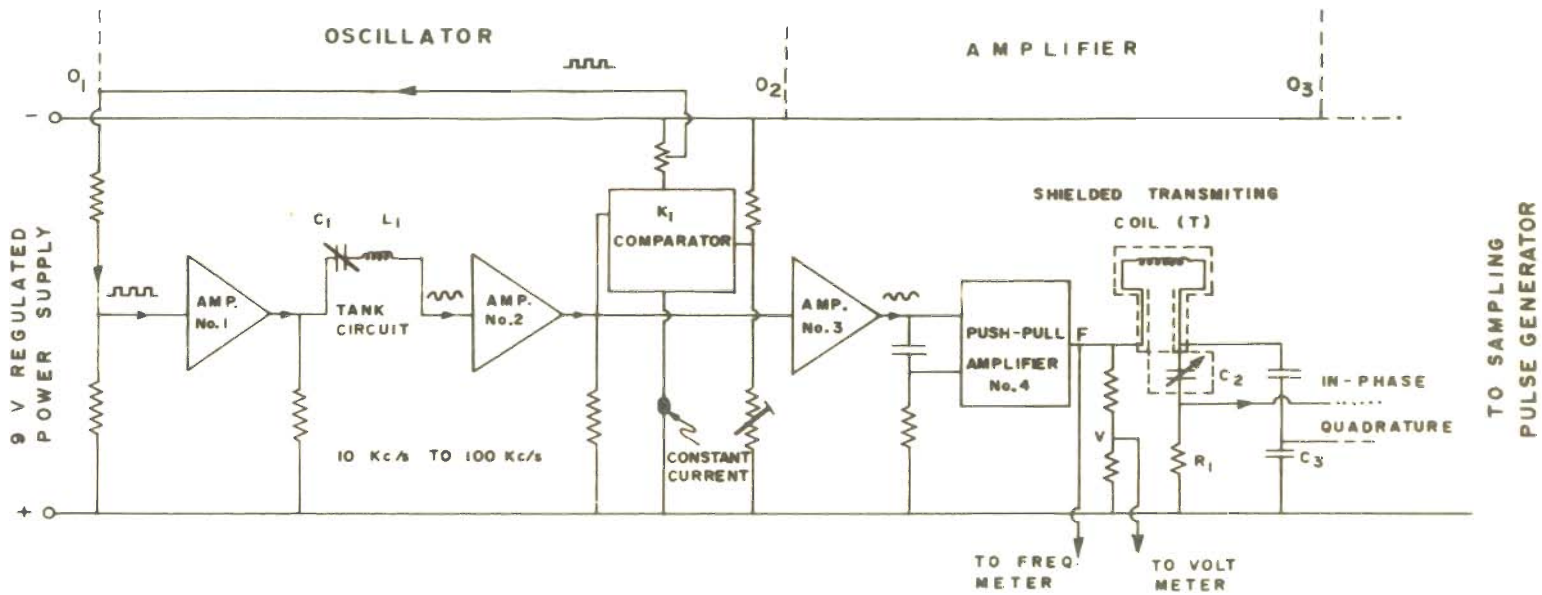
entirely geometrically similar to the prototype. In general, the significant parameter can be described as  $\sigma\mu\omega L_j L_k$  where  $L_j$  and  $L_k$  are the two characteristic dimensions which determine the response of the system under investigations.

### 3.3 Experimental Set-Up

The constituent factors of the dimensionless parameter  $\sigma\mu\omega L_j L_k$  determine the design and set-up of a scale-model experiment. Each factor, therefore, needs to be considered first individually and then collectively. A brief account of the various stages of equipment used in the present scale-model experiments (Gupta Sarma and Maru, 1971) is given below.

#### 3.3.1 Transmitter section

A stabilized sinusoidal current is fed to the transmitting coil in order to establish an alternating magnetic field in the region of investigation. From  $O_1$  to  $O_2$  is the oscillator unit (figure 3.1). Amplifiers no. 1 and no. 2 are specially designed unity-gain circuits called boot-strapped amplifiers. These have very high input impedance and very low output impedance so as to provide a high degree of isolation between the input and output circuits. Amplifier no. 1 is fed by a square wave signal and its output load is a series-tuned L-C circuit. The square wave voltage is obtained



TO SAMPLING PULSE GENERATOR

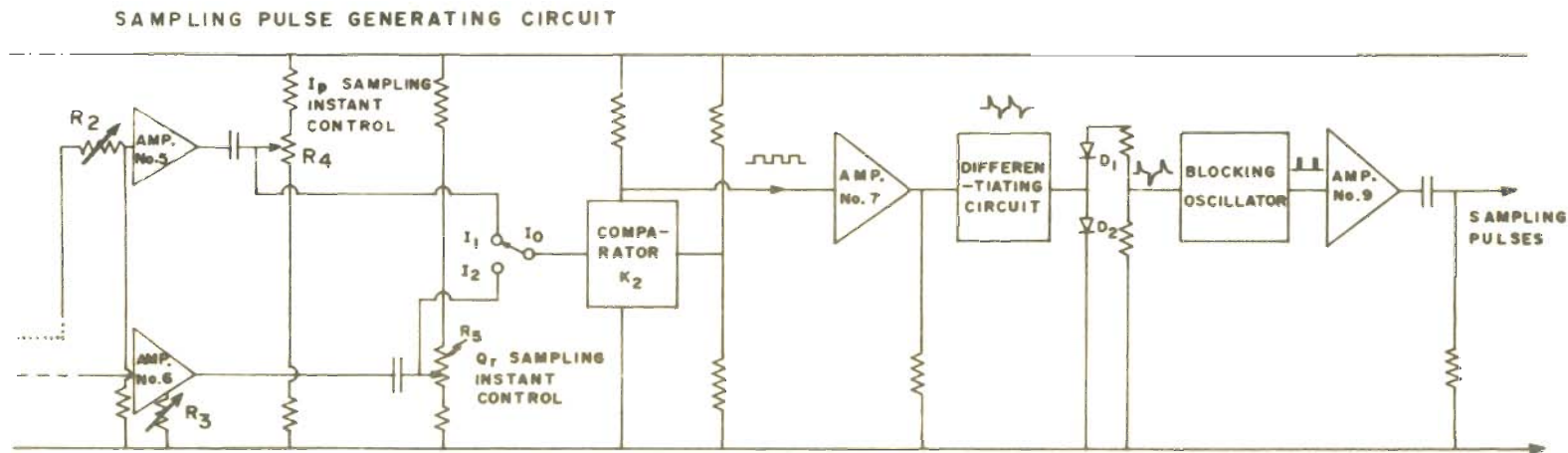


Fig.3-1 BLOCK DIAGRAM OF THE TRANSMITTER UNIT

from the comparator ( $K_1$ ) which consists of two transistor elements. One of them is fed from a regulated fixed D.C. supply and the other from the signal. As soon as the signal level becomes higher than the D.C. level, one element conducts to a saturation level and continues to do so till the signal level remains above the D.C. level. The constancy of the current is maintained with the help of a field-effect transistor. The amplitude of the square wave output is thus highly stabilized. It is fed back regeneratively to amplifier no. 1 to maintain oscillations. The frequency of oscillation depends entirely on the tank circuit which has a very high Q-value because of the high degree of isolation provided by amplifier nos. 1 and 2. The frequency can be varied from 10 khz to 100 khz and is checked to have a stability of 20 ppm/hour.

The sinusoidal signal so generated is amplified by a push-pull amplifier and fed to the transmitting coil (T) through a shielded cable. T is a small coil of mean diameter of about a cm and of about the same length having 380 turns of super-enamelled 36 s.w.g. copper wire (figure 3.2a). The coil is electrostatically shielded in order to avoid the capacitive coupling with the receiving coil through the surroundings as only an inductive interaction is required between them. The reason for this pre-requisite is to avoid the influence of stray non-conductive bodies near the T-R system. The

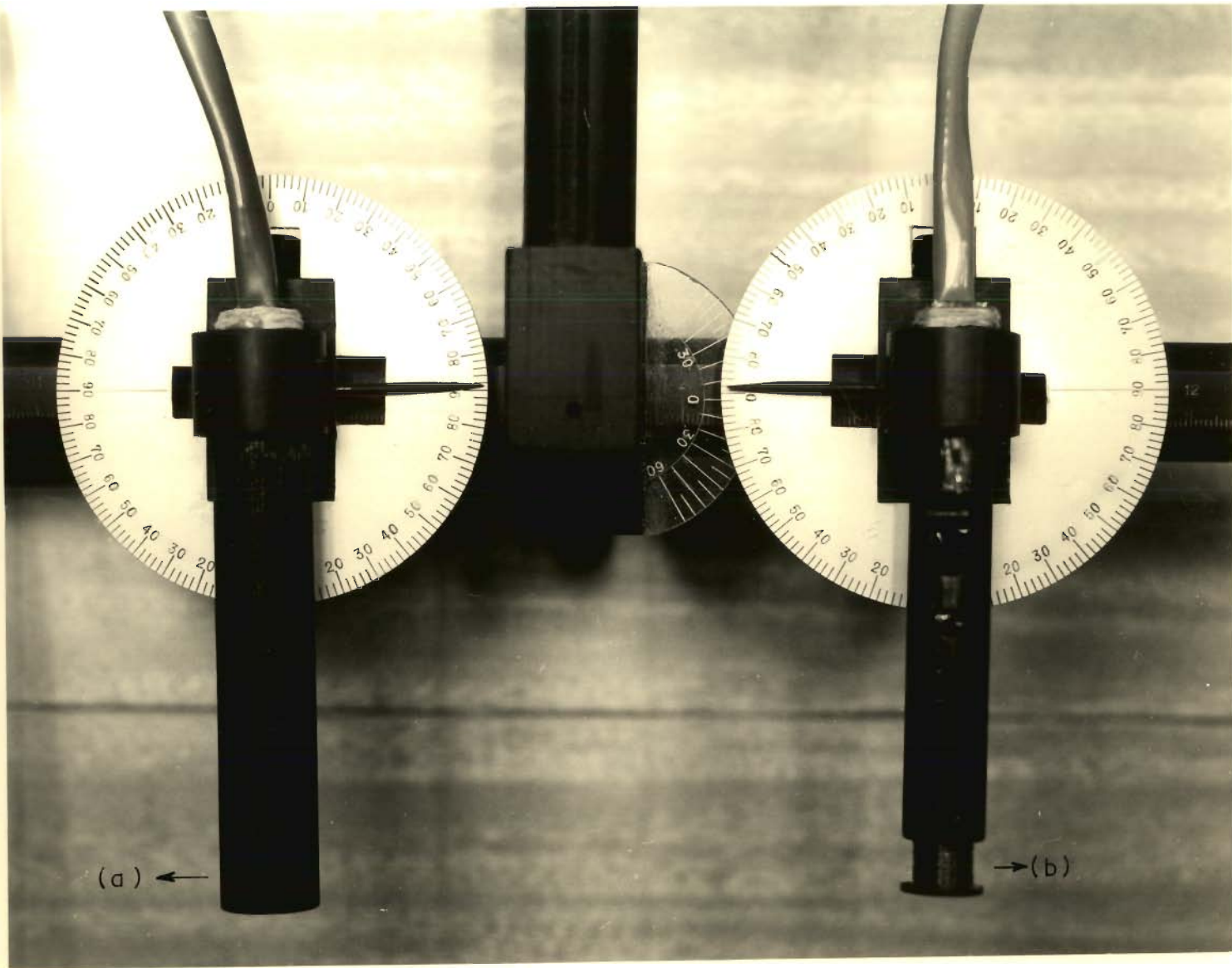


Fig.3-2 A VIEW OF THE (a) TRANSMITTING AND (b) RECEIVING COILS

coil behaves like a magnetic dipole at distances greater than about five times its diameter.

The transmitting coil is tuned with the help of variable capacitors to reduce harmonic distortions. The frequency of the signal is measured at the point F with the help of a built-in frequency-meter and the voltage at the point V. The measurement of the anomaly vector at any instant is made through the method of sampling the signal at that very instant for every cycle of the signal. Sampling pulses are obtained from the transmitter current itself. In series with the transmitting coil is a combination of a variable capacitor ( $C_2$ ) and a resistance ( $R_1$ ). The output across the resistance  $R_1$  is used to generate sampling pulses for measuring the in-phase component of the anomaly signal and the output across the capacitor  $C_3$  is used to generate sampling pulses for measuring the quadrature component.

The sampling signals are amplified with the help of amplifiers 5 and 6 and their D.C. levels are adjusted with the help of potentiometers  $R_4$  and  $R_5$ , respectively. After amplification, one of the sampling signals is fed to the comparator  $K_2$ . As explained earlier, the output of the comparator is a square wave. This is fed to a differentiating circuit which gives rise to both positive and negative pulses. However, since the



sampling of the sinusoidal wave is to be done only once a cycle, one pulse per cycle is selected through a diode system. The positive pulses are absorbed by diode  $D_2$  and only the negative going ones appear at the output. These are fed to a blocking oscillator which produces a sampling pulse of 0.3  $\mu$ sec duration and of the same frequency as that of the signal.

### 3.3.2 Receiver section

The receiving coil(R)(figure 3.2b) is also a shielded coil of nearly the same dimension as that of the transmitting coil. It consists of 500 turns of 40 s.w.g. super-enamelled copper wire and could be held at a fixed distance from the transmitting coil in any of the orthogonal or parallel orientation relative to it. The output of R is taken through a field-effect transistor source-follower which isolates the lead capacity from the receiving coil and thus the signal remains unaffected during transmission to the sampling unit (figure 3.3). The signal is fed to an amplifier which has three amplifying stages of variable gains 1-30, 1-20 and 20. Thus, the total gain can vary from 20 to 12,000. The amplifiers are highly stabilized on account of heavy feedback. The 3 db pass-band for this amplifier is from 2.2 khz to 110 khz.

The output of this amplifier is fed to another amplifier (No.13) which keeps its D.C. level highly

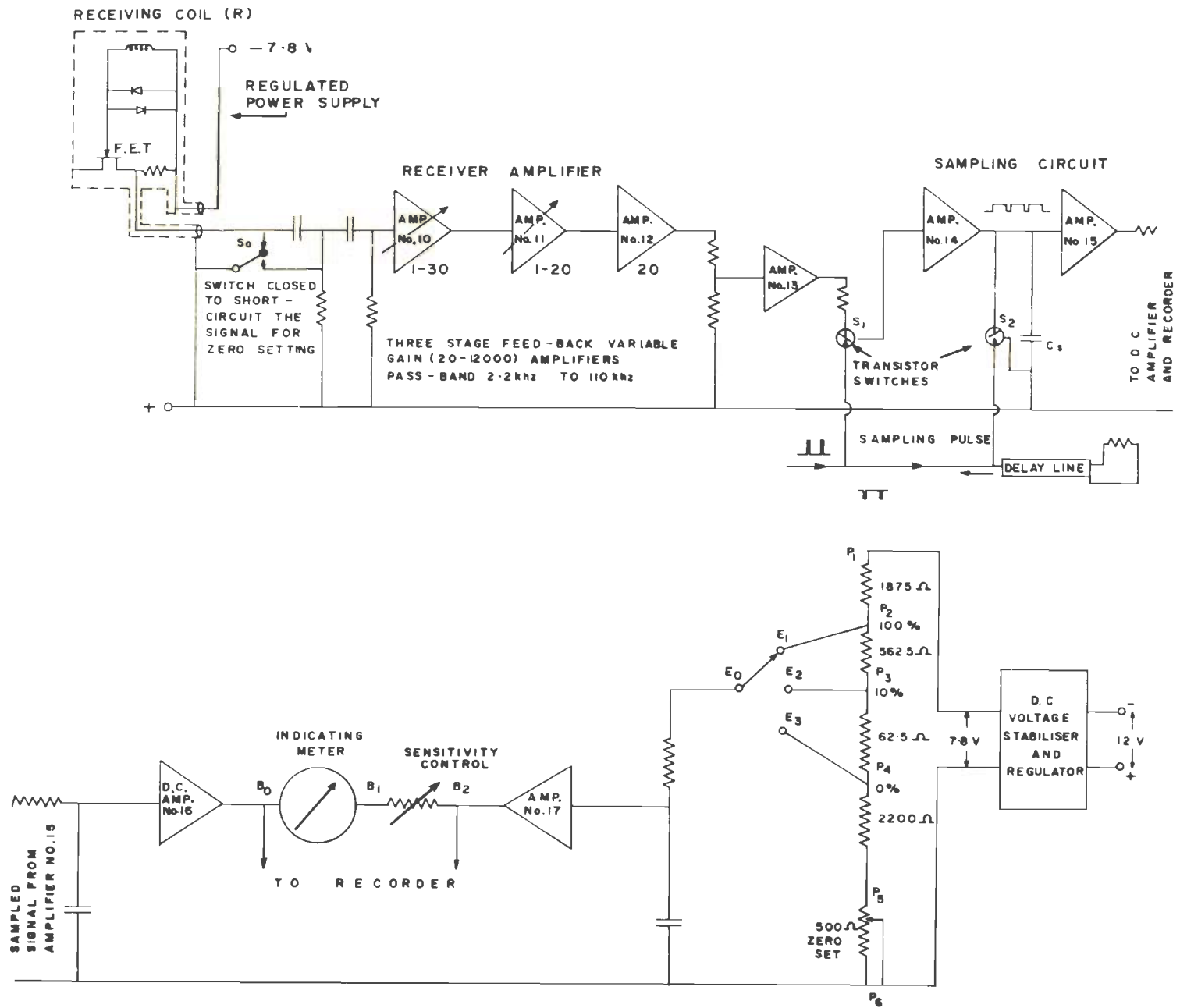


Fig.3.3 BLOCK DIAGRAM OF THE RECEIVER UNIT

constant. This, as we shall see, is vital for the signal measurements. The D.C. level is kept at  $-4V$  and over it appears a signal of  $1V$ . The output is connected to a transistor switch  $S_1$  which is normally in conduction.  $S_2$  is another transistor switch which normally remains open. To these switches are connected the output of sampling pulse generator. The arrival of a negative pulse does not have any effect on  $S_1$  which is already in conduction. But it makes  $S_2$  to conduct and thus the capacitor  $C_s$  is short-circuited.  $S_2$  remains closed only for the pulse duration i.e.  $0.3 \mu\text{sec}$ .

The pulse further travels along a delay-line which is terminated by a non-characteristic impedance of the line so that it (pulse) gets reflected with a change of sign. The total passage time through the delay line is  $0.4 \mu\text{sec}$ . The reflected pulse, which is a positive one, opens the switch  $S_1$  after a gap of  $0.1 \mu\text{sec}$  of the opening of  $S_2$  and the output terminal of the switch  $S_1$  immediately rises to the signal voltage and charges the condenser  $C_s$  to this value through the amplifier no.14. The sampling pulse at the left end meets a characteristic impedance and there is no reflection. Before the arrival of the next reflected pulse, the capacitor  $C_s$  is short-circuited by the incoming negative pulse which closes the switch  $S_2$ . Thus, at the capacitor appears a rectangular wave form of one sign only. This is filtered by an

R-C circuit. The filtered output is amplified by a D.C. amplifier and fed to the indicating meter, and/or the recording unit. The other end of the meter is connected to a stabilized D.C. voltage supply and its potential can be varied as described below for calibration. A 12V battery operates this D.C. regulated power supply of 7.8V. This is connected across a carefully designed (constantan wire-wound) potential divider  $P_1P_6$ . The resistance  $P_2P_3$  is exactly 9 times the resistance  $P_3P_4$ .

### 3.3.3 Operational procedure

For making initial adjustments, the transmitter-receiver (T-R) coil system is kept in free space away from conducting bodies. First of all, the switch  $S_0$  (figure 3.3) across the receiver coil is closed so as to short-circuit the signal. This makes the potential at  $B_0$  to be only the D.C. level of the signal.  $E_0$  is then connected to  $E_3$  and the potentiometer  $P_5P_6$  is varied such that the potential of  $R_1$  becomes the same as that of  $B_0$  so that the indicating meter reading is zero. The potential of  $P_4$  is thus set at the same level as the D.C. level of the signal.

Then  $E_0$  is connected to  $E_1$ ,  $I_0$  is connected to  $I_1$  (figure 3.1), and  $S_0$  opened. The IP sampling instant is varied till the meter shows a maximum reading which implies that the sampling is being done at the peak of the signal. The amplifier nos. 10 and 11 are adjusted so that the meter reads zero which means that the potential

of  $B_0$  and  $P_2$  are identical. Then  $I_0$  is connected with  $I_2$  and  $E_0$  with  $E_3$ , and the Qr sampling instant control is varied. A zero reading of the meter implies that the sampling is being done at the zero crossing of the signal. The potential difference across  $P_2P_4$ , thus, becomes equivalent to the value of the signal.

The calibration of the signal is now done by again short-circuiting the signal and connecting  $E_0$  to  $E_2$ . Since potential difference across  $P_3P_4$  is exactly (correct upto 0.1 per cent) 10 per cent of the potential difference between  $P_2P_4$ , the sensitivity control is adjusted for the indicating meter to get a desired value of deflection. This deflection would be 10 per cent of the signal also. As now the final measurements are made with D.C., absolute linearity is ensured. A view of the transmitter, the receiver and the recorder systems are shown in figure 3.4a.

#### 3.3.4 Mechanical system

The T-R coils together form a rigid system which is fixed to a mobile carriage (figure 3.4b). A photo-transistor is attached onto the carriage, the base of which is illuminated. The output of the photo-transistor is amplified and fed to one pen of the recorder. The carriage moves on a rail to which are attached the pointers, at certain fixed spacings. As the carriage moves, these pointers interrupt the light falling on the photo-transistor.

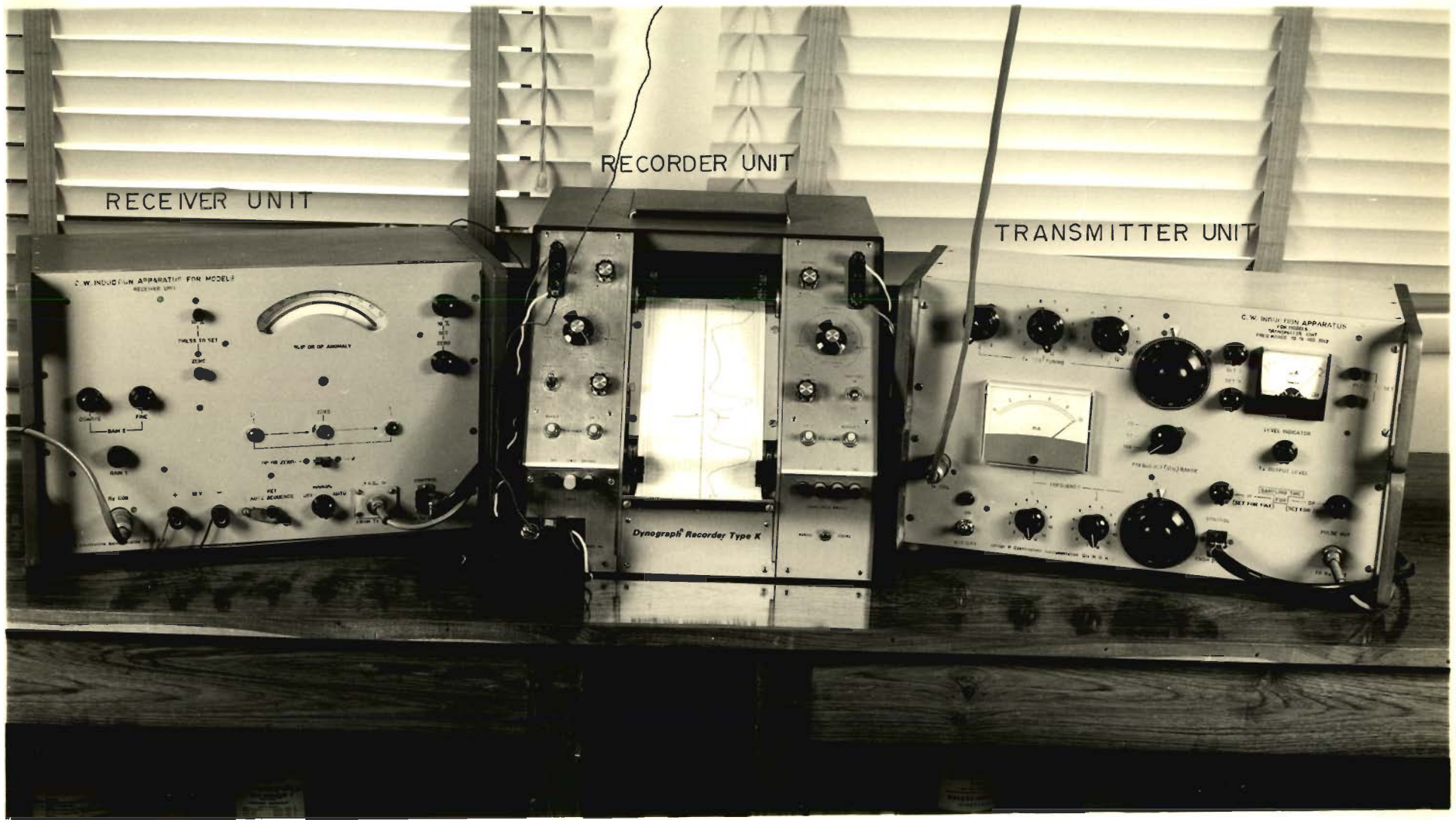


Fig.3-4(a) A VIEW OF THE TRANSMITTER, THE RECEIVER AND THE RECORDER SYSTEMS

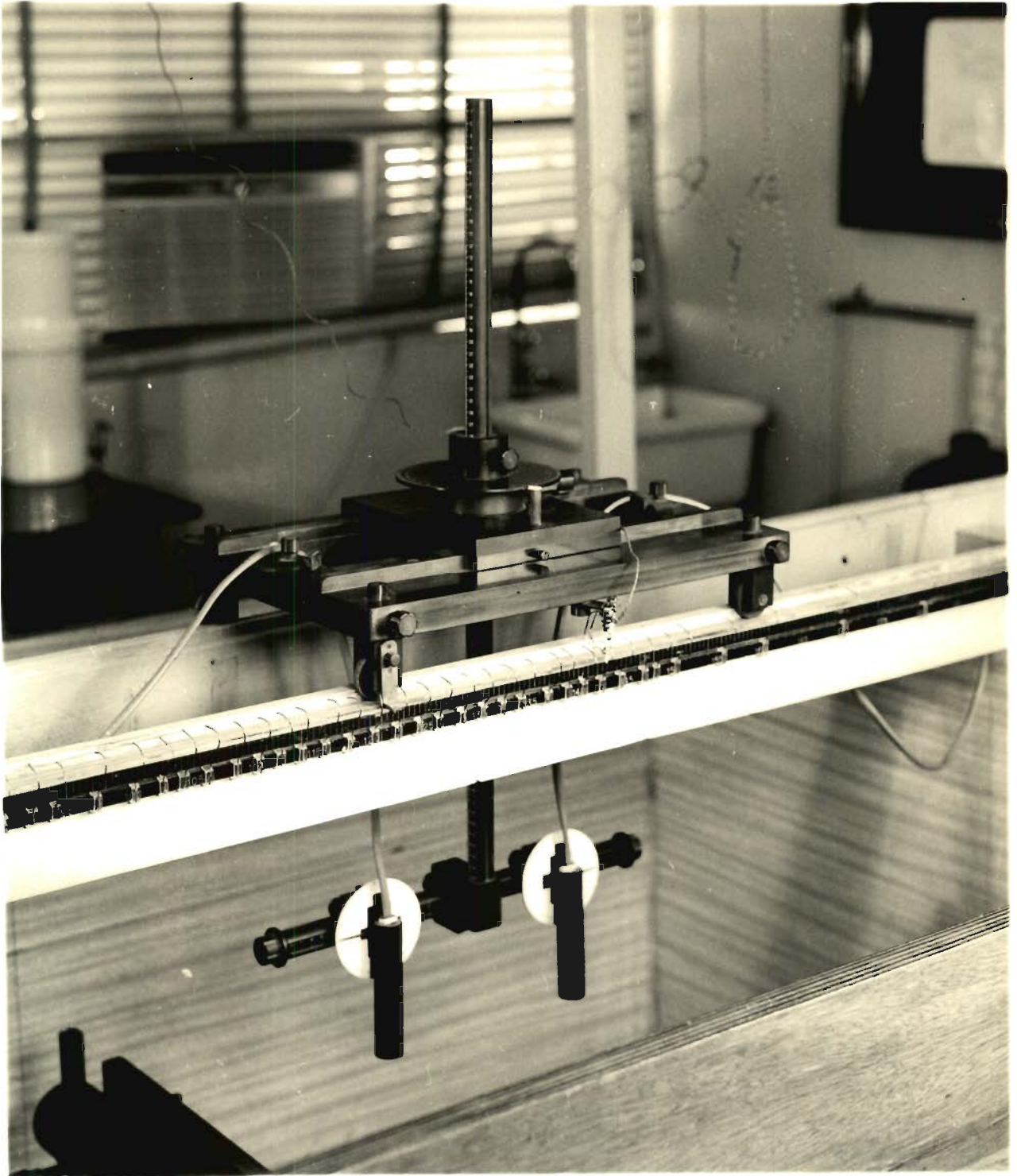


Fig.3-4(b) A VIEW OF THE T-R CARRIAGE AND THE FIDUCIAL MARKINGS



Fig. 3-4 (c) A VIEW OF THE MODEL-TANK



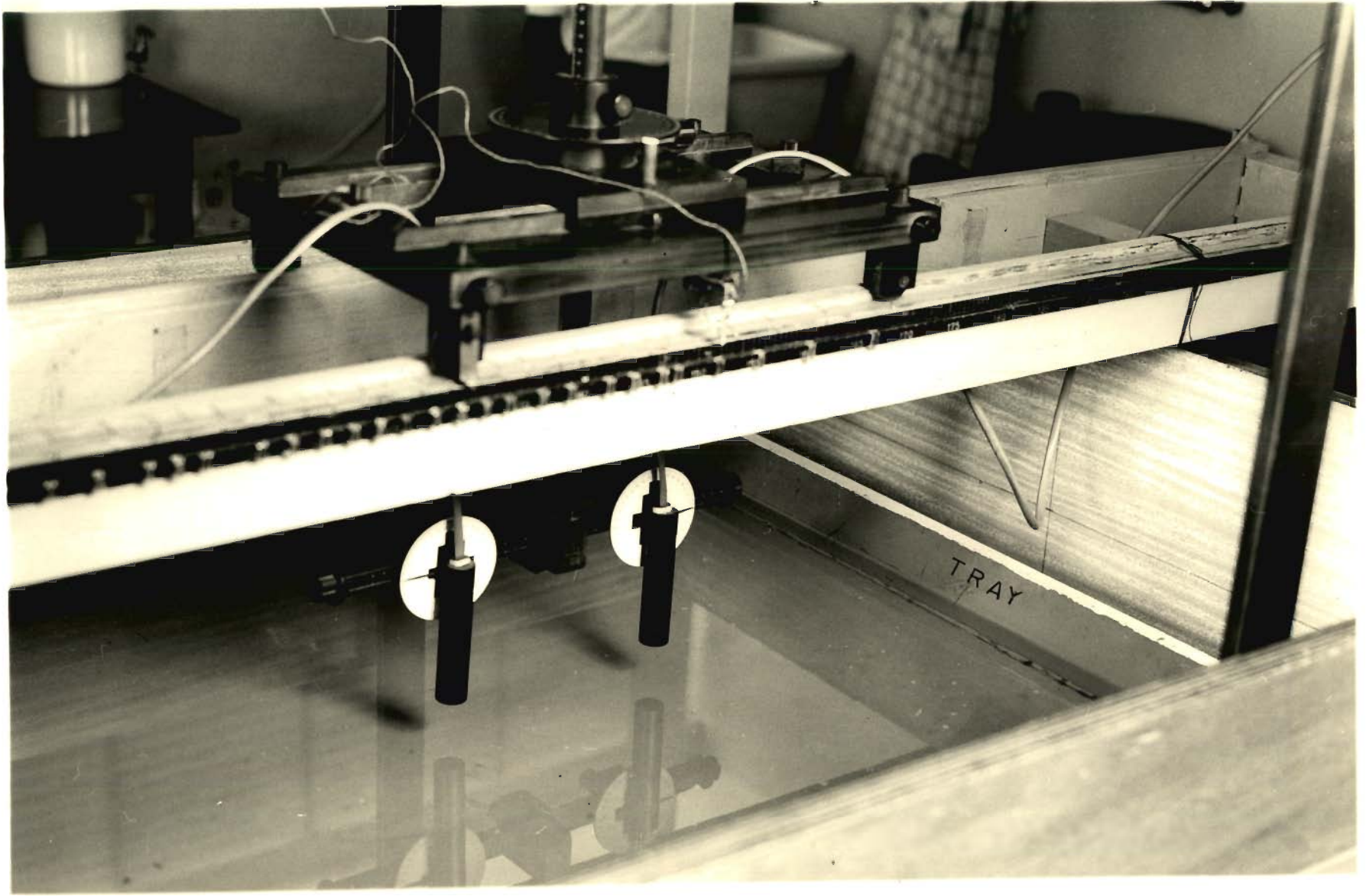


Fig.3-4(d) A VIEW OF TRAY SIMULATING AN OVERBURDEN

Each change in the output current causes a fiducial mark on the chart which will correspond to the position of the T-R system along the profile. The pointers may be fixed at suitable distances enabling the exact determination of the T-R system location relative to the target. The spot values of the anomaly components can thus be found irrespective of the speed of the carriage. The curves may be reconstructed from these discrete values.

### 3.3.5 Model tank

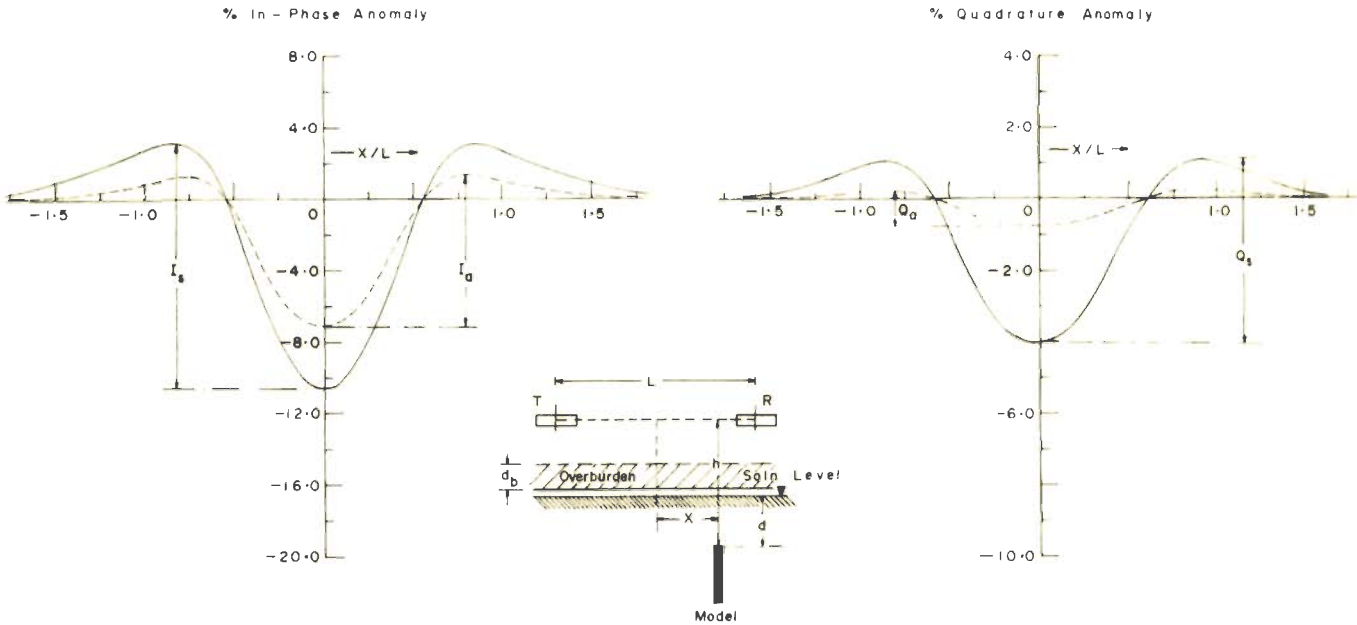
A wooden tank (1.8m x 1.2m x 0.75m) is used for filling the salt solution which simulates a conducting medium surrounding the ore-bodies (figure 3.4c). The tank is lined with an insulator sheet. A wooden tray (figure 3.4d) with a similar lining and containing acid solution has been used to simulate a conducting overburden. The T-R carriage and model-holders etc. are made of non-conducting laminated sheets which are proved to be fairly resistant to warping and corrosion by salt solutions.

The temperature of the laboratory was controlled at  $24^{\circ} \pm 1^{\circ}\text{C}$  so that the conductivity of the salt solution could be assumed to be constant against the ambient temperature variations outside the laboratory. The solution was kept periodically stirred to maintain the homogeneity of composition.

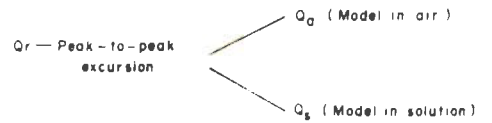
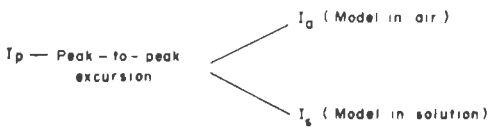
### 3.4 Mode of Measurement and Reckoning of Anomalies

The traverses above the model have been taken orthogonal to the strike of the conductor keeping the transmitting and receiving coils in horizontal coplanar arrangement denoted indicially as T001 L100 R001 by Parasnis (1970 b). The standard notations used in describing the prospecting system and the anomaly profile are shown in figure 3.5. It may be noted that the spatial points viz  $h$  and  $x$  are the same while reckoning the anomaly components from different profiles obtained when a particular model is in air or in solution. The in-phase and quadrature components in terms of the free-space field are denoted as  $I_p$  and  $Q_r$ . A subscript  $a$  or  $s$  is used depending upon the model is in air or in solution. The values of  $I_s$  and  $Q_s$  are determined by subtracting the corresponding components of the response of the solution alone from the total response. The induction index and enhancement ratios are also explained in the figure 3.5.

The reckoning of anomaly is simple for models like thin vertical sheet since there is only one negative central peak which occurs at the mid-point (i.e.  $x = 0$ ) of the profile. This is true whether the model is in air or in solution. The flanking positive peaks for different profiles also occur at the same  $x$ -points. However, different is the case with a model having large lateral extent along the profile direction e.g. a horizontal sheet.



$I_p/Q_r$  — Induction index ( $I_L$ )



$I_s/I_a$  — In-phase enhancement ratio

$Q_s/Q_a$  — Quadrature enhancement ratio

- T — Transmitting coil
- h — Height of the T-R system above the top of the model
- $\theta$  — Dip of the model
- $d_b$  — Overburden thickness
- $\sigma_m$  — Conductivity of the model

- R — Receiving coil
- d — Depth of burial of the top of the model
- X — Horizontal distance between the mid-point of the T-R System and the central section of the model
- $\sigma_s$  — Conductivity of the surrounding medium
- $\sigma_b$  — Conductivity of the overburden

Fig. 3-5 AN ILLUSTRATION OF ANOMALY RECKONING

Figure 3.6 shows the variation of anomaly components for such a model with (a) the conductivity of the surrounding medium and (b) with the increase in its depth of burial. When the model is placed in air there are two negative peaks flanking a central positive hump in this case.

If any of the four sets of figure 3.6, is considered, the profiles denoted by I, II, III etc. differ only as regards the conductivity or disposition of the surrounding medium. It is apparent that the negative peaks do not fall at the same  $x$ -values. Thus, considering the figure 3.6a-A, if the  $I_p$  anomaly for the profiles I, II and III are reckoned as difference between the anomaly values at the same points say  $x/L = 1.3$  and  $x/L = 0.48$ , only  $I_a$  is the correct peak-to-peak excursion but the other two viz  $I_s$  are not so. However, if only the peak-to-peak values are taken irrespective of their  $x$ -positions, there is no physical correlation between  $(I_a)_I$ ,  $(I_s)_{II}$ , and  $(I_s)_{III}$  (Parasnis, 1973).

Much worse is the case for the quadrature component. In profiles I and II (figure 3.6b-B) there is a slight positive hump in the middle of the profile. But if the model touches the solution, the central positive peak disappears and so do the flanking negative peaks giving place to a large single negative peak (profiles III and IV). The same is true in figure 3.6a-B. It is obvious that the

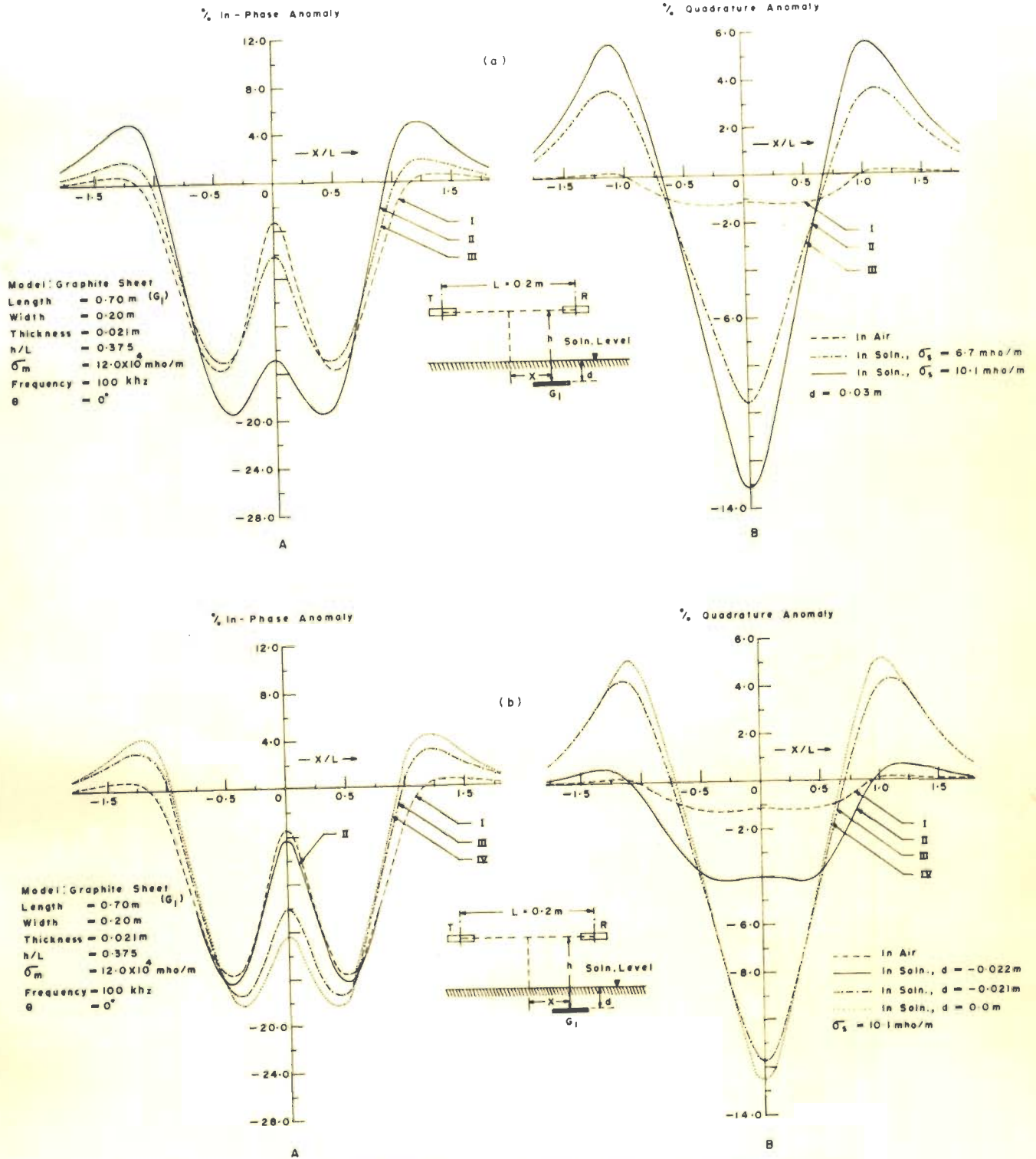


Fig 3-6 ANOMALY PROFILES OVER A GRAPHITE SHEET ILLUSTRATING THE DIFFICULTY IN RECKONING THE PEAK-TO-PEAK EXCURSIONS FOR SUCH MODELS

Qr value for profile I (figure 3.6b-B) can be reckoned as

$$Qr(-) = (Qr)_{x/L=1.14} - (Qr)_{x/L=0.34}$$

and

$$Qr(+) = (Qr)_{x/L=0.34} - (Qr)_{x/L=0} .$$

However, for profile III, the Qr will be

$$Qr(-) = (Qr)_{x/L=1.14} - (Qr)_{x/L=0} .$$

Thus, the negative peaks of these two corresponding profiles may not be compared. Therefore, no anomaly index diagram has been made for such conductors. However, in general the anomaly index diagrams have been prepared depicting the variation of response with conductivity of the surrounding medium, depth of burial, height of the T-R system etc.

Because of the practical difficulties regarding design of the coils,  $\frac{h-d}{L}$  values have been on somewhat higher side than what are used in the ground prospecting as pointed out by Parasnis (1973). It is, however, expected that the qualitative nature of the findings will remain unaffected since the most predominant influence of the surrounding medium is mainly due to a conductive contact between the target and the surrounding medium.

Detailed investigations on the influence of a conductive contact between the target and the surrounding

medium are presented in the next Chapter. The roles played by the target-geometry, variation of frequency of energisation, T-R separation etc. have also been examined for some representative configurations.



## CHAPTER IV

### RESPONSE OF TARGETS IN CONDUCTIVE CONTACT WITH THE SURROUNDING MEDIUM

#### 4.1 Introduction

The theoretical analysis of both the scattered fields and induced currents in the case of a two-layer spherical model brought out some essential aspects of the influence of a conducting surrounding medium. Many field cases also evince the ambiguities in the induction prospecting data, introduced by a conducting terrain. Braekken (1961) noticed a radical difference between the actual depth of an ore body and that estimated through electromagnetic exploration. Although he assumed a highly conducting underlying layer to explain it, Negi (1967) attributed the discrepancy to a conducting overburden.

From a detailed analysis of multi-frequency and multi-separation electromagnetic survey data over some known ore deposits of Sweden, Parasnis (1971) also found wide discrepancies between the actual values of the target parameters and those predicted from conventional anomaly index diagrams which do not take into account the conductivity of the surrounding medium. He attributed the discrepancies to the presence of a conducting overburden

which modified the magnitude as well as the phase of the response.

Earlier, Lowrie and West (1965) investigated, through scale-model experiments, the effect of a conducting overburden on a target placed in a highly resistive medium. They found the overburden to cause a reduction in magnitude and rotation in time-phase of the anomaly vector. However, significant enhancement of the electromagnetic response of a conductor by hostrock and overburden, in conductive contact with it, has been reported by Gaur (1963), Gupta Sarma and Maru (1971), and Gaur et al (1972). The important related theoretical investigations have already been referred to in Chapter II. However, the applicability of theoretical studies, although leading to a meaningful physical insight, is restricted on account of the simplicity of tractable models.

Hence, in order to have a more comprehensive investigation of generalised systems having different

(i) geometries of the conducting bodies and their dispositions relative to the conducting surrounding medium

and (ii) conductivities of targets, hostrock, and overburden,

scale-model experiments have been carried out herein employing a T001 L100 R001 prospecting system at various T-R separations and different frequencies of energisation.

When a target surrounded by a conducting medium is energized by an alternating magnetic field, the following processes are involved:

- (a) electromagnetic screening (predominantly by the overburden) which causes, as mentioned above,
  - i) a reduction of the amplitude of induced currents and
  - ii) a rotation of the current vector in time-phase;
- (b) deformation and redistribution of the induced currents due to the conductivity discontinuity at the contact-interface of the target and the surrounding medium; and
- (c) inductive interaction between the two conducting systems viz the target and the surrounding medium whether they are in conductive contact or not.

Furthermore, these factors interact in a complex manner to affect the response and thus make the quantitative interpretation of the data in terms of

target parameters viz the size, shape, conductivity, and depth of burial, extremely difficult.

The physical concepts pertinent to factor 'a' have been discussed in Chapter II. The factors 'b' and 'c', however, need further elaboration. This Chapter deals mainly with 'b' and experimental investigations on representative models have been carried out with a view to arriving at some coherent results. At the outset, some experimental findings are discussed to qualitatively elucidate the influence of the conducting surrounding medium. Later, some results on quantitatively simulated models are also presented.

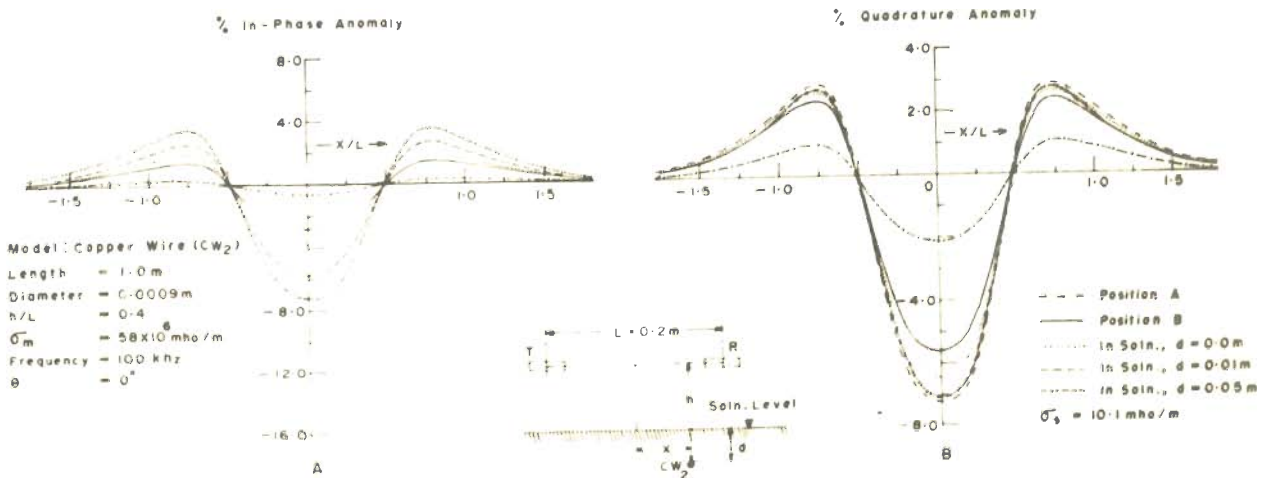
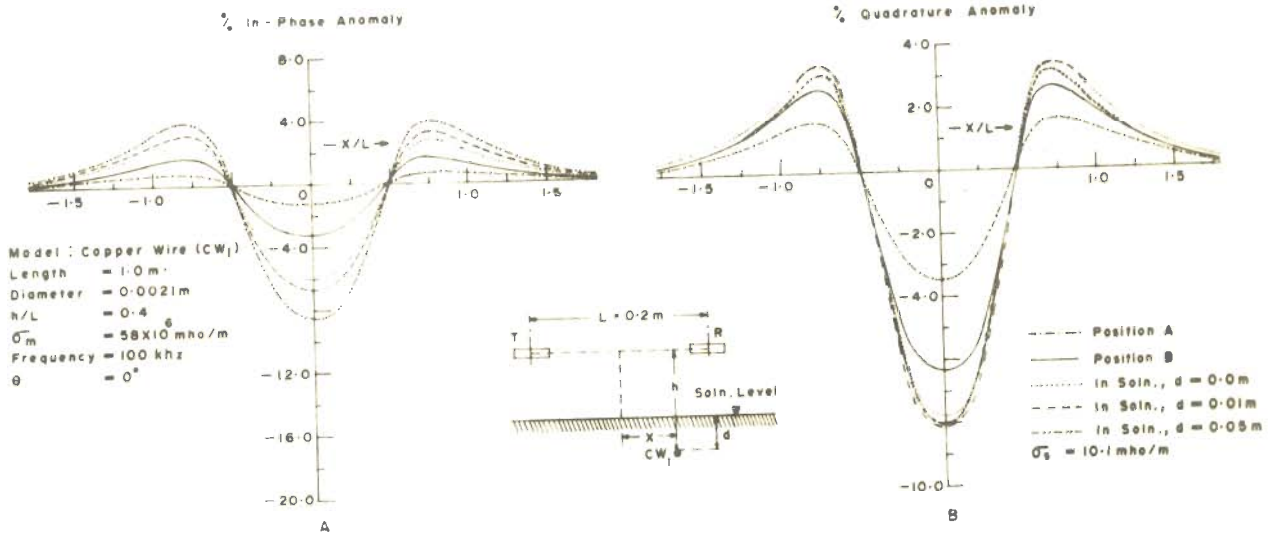
#### 4.2 Slichter's Experiment

Slichter (1959) reported a significant enhancement of the secondary field due to a bare copper wire as soon as it was dipped in a salt solution as compared with that obtained when the wire was in air. The phenomenon will be called, hereafter, as Slichter effect. As early as 1832, Faraday had also predicted an analogous effect that a measurable e.m.f. would develop in a copper wire placed across the English Channel due to the movement of sea-water in the earth's magnetic field. Such an e.m.f. varying in phase with the tides, was actually observed by Wollastan (1881) about half a century later.

When performed in this laboratory, this experiment was found to provide a valuable physical insight into the influence of a conducting hostrock (Gupta Sarma and Maru, 1971). More detailed investigations have, subsequently, been made using copper wires as well as less conducting graphite cylinders immersed at different depths in a salt solution.

#### 4.2.1 Copper wires

A bare copper wire ( $CW_1$ ) of diameter  $2.1 \times 10^{-3}$  m, and length 1.0 m was found to be undetectable when placed in air (whether underlain by the solution surface or not) through a T001 L100 R001 prospecting system ( $L = 0.2$  m and  $h/L = 0.4$ ). However, an appreciable response was produced even if its ends were dipped about half a cm each side (Position A) in the salt solution of conductivity  $\sigma_s = 10.1$  mho/m (figure 4.1). The quadrature component of the response was quite significant though the in-phase component was relatively smaller. As the depth of burial of the wire was increased, both the  $I_p$  and  $Q_r$  components were enhanced. Initially, the  $Q_r$  component increased at a much faster rate as compared to the  $I_p$  component (inset of figure 4.3). Hence, the  $I_p/Q_r$  ratio i.e. induction index  $I_i$  for position A as well as for position B (when the lower half of the wire is immersed in the solution along its entire length) is much less than unity (inset of figure 4.4). The rate of



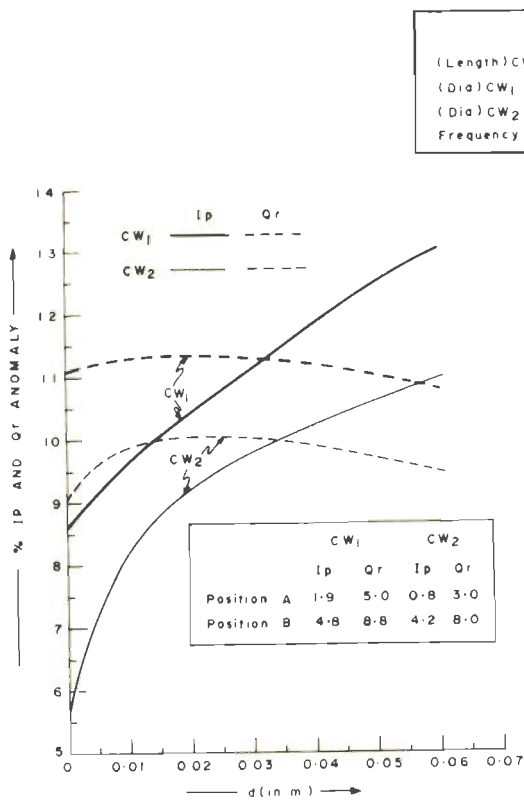


Fig. 4-3 IN-PHASE AND QUADRATURE COMPONENTS OF THE ANOMALY VERSUS THE DEPTH OF BURIAL FOR HORIZONTAL COPPER WIRES

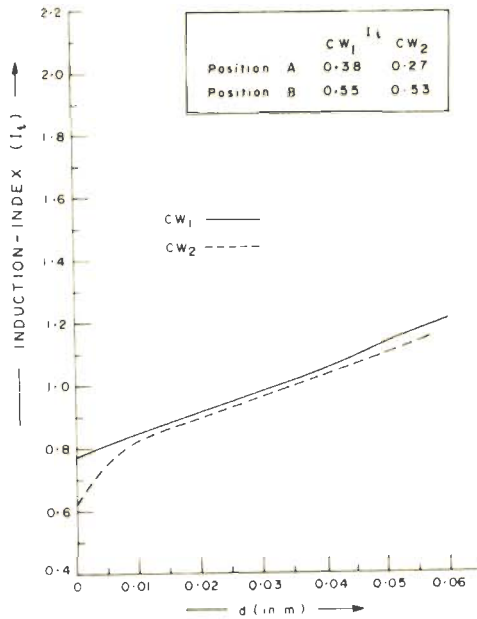


Fig. 4-4 INDUCTION INDEX (I<sub>i</sub>) VERSUS THE DEPTH OF BURIAL FOR HORIZONTAL COPPER WIRES

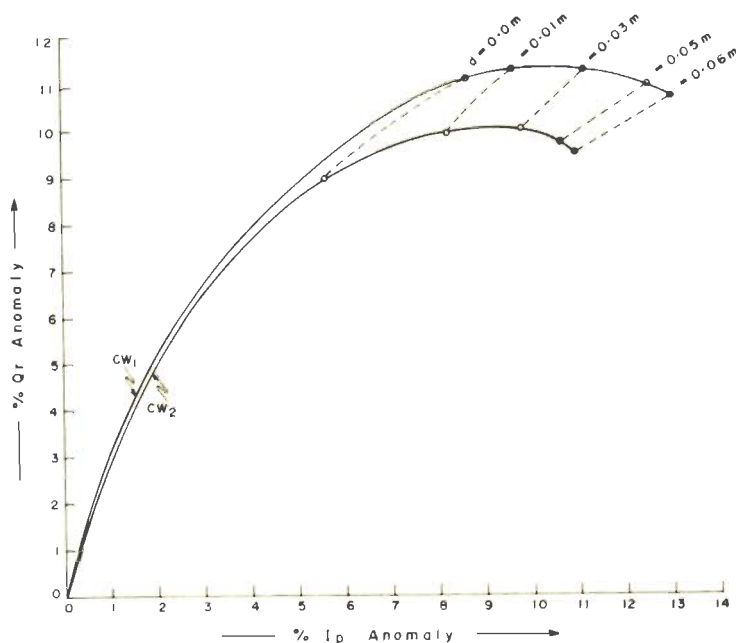


Fig. 4-5 ANOMALY INDEX DIAGRAM FOR HORIZONTAL COPPER WIRES (d VARYING)

enhancement of the  $I_p$  component, however, increased for greater depths of burial resulting in an increase of  $I_i$  (figure 4.4). Beyond  $d \approx 0.02$  m, the  $Q_r$  component starts decreasing and  $I_i$  which becomes unity for  $d = 0.03$  m is further increased. The anomaly index diagram with variation in the depth of burial is shown in figure 4.5.

The same experiment was repeated with an equally long but thinner copper wire ( $CW_2$ ) of diameter  $0.9 \times 10^{-3}$  m for which the anomaly profiles are shown in figure 4.2. The response in this case is found to be much smaller than that of the thicker wire when both are flush with the solution. However, both the  $I_p$  and  $Q_r$  components increase rapidly as the wire is moved from the position A to the position B (figure 4.3). With increasing depth of burial, the  $I_p$  component continues to increase while the  $Q_r$  component attains a maximum value and then decreases in the same way as observed for a thicker wire. It is noticed that the depth of burial for  $CW_1$  beyond which the  $Q_r$  component starts decreasing is relatively smaller than that for  $CW_2$ . This observation will be further discussed in Section 4.2.3.1. In general, however, the qualitative behavior of the responses of two wires are similar. For greater depths of burial, the induction indices for both the wires are also found to be almost equal. It may, therefore, be inferred that the enhancement in the

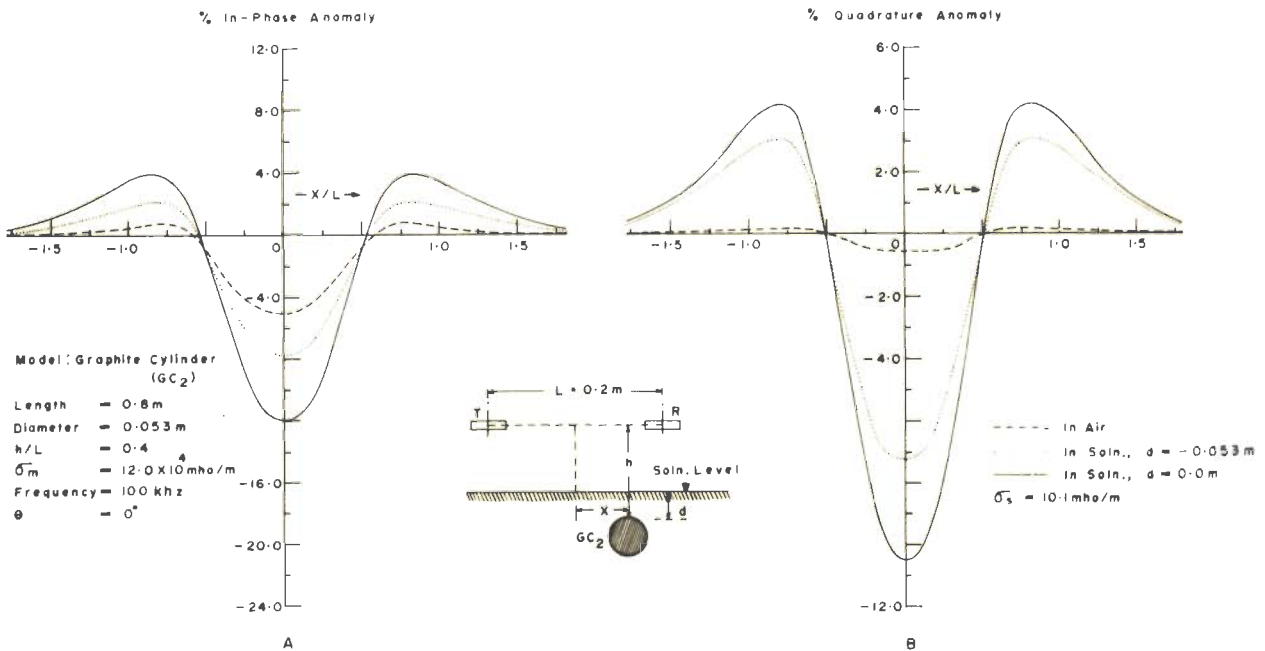
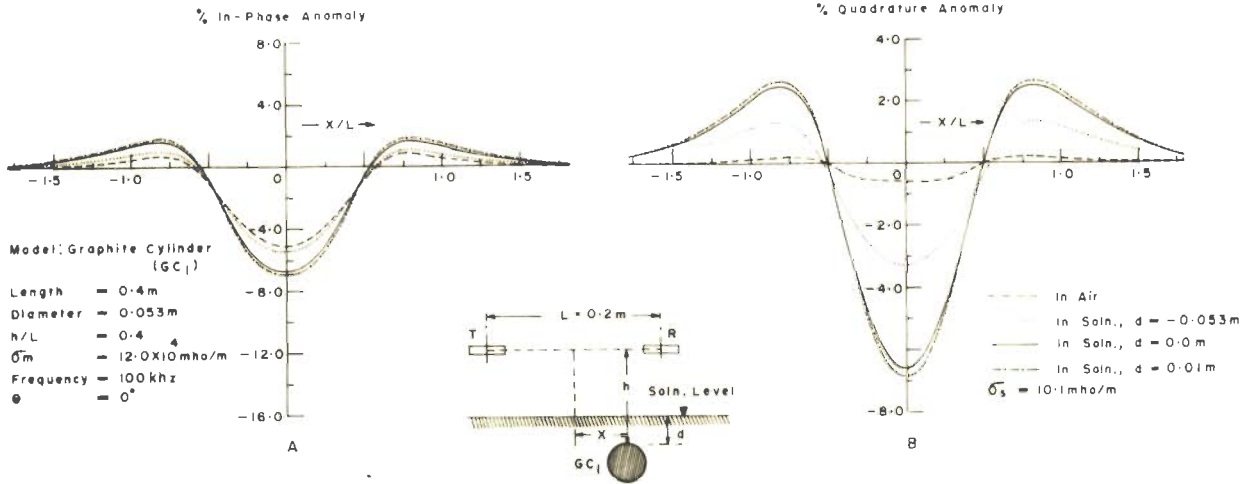


response of the wires is primarily diagnostic of the conductivity of the surrounding medium.

#### 4.2.2 Horizontal graphite cylinders

Responses of graphite cylinders ( $\sigma_m = 12.0 \times 10^4$  mho/m) of different diameters and lengths have also been studied since they represent more realistic physical models than a copper wire. A cylinder immersed in a salt solution may simulate a concentrated mineralised manto with a zone of disseminated mineralisation around it. The results on graphite cylinders thus have relatively greater implicit pertinence to the field problems. Figures 4.6 to 4.9 present the anomaly profiles for four representative cylindrical models whose dimensions are indicated there.

It may be pertinent to mention here that the anomaly components are reckoned from the background level away from the target. Effectively, the  $I_p$  and  $Q_r$  components of the solution are subtracted from the components of the total response so as to get the response of the target alone in presence of the conducting surrounding medium. Of course, since the observations are made over a region free from wall effect, the peak-to-peak excursion remains unaltered. It may also be noted that the transverse positioning of the anomaly profiles has no effect on the peak-to-peak excursion and therefore



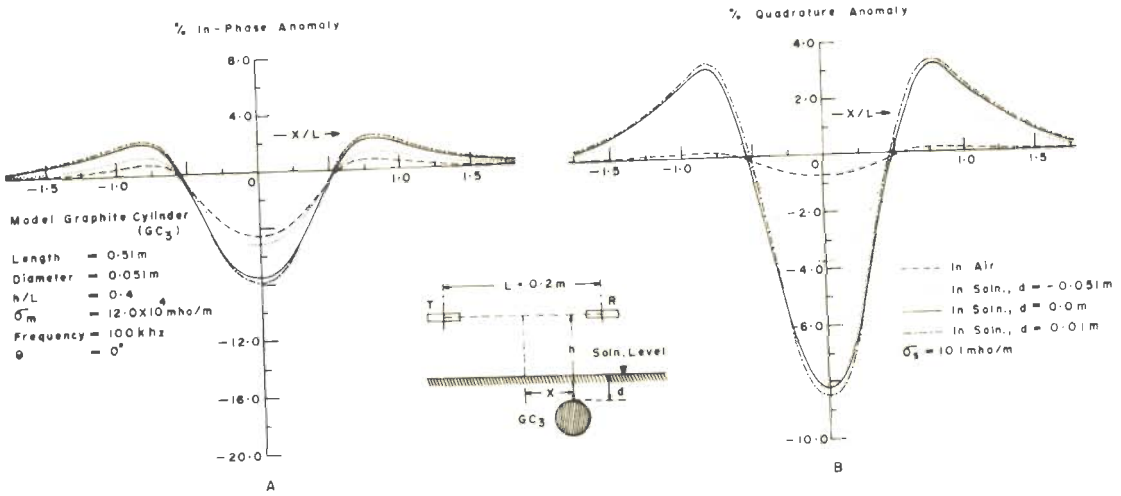


Fig. 4-8 ANOMALY PROFILES OVER A GRAPHITE CYLINDER

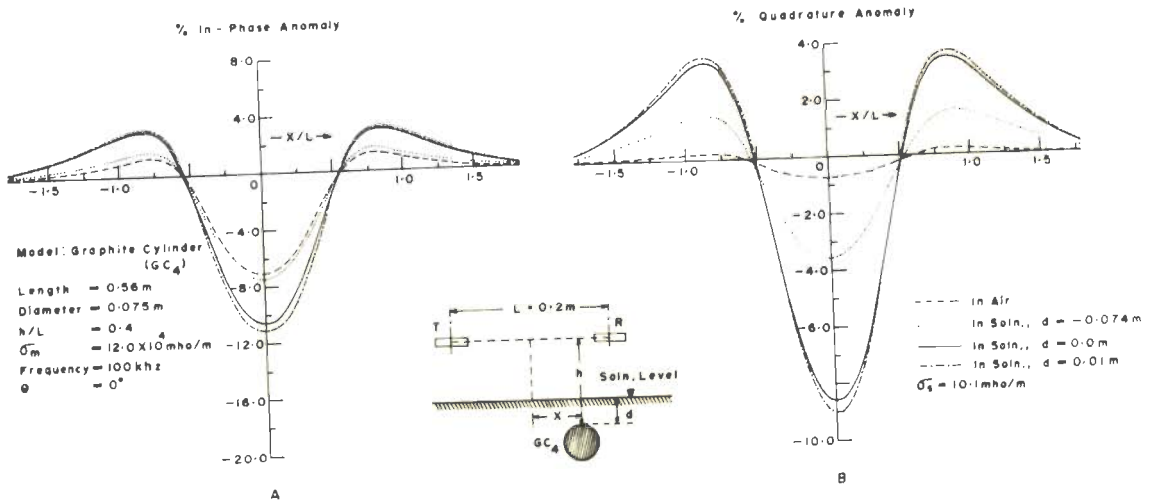


Fig. 4-9 ANOMALY PROFILES OVER A GRAPHITE CYLINDER

to avoid mixing up of the profiles, a transverse shifting of the anomaly profiles has sometimes been made in the subsequent figures.

The anomaly components of a cylinder ( $GC_1$ ) of length  $2L$  held in air are found to be identical to those of a cylinder ( $GC_2$ ) of length  $4L$  ( $h/L = 0.4$ ). This implies that, when kept in air, even the cylinder of smaller length appears to be infinite with respect to the prospecting system since its ends are not discernible. The situation, however, changes remarkably as soon as the cylinder and the solution ( $\sigma_s = 10.1$  mho/m) are brought in conductive contact with each other and the response of the longer cylinder becomes much greater than that of the smaller one as shown in figure 4.10 in which the marks on each curve corresponds to the same depth of burial. Also, with increasing depth of burial, the response enhancement ratios ( $I_s/I_a$  and  $Q_s/Q_a$  as defined in Section 3.4) are greater the longer the cylinder is (figure 4.12).

It may be further noted from what follows that the enhancement of the response, though greatly depends on the linear dimension, is much less affected by the variation of the diameter. The  $Q_r$  components of the anomaly due to  $GC_1$  and  $GC_3$  (figure 4.10) are almost identical and the  $I_p$  component for  $GC_3$  which is slightly

	GC <sub>1</sub>	GC <sub>2</sub>	GC <sub>3</sub>	GC <sub>4</sub>
Length	0.4 m	0.8 m	0.51 m	0.56 m
Diameter	0.053 m	0.053 m	0.051 m	0.075 m
$[I_i]_{GC_1 \text{ in air}}$	7.6			
$[I_i]_{GC_2 \text{ in air}}$		7.6		
$[I_i]_{GC_3 \text{ in air}}$			5.8	
$[I_i]_{GC_4 \text{ in air}}$				6.7

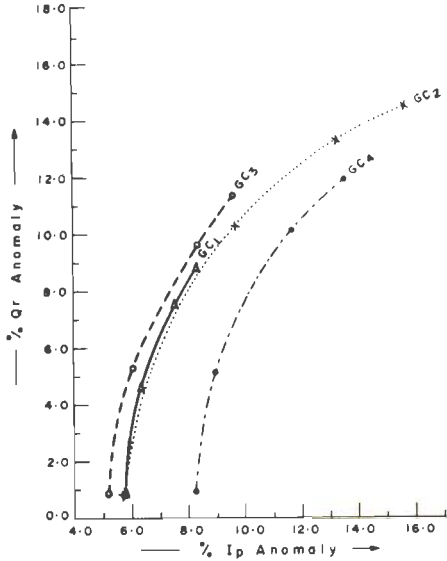


Fig. 4-10 ANOMALY INDEX DIAGRAMS FOR GRAPHITE CYLINDERS ( $d$  VARYING)

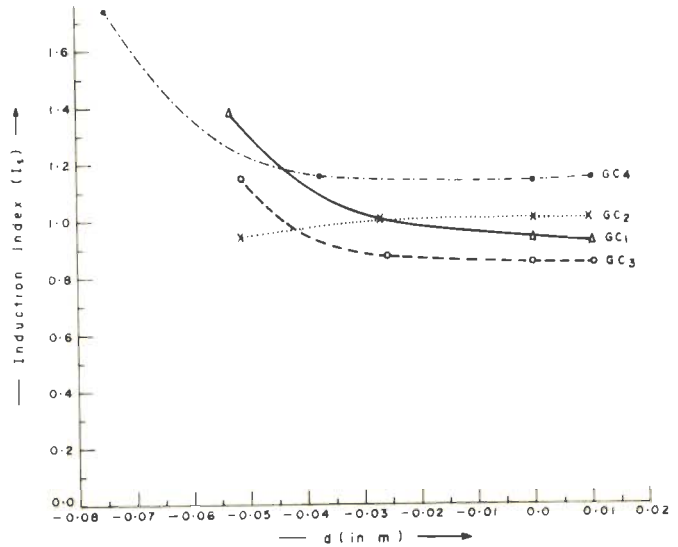


Fig. 4-11 INDUCTION INDEX ( $I_i$ ) VERSUS DEPTH OF BURIAL FOR GRAPHITE CYLINDERS

Model: Horizontal Graphite Cylinders			
$h/L$	= 0.4	$L$	= 0.2 m
$\sigma_m$	= $12.0 \times 10^4$ mho/m	$\sigma_s$	= 10.1 mho/m
Frequency	= 100 kHz	$\theta$	= $0^\circ$

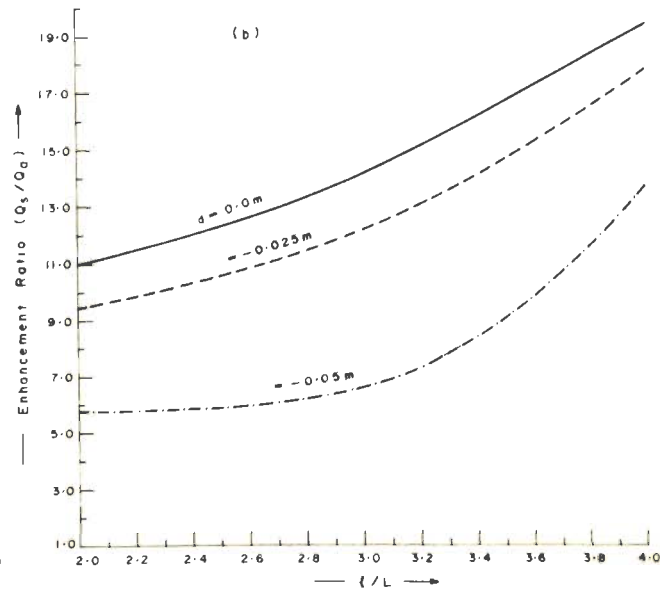
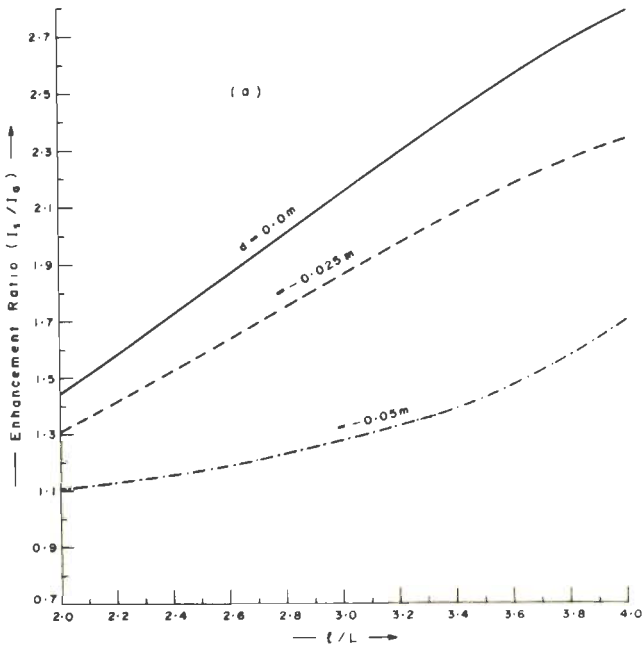


Fig. 4-12 ENHANCEMENT RATIOS (a)  $I_i/I_0$  AND (b)  $O_3/O_0$  VERSUS THE LENGTH OF HORIZONTAL GRAPHITE CYLINDERS

thinner than  $GC_1$ , is smaller than that for the latter (viz  $GC_1$ ) when both are kept in air. The greater length of  $GC_3$  than that of  $GC_1$  is expectedly of no consequence as both appear to be infinite when placed in air. However, as soon as they are immersed in the salt solution, both the  $I_p$  and  $Q_r$  components of the response of  $GC_3$  become distinctly greater than those of  $GC_1$ . In contrast, the response behaviors of  $GC_3$  and  $GC_4$  evince that the enhancement ratios ( $I_s/I_a$  and  $Q_s/Q_a$ ) for the cylinders are not very much different from each other, in spite of the fact that the diameter of  $GC_4$  is about one and a half times greater than that of  $GC_3$ .

It may, thus, be inferred that for this prospecting system it is the length along which the higher conducting target touches the solution, that plays a significant role in the enhancement of the response. The contact in the depth direction does not contribute much to the enhancement.

Figure 4.11 depicts the values of  $I_i$  for these cylinders. It is seen that whereas the value of  $I_i$  for  $GC_3$  is less than that of  $GC_1$  for all the depths of burial considered here,  $I_i$  for  $GC_2$  is less than that for  $GC_1$  initially but overtakes it as the depth of burial is increased. Such a complex variation of  $I_i$  for different models with depth of burial greatly reduces its

significance as an interpretational parameter in drawing an inference about the properties of the target in a conducting surrounding medium.

#### 4.2.3 Physical explanation

The enhancement of the response of the above models (wires and cylinders) even when they are partially immersed in the solution and a further increase with increasing depth of burial is quite interesting. This phenomenon may be ascribed to the collection of additional current lines from the less conducting solution by the better conducting target. The redistribution of current lines naturally takes place from all sides. Therefore, as the target is immersed deeper, a larger volume of the solution is available around it from which to collect and thereby concentrate the current through itself. This explanation is supported by the analysis of the induced current distribution (cf. Section 2.2.4.4) where the current density in a less conducting surrounding medium was found to decrease with increase in the conductivity of the core. The process of redistribution of currents in a spherical system has, of course, been much less pronounced because of its symmetry than what is observed in the above experiments. A greater dependence of the response on the length of the target when surrounded by a conducting medium as compared to that when it is placed in air is obviously due to the possibility of collection

of larger current by a longer conductor in accordance with this explanation.

The magnitude and nature of the enhancement is expected to depend upon

(i) the conductivity contrast between the target and the surrounding medium besides the absolute values of the conductivities of both

and (ii) the nature and surface area of contact of the target with the surrounding medium.

The phenomenon of enhancement may appear to have been amplified in the case of copper wires and such a large enhancement as this may not be observable in realistic situations. But the enhancement of response in the case of much less conducting graphite cylinders certainly indicates the applied significance of the results and one may expect similar situations in the field surveys.

#### 4.2.3.1 Relative enhancement of the in-phase and quadrature components

For all the models investigated here,  $Q_s/Q_a$  has been found to be very much greater than  $I_s/I_a$  i.e. the quadrature component of the response is enhanced



relatively much more than its in-phase counterpart when the target is immersed in a solution. This in turn may be regarded as the corollary to the phase of the currents induced in a solution of low conductivity. This effect causes a significant reduction of the induction index  $I_i$  (figures 4.4 and 4.11) when the model is in the solution as compared to that when it is in air.

The behavior of  $I_i$  with increase in the depth of burial in the case of graphite cylinders is found to be different from that for copper wires. It appears that there exists a limiting depth of burial upto which the collection of current keeps on increasing. Beyond this limit, it is mainly the phase rotation which gives rise to an increase in the  $I_p$  component and reduction of the  $Q_r$  component. The longer is the conductor and the higher its conductivity the sooner this limit will be attained. Thus, for a less conducting target such as a graphite cylinder this limit approaches at a greater depth of burial, while for a higher conducting model like a copper wire it is attained at shallower levels. Further, in the case of latter, the limit is deeper for a thinner wire. This explains why  $I_i$  in the case of a copper wire is found to enhance with increase in the depth of burial beyond shallow depths but different is the case with less conducting graphite cylinders. It will be seen subsequently that the  $I_i$  values for sheets of copper

and stainless steel begin to increase with increase in  $d$  right from the position when the model top is flush with the solution surface.

The modification of the response components as well as their ratio i.e.  $I_1$  for a target as brought about by a conductive contact with the surrounding medium will greatly impair the interpretational sensitivity in the induction prospecting. The first order inference about the grade of an anomaly from the induction index will, also be in error if the influence of the conducting surrounding is not appropriately taken into account.

#### 4.3 Isometric Conductors

Isometric conductors may be assumed to represent localised concentrated pockets of sulfide ore-bodies. Because of their small cross-sections orthogonal to the profile direction and symmetrical shapes, the redistribution of the current lines and their consequent concentration in and around the target is not expected to be appreciable in this case. The experimental investigation of their response supports this hypothesis. In particular, the effect of a conducting surrounding medium on the  $I_p$  component is almost insignificant although the enhancement of the  $Q_r$  component is found to be relatively greater but still remaining much less than that observed in the case of elongated conductors.

#### 4.3.1 Spherical models

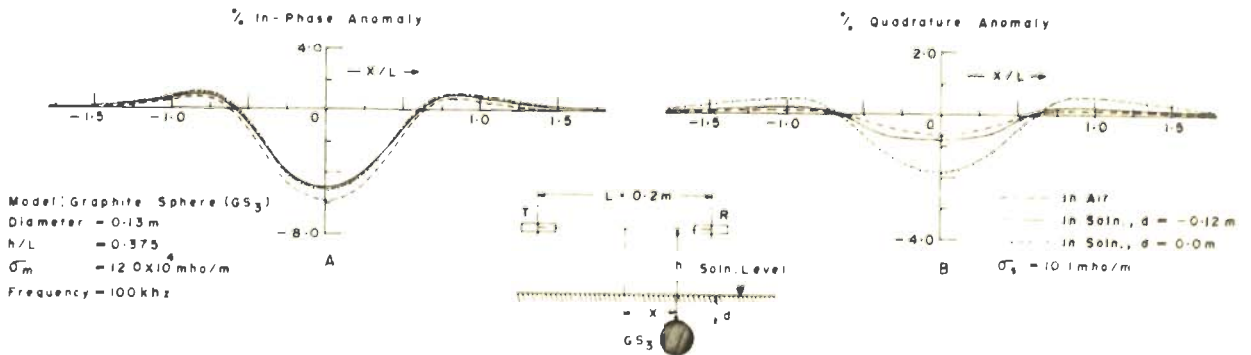
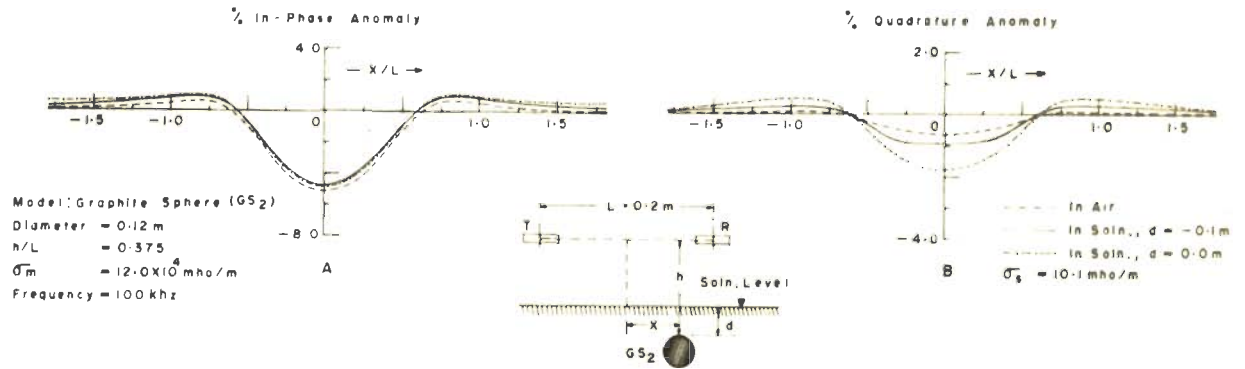
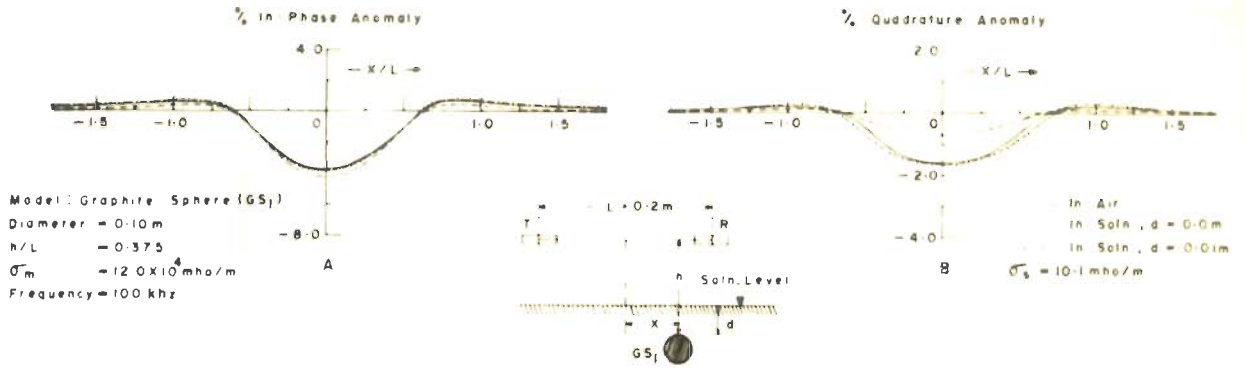
The response variation of spherical bodies has been studied for different conductivities of the target and the surrounding medium. The  $I_p$  component is found to decrease if a sphere is held just above the solution i.e. insulated from it or even when its lower portion touches the solution. This observation, noticed for spheres of various diameters, is different from, and in a way contradictory to, what was observed in Section 4.2. A similar interesting effect was noticed by Rikitake (1961) while studying the effect of conducting oceans on long period geomagnetic variations. He discovered that if allowance was made for the conducting mantle underlying the oceans, the inductive effect was found to be greatly reduced as compared to that when the underlying layer was neglected. Recently, Hill and Wait (1972) have discussed the inductive interaction between a sphere and an underlying conducting ground.

The reduction of the  $I_p$  component merely because of the vicinity of the solution, when there is neither electromagnetic screening nor a conductive contact between the target and the underlying solution, resembles a transformer action. In the configuration mentioned above, the inductive interaction between the sphere and the solution appears to be opposed to the enhancing influence arising from a conductive contact.

The contrast between the target geometries, viz a sphere of symmetrical shape having much less lateral extent than the elongated targets, is also to be noted. Figures 4.13 to 4.17 give the anomaly profiles for spheres of different conductivities and diameters.

As a spherical conductor is gradually lowered down in the solution, the  $I_p$  component shows a slight increase presumably because of the increased Slichter effect. In the case of a graphite sphere (dia.= 0.12 m), it is observed that on completely dipping it in the solution (so that its top is flush with the solution surface) the  $I_p$  component of its response becomes slightly greater than that obtained when it is placed in air (figure 4.14). However, in the case of spheres of other diameters, whether larger or smaller, the values of  $I_s$  remain more or less the same as the corresponding  $I_a$  values. A selective enhancement of the  $I_p$  component for a particular case, though not significant needs further investigation.

However, the  $Q_r$  component is found to be enhanced for all the configurations and depths of burial and it further increases as the model is progressively lowered in the solution. The anomaly amplitude as a whole is, thus, found to increase. In accordance to the logic of Section 4.2.3.1 the induction index  $I_i$  undergoes



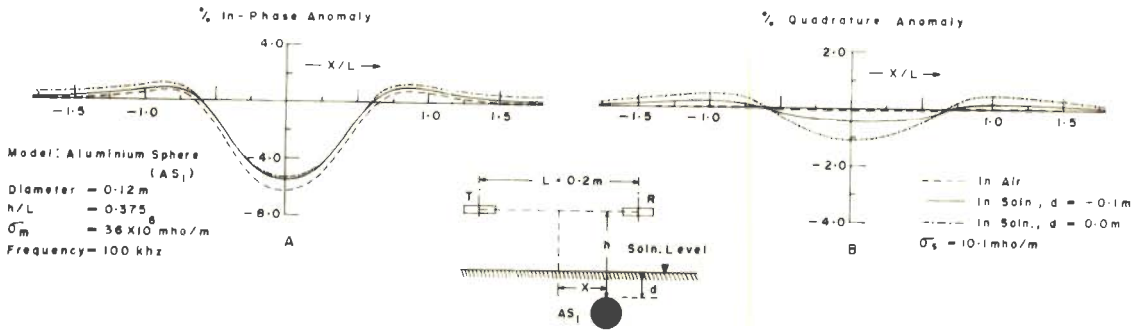


Fig.4-16 ANOMALY PROFILES OVER AN ALUMINIUM SPHERE

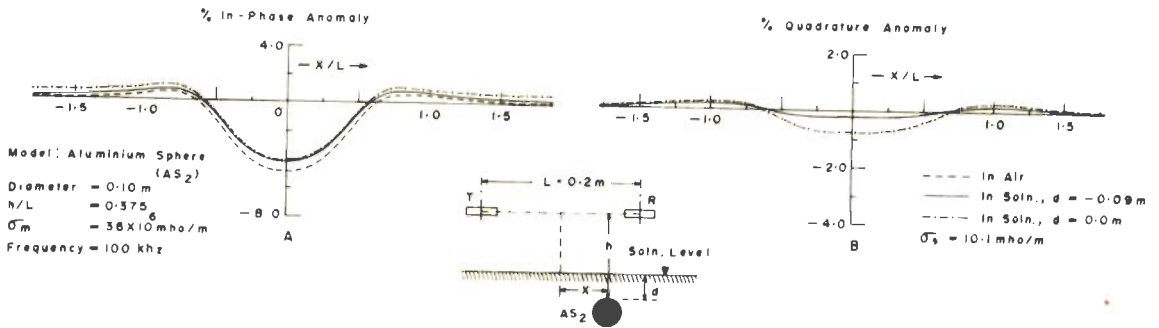


Fig.4-17 ANOMALY PROFILES OVER AN ALUMINIUM SPHERE

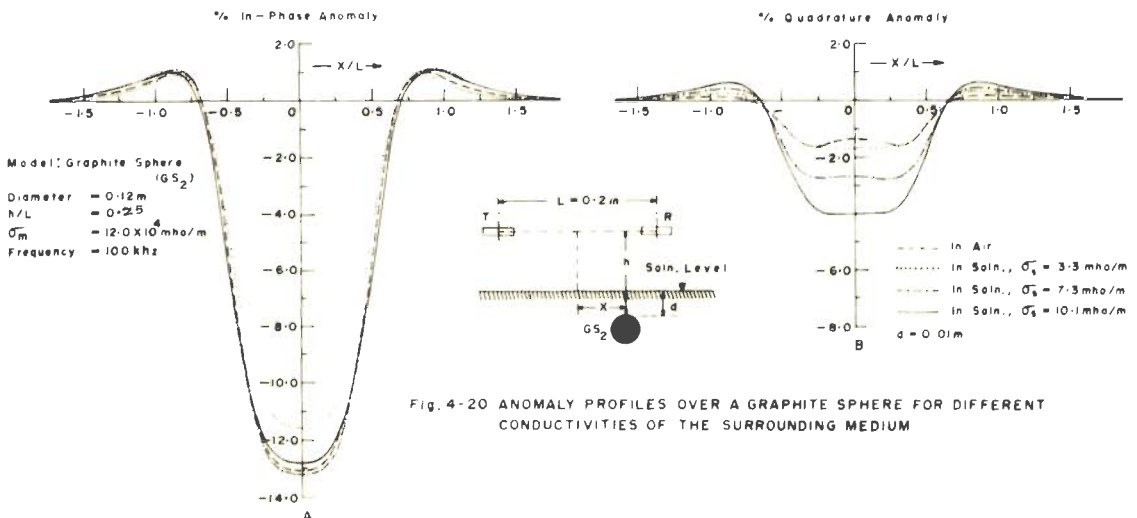
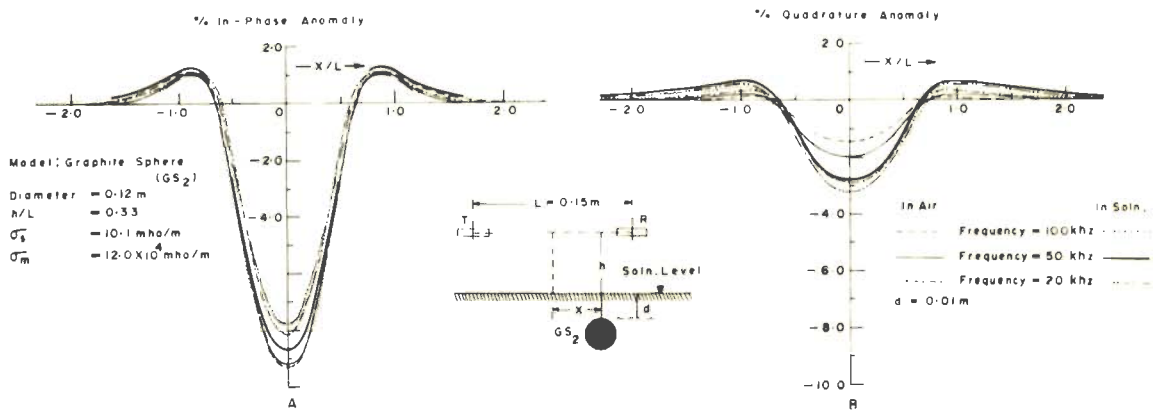
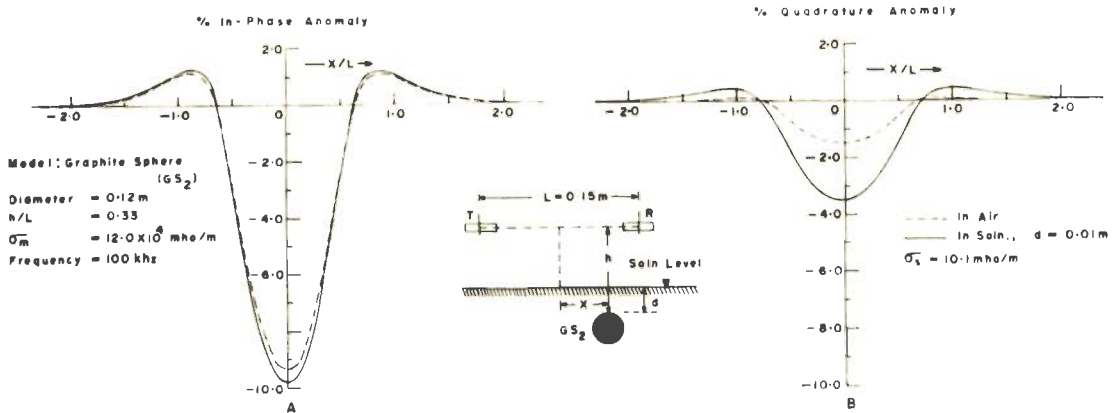
a reduction as the sphere is immersed in the solution.

From the observations on the spheres, it is further confirmed that for the situations considered presently, the linear dimension rather than the conductivity of the target plays a predominant role in the enhancement of the anomaly.

#### 4.3.1.2 Variation of the conductivity of the surrounding medium and the frequency of energisation

Since an increase was noticed in the  $I_p$  as well as the  $Q_r$  components of the response of the graphite sphere of diameter = 0.12 m, the model was studied in further detail by changing the conductivity of the surrounding medium and the frequency of the energising field. It was seen that the anomaly components for this sphere get enhanced on immersing it in the solution for a reduced T-R separation ( $L = 0.15$  m) also (figure 4.18).

The conductivity of the solution was varied in the range from 1.55 mho/m to 10.1 mho/m and the behavior of the response studied. The  $I_p$  component is found to be enhanced (figure 4.20) for higher values of  $\sigma_s$  lying between 10.1 mho/m and 6.7 mho/m. However, for lower conductivities ( $\sigma_s < 6.7$  mho/m) the enhancement is inappreciable. For this range of  $\sigma_s$  (low values) and at shallow depths,  $I_s$  is less than even  $I_a$ . But as the depth





of burial is increased,  $I_s$  resumes the same value as  $I_a$ . The value of  $Q_s$  is, however, found to be increasing even for the lowest conductivity of the solution used.

Though, of course, for  $\sigma_s \approx 1.55$  mho/m the enhancement of the  $Q_r$  component is negligibly small.

The effect of reducing the frequency upon the enhancement is in general similar, as it should be, to diminishing  $\sigma_s$ . But, while the variation in  $\sigma_s$  causes a change in the response parameter of the surrounding medium alone, the frequency variation affects the response parameter of the target as well. Hence by decreasing  $\sigma_s$ , the  $Q_r$  component decreases but the same is not true if the frequency is reduced. Figure 4.19 shows that within the frequency range studied, the  $Q_r$  component is enhanced with decrease in frequency when the model is kept in air but the trend is reversed when it is placed in a conducting surrounding. If  $\sigma_s$  becomes so low that the Slichter effect is negligible, the same trend i.e. enhancement of the  $Q_r$  component with decrease in frequency is restored. As will be seen subsequently, similar variation of the  $Q_r$  component with frequency takes place for other models also. It is found to be more pronounced for elongated sheets.

The reversal of the  $Q_r$  variation with frequency, as  $\sigma_s$  is increased, may also be attributed to the

characteristics of the induced currents collected by the sphere from the solution. Since these currents in the solution are mainly in quadrature with the primary field, the reduction in the frequency of energisation decreases their magnitudes because of the reduced induction. This manifests itself in the variation of the  $Q_r$  component of the response with change in the frequency when the sphere is placed in the solution.

#### 4.3.2 Thick short cylinders

Investigations on thick short cylinders were made in continuation with the studies on spherical models. Though the dimensions of the cylinders were greater than those of the spheres studied above, yet the length/diameter ratio was approximately unity and these cylinders could also be regarded as approximately isometric. However, probably because of the edges of the cylinder (in contrast to the smooth surface of a sphere) and their larger sizes, the effect of the conducting surrounding medium ( $\sigma_s = 11.6$  mho/m) on the response of these conductors is found to be much greater than that observed in the case of spheres.

Figure 4.21 (a, b, c) shows the anomaly profiles for a cylinder ( $L_1 = 0.13$  m,  $D_1 = 0.14$  m) and figure 4.22 (a, b, c) for another cylinder ( $L_2 = 0.15$  m,  $D_2 = 0.16$  m). The axes of the cylinders were kept vertical. Figure 4.23

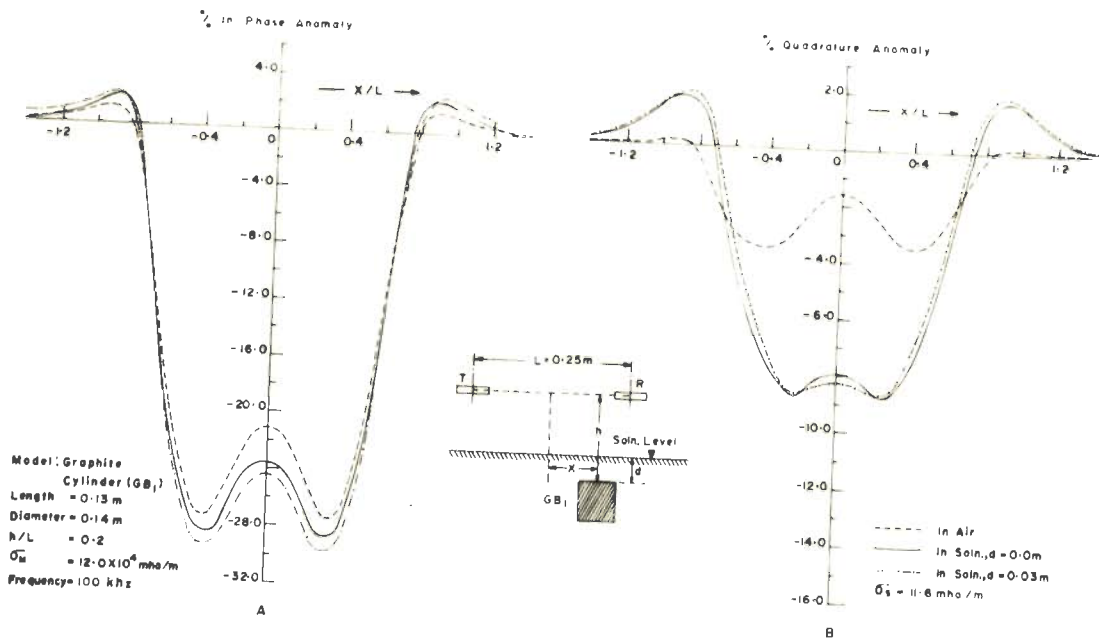


Fig. 4-21a ANOMALY PROFILES OVER A GRAPHITE CYLINDER

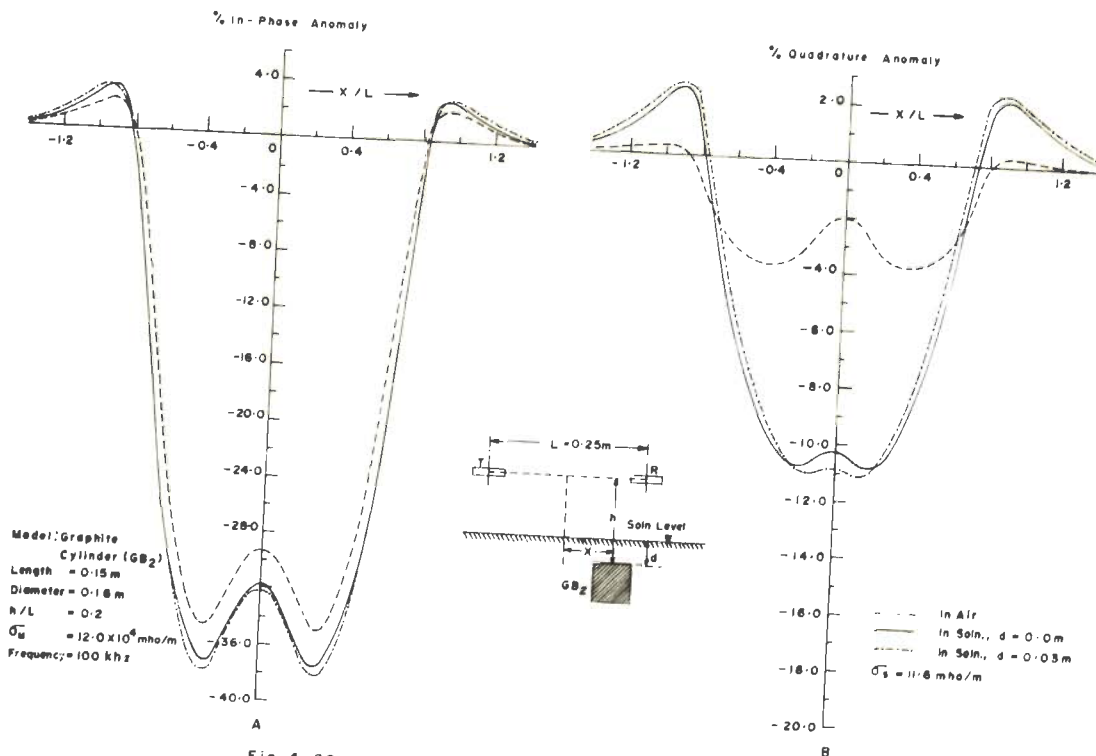


Fig. 4-22a ANOMALY PROFILES OVER A GRAPHITE CYLINDER

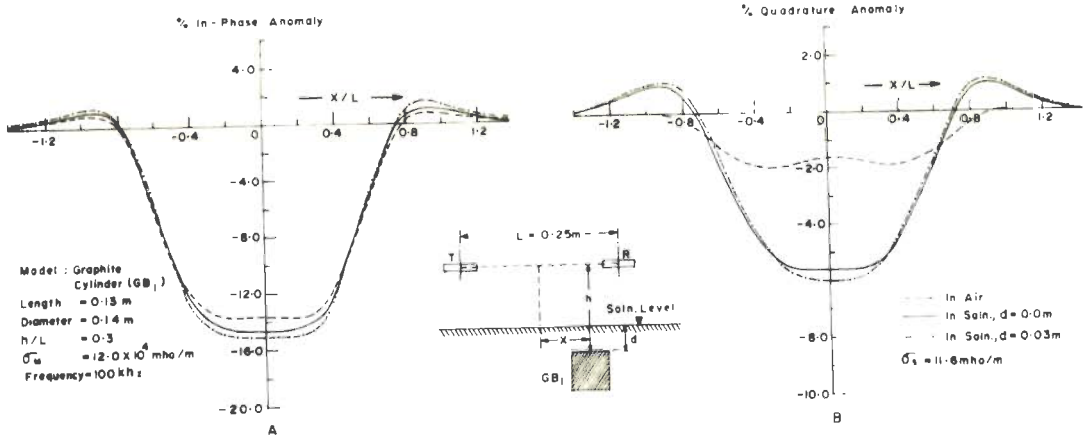


Fig 4-21b ANOMALY PROFILES OVER A GRAPHITE CYLINDER

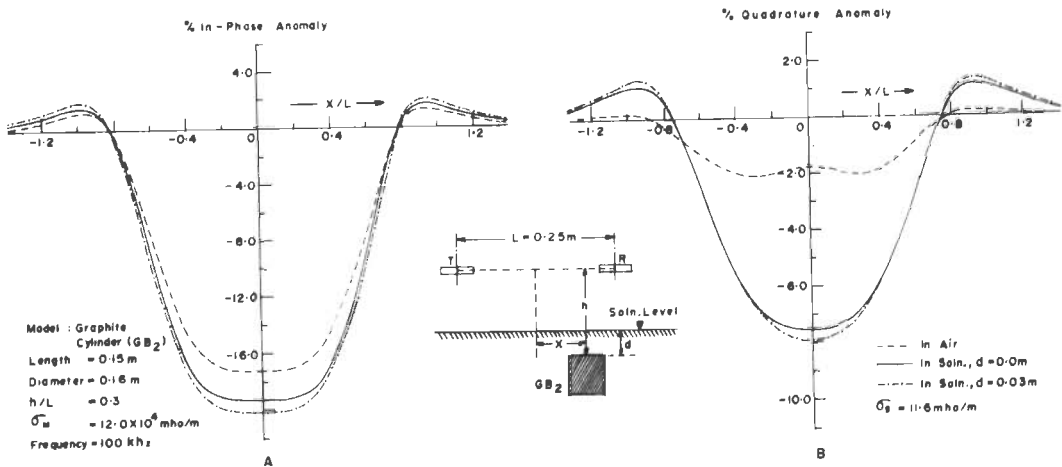


Fig. 4-22b ANOMALY PROFILES OVER A GRAPHITE CYLINDER

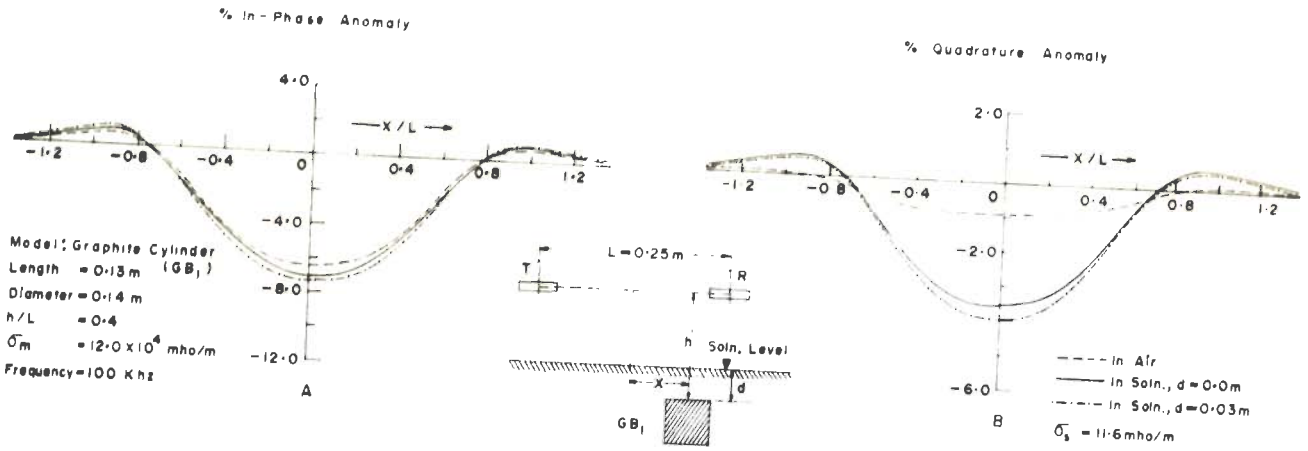


Fig. 4-21c ANOMALY PROFILES OVER A GRAPHITE CYLINDER

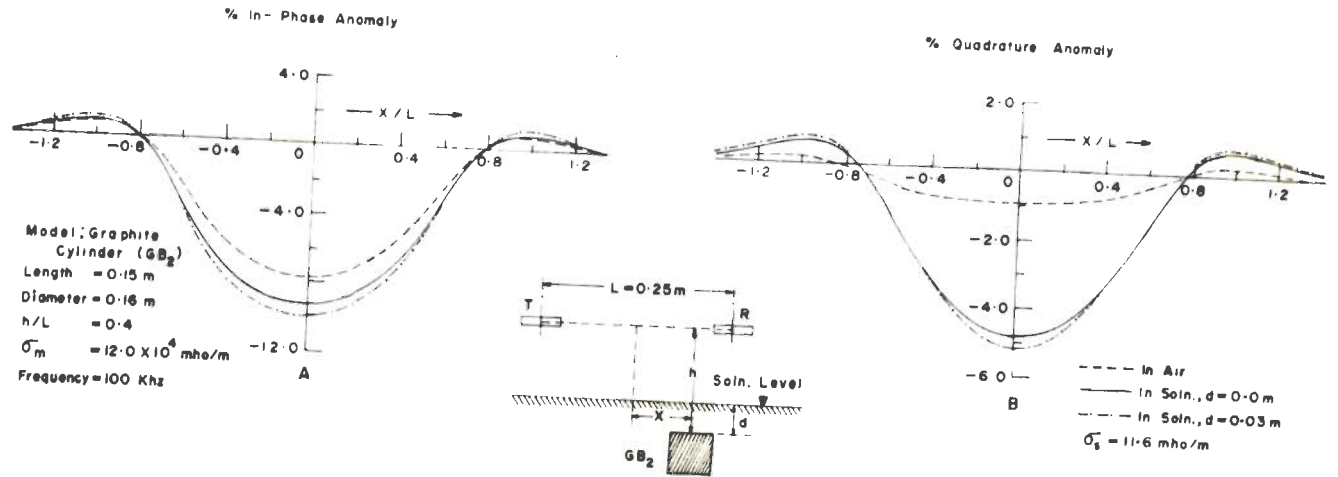


Fig. 4-22c ANOMALY PROFILES OVER A GRAPHITE CYLINDER

Model	Graphite Cylinders (GB <sub>1</sub> and GB <sub>2</sub> )
L	= 0.25 m
Frequency	= 100 kHz
$\sigma_s$	= 11.6 mho/m
$\sigma_m$	= $12.0 \times 10^{-4}$ mho/m

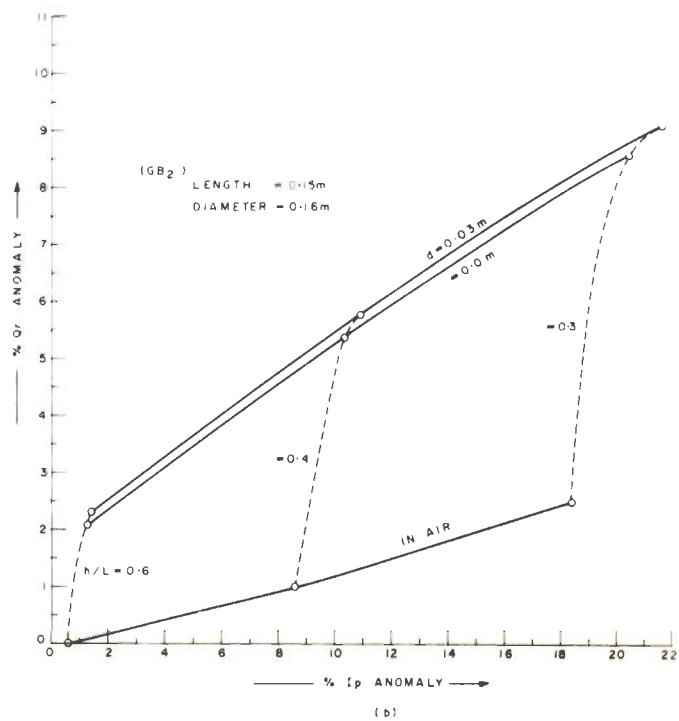
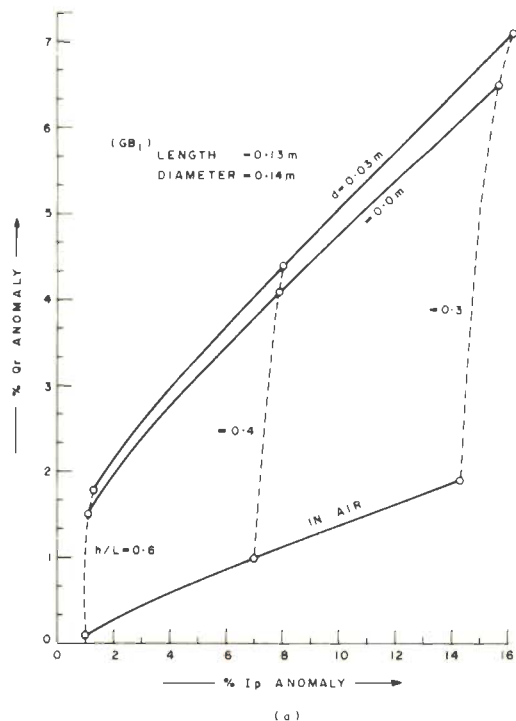


Fig.4-23 ANOMALY INDEX DIAGRAMS FOR GRAPHITE CYLINDERS (a) GB<sub>1</sub> AND (b) GB<sub>2</sub>

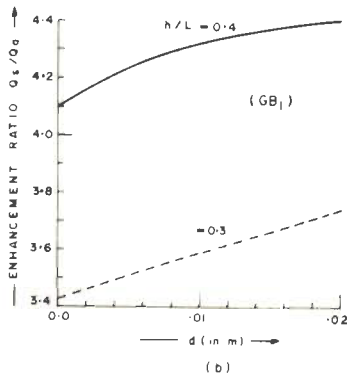
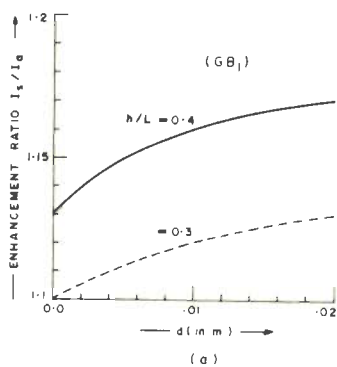


Fig.4-24 ENHANCEMENT RATIOS (a)  $I_s/I_a$  AND (b)  $Q_s/Q_a$  VERSUS DEPTH OF BURIAL FOR A GRAPHITE CYLINDER (GB<sub>1</sub>)

(a, b) presents the anomaly index diagrams for them with variation in  $d$  for different  $h/L$  values. Both the  $I_p$  and  $Q_r$  components are enhanced with increasing depth of burial of the target in the salt solution.

Figure 4.24 (a, b) and 4.25 (a,b) show the plots of  $I_s/I_a$  and  $Q_s/Q_a$  versus  $d$ . For these models also, the enhancement ratio for the quadrature component is found to be much greater than that for the in-phase component. This difference is further accentuated for greater heights of the T-R system. The induction index, therefore, reduces to about one-fourth ( $d = 0.0m$ ) of that obtained when the cylinder is kept in air (figure 4.26). The reduction in  $I_1$  is more or less of the same order for both the models. The variation of the enhancement ratio with the depth of burial is inappreciable notwithstanding the significant differential increments viz  $I_s - I_a$  and  $Q_s - Q_a$ . The behaviour of the anomalies due to these short cylinders is observed to lie between those of the long horizontal cylinders and spheres.

The profiles of the anomaly components for these cylinders at low heights of the T-R system (say  $h/L = 0.2$ ) have a positive hump in the middle similar to what was observed in Section 2.5 for spheres. The difficulty in making an anomaly index diagram for such profiles has already been discussed in Section 3.4. But contrary to

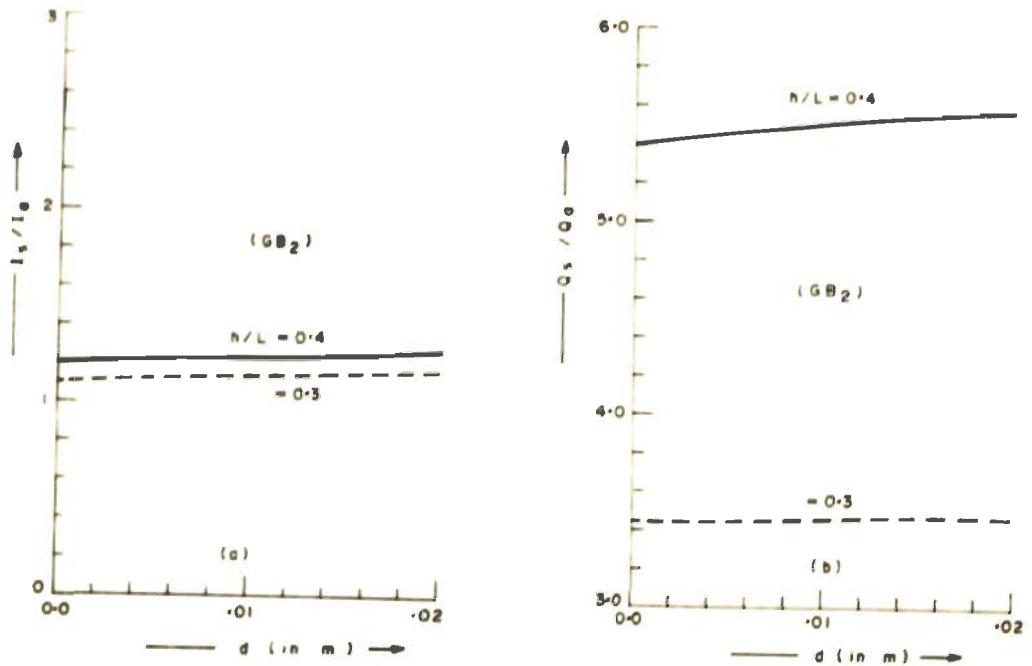


Fig. 4-25 ENHANCEMENT RATIOS (a)  $I_s/I_d$  AND (b)  $Q_s/Q_d$  VERSUS DEPTH OF BURIAL FOR A GRAPHITE CYLINDER (GB<sub>2</sub>)

MODEL	: GRAPHITE CYLINDERS
L	: 0.25 m (GB <sub>1</sub> and GB <sub>2</sub> )
FREQUENCY	: 100 kHz
$\sigma_m$	: $12.0 \times 10^4$ mho/m
$\sigma_s$	: 11.6 mho/m

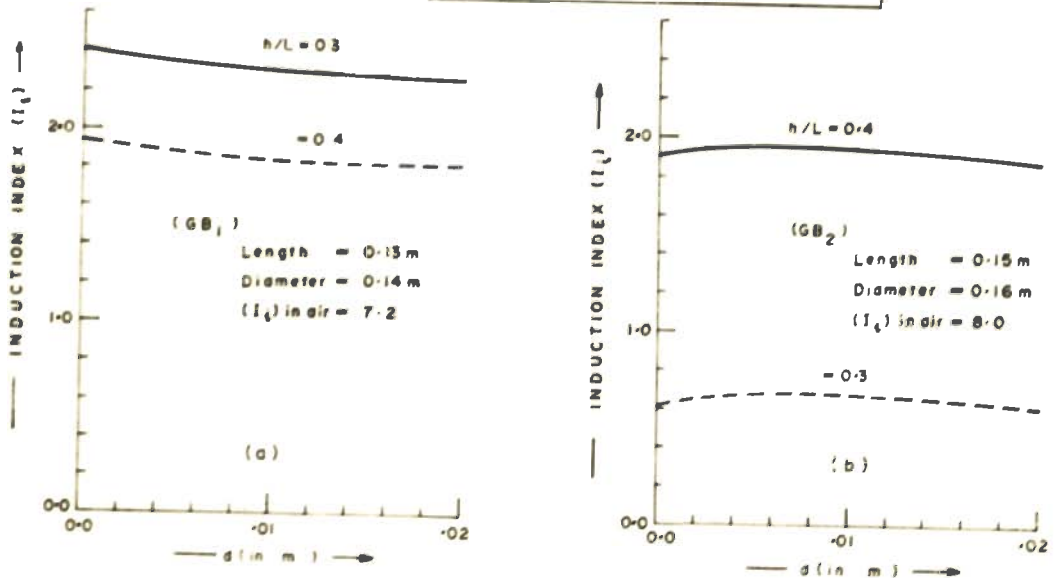


Fig. 4-26 INDUCTION INDEX ( $I_s$ ) VERSUS DEPTH OF BURIAL FOR GRAPHITE CYLINDERS (a) GB<sub>1</sub> AND (b) GB<sub>2</sub>



the response variation illustrated in figure 3.6, in the case of thick short cylinders both negative peaks and central hump of the  $I_p$  component increase as the model is dipped in the solution (figure 4.21a and 4.22a). Of course, the central hump of the  $Q_r$  profile is reduced on immersing the cylinder in solution and the negative peaks are greatly enhanced and they come closer to each other as the depth of burial is increased.

#### 4.4 Tabular Sheet Type Bodies

Sheet models simulate vein type mineralised deposits. Such a structure of sulfide ore bodies is known to occur most commonly. Majority of the scale-model experiments, reported in geophysical literature, have been carried out on sheet type models. A number of anomaly index diagrams pertaining to thin sheets when kept in air for different dip values are available (Strangway, 1966a). The results presented in this section are expected to offer useful guidelines in the interpretation of induction prospecting data where the hostrock/overburden is also anticipated to be partially conducting.

##### 4.4.1 Steeply dipping graphite sheet

The length and depth extent of a graphite sheet of dimensions 0.70m x 0.20m x 0.021m could be regarded

as about infinite since the lower edge and side ends do not have measurable influence on the response. But the situation is drastically different if the sheet is brought in conductive contact with the solution (cf. Section 4.2.2). The thickness of the sheet also could not be regarded as very small since the skin depth for the sheet material at a frequency of 100 khz is about 0.004m. Yet, this sheet was chosen for a more realistic representation of thick vein type ore deposits. Figures 4.27 to 4.31 depict some anomaly profiles for the sheet at different  $h/L$  values using different frequencies of energisation and conductivities of the surrounding medium.

#### 4.4.1.1 Variation of the conductivity of the surrounding medium

Figure 4.32 (a, b) shows the anomaly index diagrams for 100 khz and figure 4.33 (a, b) those for 50 khz at two depths of burial. As the model is immersed in the salt solution, both the  $I_p$  and  $Q_r$  components increase monotonically with increase in  $\sigma_s$ . For low values of  $\sigma_s$ , the  $I_p$  component shows an insignificant increase but the  $Q_r$  component increases relatively faster. However, if the conductivity of the surrounding medium is increased ( $\sigma_s \geq 6.7$  mho/m), the enhancement of the  $I_p$  component also becomes significant. At a larger depth of burial ( $d \geq 0.03$ m), the rate of enhancement of the  $I_p$  component is more than that of the  $Q_r$  component.

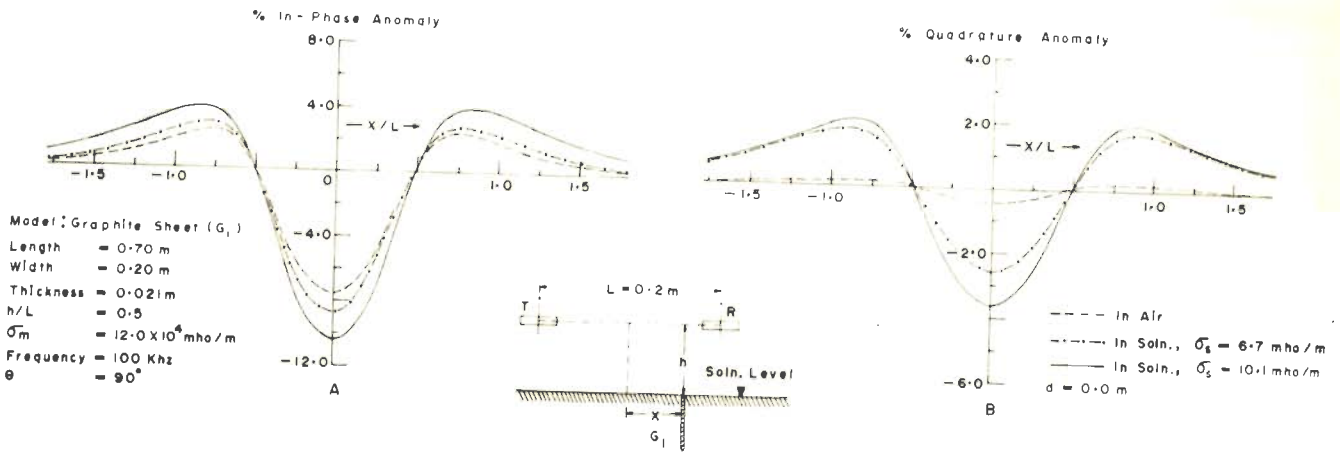


Fig.4-27 ANOMALY PROFILES OVER A GRAPHITE SHEET ( $h/L = 0.5$ )

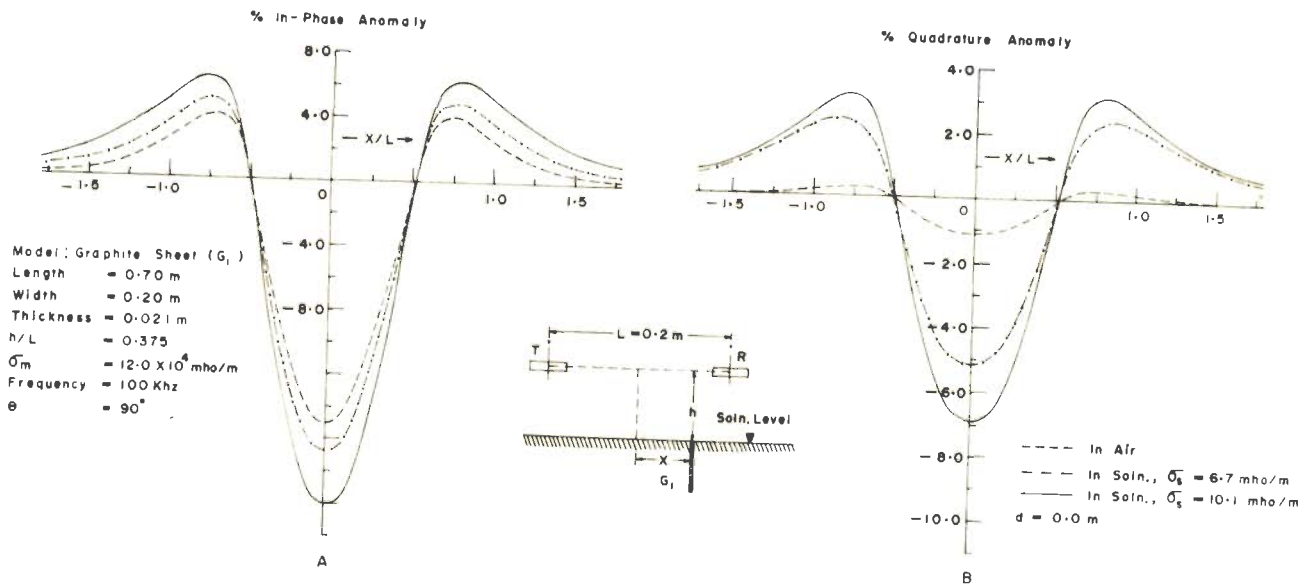


Fig.4-28 ANOMALY PROFILES OVER A GRAPHITE SHEET ( $h/L = 0.375$ )

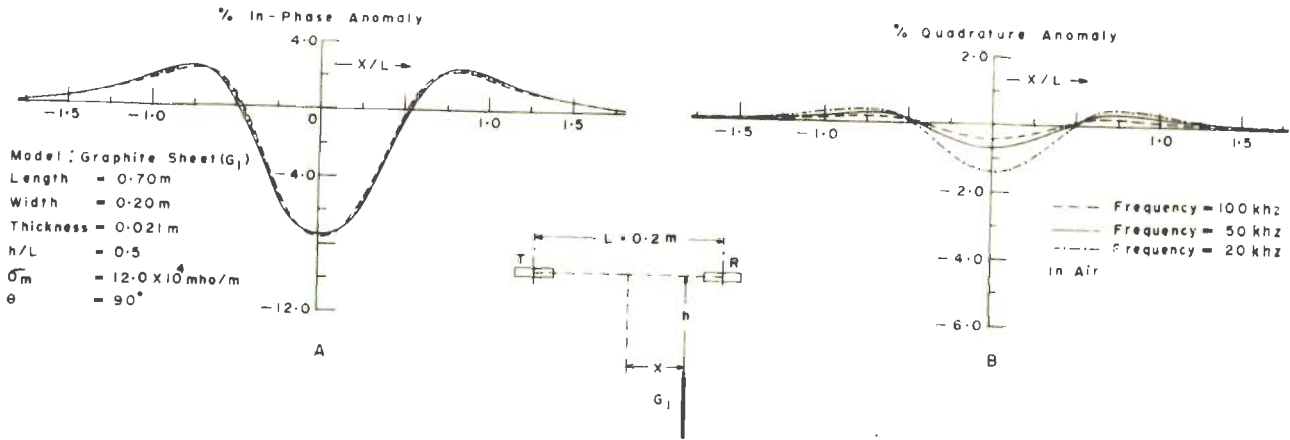


Fig.4-29 ANOMALY PROFILES OVER A GRAPHITE SHEET

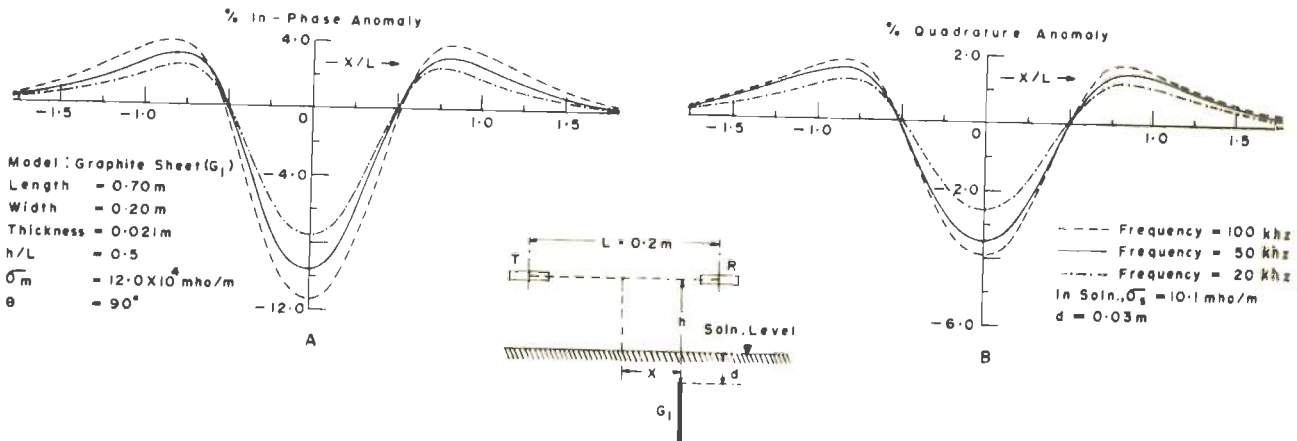


Fig.4-30 ANOMALY PROFILES OVER A GRAPHITE SHEET

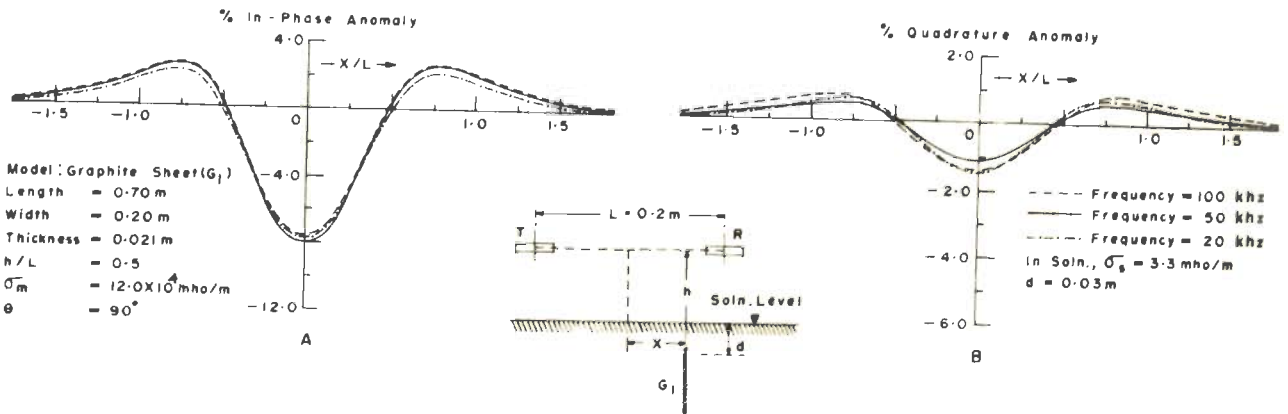


Fig.4-31 ANOMALY PROFILES OVER A GRAPHITE SHEET

Model : Graphite Sheet ( $G_1$ )			
Length	= 0.70 m	$\sigma_m$	= $12.0 \times 10^4$ mho/m
Width	= 0.20 m	$\sigma_s$	= 10.1 mho/m
Thickness	= 0.021 m	$\theta$	= $90^\circ$
L	= 0.20 m		

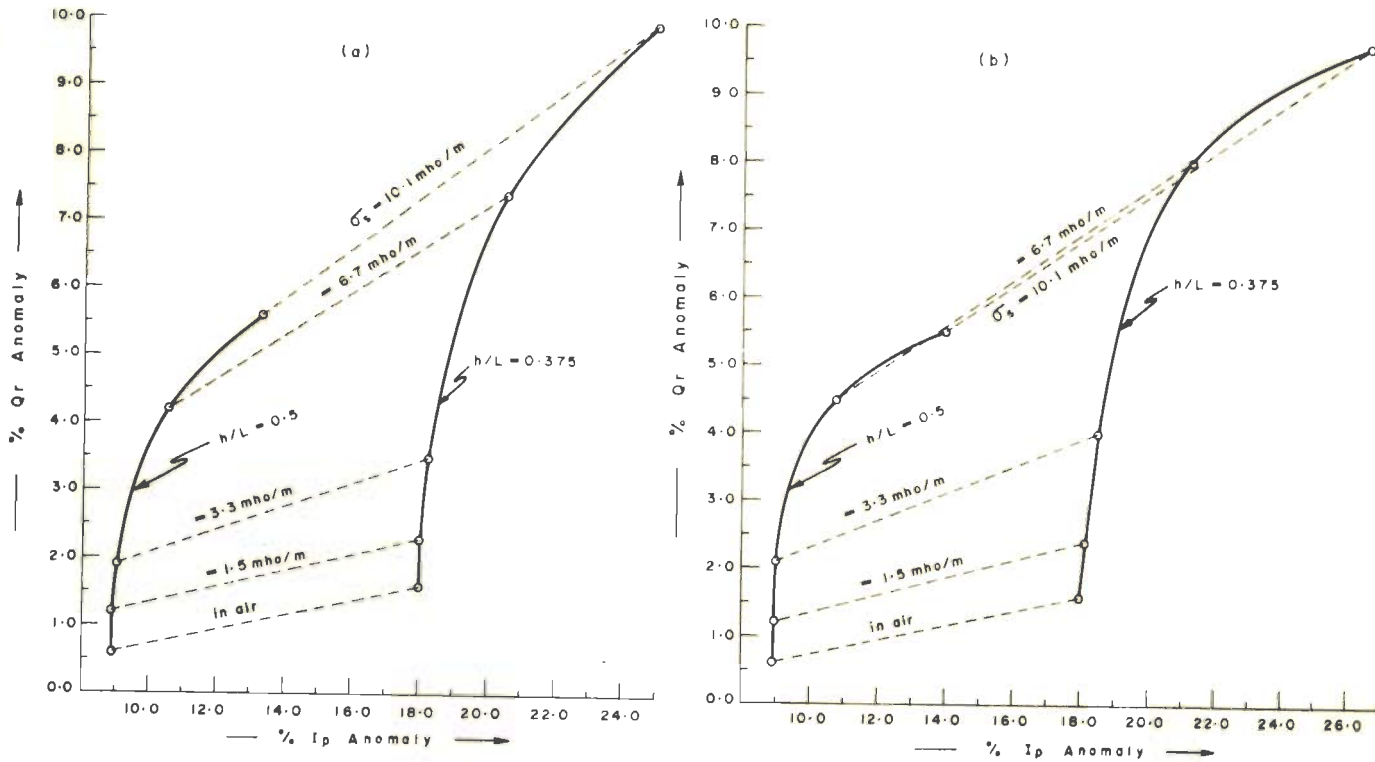


Fig. 4-32 ANOMALY INDEX DIAGRAMS FOR A VERTICAL GRAPHITE SHEET ; (a)  $d = 0.0$  m (b)  $d = 0.03$  m FOR 100 kHz

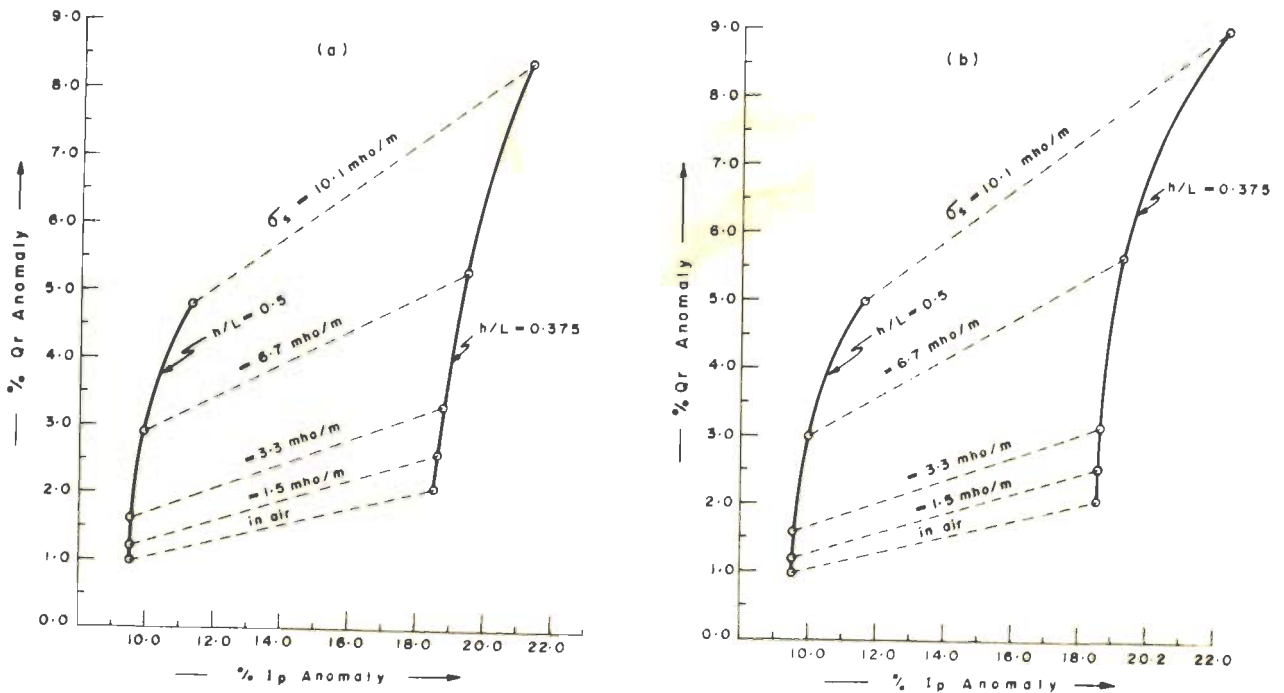


Fig. 4-33 ANOMALY INDEX DIAGRAMS FOR A VERTICAL GRAPHITE SHEET ; (a)  $d = 0.0$  m (b)  $d = 0.03$  m FOR 50 kHz

Figure 4.34 illustrates the variation of the  $I_s/I_a$  and  $Q_s/Q_a$  with  $\sigma_s/\sigma_m$ . The ratio  $Q_s/Q_a$  continues to increase for shallow depths of burial with increase in  $\sigma_s$ . The rate of increase of  $Q_s/Q_a$  for larger value of  $d$  ( $\geq 0.03m$ ) is, however, reduced with increase in  $\sigma_s$ . A non-uniform increase of the enhancement ratios and a depression in the curve for  $Q_s/Q_a$  (and also in that for  $I_s/I_a$  to a slight extent) may be compared with that observed in figure 2.14. It corresponds to the transition zone when the effect of the conducting surrounding medium becomes appreciable. Figure 4.35 shows the variation of the enhancement ratios with a continuous increase in the depth of burial for different values of  $\sigma_s$ .

The induction index for this model decreases initially with increasing conductivity of the surrounding medium (figure 4.36). But for larger values of  $\sigma_s/\sigma_m$  ( $\approx 6 \times 10^{-5}$ ) and  $d (= 0.03m)$ ,  $I_i$  shows an increasing trend with increase in  $\sigma_s$  because of the phase rotation of the induced currents towards the in-phase axis.

#### 4.4.1.2 Variation of the frequency of energisation

Measurements were made at a number of frequencies between 10 khz and 100 khz in this case. But the results presented here pertain to only three characteristic frequencies viz 20 khz, 50 khz, and 100 khz to exhibit all the essential in-

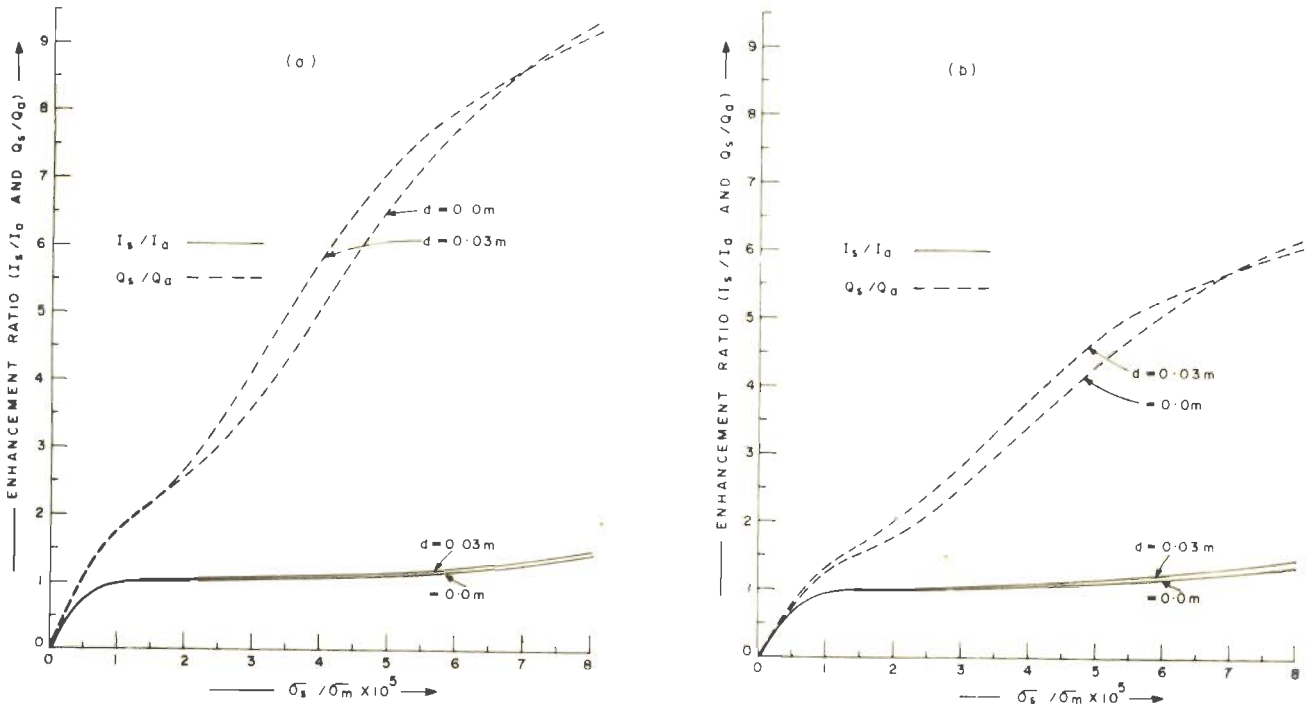


Fig.4-34 ENHANCEMENT RATIOS ( $I_s/I_a$  AND  $Q_s/Q_a$ ) VERSUS CONDUCTIVITY RATIO ( $\sigma_s/\sigma_m$ ) AT  $h/L = (a) 0.5$  AND (b)  $0.375$  FOR A VERTICAL GRAPHITE SHEET

MODEL	: GRAPHITE SHEET
LENGTH	: $0.70\text{ m}$ ( $G_1$ )
WIDTH	: $0.20\text{ m}$
THICKNESS	: $0.02\text{ m}$
FREQUENCY	: $100\text{ kHz}$
L	: $0.2\text{ m}$
$\theta$	: $90^\circ$

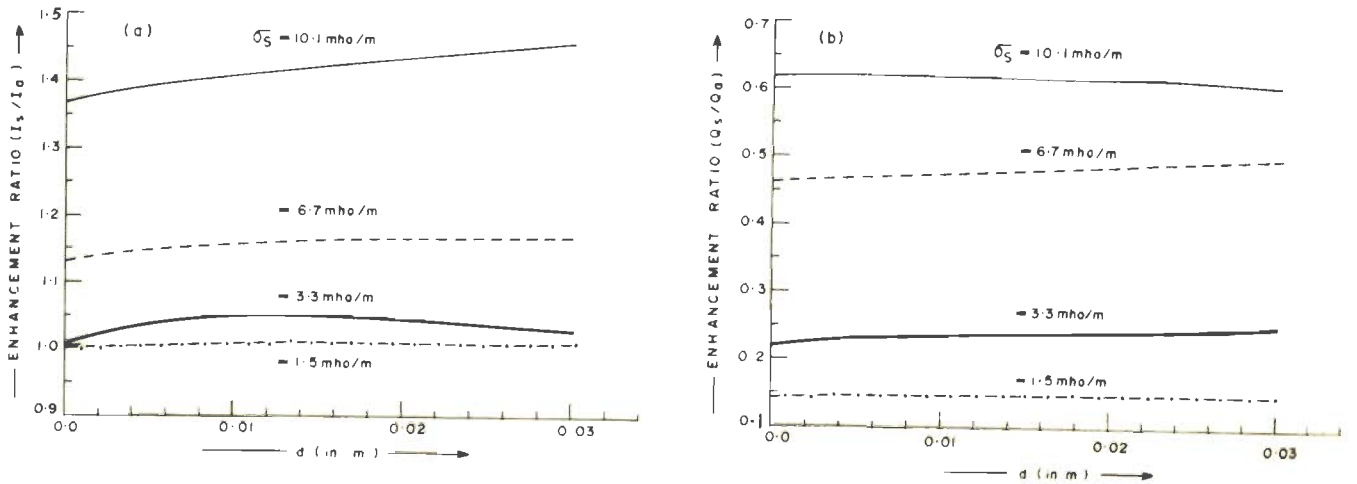
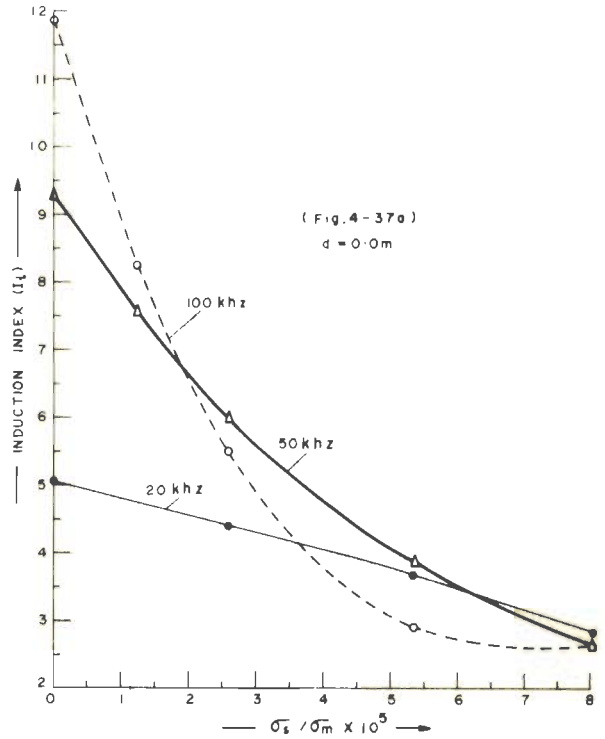
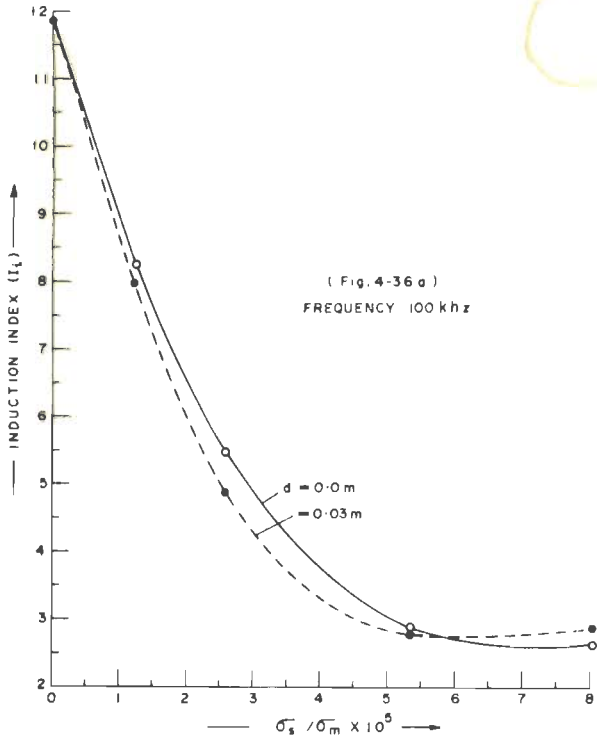


Fig.4-35 ENHANCEMENT RATIOS (a)  $I_s/I_a$  AND (b)  $Q_s/Q_a$  VERSUS DEPTH OF BURIAL FOR A VERTICAL GRAPHITE SHEET



MODEL	: GRAPHITE SHEET ( $G_1$ )
LENGTH	: 0.70 m
WIDTH	: 0.20 m
THICKNESS	: 0.021 m
$\theta$	: 90°

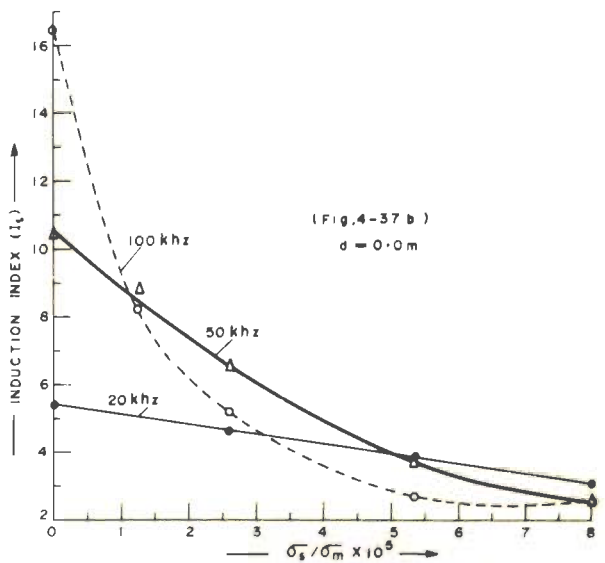
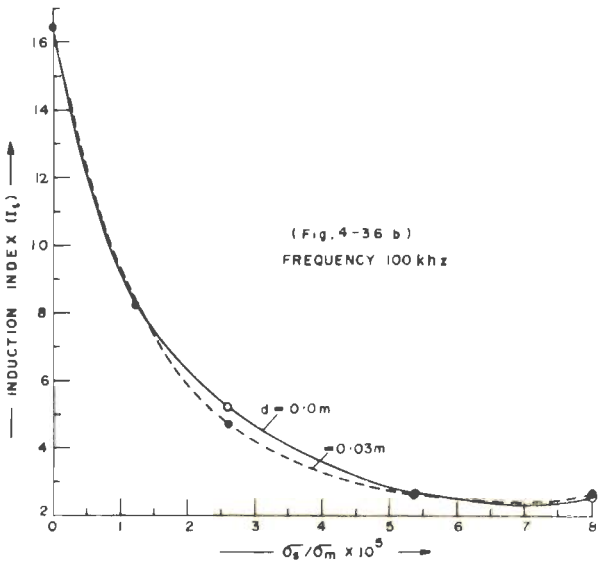


Fig.4-36 INDUCTION INDEX ( $I_t$ ) VERSUS THE CONDUCTIVITY RATIO ( $\sigma_s / \sigma_m$ ) FOR A VERTICAL GRAPHITE SHEET FOR DIFFERENT DEPTHS OF BURIAL; (a)  $h/L = 0.375$  AND (b)  $h/L = 0.5$

Fig.4-37 INDUCTION INDEX ( $I_t$ ) VERSUS THE CONDUCTIVITY RATIO ( $\sigma_s / \sigma_m$ ) FOR A VERTICAL GRAPHITE SHEET FOR DIFFERENT FREQUENCIES; (a)  $h/L = 0.375$  AND (b)  $h/L = 0.5$



in the entire range.

The rate of enhancement of the response at 50 khz is less than that at 100 khz (cf. figure 4.32 and 4.33). Figure 4.37 shows the variation of the induction index with  $\sigma_s$  at 100 khz, 50 khz, and 20 khz. When the sheet is in air, the value of  $I_i$  is greater the higher the frequency. But when it is dipped in the solution, particularly of a high conductivity, the variation of  $I_i$  is noticed to be in reverse order. This effect also is attributable to the fact that the enhancement rate of the  $Q_r$  component due to a conducting surrounding medium is more than that of the  $I_p$  component at higher frequencies (say 100 khz) and hence the induction index is reduced with increase in the frequency. However, further increase of  $\sigma_s$  or  $f$  would again reverse the trend of variation of  $I_i$  since the currents induced in the solution will then be more in phase with the primary field and thus enhance the  $I_p$  component. But in the present work only a marginal increase of the either quantity could be realised owing to the restriction offered by the maximum available conductivity of the salt solution and difficulties in instrumentation.

It has been noticed that when the model is kept in air or in a solution of low conductivity, the

$I_p$  component of its response, studied at different frequencies, is maximum at 50 khz. This observation appears to be akin to the resonance-like effect observed for induced currents. An anti-resonance is observed for the  $Q_r$  component which is minimum at 50 khz and  $\sigma_s = 3.3$  mho/m.

#### 4.4.1.3 Variation of the depth of burial

Further study of the variation of response with the depth of burial was made at an increased T-R separation ( $L = 0.25$ m) enabling a larger penetration of the inducing field. The absolute value of  $h$  could, thus, be increased maintaining the  $h/L$  values and hence the response unchanged. This made feasible the study of the effect of a thicker overburden. The conductivity of the surrounding medium was also increased to 11.6 mho/m. Figures 4.38 and 4.39 show anomaly profiles for different depths of burial. The anomaly index diagrams are presented in figure 4.40 and the variation of the enhancement ratios ( $I_s/I_a$  and  $Q_s/Q_a$ ) with depth of burial, in figure 4.41. It may be seen that the  $I_p$  component continues to be enhanced with increasing depth of burial even upto  $d = 0.1$  m but the  $Q_r$  component shows a monotonic decrease with increasing  $d$  in contrast to what was observed for small values of  $L$  (cf. Section 4.2.3.1). Thus in this case, the induction index increases with increase in the depth of burial.

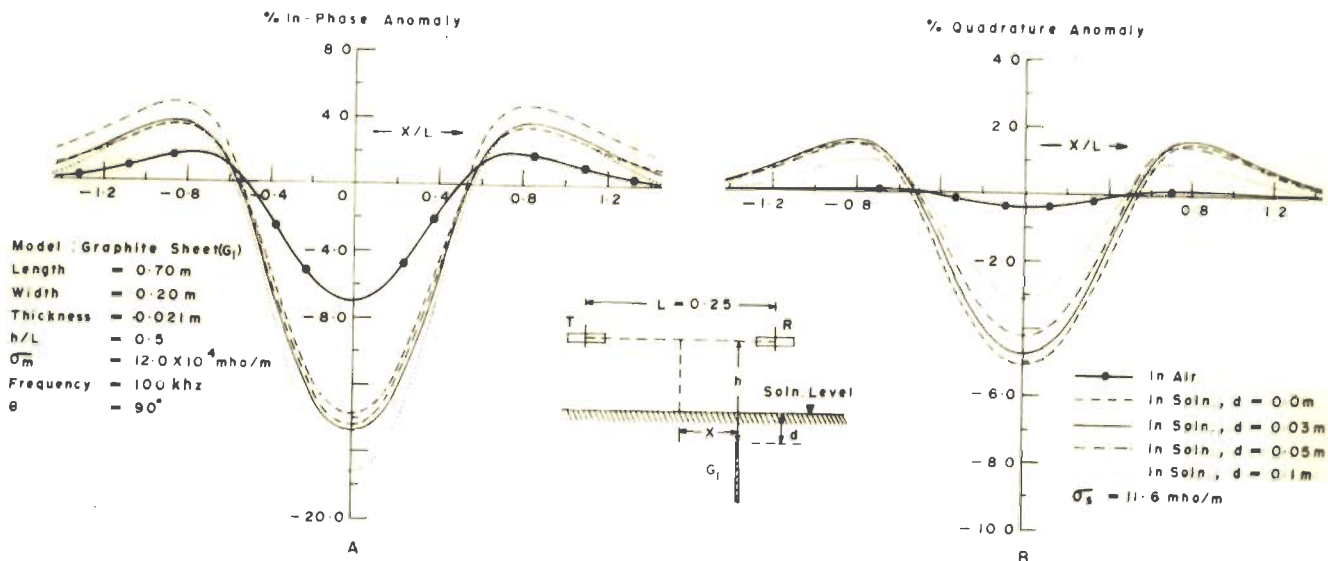


Fig.4-38 ANOMALY PROFILES OVER A VERTICAL GRAPHITE SHEET ( $h/L = 0.5$ )

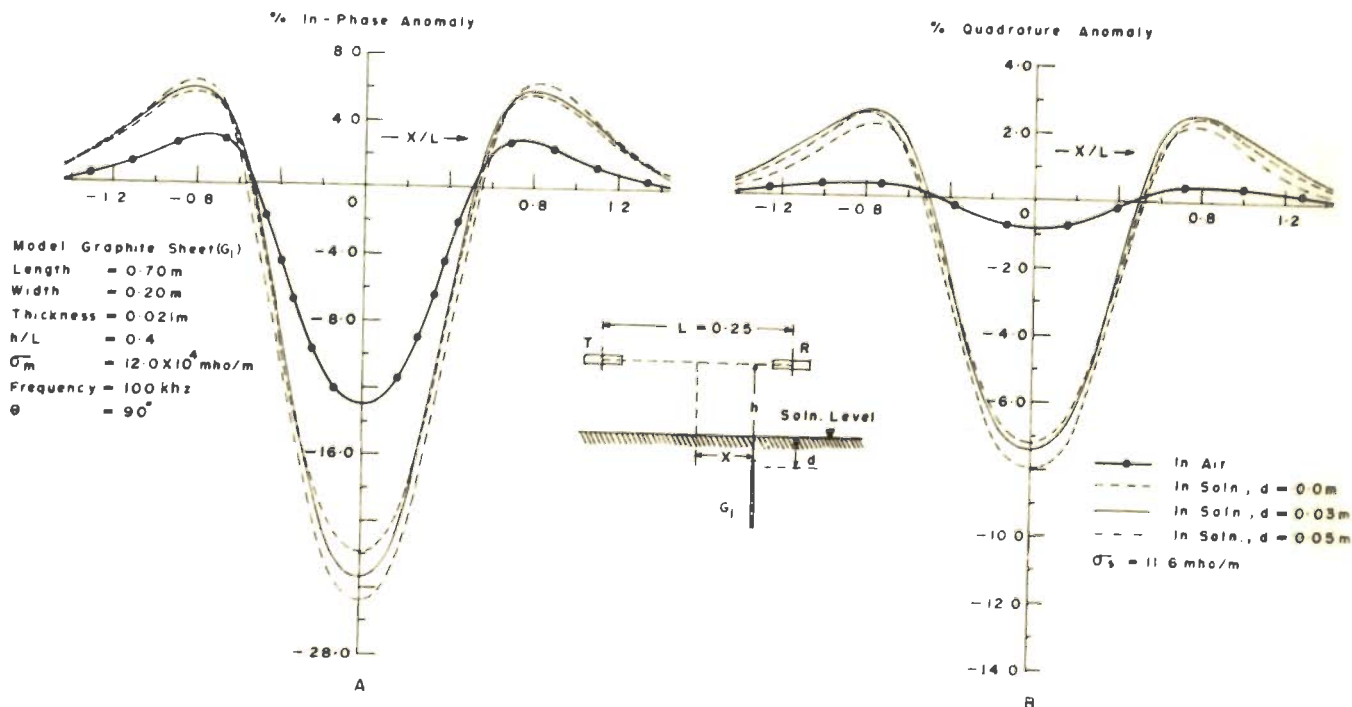


Fig.4-39 ANOMALY PROFILES OVER A VERTICAL GRAPHITE SHEET ( $h/L = 0.4$ )

Model : Graphite Sheet ( $G_1$ )			
Length	= 0.70 m	Frequency	= 100 kHz
Width	= 0.20 m	L	= 0.25 m
Thickness	= 0.021 m	$\theta$	= 90°
$\sigma_m$	= $12.0 \times 10^4$ mho/m		

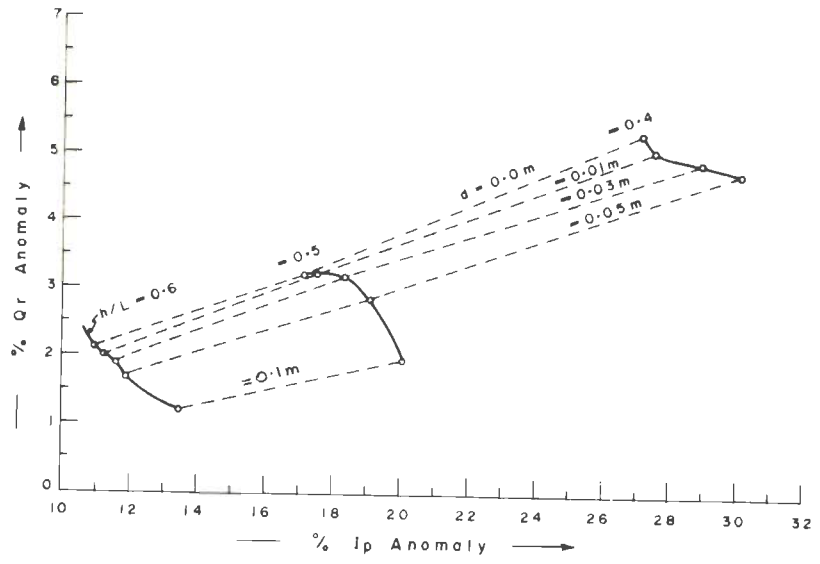


Fig. 4-40 ANOMALY INDEX DIAGRAM FOR A VERTICAL GRAPHITE SHEET FOR DIFFERENT DEPTHS OF BURIAL

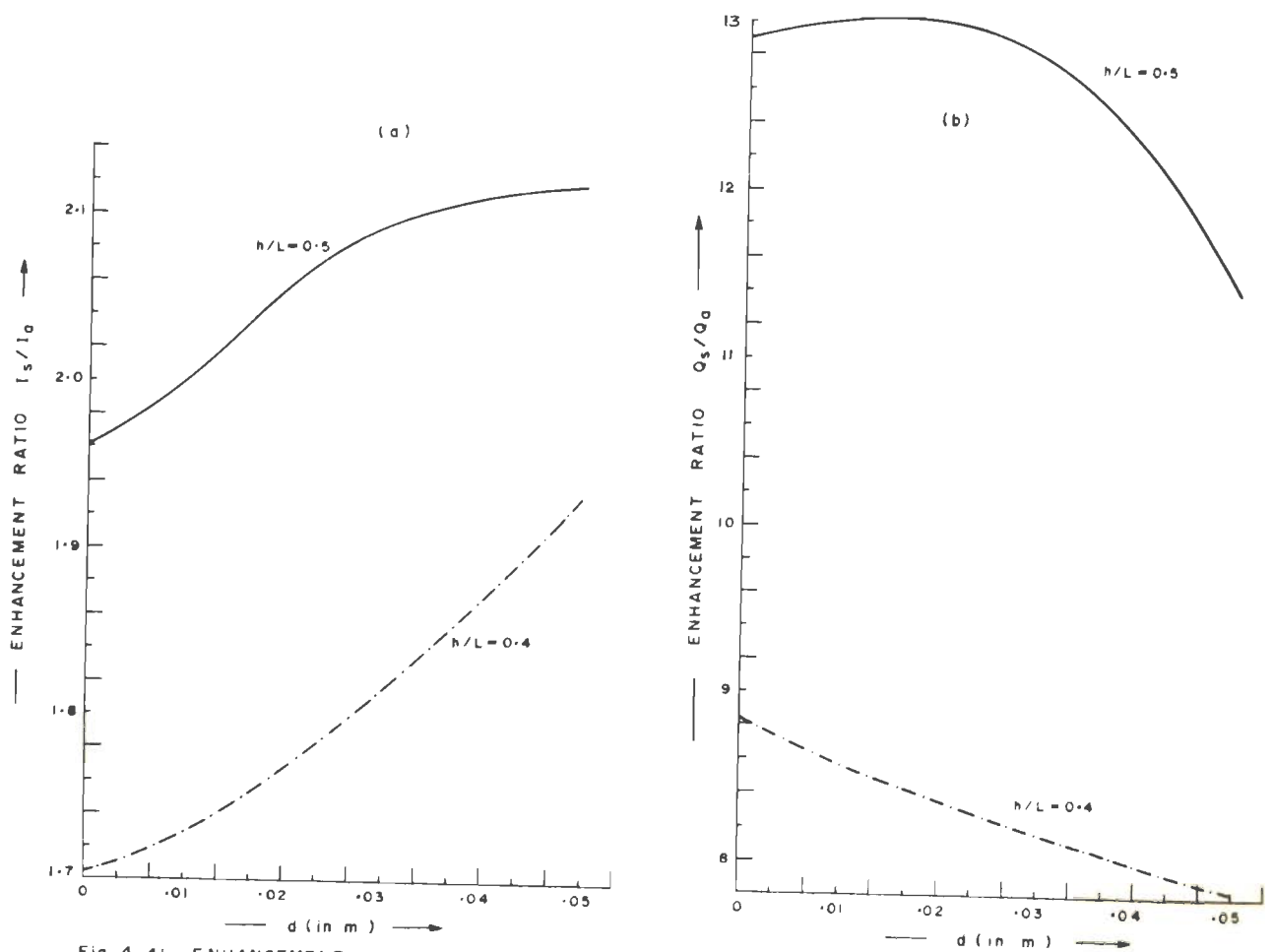


Fig. 4-41 ENHANCEMENT RATIOS (a)  $I_s/I_0$  and (b)  $Q_s/Q_0$  VERSUS DEPTH OF BURIAL FOR A VERTICAL GRAPHITE SHEET

#### 4.4.2 Thin sheets

Thin sheets of stainless steel ( $\sigma_m = 14.0 \times 10^5$  mho/m) which could be regarded as half-planes, were also investigated for a comparative study with the existing data. Figures 4.42 and 4.43 give some of the anomaly profiles for a sheet of stainless steel ( $SS_1$ ) of  $\sigma_m t = 686$  mho and figure 4.44 and 4.45 those for another sheet ( $SS_2$ ) of  $\sigma_m t = 266$  mho. The anomaly index diagrams for the two sheets are shown in figures 4.46 and 4.47 for different depths of burial. Figures 4.48 and 4.49 give the induction index and figures 4.50 and 4.51 the variations in the enhancement ratio with  $d$ . The conductivity of the surrounding medium is taken to be 11.6 mho/m.

In this case the  $Q_r$  component is found to reduce with increasing depth of burial right from  $d = 0.0$  m while the  $I_p$  component continues to increase. This observation is in accordance with the explanation given in Section 4.2.3.1. The saturation limit for a stainless steel sheet here appears to have reached when the top of the sheet is just flush with the solution surface because of its high conductivity and large surface area. It causes a monotonic increase of the induction index with increase in the depth of burial.

The effect of varying  $\sigma_s$  on the response of

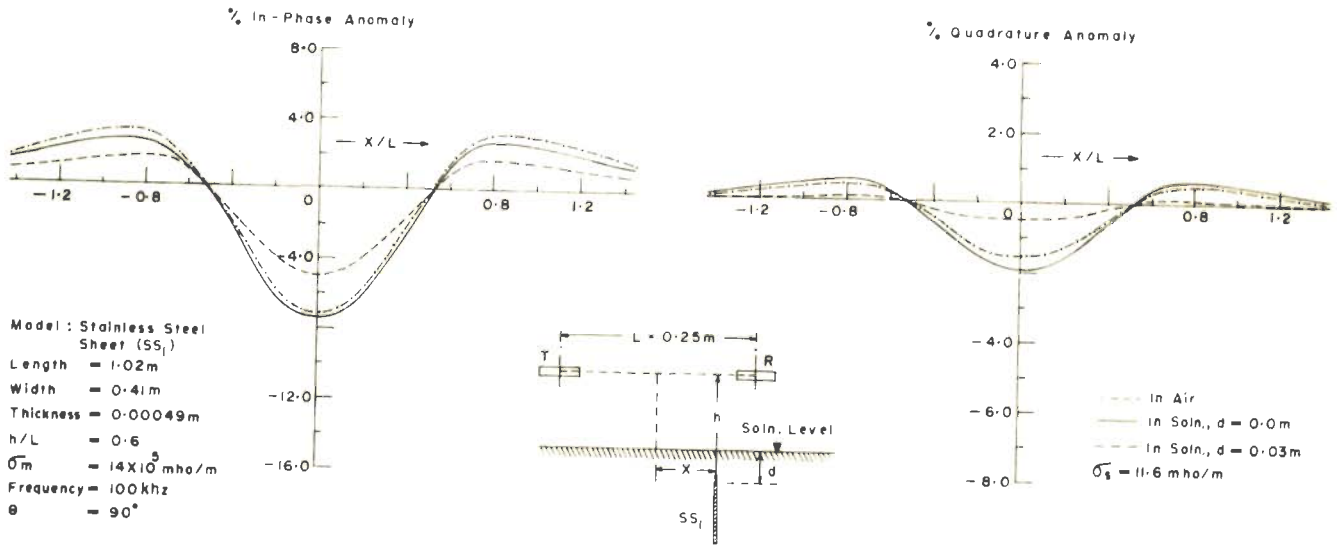


Fig. 4-42 ANOMALY PROFILES OVER A STAINLESS STEEL SHEET ( $h/L = 0.6$ )

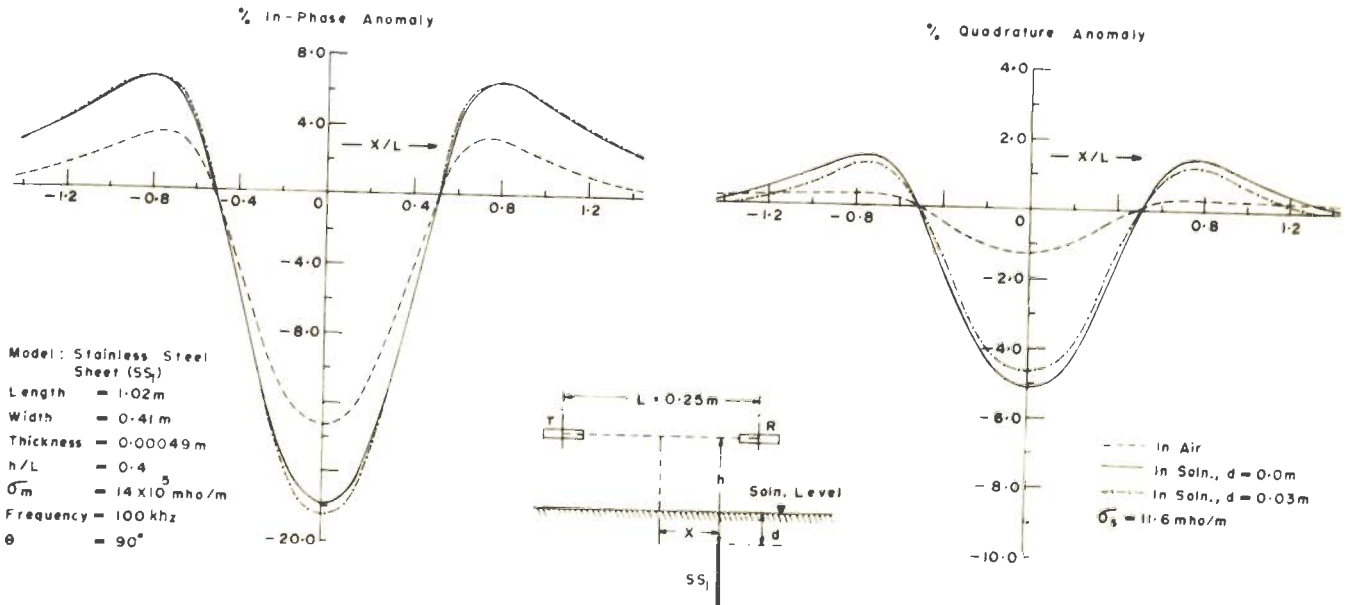
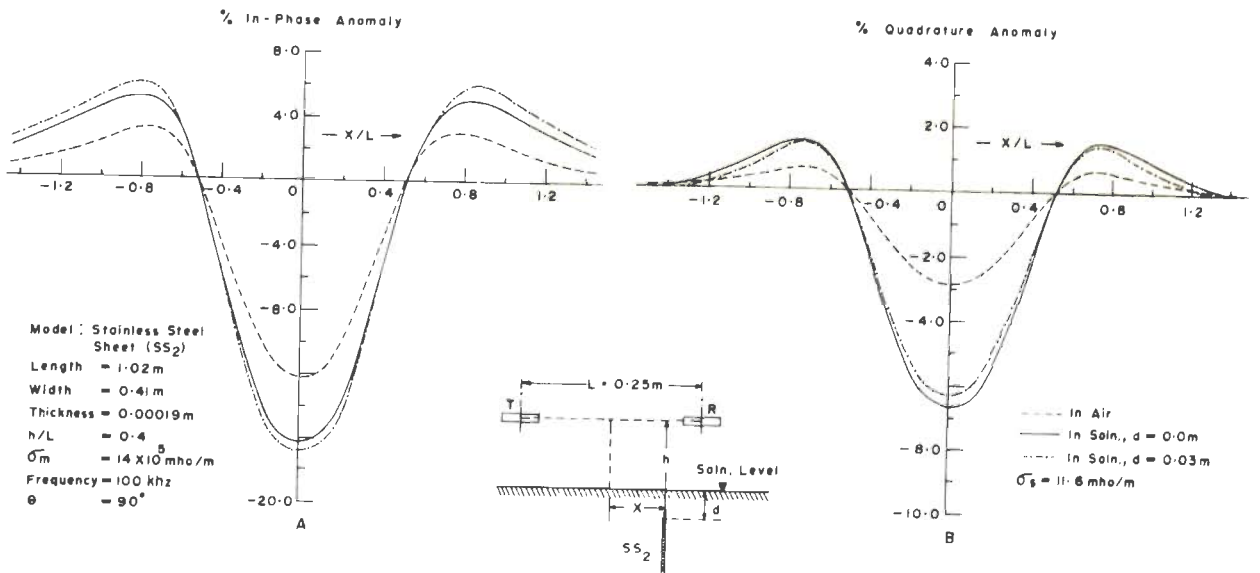
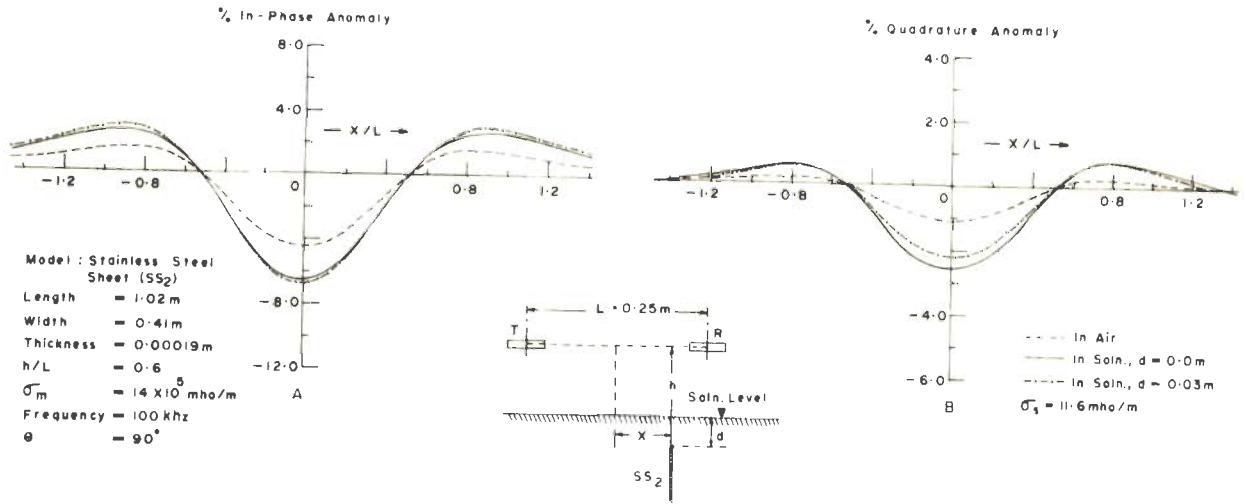


Fig. 4-43 ANOMALY PROFILES OVER A STAINLESS STEEL SHEET ( $h/L = 0.4$ )



Model : Stainless Steel Sheet (SS <sub>1</sub> )			
Length	= 1.02 m	Frequency	= 100 kHz
Width	= 0.41 m	$\sigma_m$	= $14 \times 10^5$ mho/m
Thickness	= 0.00049 m	$\sigma_s$	= 11.6 mho/m
L	= 0.25 m	$\theta$	= $90^\circ$

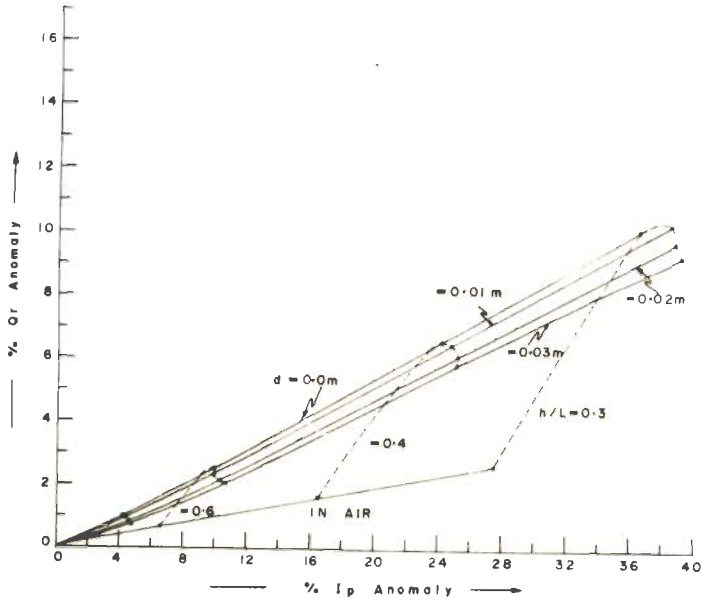


Fig. 4-46 ANOMALY INDEX DIAGRAM FOR A VERTICAL STAINLESS STEEL SHEET FOR DIFFERENT DEPTHS OF BURIAL

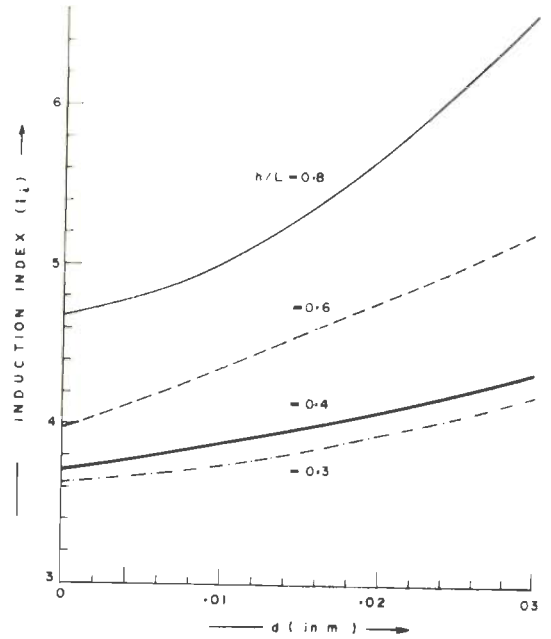


Fig. 4-48 INDUCTION INDEX ( $I_i$ ) VERSUS THE DEPTH OF BURIAL FOR A VERTICAL STAINLESS STEEL SHEET

Model : Stainless Steel Sheet (SS <sub>2</sub> )			
Length	= 1.02 m	Frequency	= 100 kHz
Width	= 0.41 m	$\sigma_m$	= $14 \times 10^5$ mho/m
Thickness	= 0.00019 m	$\sigma_s$	= 11.6 mho/m
L	= 0.25 m	$\theta$	= $90^\circ$

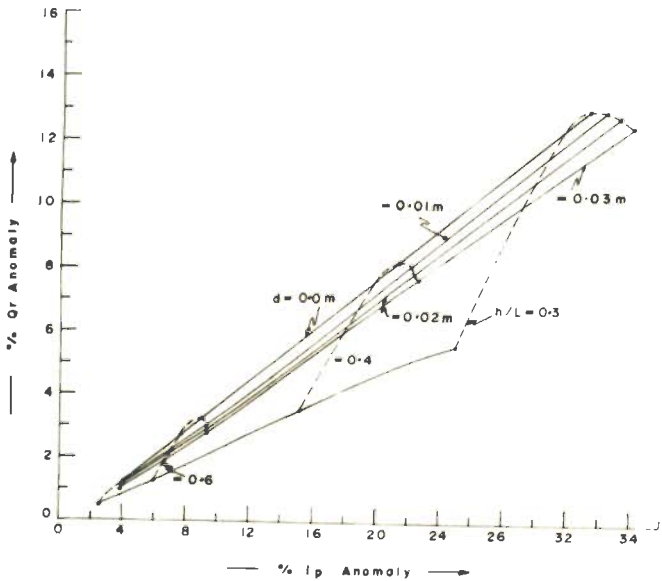


Fig. 4-47 ANOMALY INDEX DIAGRAM FOR A VERTICAL STAINLESS STEEL SHEET FOR DIFFERENT DEPTHS OF BURIAL

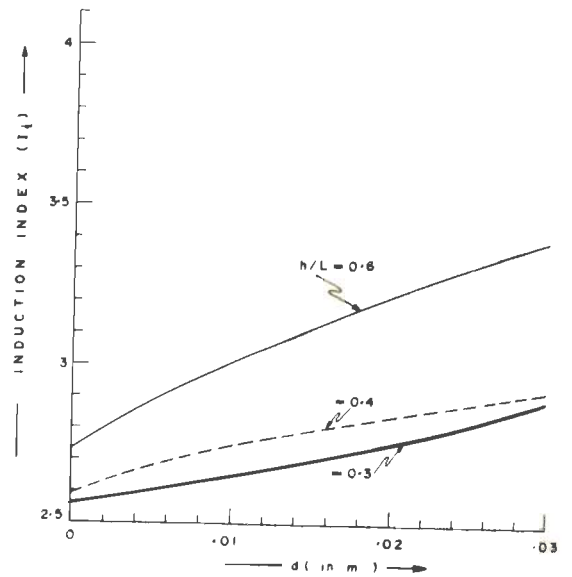
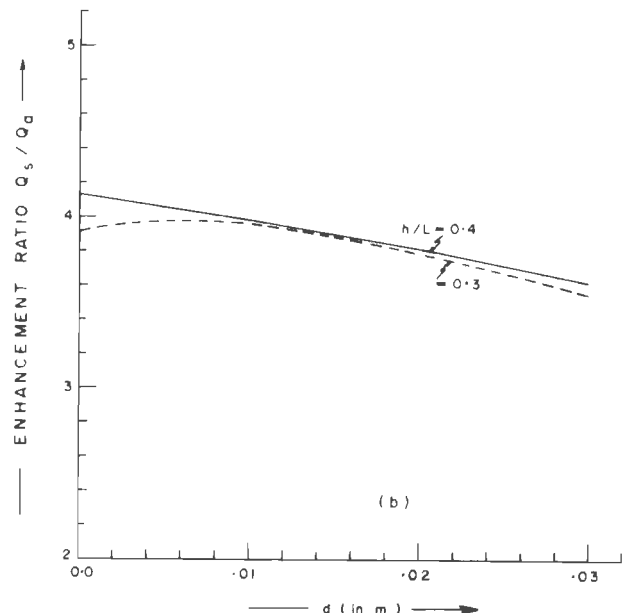
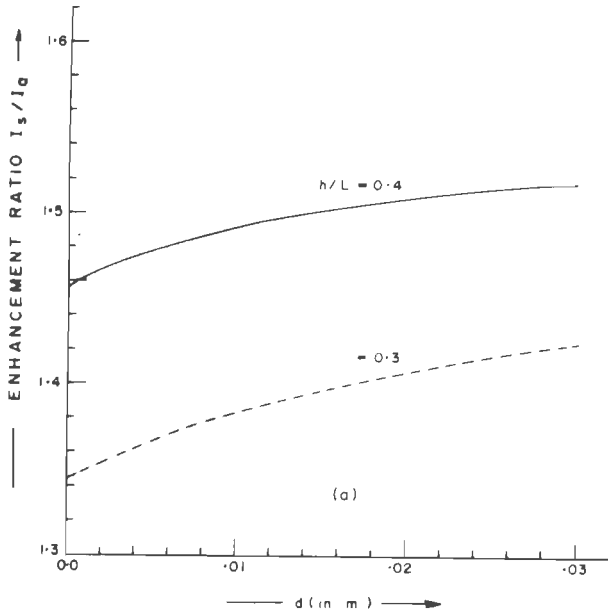


Fig. 4-49 INDUCTION INDEX ( $I_i$ ) VERSUS THE DEPTH OF BURIAL FOR A VERTICAL STAINLESS STEEL SHEET

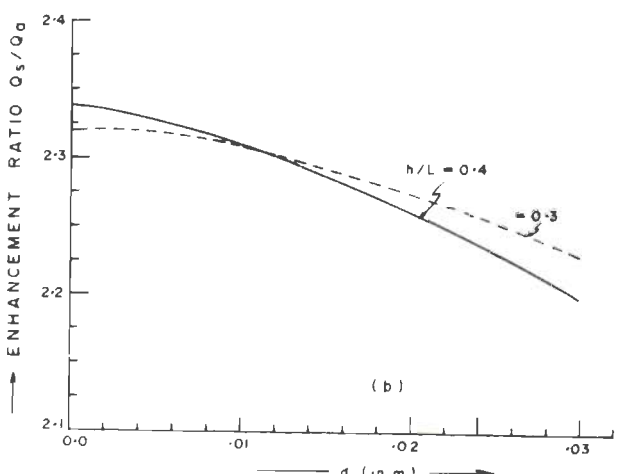
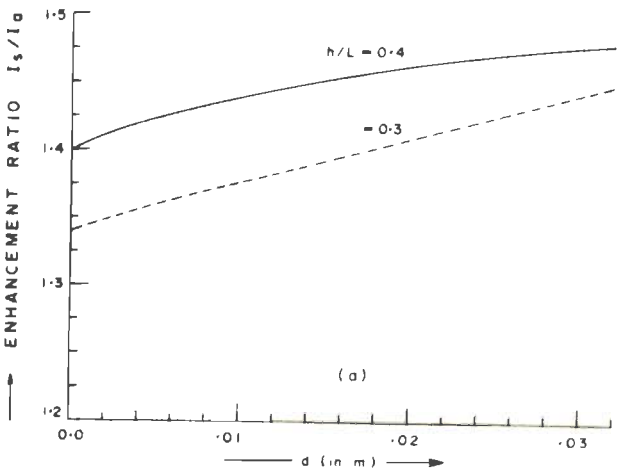


Model : Stainless Steel Sheet (SS <sub>1</sub> )			
Length	= 1.02 m	L	= 0.25 m
Width	= 0.41 m	$\sigma_s$	= 11.6 mho/m
Thickness	= 0.00049 m	$\sigma_m$	= $14 \times 10^5$ mho/m
Frequency	= 100 khz	$\theta$	= $90^\circ$



g.4-50 ENHANCEMENT RATIOS (a)  $I_s/I_0$  AND (b)  $Q_s/Q_0$  VERSUS DEPTH OF BURIAL FOR A VERTICAL STAINLESS STEEL SHEET

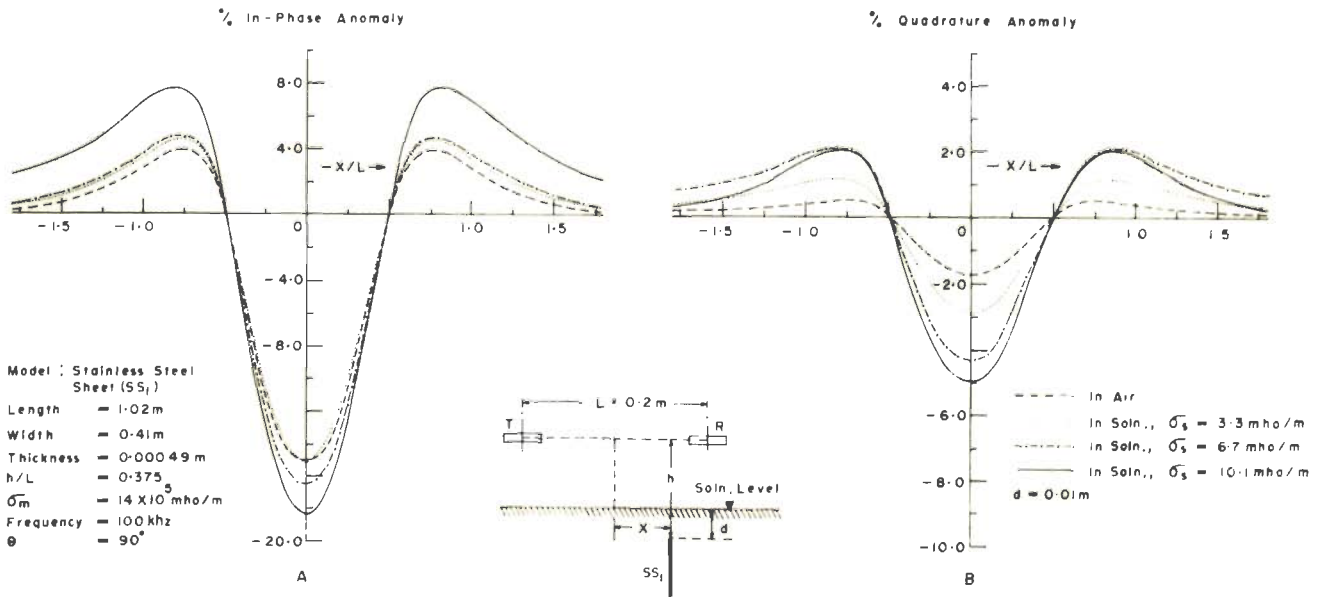
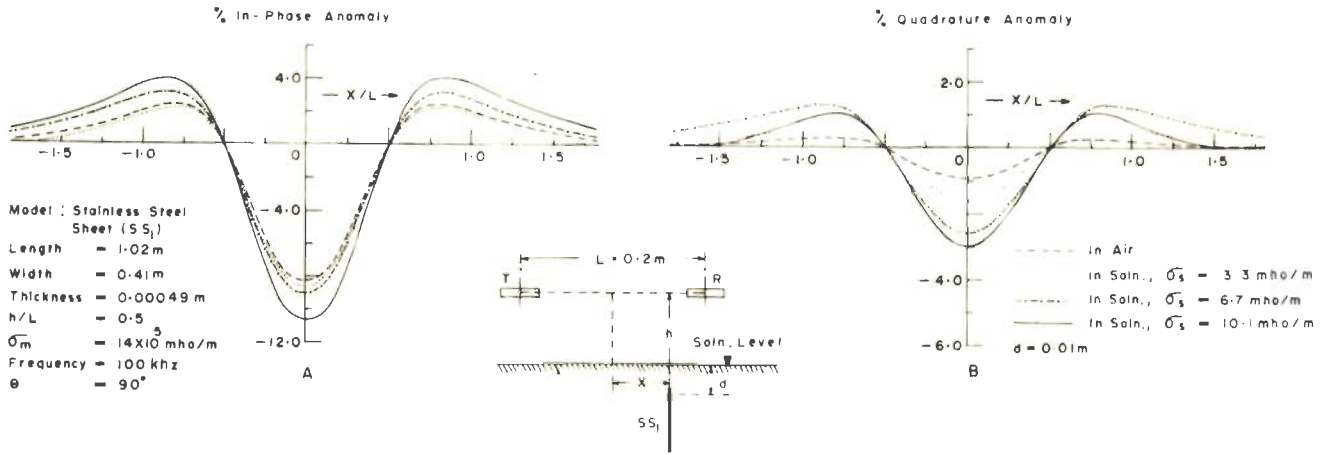
Model : Stainless Steel Sheet (SS <sub>2</sub> )			
Length	= 1.02 m	L	= 0.25 m
Width	= 0.41 m	$\sigma_s$	= 11.6 mho/m
Thickness	= 0.00019 m	$\sigma_m$	= $14 \times 10^5$ mho/m
Frequency	= 100 khz	$\theta$	= $90^\circ$



g.4-51 ENHANCEMENT RATIOS (a)  $I_s/I_0$  AND (b)  $Q_s/Q_0$  VERSUS DEPTH OF BURIAL FOR A VERTICAL STAINLESS STEEL SHEET

$\text{SS}_1$  was also studied. Figures 4.52 to 4.55 give the anomaly profiles and figures 4.56 and 4.57 the anomaly index diagrams for this sheet. Broadly, the nature of the anomaly index diagrams are similar to those for the graphite sheet except that for higher  $\sigma_s$  values the Qr component shows a greater tendency of decreasing with increasing  $\sigma_s$ . The variations of the enhancement ratios and the induction indices are shown in figures 4.58 and 4.59 respectively.

In order to cover the extreme values of conductivities of target models, the responses of a thick copper sheet (almost perfectly conducting) and sheets of perspex (almost perfectly resistive) were also examined. Figures 4.60 and 4.61 show the anomaly profiles and figure 4.62, the anomaly index diagrams for a copper sheet ( $\sigma_m t = 9.86 \times 10^4$  mho). As is expected, in this case the decrease in the Qr component with increasing depth of burial becomes still more pronounced than what is observed for stainless steel sheets. The enhancement ratio  $I_s/I_a$  either increases (at small  $h/L$ ) or remains unaltered (for large  $h/L$ ) with increase in the depth of burial while  $Q_s/Q_a$  is invariably found to diminish (figure 4.63). Consequently, the induction index  $I_i$  shows a monotonic increase with increase in  $d$  (figure 4.62b). The effect of increasing  $h/L$  is found to enhance the ratio  $I_s/I_a$  but reduce the value of  $Q_s/Q_a$  and hence  $I_i$  increases with increase in  $h/L$ .



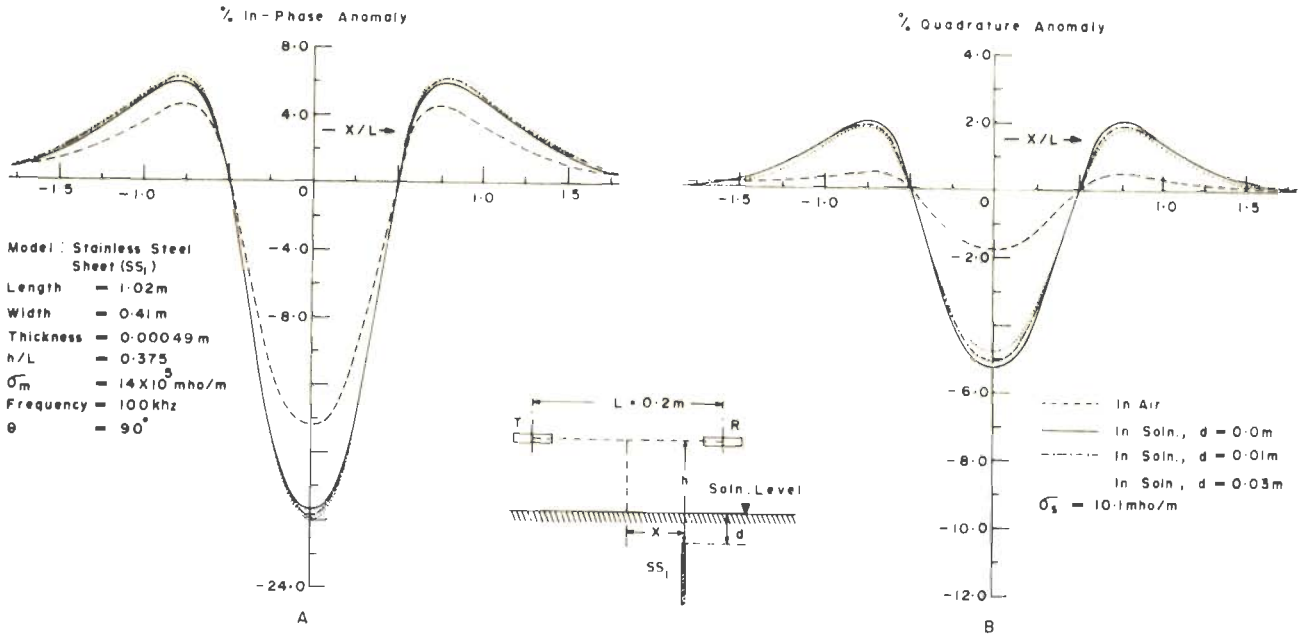


Fig. 4-54 ANOMALY PROFILES OVER A STAINLESS STEEL SHEET

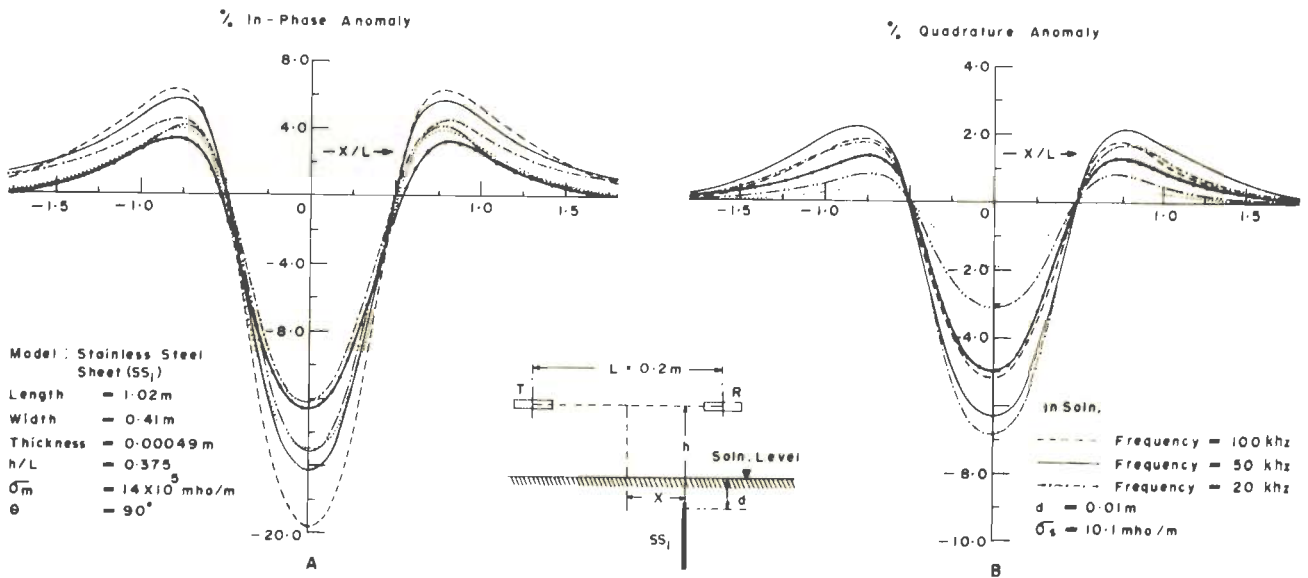


Fig. 4-55 ANOMALY PROFILES OVER A STAINLESS STEEL SHEET

Model: Stainless Steel Sheet (SS<sub>1</sub>)  
 Length = 1.02 m ; L = 0.2 m  
 Width = 0.41 m ;  $\sigma_m = 14 \times 10^3$  mho/m  
 Thickness = 0.00049 m ;  $\theta = 90^\circ$

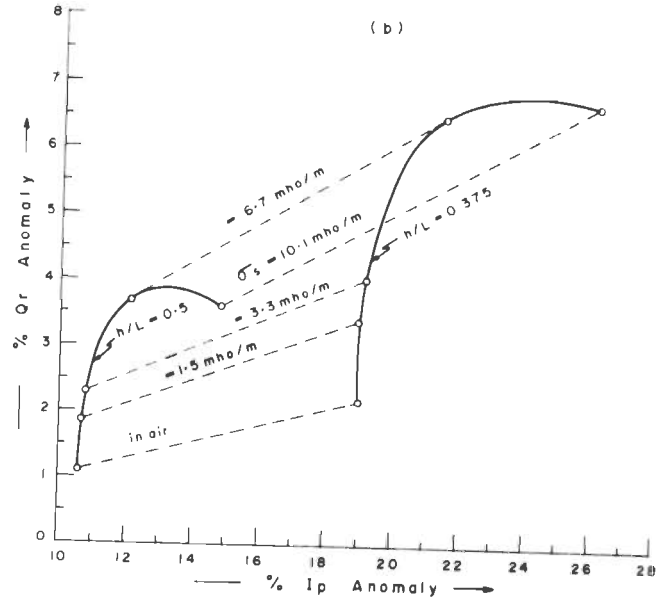
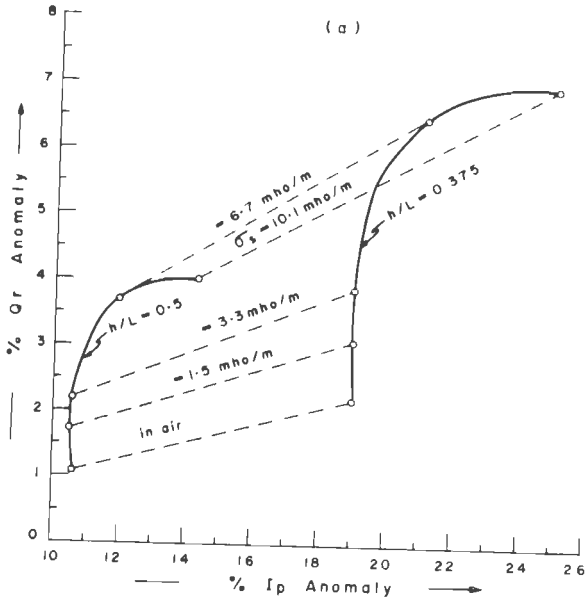


Fig. 4-56 ANOMALY INDEX DIAGRAMS FOR A VERTICAL STAINLESS STEEL SHEET FOR DIFFERENT CONDUCTIVITIES OF THE SURROUNDING MEDIUM AT (a)  $d = 0.0$  m and (b)  $d = 0.03$  m FOR 100 kHz

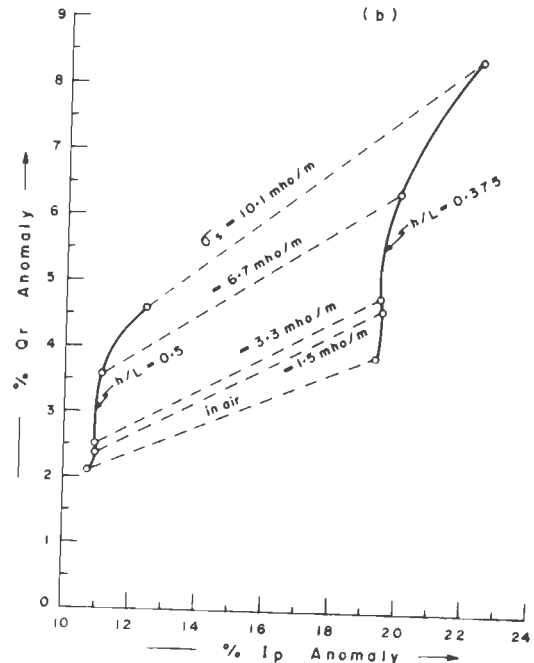
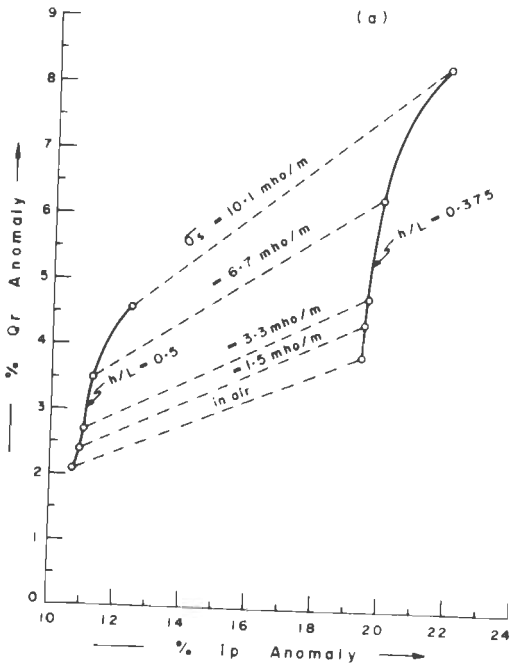


Fig 4-57 ANOMALY INDEX DIAGRAMS FOR A VERTICAL STAINLESS STEEL SHEET FOR DIFFERENT CONDUCTIVITIES OF THE SURROUNDING MEDIUM AT (a)  $d = 0.0$  m and (b)  $d = 0.03$  m FOR 50 kHz

Model : Stainless Steel Sheet (SS<sub>1</sub>)  
 Length = 1.02 m ; L = 0.2 m  
 Width = 0.41 m ;  $\bar{\sigma}_m = 14 \times 10^5$  mho/m  
 Thickness = 0.00049 m ;  $\theta = 90^\circ$

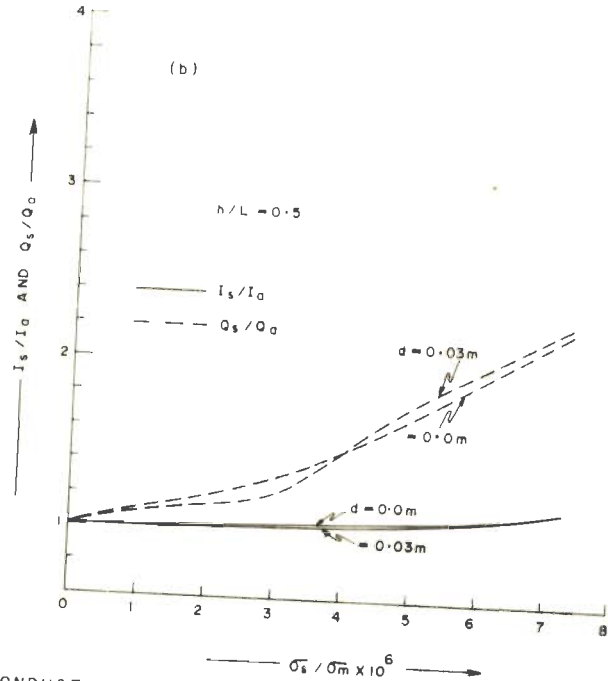
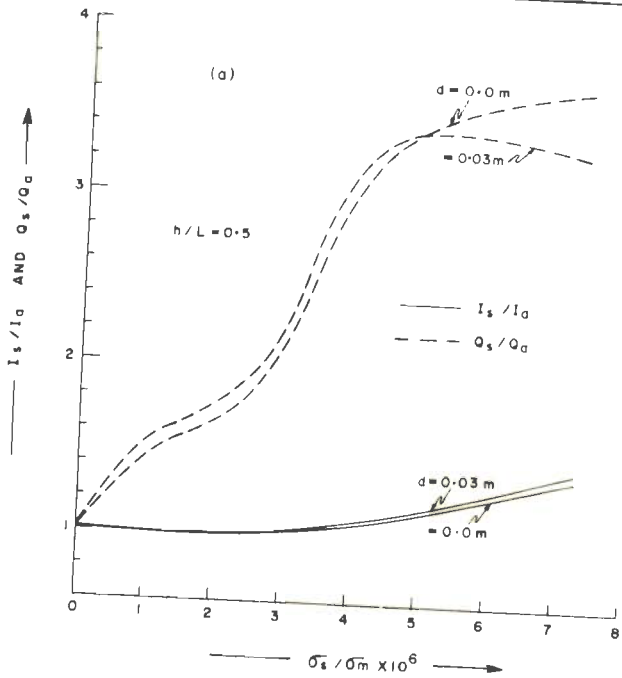
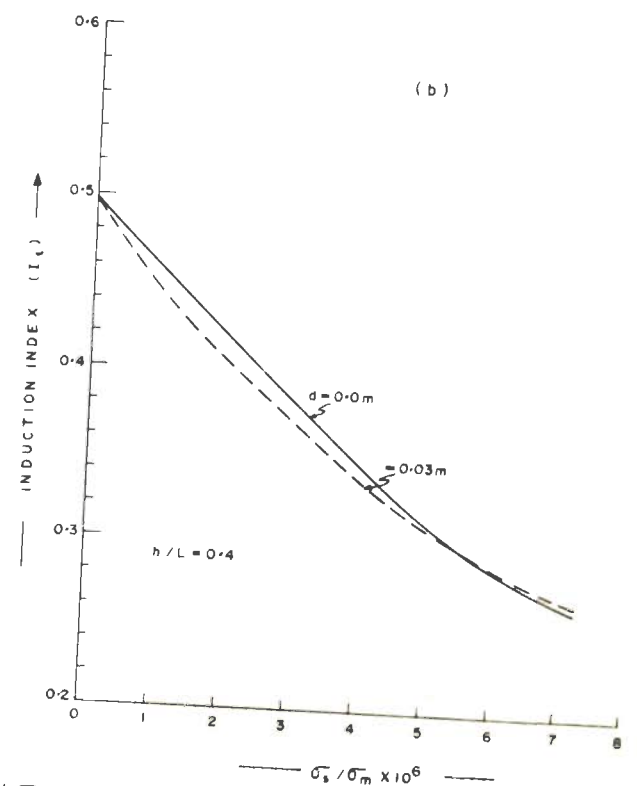
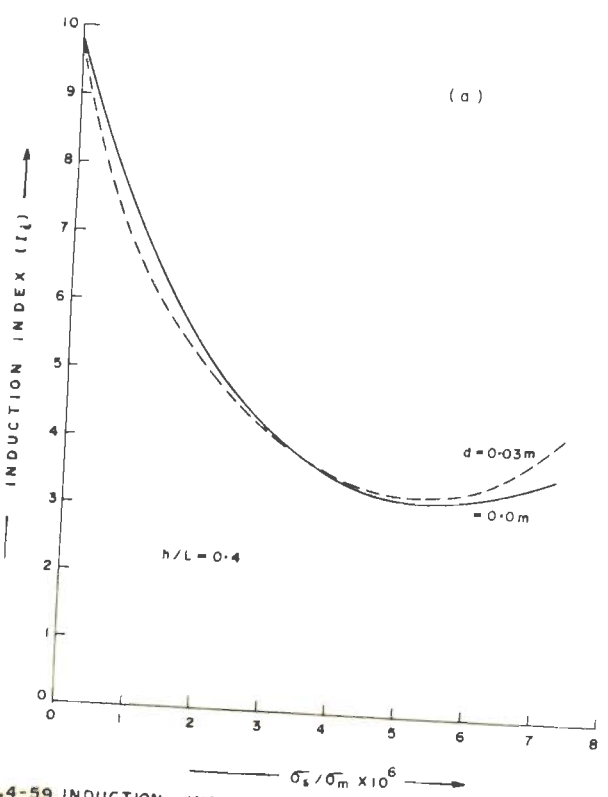
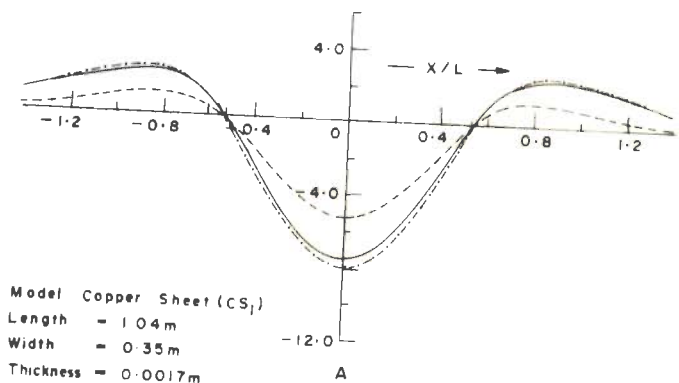


Fig.4-58 ENHANCEMENT RATIOS  $I_s/I_a$  AND  $Q_s/Q_a$  VERSUS THE CONDUCTIVITY RATIO ( $\bar{\sigma}_s/\bar{\sigma}_m$ ) FOR A VERTICAL STAINLESS STEEL SHEET FOR (a) 100 kHz AND (b) 50 kHz

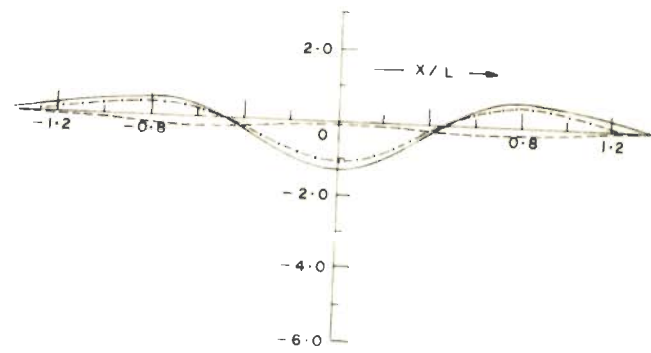


4-59 INDUCTION INDEX ( $I_L$ ) VERSUS THE CONDUCTIVITY RATIO ( $\bar{\sigma}_s/\bar{\sigma}_m$ ) FOR A VERTICAL STAINLESS STEEL SHEET (a) 100 kHz AND (b) 50 kHz

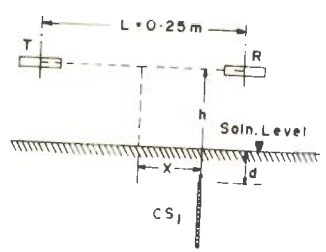
% In-Phase Anomaly



% Quadrature Anomaly



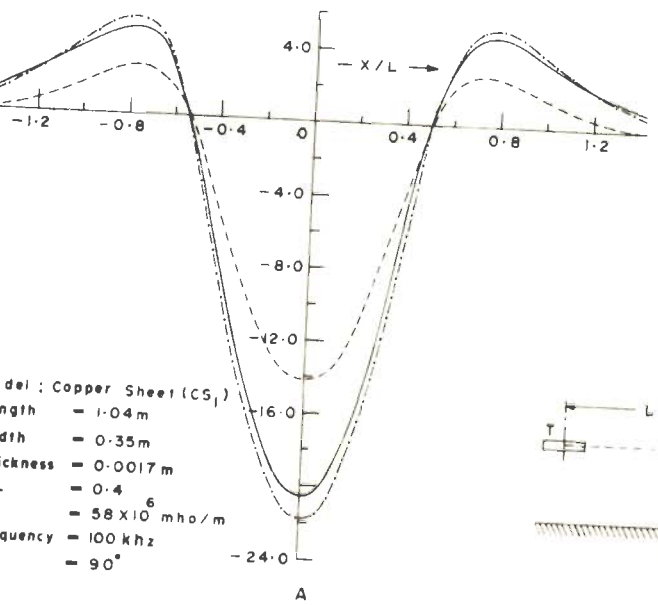
Model: Copper Sheet (CS<sub>1</sub>)  
 Length = 1.04m  
 Width = 0.35m  
 Thickness = 0.0017m  
 h/L = 0.6  
 $\sigma_m = 58 \times 10^6$  mho/m  
 Frequency = 100 kHz  
 $\theta = 90^\circ$



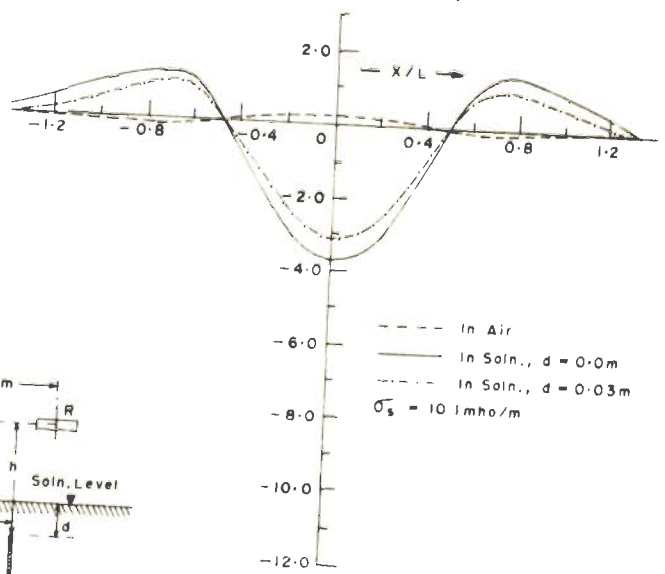
--- In Air  
 — In Soln., d = 0.0m  
 - · - In Soln., d = 0.03m  
 $\sigma_s = 10.1$  mho/m

Fig.4-60 ANOMALY PROFILES OVER A COPPER SHEET (h/L = 0.6)

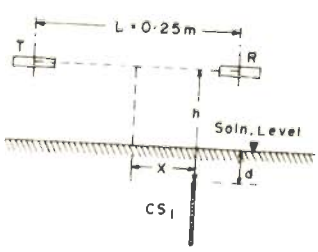
% In-Phase Anomaly



% Quadrature Anomaly



Model: Copper Sheet (CS<sub>1</sub>)  
 Length = 1.04m  
 Width = 0.35m  
 Thickness = 0.0017m  
 h/L = 0.4  
 $\sigma_m = 58 \times 10^6$  mho/m  
 Frequency = 100 kHz  
 $\theta = 90^\circ$



--- In Air  
 — In Soln., d = 0.0m  
 - · - In Soln., d = 0.03m  
 $\sigma_s = 10.1$  mho/m

Fig.4-61 ANOMALY PROFILES OVER A COPPER SHEET (h/L = 0.4)

Model : Copper Sheet (CS <sub>1</sub> )	
Length = 1.04 m	L = 0.25
Width = 0.35 m	$\sigma_m = 58 \times 10^6$ mho/m
Thickness = 0.0017 m	$\sigma_s = 10.1$ mho/m
Frequency = 100 kHz	$\theta = 90^\circ$

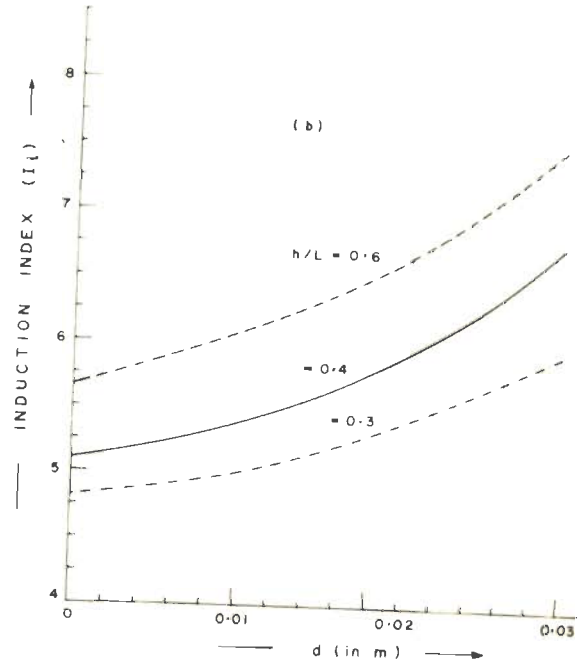
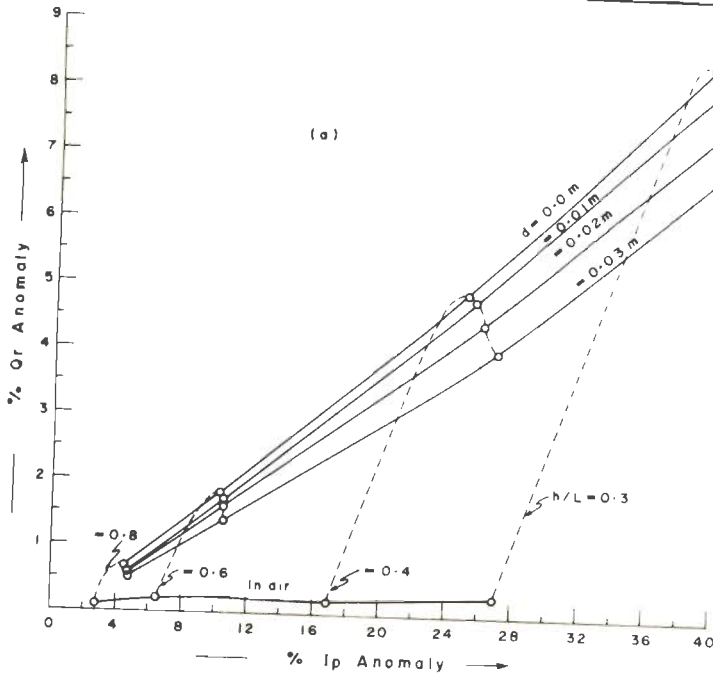


Fig. 4-62 (a) ANOMALY INDEX DIAGRAM AND (b) INDUCTION INDEX ( $I_L$ ) VERSUS DEPTH OF BURIAL FOR A VERTICAL COPPER SHEET

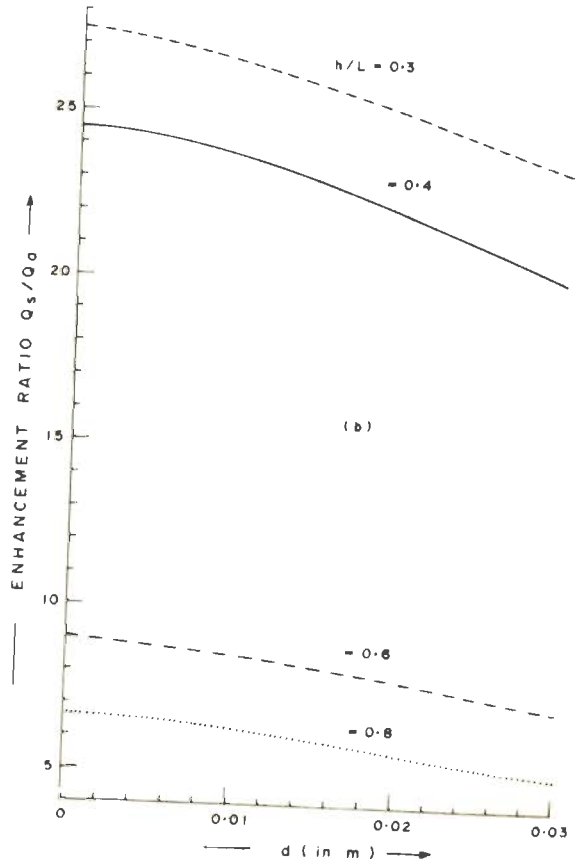
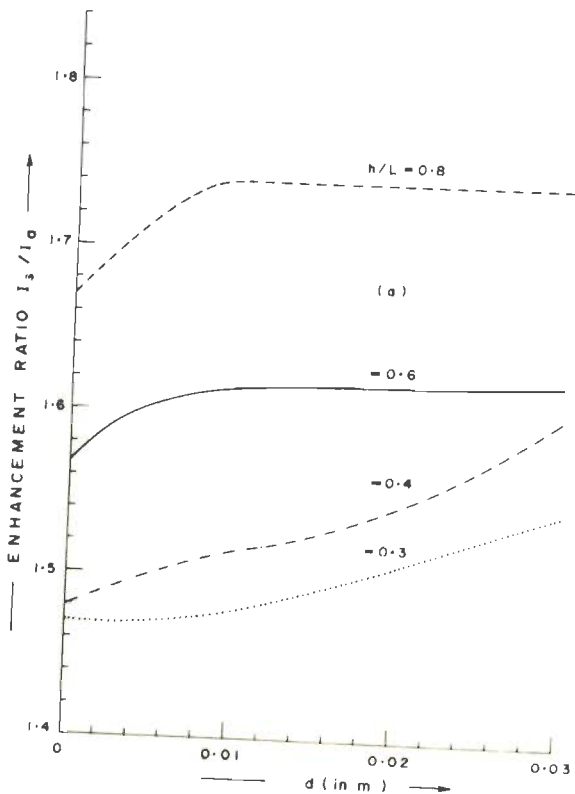


Fig. 4-63 ENHANCEMENT RATIOS (a)  $I_s/I_0$  AND (b)  $Q_s/Q_0$  VERSUS DEPTH OF BURIAL FOR A VERTICAL COPPER SHEET



It may be of interest to notice that the differential increments  $I_s - I_a$  and  $Q_s - Q_a$  of the anomaly components in this case are of the same order as that for a stainless steel sheet or a graphite sheet. The order of differential enhancements for similar  $\sigma_s$  and  $d$  values in the case of a copper wire also was not much different. This fact indicates that the differential enhancement of the response of a highly conducting sheet or any other elongated model is primarily dependent upon the conductivity of the surrounding medium rather than that of the target. Of course, the behavior of the enhancement ratios and induction indices depends on both.

Sheets of perspex ( $t = 0.0069m$  and  $0.0016m$ ) do not produce any e.m. response when placed in air because of their negligibly small conductivity. But when they are dipped in a salt solution (they simulate a cavity in a conducting medium) a negative anomaly is produced which does not cross the zero level at any point on the profile (figures 4.64 to 4.67).

For both the sheets, the  $I_p$  and  $Q_r$  components decrease with increasing  $d$  (figure 4.68 and 4.69) but the induction indices show an enhancement (figure 4.70 and 4.71). In fact, the anomalies due to these sheets are simply geometrical effects similar to the wall effect, because of a resistivity discontinuity between a sheet

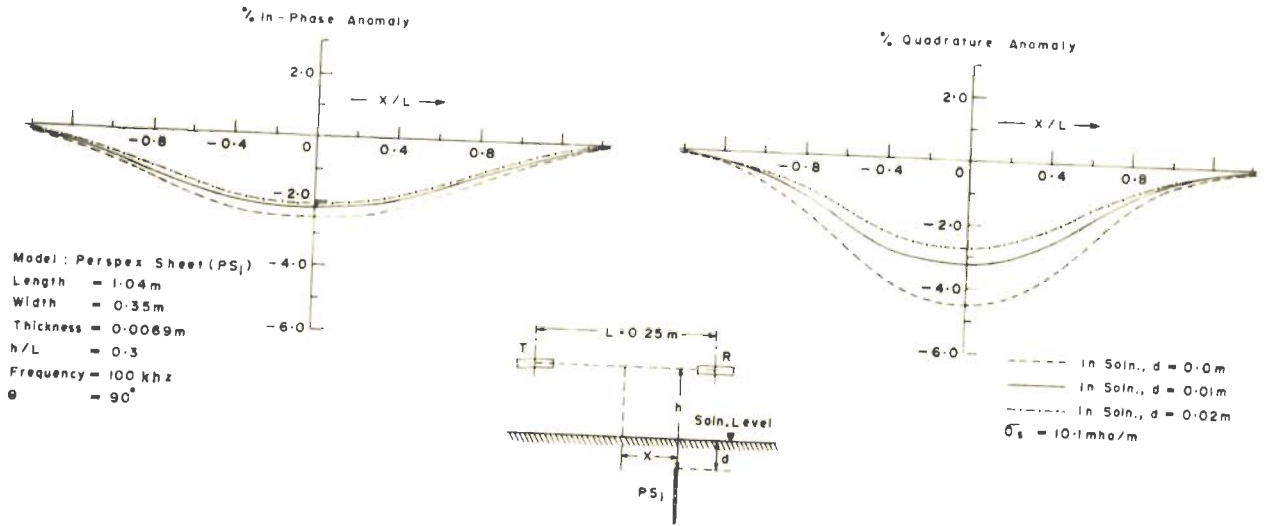


Fig. 4-64 ANOMALY PROFILES OVER A PERSPEX SHEET (h/L = 0.3)

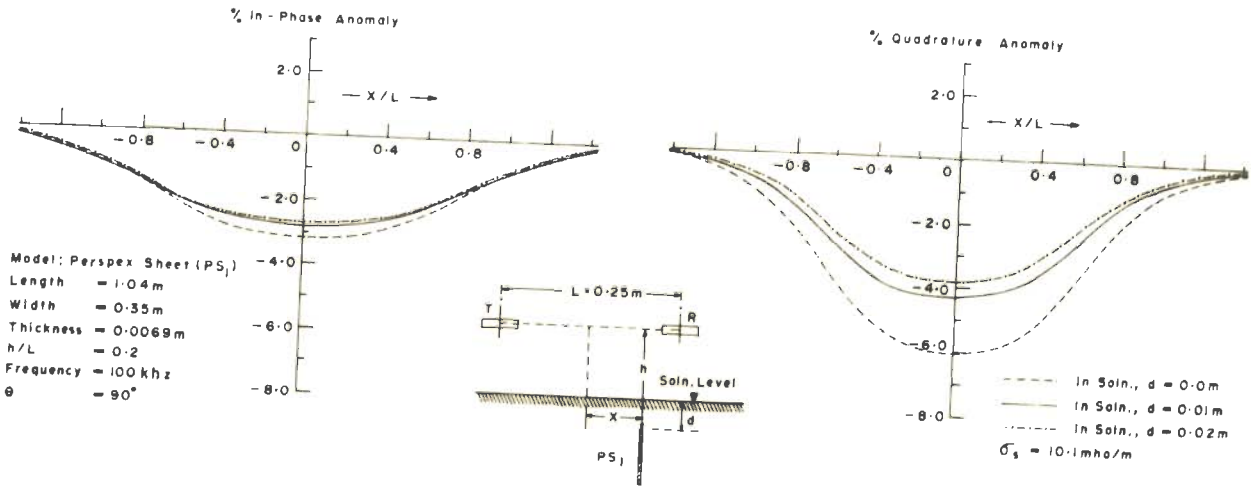


Fig. 4-65 ANOMALY PROFILES OVER A PERSPEX SHEET (h/L = 0.2)

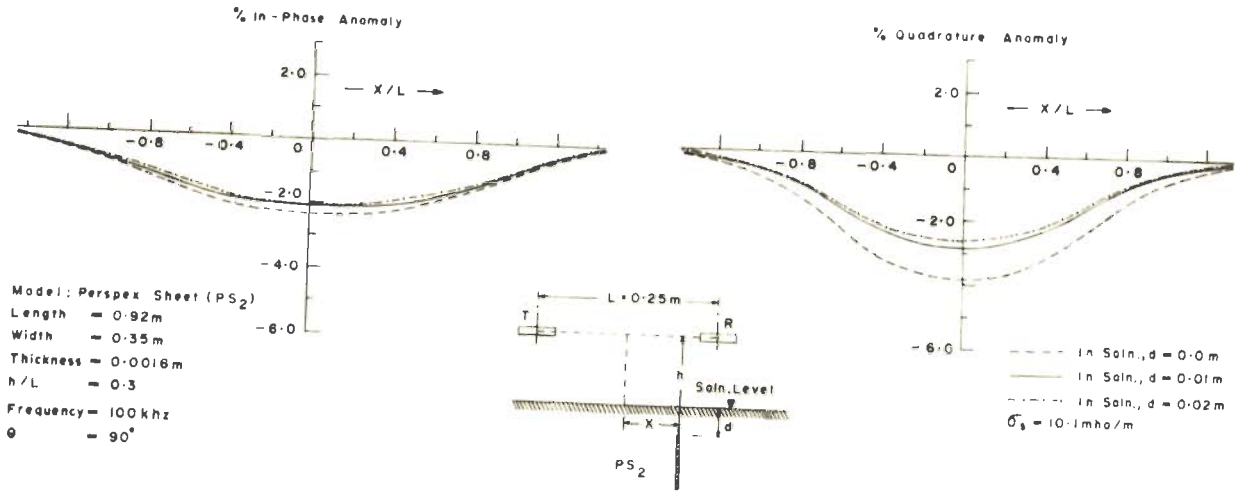


Fig.4-66 ANOMALY PROFILES OVER A PERSPEX SHEET ( $h/L = 0.3$ )

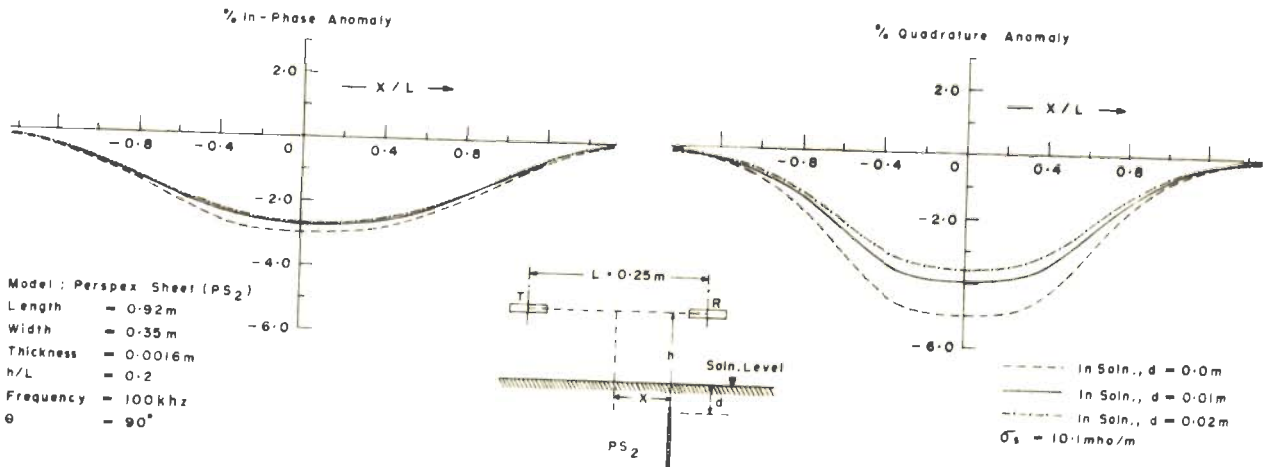


Fig.4-67 ANOMALY PROFILES OVER A PERSPEX SHEET ( $h/L = 0.2$ )

Model: Perspex Sheet (PS <sub>1</sub> )			
Length	= 1.04 m	L	= 0.25 m
Width	= 0.35 m	Frequency	= 100 kHz
Thickness	= 0.0069 m	$\sigma_s$	= 10.1 mho/m

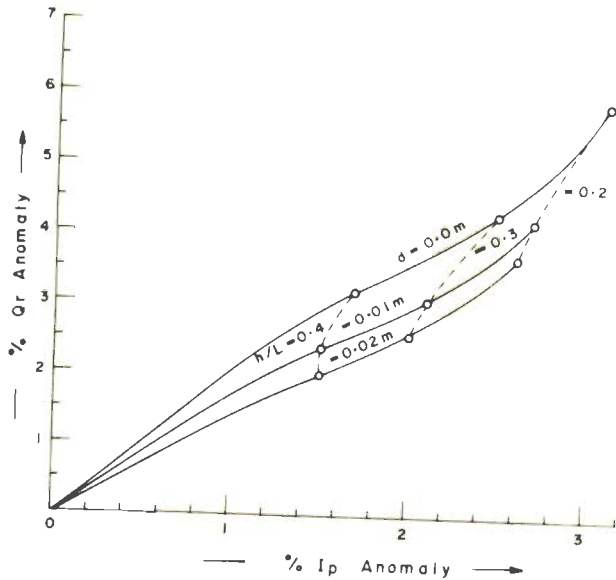


Fig. 4-68 ANOMALY INDEX DIAGRAM FOR A PERSPEX SHEET FOR DIFFERENT DEPTHS OF BURIAL

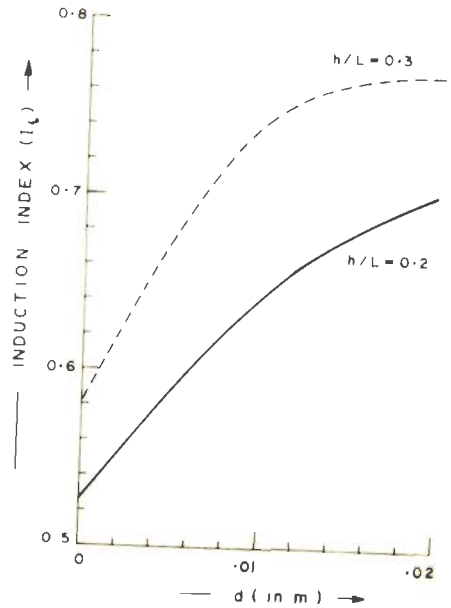


Fig. 4-70 INDUCTION INDEX ( $I_q$ ) VERSUS DEPTH OF BURIAL FOR A PERSPEX SHEET

Model: Perspex Sheet (PS <sub>2</sub> )			
Length	= 0.92 m	L	= 0.25 m
Width	= 0.35 m	Frequency	= 100 kHz
Thickness	= 0.0016 m	$\sigma_s$	= 10.1 mho/m

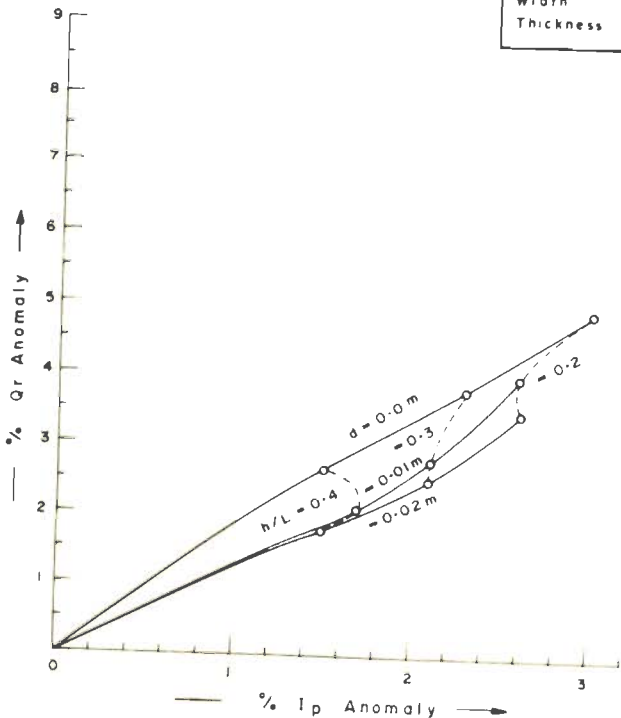


Fig. 4-69 ANOMALY INDEX DIAGRAM FOR A PERSPEX SHEET FOR DIFFERENT DEPTHS OF BURIAL

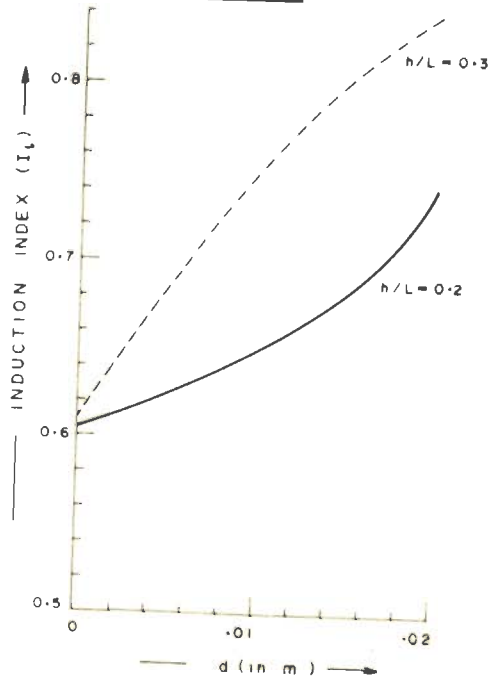


Fig. 4-71 INDUCTION INDEX ( $I_q$ ) VERSUS DEPTH OF BURIAL FOR A PERSPEX SHEET

and the solution medium. Such an effect is inherent for conducting sheets also and it decreases in all the cases with increasing depth of burial. Gaur et al (1972) have obtained a positive anomaly for a similar perspex sheet when kept horizontally.

#### 4.4.3 Horizontal graphite sheets

A shallow ore body of large lateral dimensions and small depth extent can be represented by a horizontal conducting sheet. Experimental investigations on thin sheets with zero dip have been carried out by Frischknecht and Mangan (1960), Strangway (1966a) etc. Recently, Gaur et al (1972) and Verma (1972) have reported some results of scale model experiments on determining the influence of a conducting surrounding medium on the e.m. response of a horizontal sheet to different dipolar prospecting systems. Though in all the cases, an enhancement of the response caused by a conducting surrounding medium was observed, it was most pronounced for a T100 L001 R100 prospecting system.

This model has been further investigated for different frequencies and conductivities of the surrounding medium. The influence of the conducting surrounding was expected to be greater for this model than for a vertical sheet because of a lesser distance of the prospecting system from the linear parallel

conducting elements (cf. Section 3.5.3) of which a sheet may be assumed to be composed of ( $h$  being identical in the two cases). Though this is generally found to be true, still a direct comparison of the anomalies could not be made because of the difference in the shapes of anomaly profiles. In the case of horizontal sheets, a central positive hump appears in the anomaly profile besides two negative peaks flanking it, similar to what was observed for spheres and thick cylinders (cf. Section 3.4). The relative amplitudes of the positive and negative peaks vary with the height of the prospecting system. Also, in this case the Slichter effect was found to cause a reduction of the positive peak and an enhancement of the negative peak. This makes, as seen below, the influence of the conducting surrounding on the electromagnetic response of a horizontal sheet to have a qualitative dependence on the height of the prospecting system. Details of some salient findings are given below.

#### 4.4.3.1 Variation of the depth of burial and the conductivity of the surrounding medium

The conductivity of the salt solution was varied from 3.3 mho/m to 10.1 mho/m to study its influence on the response of a horizontal graphite sheet (0.70m x 0.20m x 0.009m). Figure 4.72 (a, b) shows profiles of the  $I_p$  and  $Q_r$  components at  $h/L = 0.5$  and  $h/L = 0.4$  ( $L = 0.20m$ ) for different values of  $d$  at

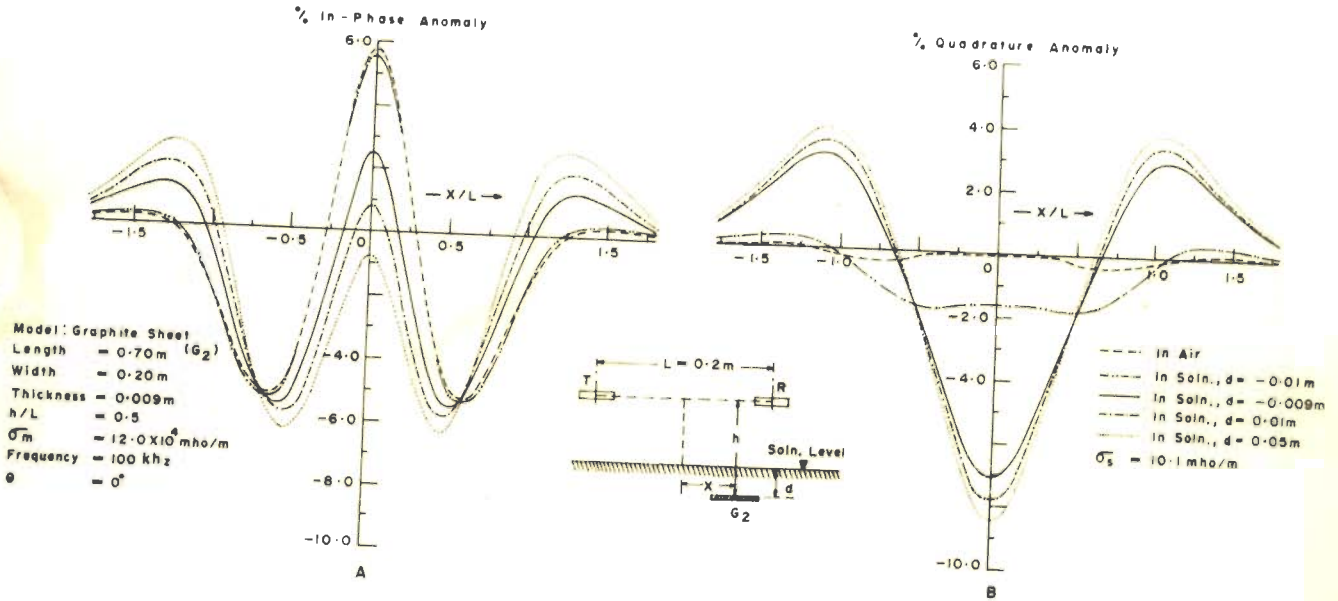


Fig.4-72a ANOMALY PROFILES OVER A GRAPHITE SHEET ( $h/L=0.5$ )

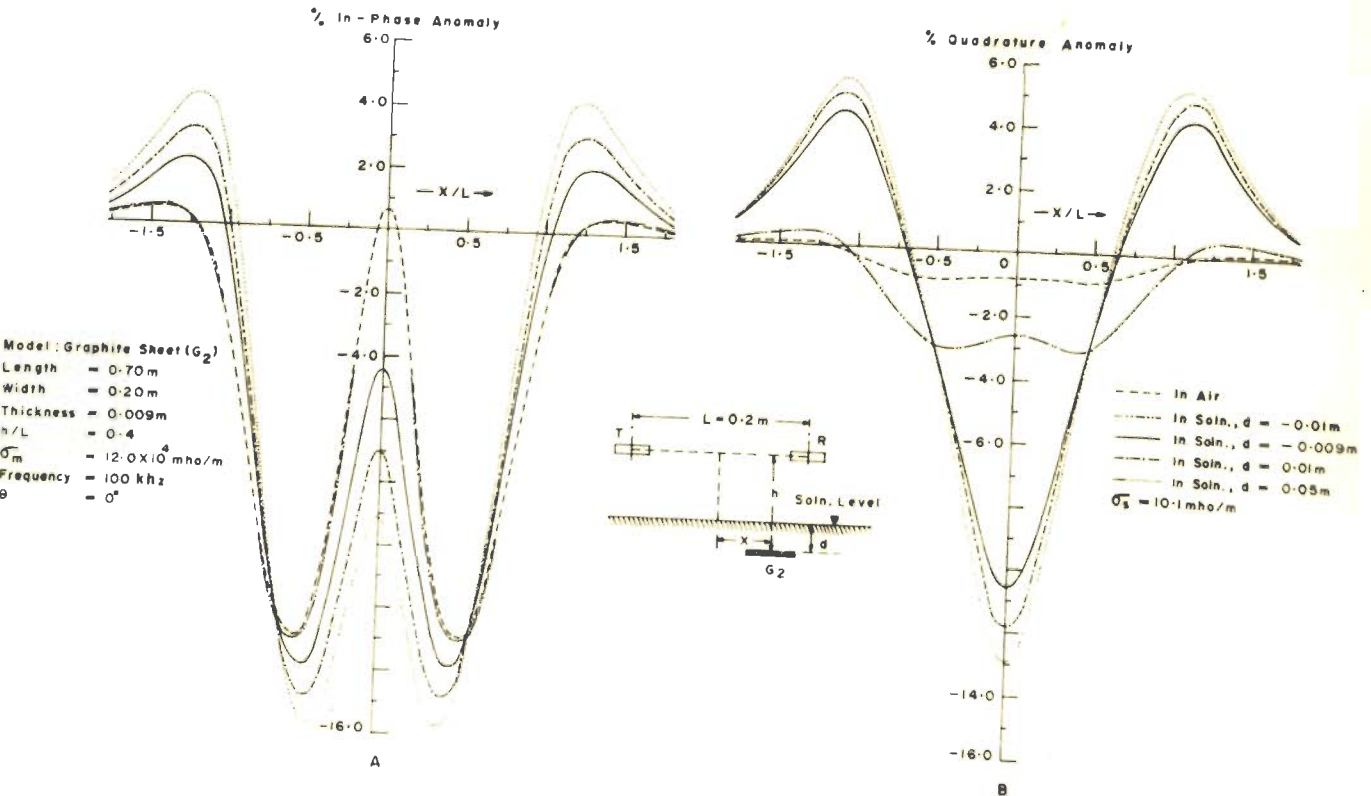


Fig 4-72b ANOMALY PROFILES OVER A GRAPHITE SHEET ( $h/L=0.4$ )

100 khz and  $\sigma_s = 10.1$  mho/m. For a height of  $h/L = 0.5$ , the  $I_p$  profile has a predominantly positive peak when the sheet is kept in air. If the height exceeds  $0.5L$ , the positive peak increases further till at  $h/L = 1.0$ , the  $I_p$  component is positive all along the profile. The  $Q_r$  component also behaves similarly though its value is very small when the sheet is in air. As the height of the T-R system is reduced, the positive peaks of both the components decrease and the negative peaks are enhanced.

As soon as the lower surface of the sheet touches the solution, a remarkable change occurs due to the Slichter effect. The negative peaks are greatly enhanced and the positive peak is decreased making the sheet appear thinner and of greater depth extent. This behavior gives rise to a characteristic variation of the  $I_p$  component different from those seen for vertical sheets, at those heights for which the  $I_p$  component of the anomaly is predominantly positive. In such cases e.g. at  $h/L = 0.5$ , the reduction of the positive peak of the  $I_p$  component is much more than the enhancement of the negative peaks. The net result is, therefore, a reduction of the  $I_p$  profile amplitude (maximum peak-to-peak excursion along it) due to the conducting surrounding medium (figure 4.72a). However, at lower heights of the prospecting system the situation is different. At  $h/L = 0.4$ , the peak-to-peak excursions for both negative



and positive peaks are nearly equal when the sheet is kept in air (figure 4.72b). On dipping it in a solution of conductivity 10.1 mho/m, the central positive hump of the  $I_p$  profile is reduced significantly, whilst the negative peaks increase and hence the anomaly amplitude is greatly enhanced.

The  $Q_r$  component of the anomaly, however, shows a uniform enhancement for all the  $h/L$  values studied herein. Of course, the central positive hump of the  $Q_r$  profile also is reduced by the conducting surrounding medium. As soon as the sheet is flush with the solution surface, a single enhanced negative peak is obtained. For a configuration when the sheet is just above the solution without touching it, the magnitude of the central hump does not change much but the negative peaks are enhanced. This effect viz the modification of the  $Q_r$  component even when there is no conductive contact between the target and surrounding medium, is similar to that observed in the case of spheres (Section 4.3.1). The difference between the two cases, however, arises due to the nature of interaction between the target and the solution surface. The negative peaks of both the  $I_p$  and  $Q_r$  components increase monotonically with increasing depths of burial upto  $d = 0.05\text{m}$  for which measurements are made.

Investigations have also been carried out for  $\sigma_s = 7.3$  mho/m and 4.4 mho/m. Figures 4.73 (a, b) and 4.74 (a, b) present the anomaly profiles for these cases. The effect of a conducting solution, as for other models studied above, diminishes as  $\sigma_s$  is reduced but no qualitative change is observed. A direct comparison of the anomaly values for different values of  $\sigma_s$  is shown in figure 4.75 (a, b).

Preparation of the anomaly index diagrams posed a special problem for this model as discussed in Section 3.4 and also by Gaur et al (1972). It is therefore considered that the anomaly index diagrams for this model, where we get two negative peaks and one central positive peak, may not have much physical importance.

Figure 4.76 (a, b) gives the anomaly profiles for a thicker graphite sheet (0.70m x 0.20m x 0.021m) at different depths of burial ( $\sigma_s = 10.1$  mho/m). Figure 4.77 (a, b) depicts the influence of the surrounding medium for different values of  $\sigma_s$  and figure 4.78 (a, b) that for different frequencies.

#### 4.5 Concluding Remarks

The influence of a conducting surrounding medium on the e.m. response of a target conductor, is dependent not only on the response parameter of

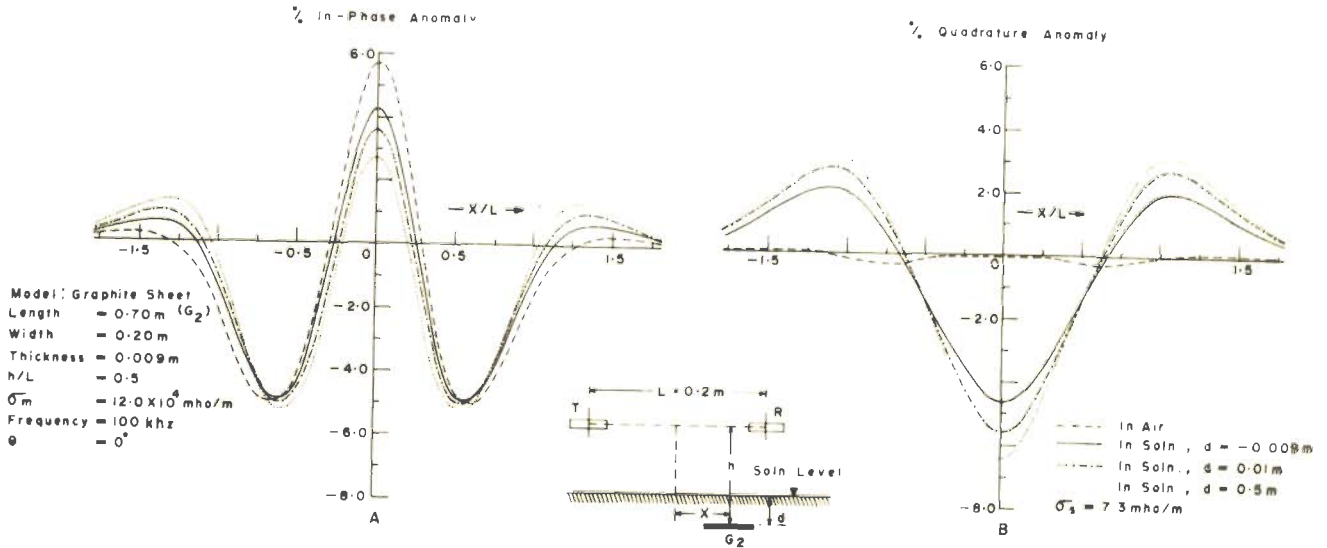


Fig. 4-73a ANOMALY PROFILES OVER A GRAPHITE SHEET ( $h/L = 0.5$ )

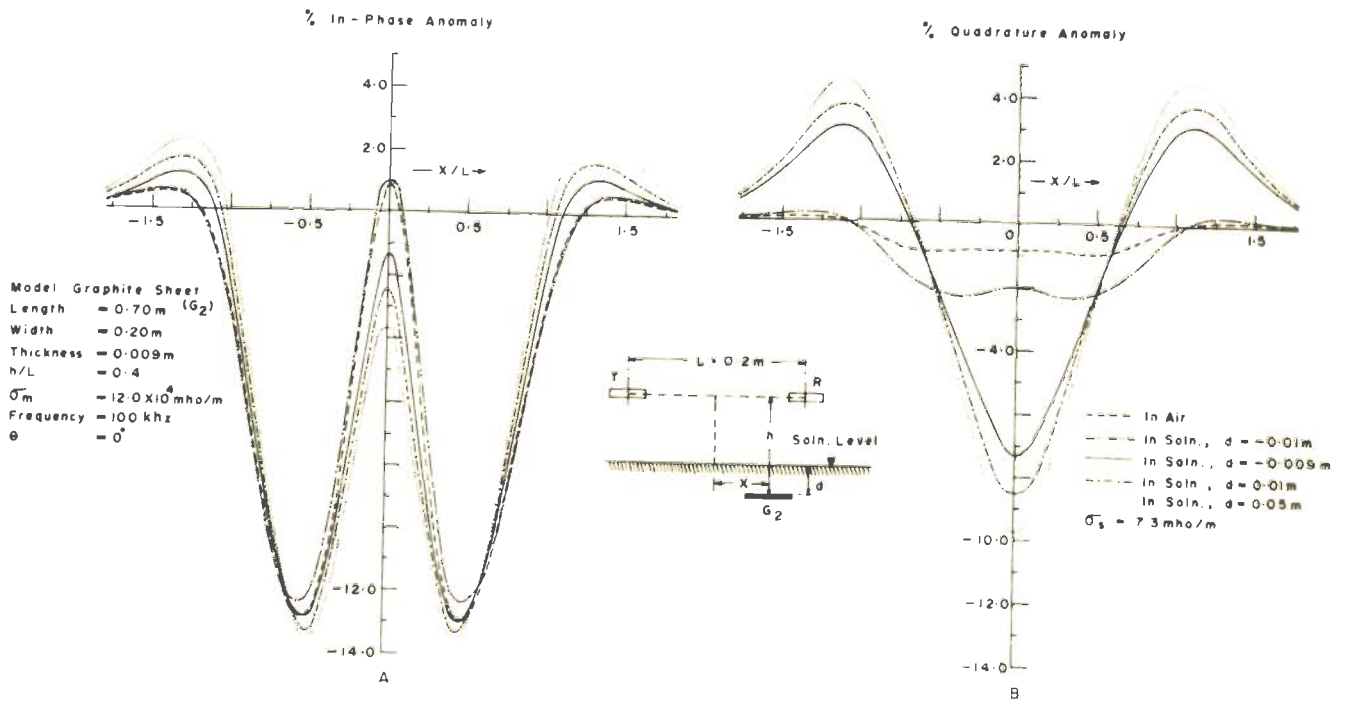


Fig. 4-73b ANOMALY PROFILES OVER A GRAPHITE SHEET ( $h/L = 0.4$ )

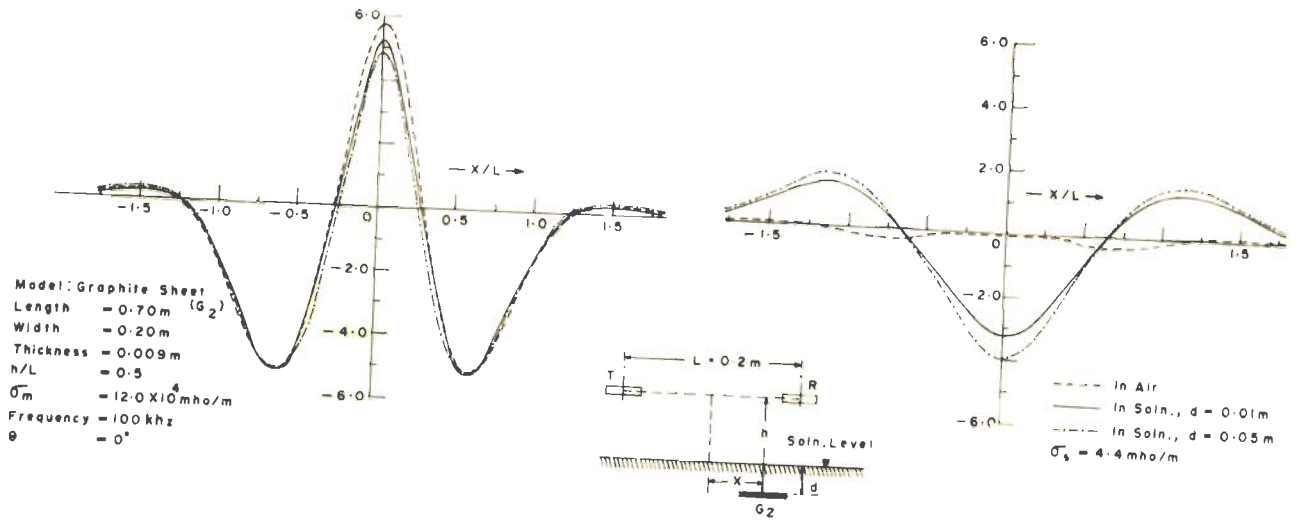


Fig. 4-74a ANOMALY PROFILES OVER A GRAPHITE SHEET ( $h/L = 0.5$ )

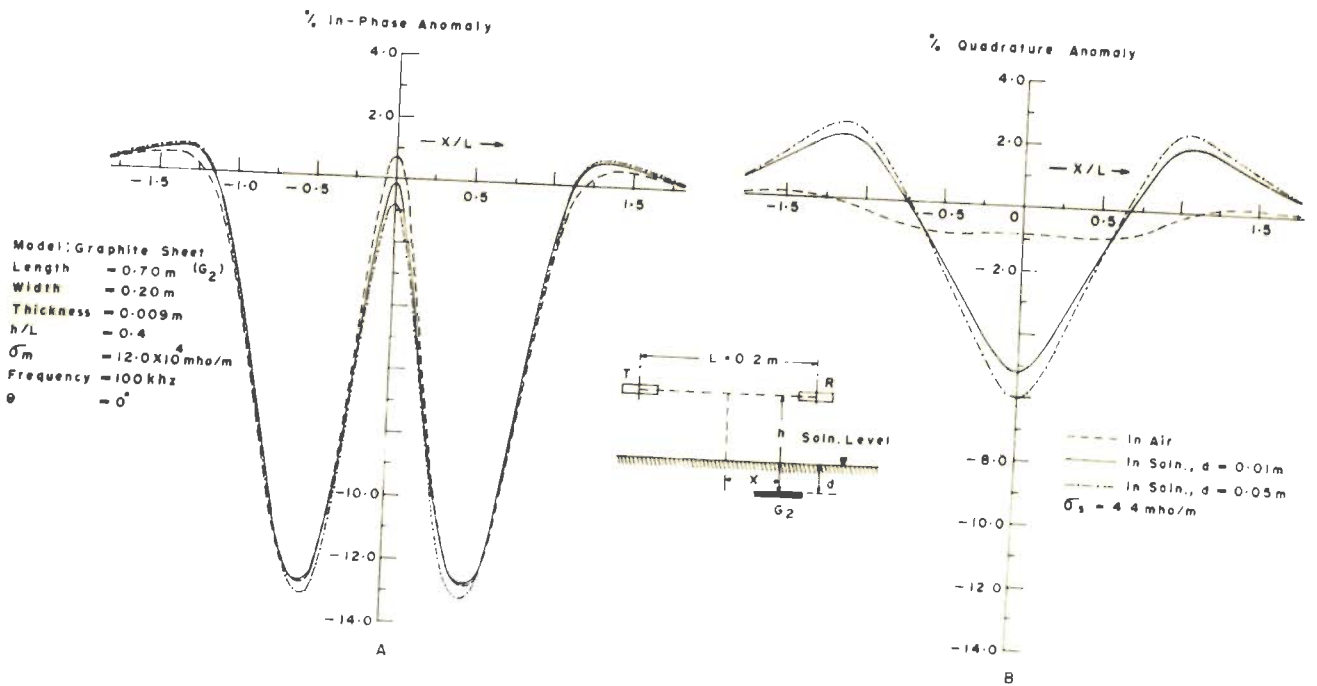


Fig. 4-74b ANOMALY PROFILES OVER A GRAPHITE SHEET ( $h/L = 0.4$ )

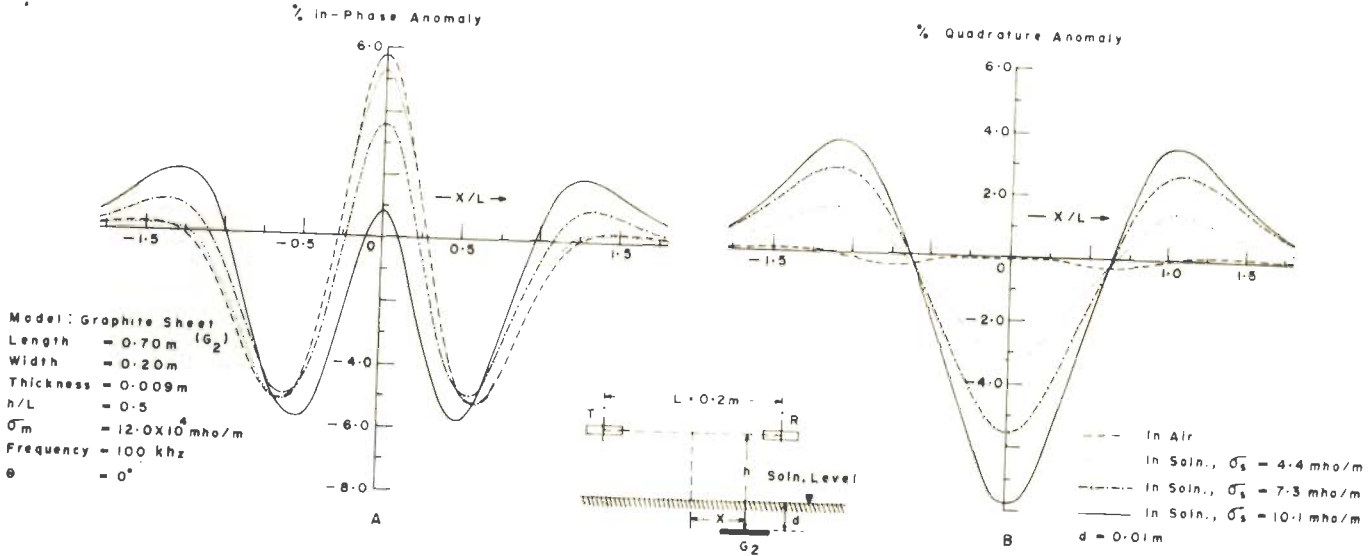


Fig.4-75a ANOMALY PROFILES OVER A GRAPHITE SHEET ( $h/L = 0.5$ )

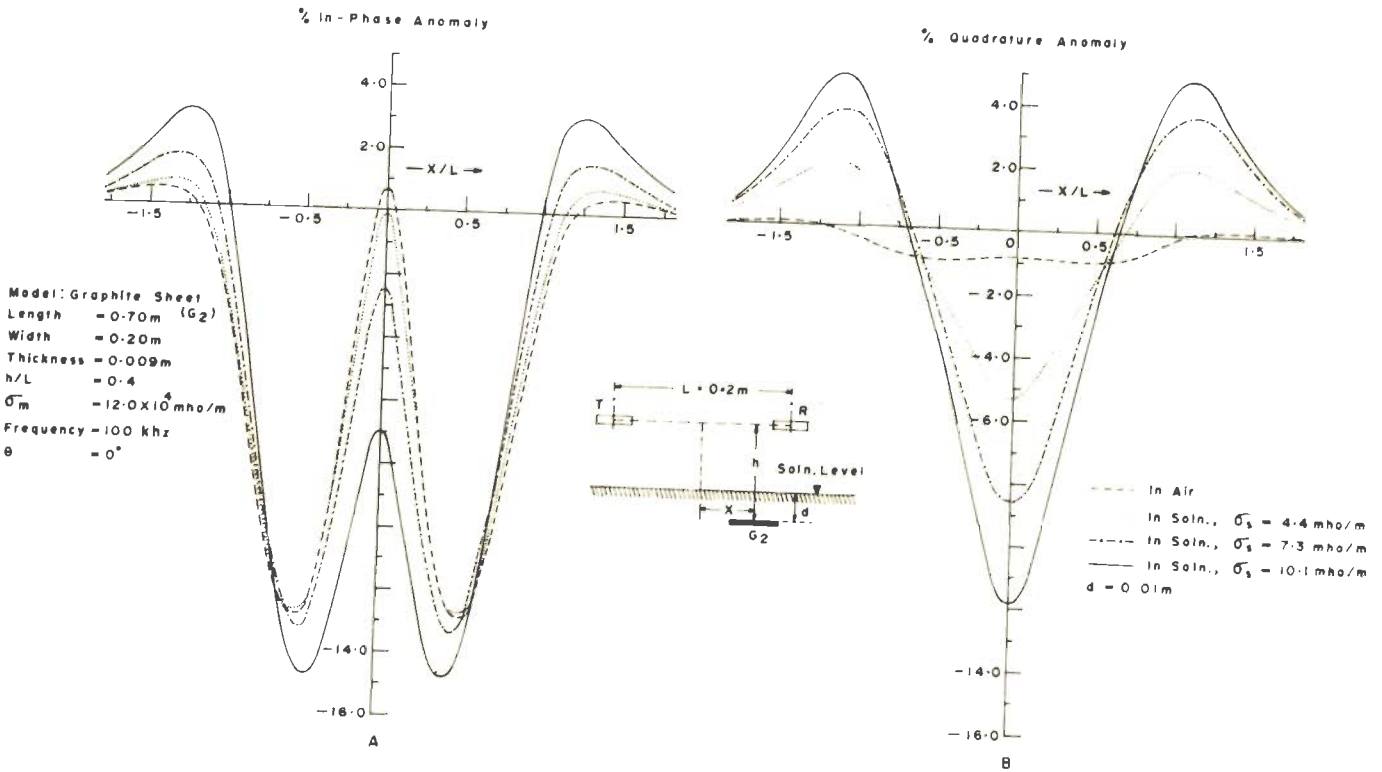


Fig.4-75b ANOMALY PROFILES OVER A GRAPHITE SHEET ( $h/L = 0.4$ )

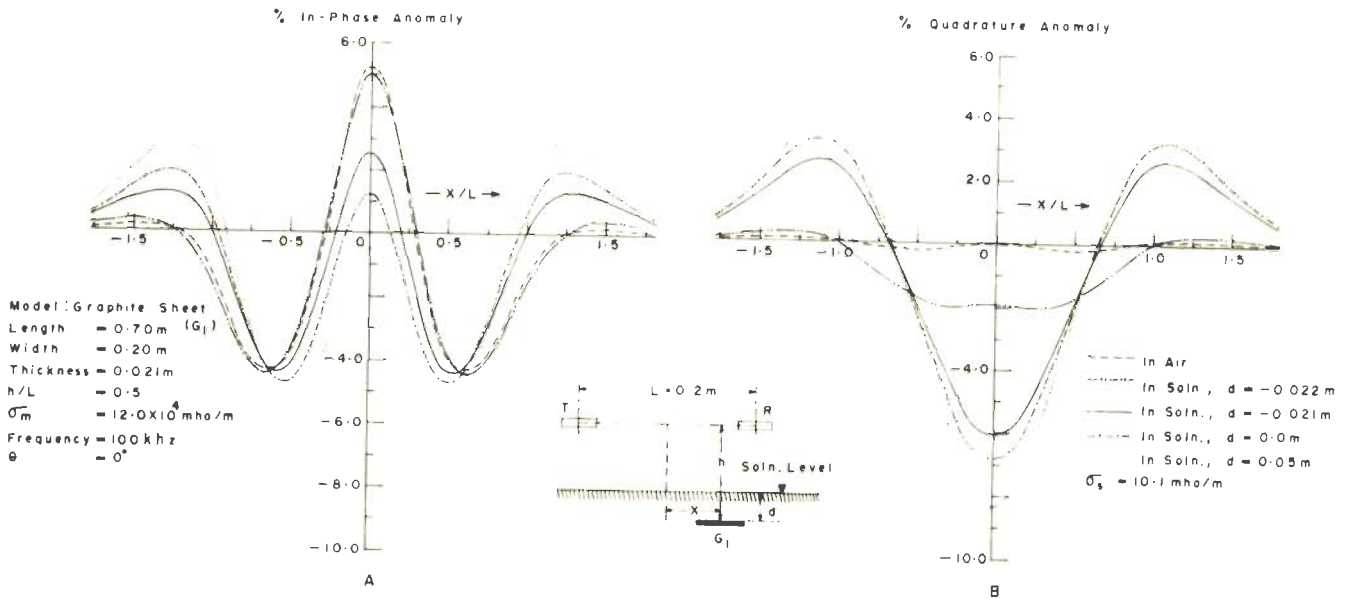


Fig.4-76a ANOMALY PROFILES OVER A GRAPHITE SHEET ( $h/L=0.5$ )

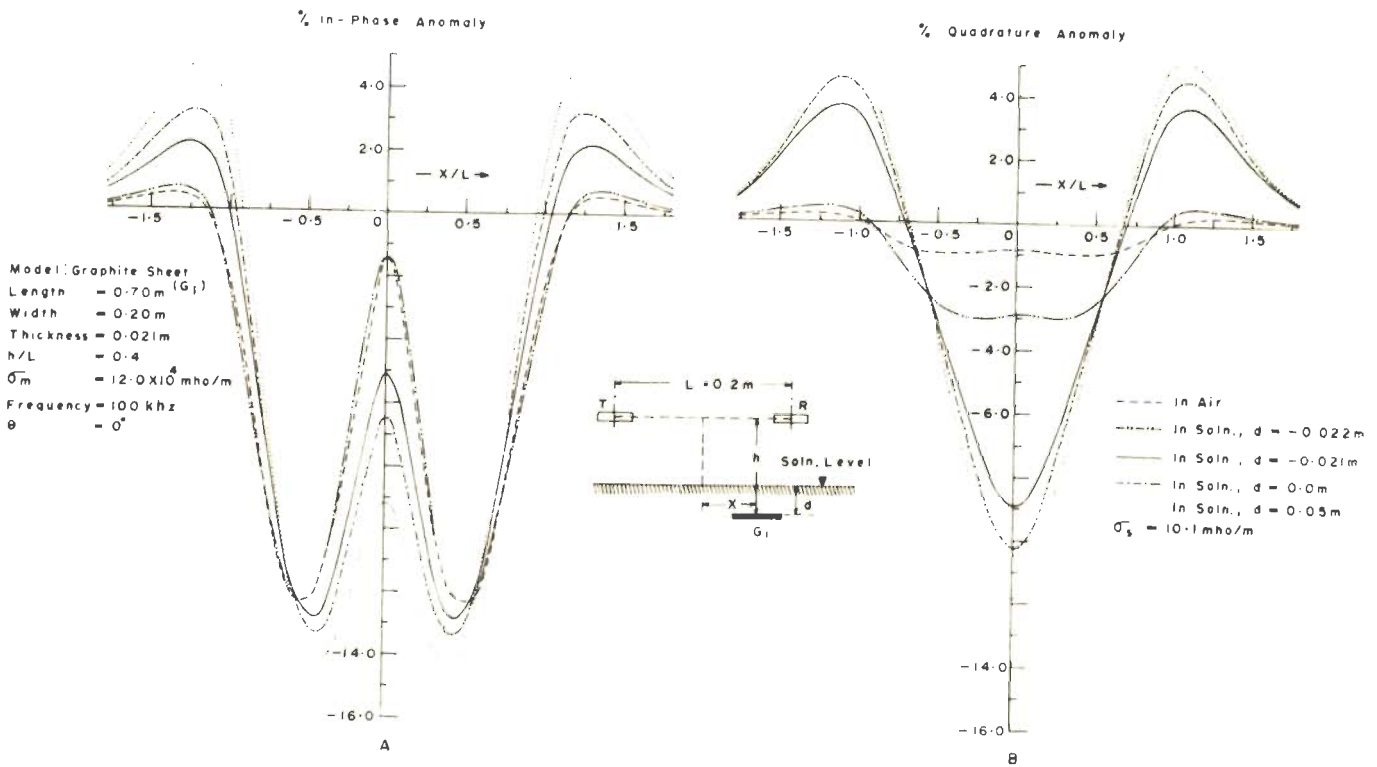


Fig.4-76b ANOMALY PROFILES OVER A GRAPHITE SHEET ( $h/L=0.4$ )

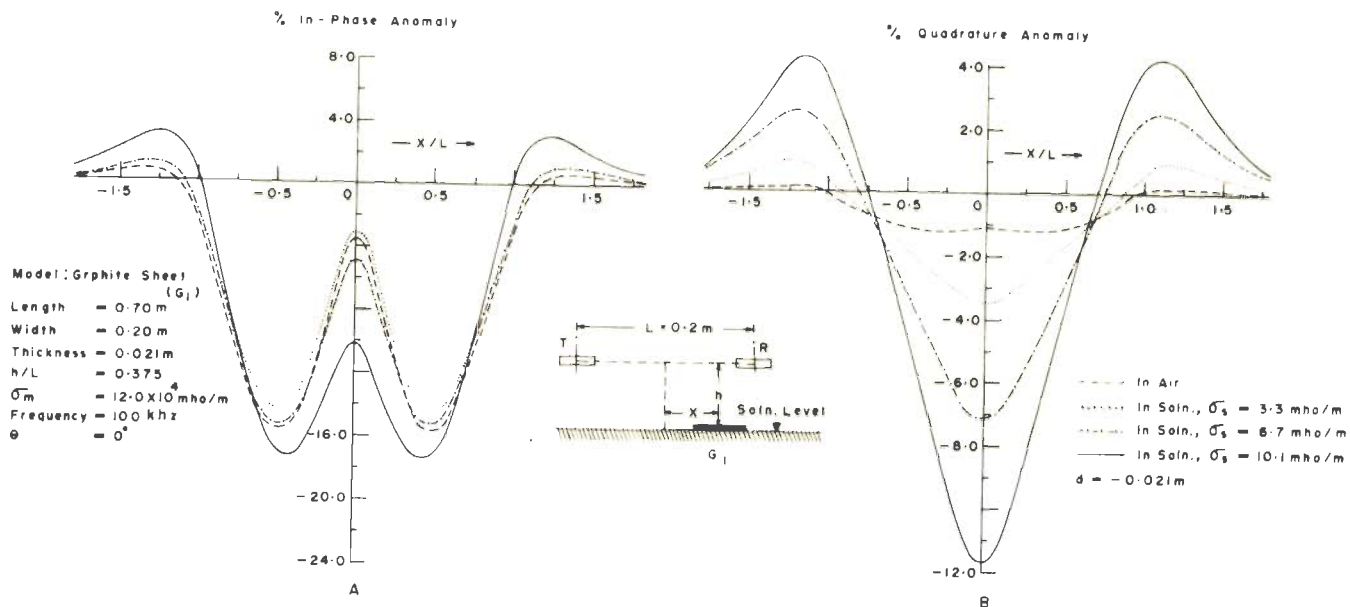


Fig. 4-77a ANOMALY PROFILES OVER A GRAPHITE SHEET

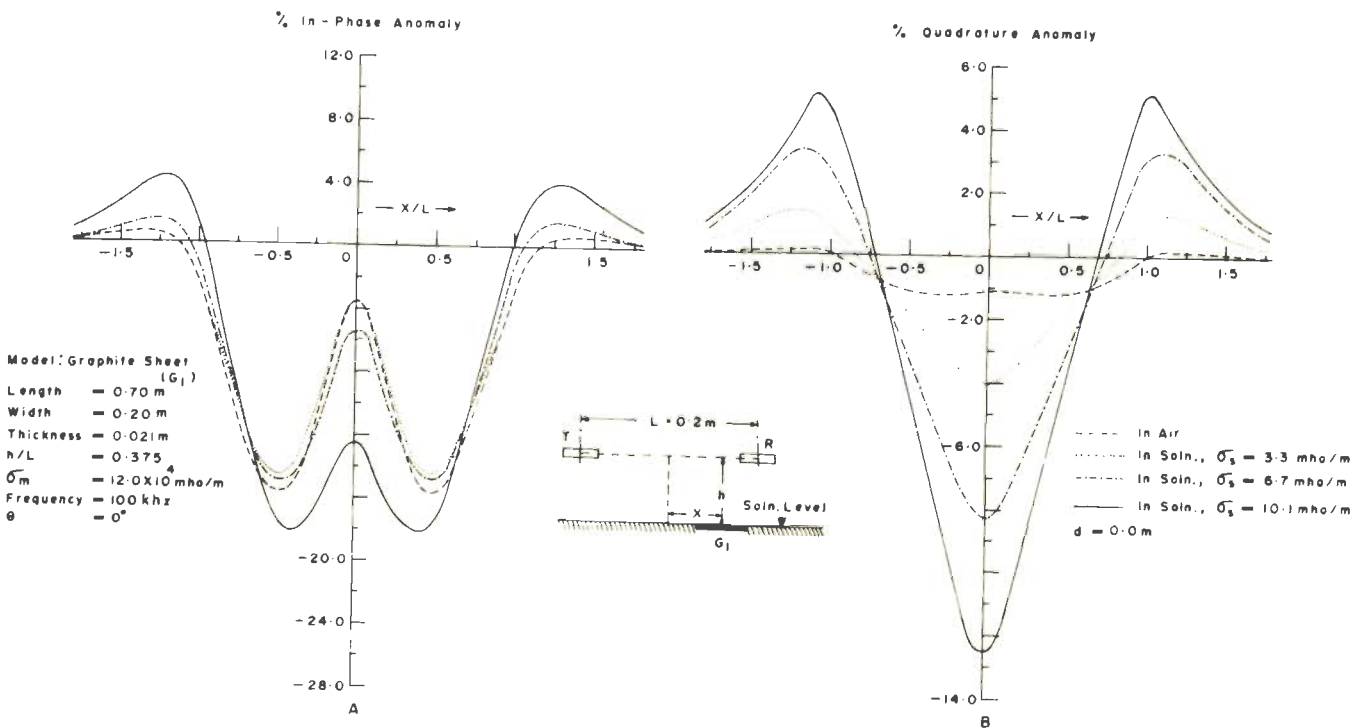
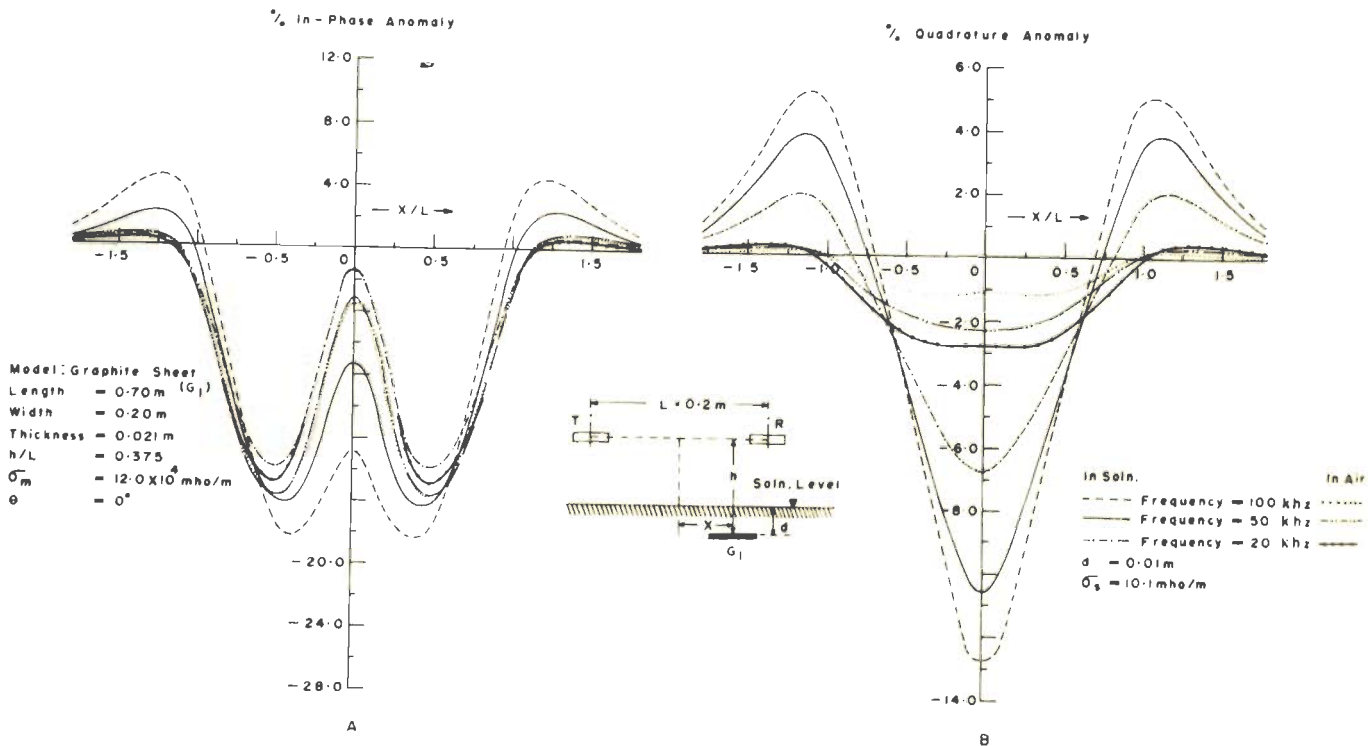
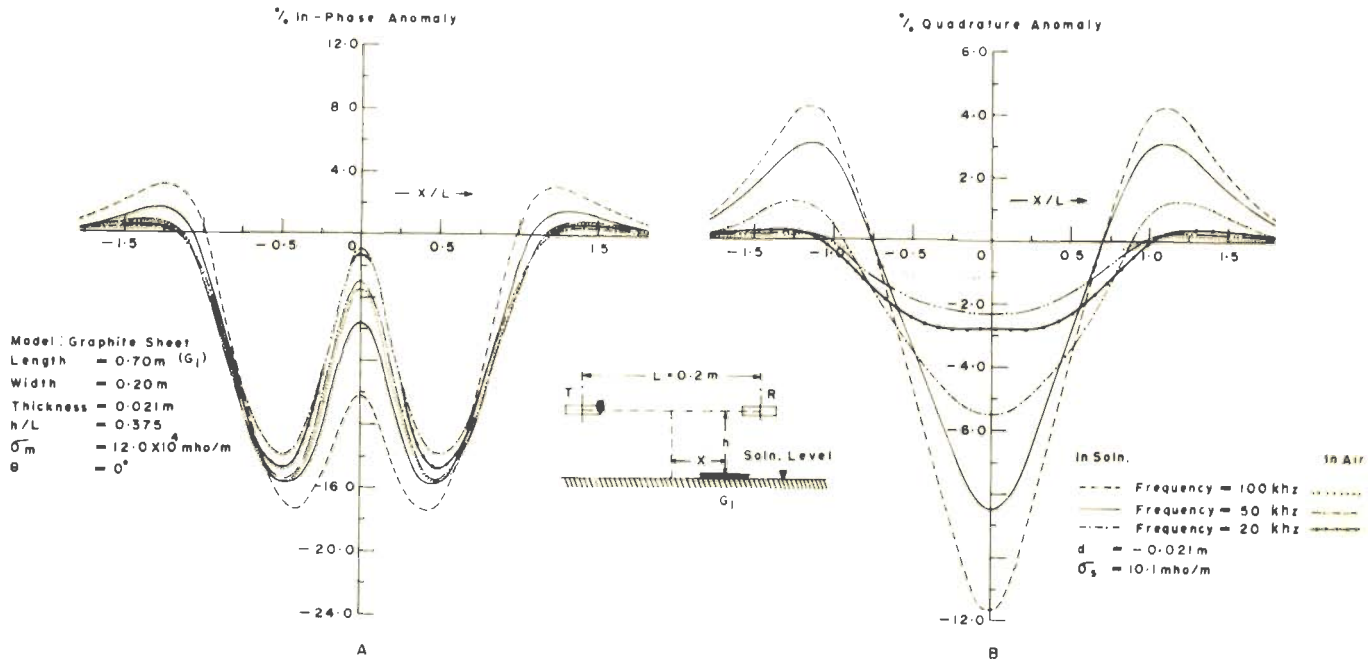


Fig. 4-77b ANOMALY PROFILES OVER A GRAPHITE SHEET





surrounding medium but also on the shape of the target and the nature of contact. As studied above, the length (orthogonal to the profile direction) along which a conductive contact occurs between the target and the surrounding medium as well as the depth of burial appears to play a significant role. In all the cases of models of different geometries, the quadrature component of the anomaly has been found to be enhanced by the conductive contact. The enhancement of the in-phase component is, however, significant only for models of elongated shapes.

In the next Chapter are presented some salient results for cases when the contact between the target and surrounding medium is non-conductive. The influence of the conducting surrounding medium and overburden will be found to be quite different from what has been observed in this Chapter. The inherent dependence of the influence of type of contact on e.m. response of a target does introduce serious difficulties in an unambiguous interpretation of the induction prospecting data.

In between the two extreme cases of conductive and non-conductive contacts lie some more realistic situations when there is a partial conductive contact of the target with the overburden. Study on such configurations is being undertaken.

## CHAPTER V

### INDUCTIVE INTERACTION OF THE TARGET WITH SURROUNDING MEDIUM AND NEIGHBOURING BODIES

#### 5.1 Introduction

The investigations described in Chapter IV related to the influence of a conducting hostrock and an overburden in conductive contact with the target. The resultant effect in such a situation depends on conductive (termed as Slichter effect) as well as on inductive interaction. In the first part of this Chapter are presented experimental findings on the response characteristics of a target when it is insulated from the surrounding medium and the overburden. In the second part, results of investigations on inductive interaction of closely spaced bodies are discussed.

#### 5.2 Effect of a Conducting Surrounding Medium and/or Overburden Insulated from the Target.

Some experimental investigations on models insulated from the overburden were reported by Hedström and Parasnis (1958) and Lowrie and West (1965). Wait (1969) and Fuller (1971) studied theoretically a two-layer spherical model in which the cover is insulated from the core. A more recent contribution is by Hill and Wait (1972) on the inductive interaction between a sphere and an

underlying conducting ground. A reduction in the response of a sphere, placed above the solution surface without a conductive contact with it, was noticed in Section 4.3. In contrast, the response of a horizontal graphite sheet was found to increase under similar conditions.

Presently, both spherical and sheet-type models have been investigated so that the influence of the target geometry, if there be any, on the response variation due to a surrounding medium and/or overburden insulated from the target may also be delineated. Such a dependence of the Slichter effect on the target geometry has already been seen in Chapter IV.

### 5.2.1 Spherical models

An experiment was designed to distinguish the effect of the conductive contact from the inductive interaction. A sphere of aluminium (diameter = 0.10 m) and another of graphite of the same diameter were chosen. A solution of conductivity  $\sigma_s = 11.6$  mho/m was used to simulate the conducting surrounding medium. A conductive contact between the target and the surrounding medium could possibly be avoided by coating the sphere with an insulating paint. But, this was apprehended to have caused distortion of current lines at the sphere-solution boundary on account of the conductivity discontinuity there and produce an anomaly. This was confirmed

through a feeble anomaly observed due to an equal-size wooden sphere placed in the solution. Thus, in addition to inductive influence of the surrounding medium a geometrical distortion of the currents would also have had its effect.

A water-tight plastic container was, therefore, used to hold the spherical model within it. Firstly, the anomaly produced by keeping the empty container inside the solution was measured. Without disturbing the position of the container, the sphere was then introduced in it and the anomaly due to the composite system measured. This ensured that there is only an inductive interaction between the sphere and the surrounding medium. The anomaly components obtained when the empty container alone was placed in the solution was appropriately subtracted from the anomaly components of the composite system to derive the response of the sphere in the presence of a conducting surrounding medium.

An objection to such an arrangement could be that the container-solution boundary may deform the energisation field and render it non-dipolar. Actual observations have, however, proved that if the response of the container and its holder is appropriately accounted for, this objection is not serious and the usual form of the anomaly profile is obtained at least for the

$I_p$  component. The noise in the  $Q_r$  profile (particularly for the aluminium sphere), however, is found to be relatively greater.

Anomaly profiles for the two spheres are shown in figures 5.1 and 5.2 respectively. For the aluminium sphere only the  $I_p$  profiles are given. For both the spheres, the changes in the  $I_p$  component brought about by the conducting surrounding medium are almost inappreciable to draw any specific conclusion from these observations. The  $Q_r$  response of the graphite sphere is found to be slightly enhanced, particularly the central positive peak. This may be possibly due to geometrical distortion of the energising field. Nonetheless, it can be inferred from this experiment coupled with the results of Section 4.3.1 that for spherical targets of the dimensions as studied here, the effect of a conducting surrounding medium whether in conductive contact or insulated from the target, is not significant. Further work on bigger spheres and for higher  $\sigma_s$  values is in progress.

#### 5.2.2 Tabular sheet type bodies

A simulation of the situation depicted in figure 1.2 was attempted by employing a graphite sheet (0.70m x 0.20m x 0.021m) to represent an ore body, a solution of conductivity 3.3 mho/m to represent a poorly conducting hostrock, and a layer of acidic solution

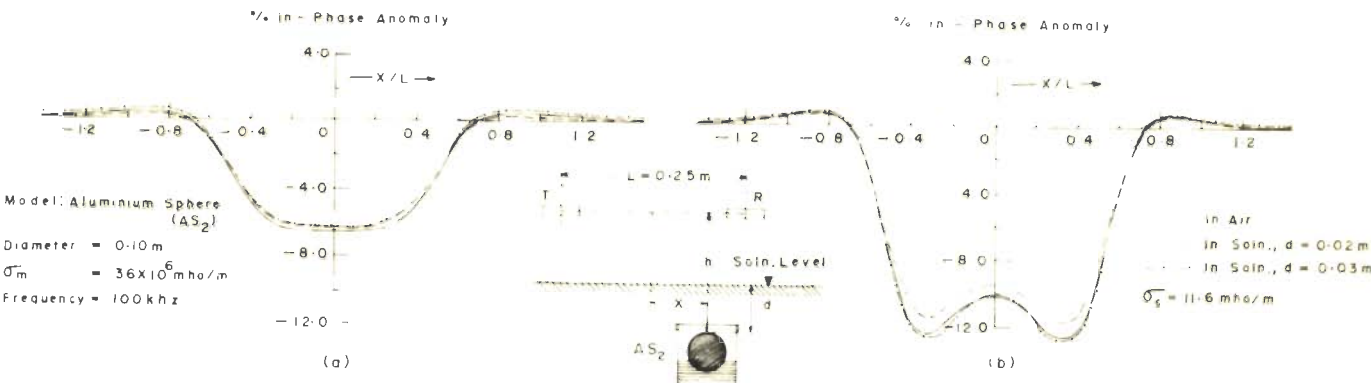


Fig. 5-1 ANOMALY PROFILES OVER AN ALUMINIUM SPHERE IN A CONTAINER AT (a)  $h/L = 0.3$  AND (b)  $h/L = 0.2$

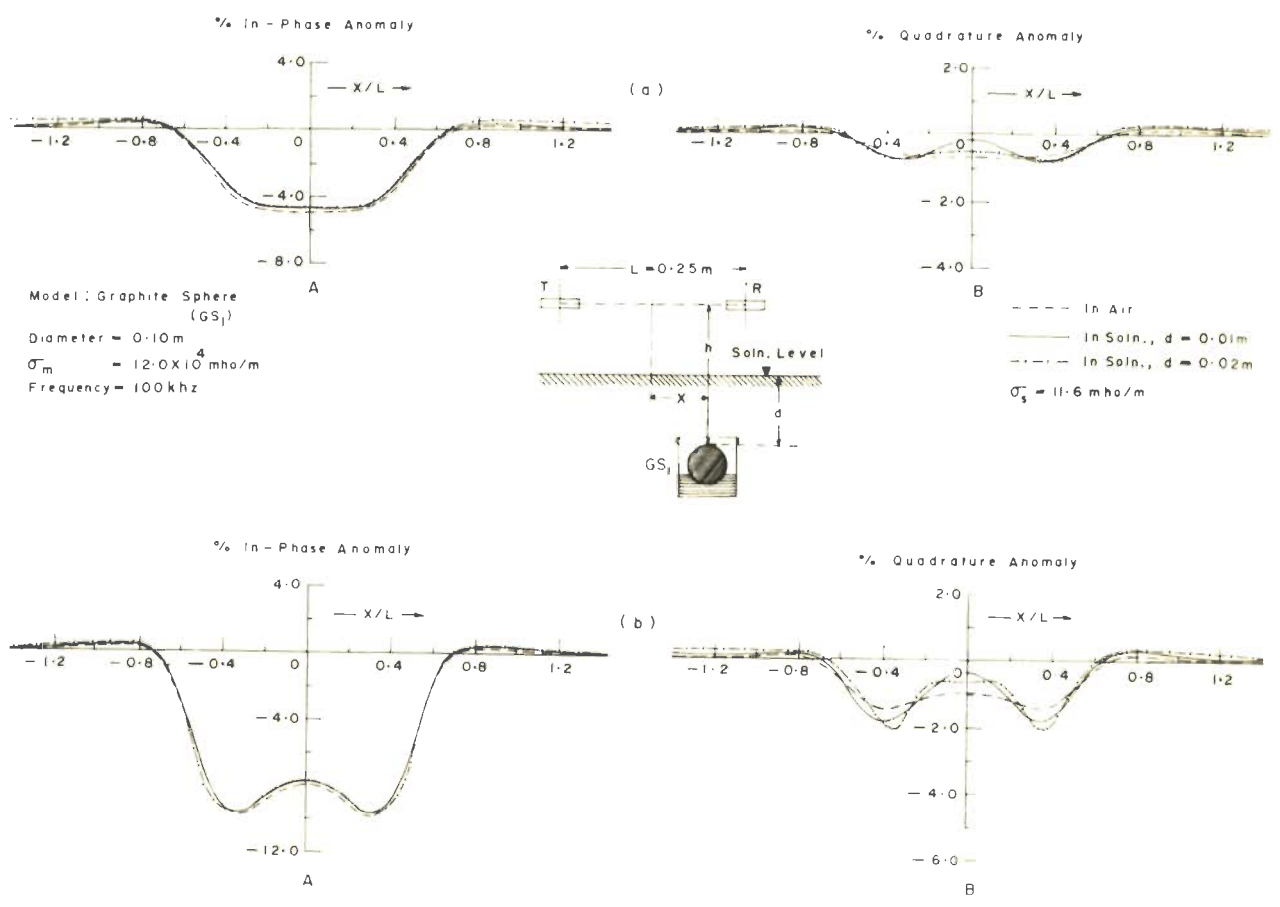


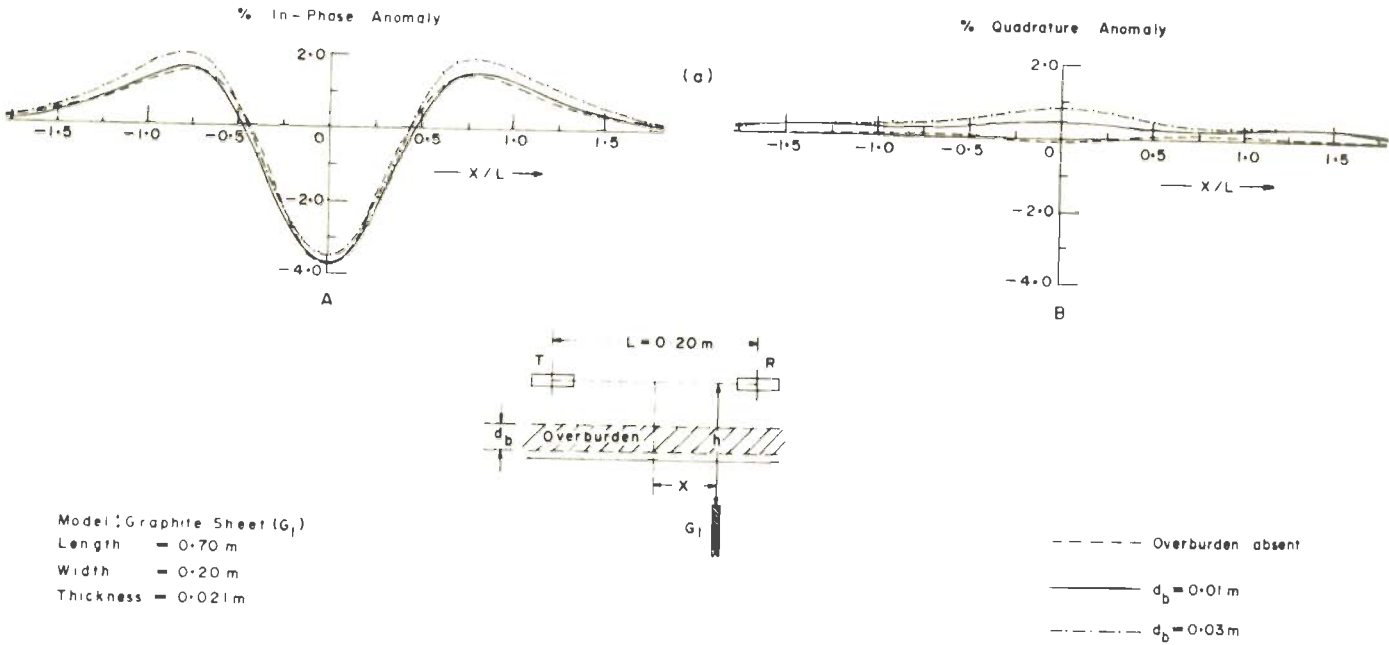
Fig. 5-2 ANOMALY PROFILES OVER A GRAPHITE SPHERE IN A CONTAINER AT (a)  $h/L = 0.3$  AND (b)  $h/L = 0.2$

( $\sigma_b = 17.0$  mho/m and maximum  $\sigma_b d_b = 0.5$  mho) in a tray to represent a thin overburden. The effect of the overburden alone i.e. when the hostrock is highly resistive has also been investigated. Because of the design of the tray the T-R height could not be reduced less than a certain minimum.

#### 5.2.2.1 Effect of the overburden when the hostrock is highly resistive ( $\sigma_s = 0$ )

Figure 5.3 shows the anomaly profiles for the graphite sheet in vertical position ( $h/L = 0.625$ ) for frequencies of energisation as (a) 100 khz and (b) 50 khz respectively. Contrary to what is observed when the surrounding medium is in conductive contact with the target (Section 4.4.1), the effect of an insulated overburden is not significant even over an elongated sheet. Of course, a slight reduction and inversion of the Qr component and a small enhancement of the Ip component is found to occur with increase in the overburden thickness ( $\sigma_b d_b = 0.5$  mho) at 100 khz. At 50 khz the effect is correspondingly reduced.

Figure 5.4 depicts the anomaly profiles when the same sheet is horizontal for (a) 100 khz and (b) 50 khz. The anomaly profiles for this orientation of the sheet is predominantly positive at  $h/L = 0.625$ . The Ip component shows a slight reduction with increase in the overburden thickness while the Qr component, is enhanced, though to a



$\theta = 90^\circ$ ,  $h/L = 0.625$ ,  $\sigma_m = 12.0 \times 10^4$  mho/m,  $\sigma_b = 17.0$  mho/m

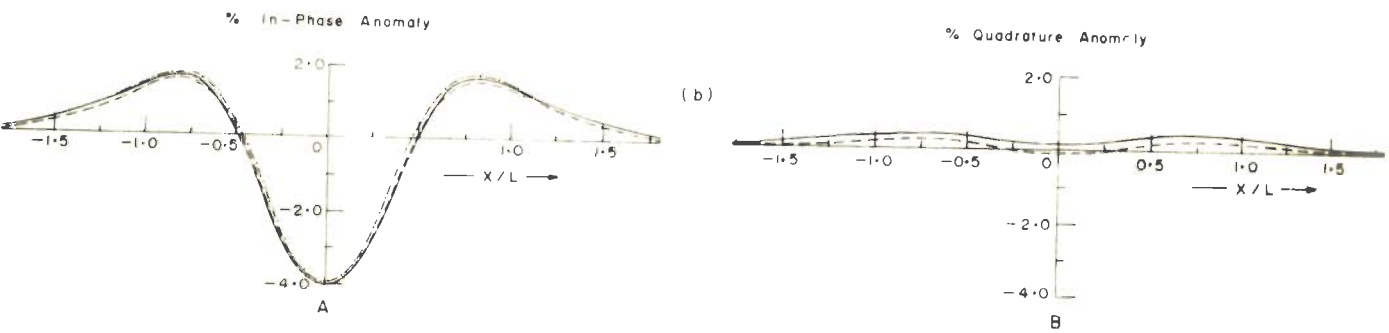


Fig. 5-3 ANOMALY PROFILES OVER A GRAPHITE SHEET FOR DIFFERENT OVERBURDEN THICKNESSES ( $d_b$ ) WHEN THE SURROUNDING MEDIUM IS NON-CONDUCTING FOR (a) 100 kHz AND (b) 50 kHz



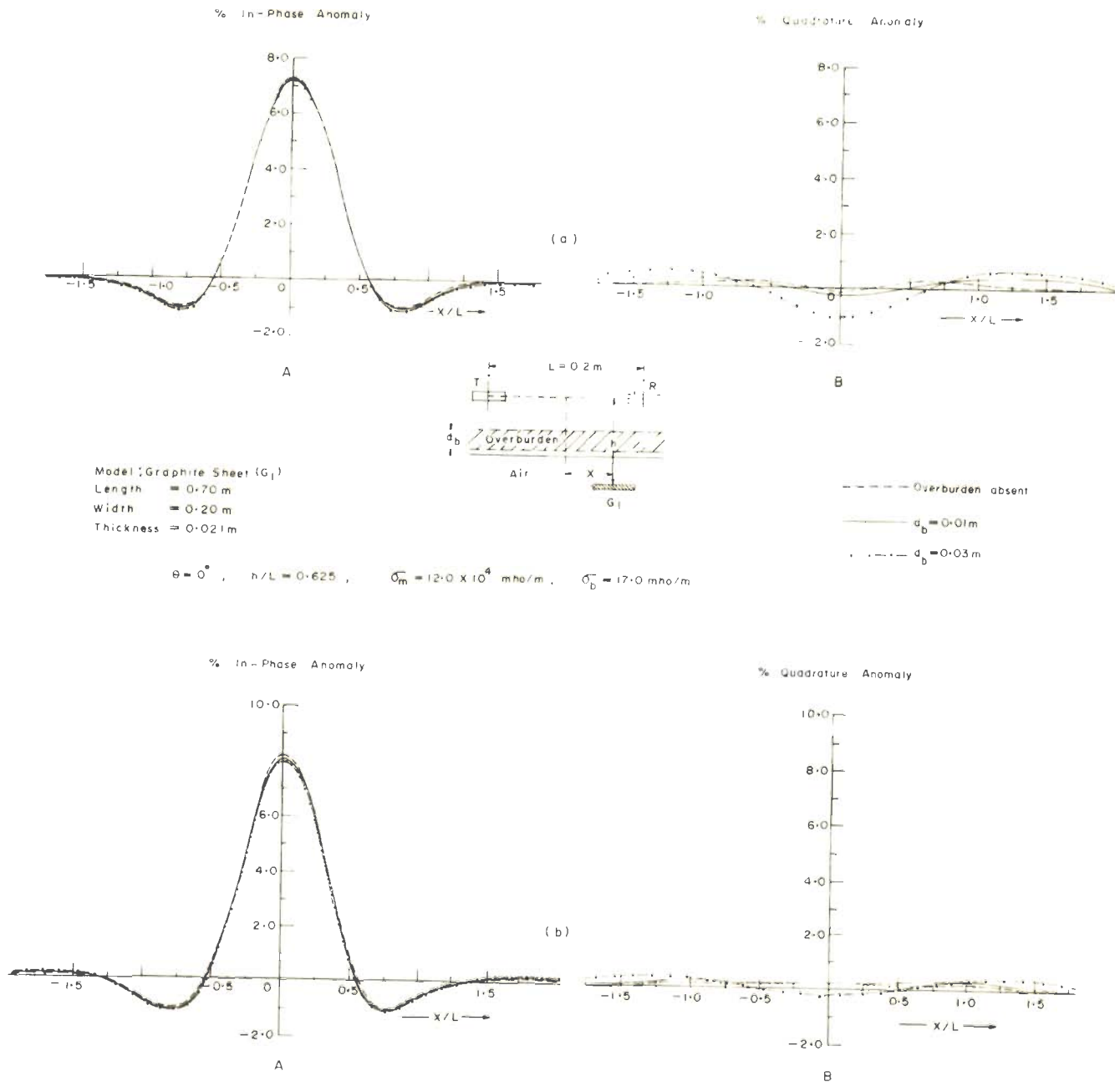


Fig. 5-4 ANOMALY PROFILES OVER A GRAPHITE SHEET FOR DIFFERENT OVERBURDEN THICKNESSES ( $d_b$ ) WHEN THE SURROUNDING MEDIUM IS NON-CONDUCTING FOR (a) 100 kHz AND (b) 50 kHz

small extent, with increase in the overburden thickness.

The behavior of the  $I_p$  and  $Q_r$  components with increase in overburden thickness for both the orientations of the sheet, thus, appears to be complementary to each other. This indicates that the effect of the overburden, for low values of surface conductivity ( $\sigma_b d_b$ ) is mainly the phase rotation and a slight reduction of the anomaly vector.

#### 5.2.2.2 Effect of the overburden when the hostrock is finitely conducting ( $\sigma_s > 0$ )

The above observations were repeated employing a salt solution ( $\sigma_s = 3.3$  mho/m) to simulate the hostrock and the variations in the anomaly components were found to have a similar behavior. Figure 5.5 shows the anomaly profiles for the vertical sheet. As the overburden thickness is gradually increased upto 0.01 m, the  $I_p$  component shows a slight reduction and the  $Q_r$  component is enhanced. However, if the thickness of the overburden is further increased, the  $Q_r$  component also starts decreasing. For a horizontal orientation of the same sheet, the  $Q_r$  component shows a monotonic increase rather substantially with increase in  $d_b$  (figure 5.6), although the peak-to-peak excursion of the  $I_p$  component remains almost unaltered.

Thus, in all the above cases, the effect of an

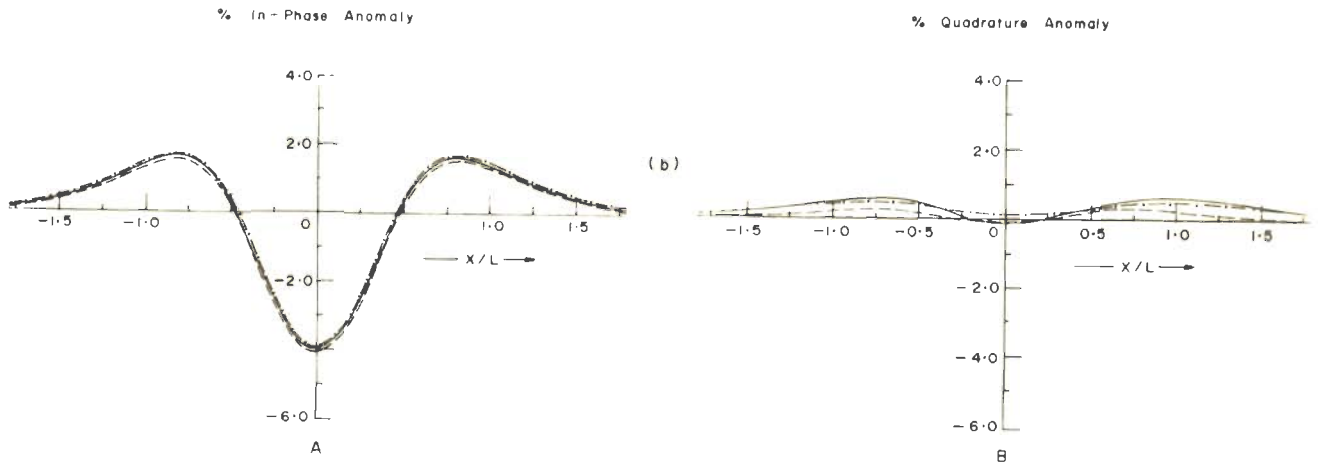
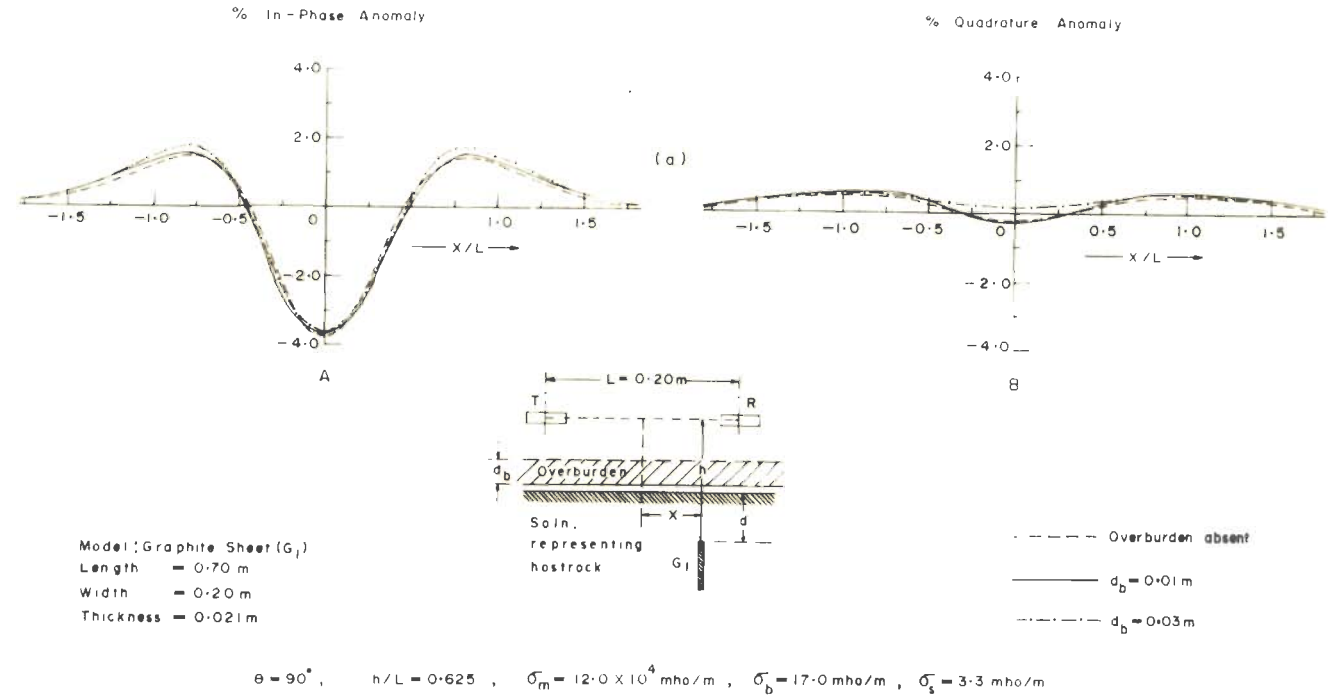


Fig. 5-5 ANOMALY PROFILES OVER A GRAPHITE SHEET FOR DIFFERENT OVERBURDEN THICKNESSES ( $d_b$ ) WHEN THE SURROUNDING MEDIUM IS A CONDUCTING SOLUTION FOR (a) 100 kHz AND (b) 50 kHz

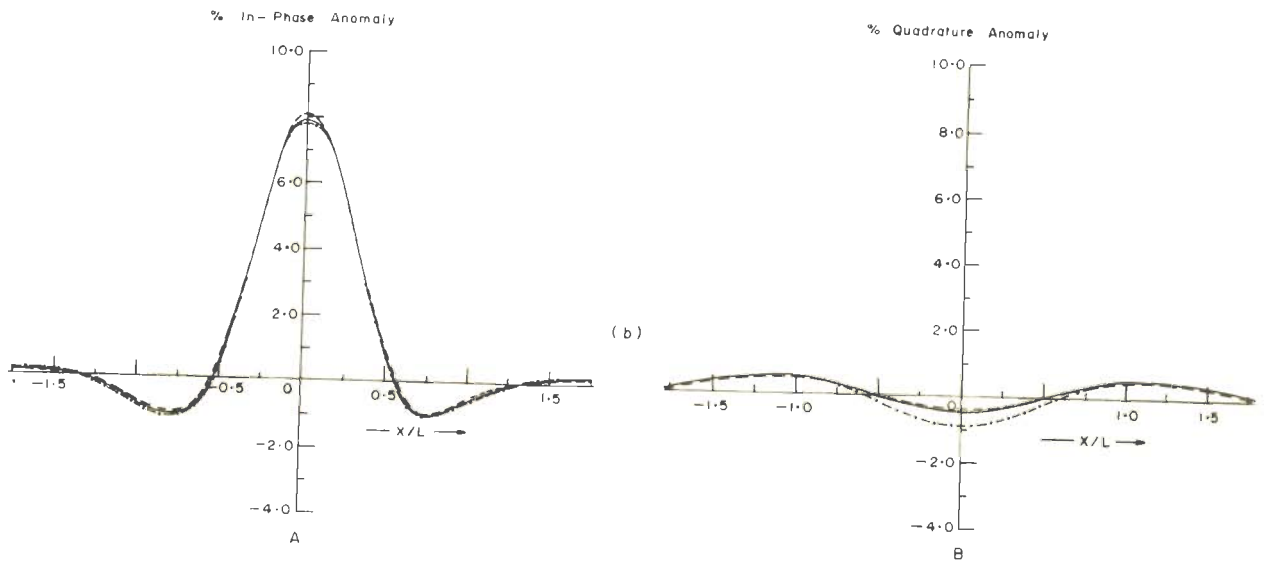
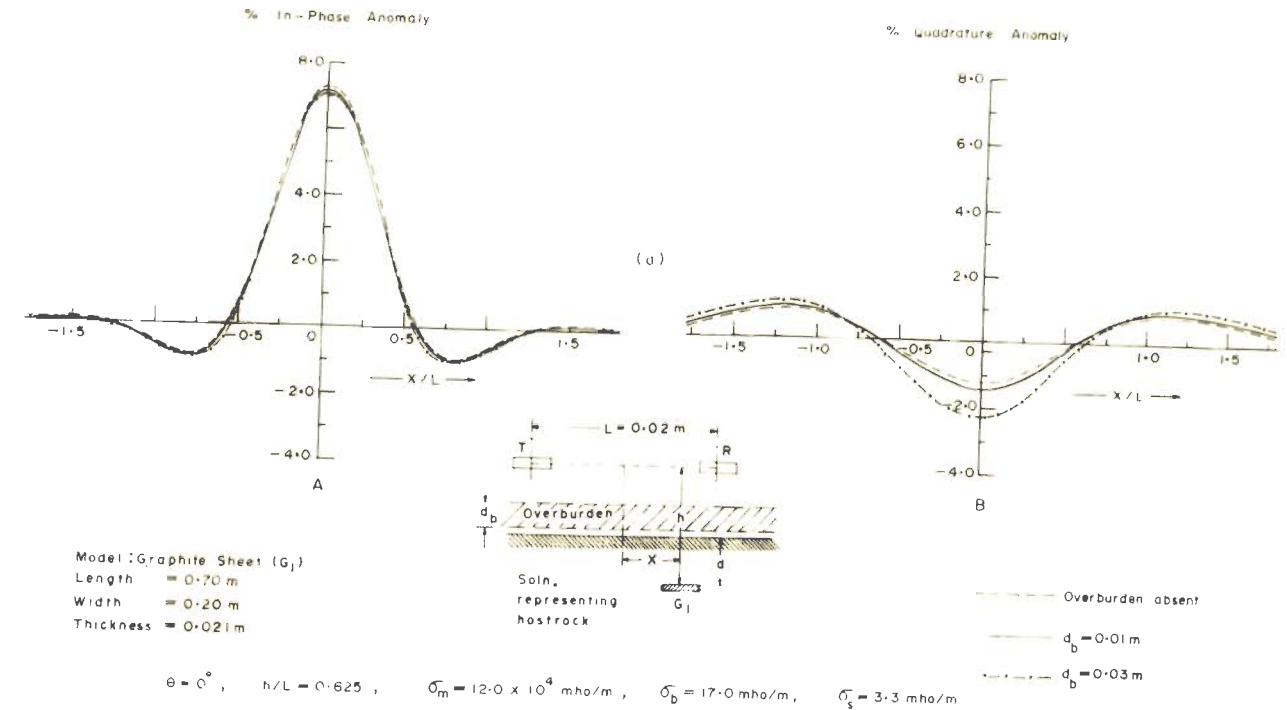


Fig. 5-6 ANOMALY PROFILES OVER A GRAPHITE SHEET FOR DIFFERENT OVERBURDEN THICKNESSES ( $d_b$ ) WHEN THE SURROUNDING MEDIUM IS A CONDUCTING SOLUTION FOR (a) 100 kHz AND (b) 50 kHz

overburden of a small surface conductivity, as could be achieved using a solution layer, has not been significant.

An aluminium foil of thickness  $d_b = 0.015$  m ( $\sigma_b d_b \approx 500$  mho) has also, therefore, been used even though its conductivity falls on relatively higher side of the expected values of the overburden. The same graphite sheet has been used to simulate an ore body but the hostrock is represented by a solution of higher conductivity ( $\sigma_s = 9.0$  mho/m). Figure 5.7 shows the anomaly profiles when the sheet is held in (a) vertical and (b) horizontal orientations for 50 khz. For the horizontal sheet, the two negative peaks of  $Q_a$  merge into one though the peak-to-peak values remain unaltered. For a vertical sheet, the  $Q_r$  profile becomes inverted. But curiously, the peak-to-peak excursion for this orientation also is nearly the same as  $Q_a$ . It implies that in this situation, the shielding effect of the overburden on the  $Q_r$  component is offset by the enhancement due to Slichter effect. The  $I_p$  component is, however, reduced to a great extent and it becomes much smaller than even  $I_a$ . The response components in the absence of the Al-foil have also been shown for the sake of comparison.

It is desirable that between these two extreme values of  $\sigma_b d_b$  for the overburden studied here, some

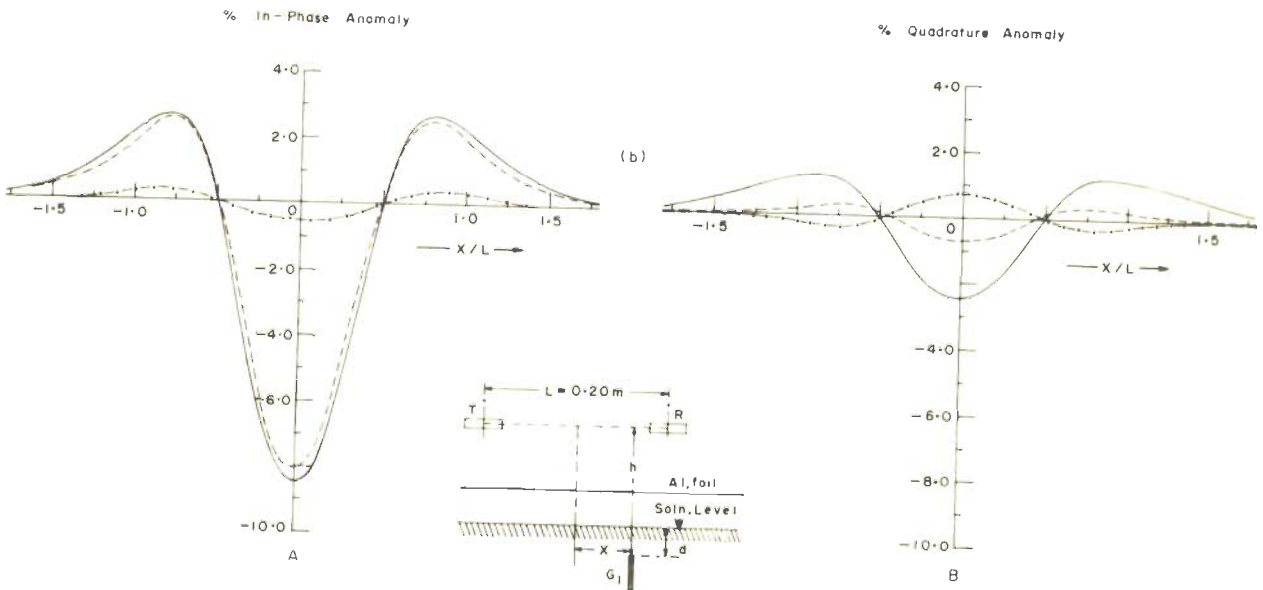
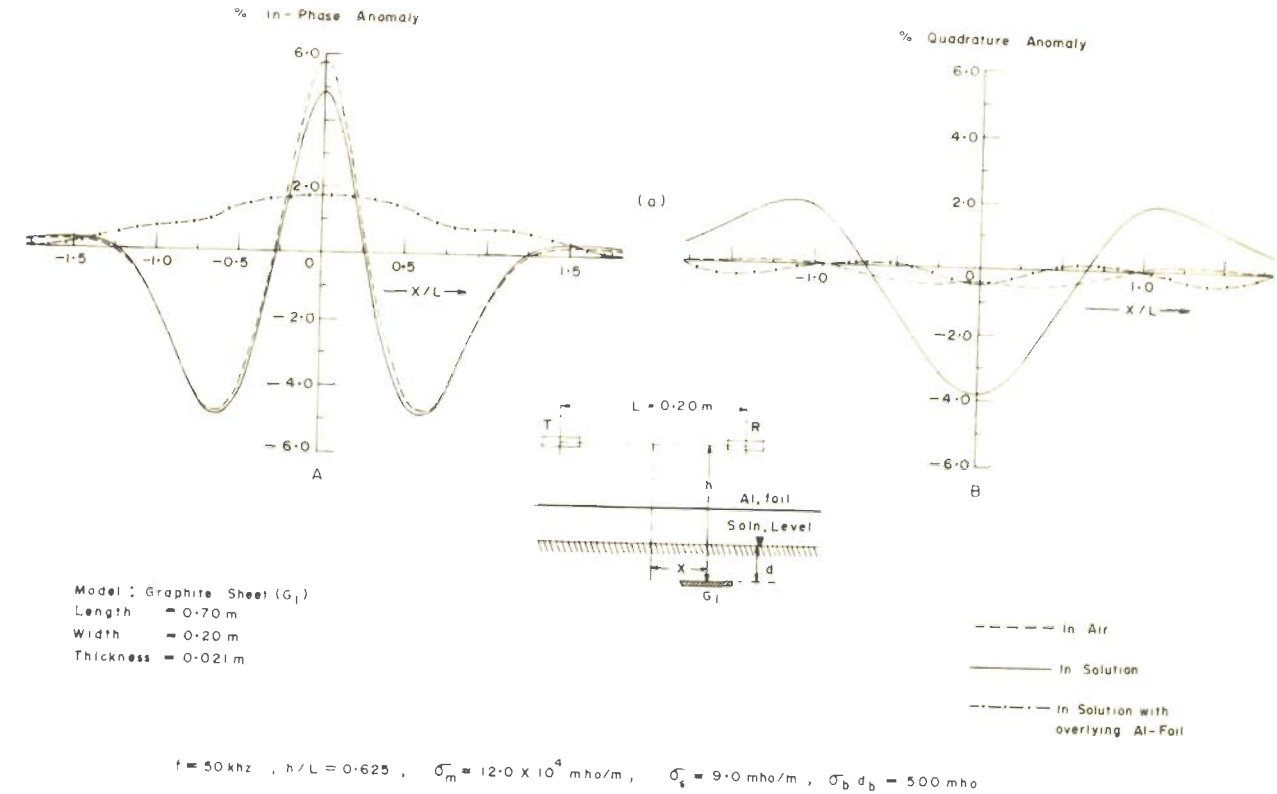


Fig. 5-7 ANOMALY PROFILES OVER A GRAPHITE SHEET HELD IN A CONDUCTING SOLUTION AND OVERLAIN BY AN ALUMINIUM FOIL WHEN SHEET IS (a) HORIZONTAL AND (b) VERTICAL

intermediate values also should be investigated to ascertain the overburden effect in more realistic situations. Further, an important configuration would be the simulation of a conductive contact between the overburden and the target-top (Parasnis, 1973) embedded in a poorly conducting surrounding medium. In such a case, an appreciable Slichter effect is expected to modify the response. The design for this experimental set-up is in progress.

### 5.3 Closely Spaced Ore Bodies

Closely spaced groups of sulphide ore bodies are known to occur commonly in nature. The existence of such group-deposits could be due to

- (i) separate hydrothermal intrusions during the ore genesis and/or
- (ii) tectonic movements and alteration of a single massive deposit to form multiple bodies.

The electromagnetic response of a body in a group depends not only on its own electrical properties, geometry and disposition but also upon those of other bodies in the vicinity. The effect of inductive interaction between the components of a two-body system has, therefore, been investigated employing planar, cylindrical and spherical models. For a pair of sheet models, investigations have been made both for non-conducting as well as conducting intervening and surrounding medium.

### 5.3.1 Two equal sheets

The response of two identical vertical graphite sheets of dimensions 0.70m x 0.20m x 0.021m with parallel strikes has been studied for different values of horizontal distance  $d_s$  between them. Figure 5.8 shows the anomaly profiles for the system at (a)  $h/L = 0.4$  and (b)  $h/L = 0.2$ . The responses of individual sheets are also given for the sake of comparison.

At such low heights of the prospecting system as  $h/L = 0.2$ , slight resolution of the sheets is noticeable from the Qr profile when  $d_s = 0.6L$ . The Ip profile has a pronounced depression in the middle which may possibly help to differentiate a two-body system from a single horizontal sheet. The peak-to-peak excursion also is greater than that for a single vertical sheet. At  $h/L = 0.4$ , both the Ip and Qr profiles have flat single peaks for this separation between the sheets, whose peak-to-peak excursion is of the same order as that for a single sheet. The spread of the peak, however, is much more than for a single sheet. As the separation between the sheets is increased ( $d_s = 0.7L$ ), the resolution is noticeable upto a height  $h/L = 0.5$  (figure 5.9). For still greater values of  $h/L$  only a single peak is obtained.

The behavior of the response of the composite



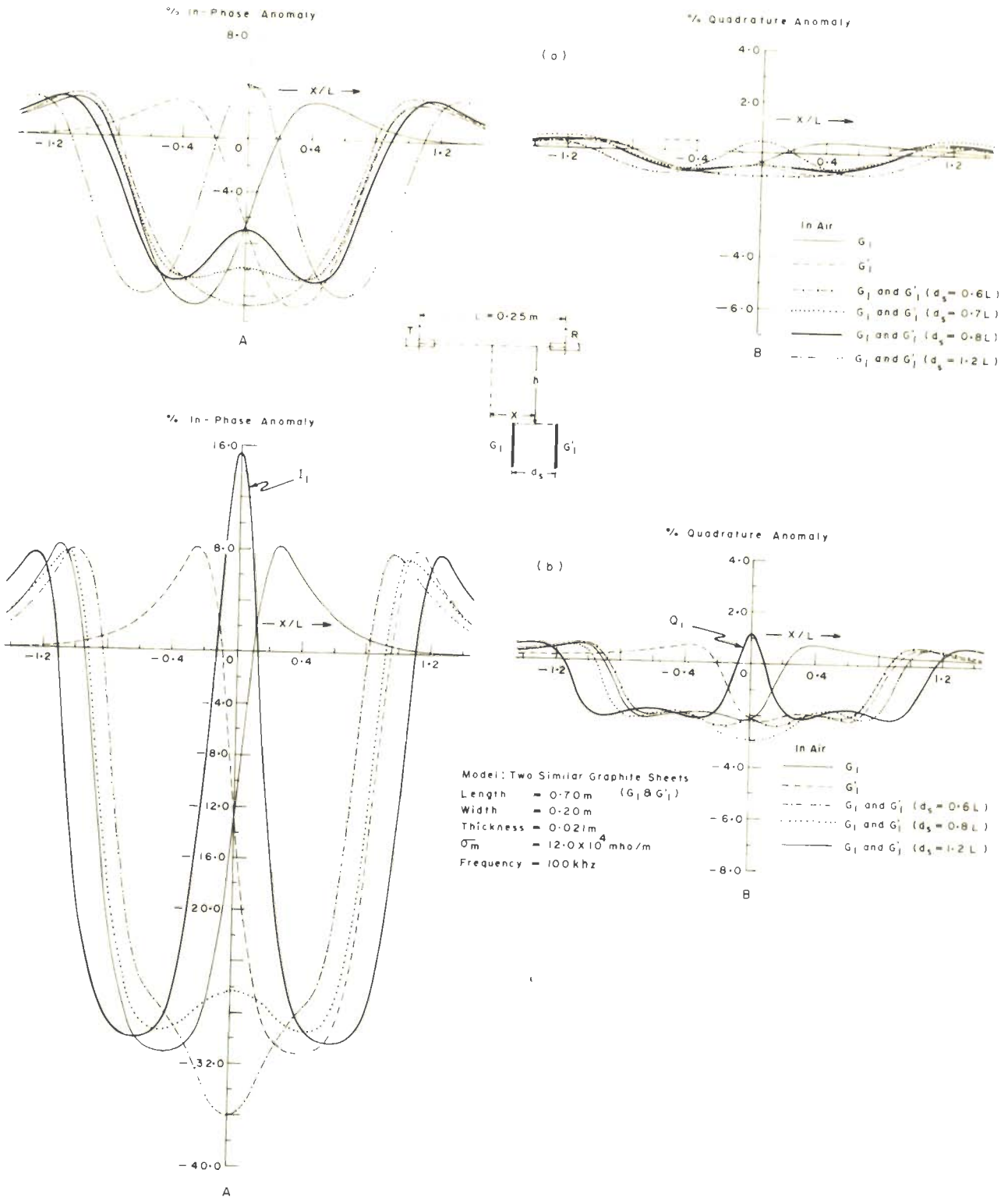


Fig.5-8 ANOMALY PROFILES OVER TWO EQUAL AND PARALLEL GRAPHITE SHEETS WITH VARIATION OF THE HORIZONTAL SEPARATION ( $d_s$ ) BETWEEN THEM AT (a)  $h/L = 0.4$  AND (b)  $h/L = 0.2$

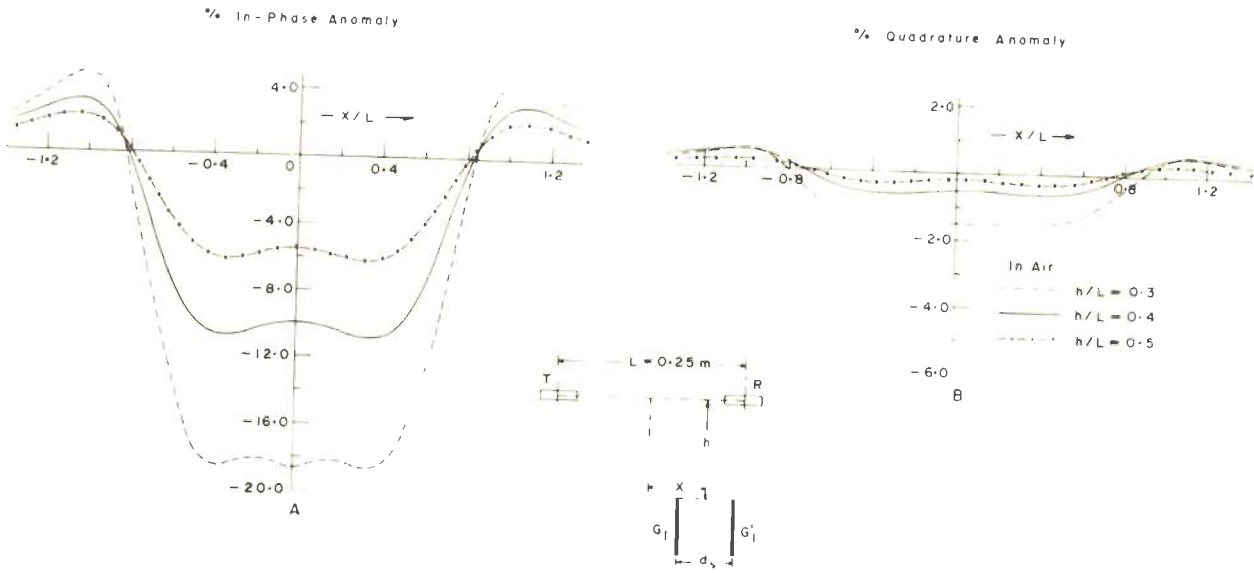


Fig.5-9 ANOMALY PROFILES OVER TWO EQUAL AND PARALLEL GRAPHITE SHEETS WITH VARIATION OF  $h/L$

Model: Two Similar Graphite Sheets ( $G_1 \& G_1'$ )  
 Length = 0.70 m  
 Width = 0.20 m  
 Thickness = 0.021 m  
 $\sigma_m = 12.0 \times 10^4$  mho/m  
 Frequency = 100 kHz  
 $d_s = 0.7L$   
 $\theta = 90^\circ$

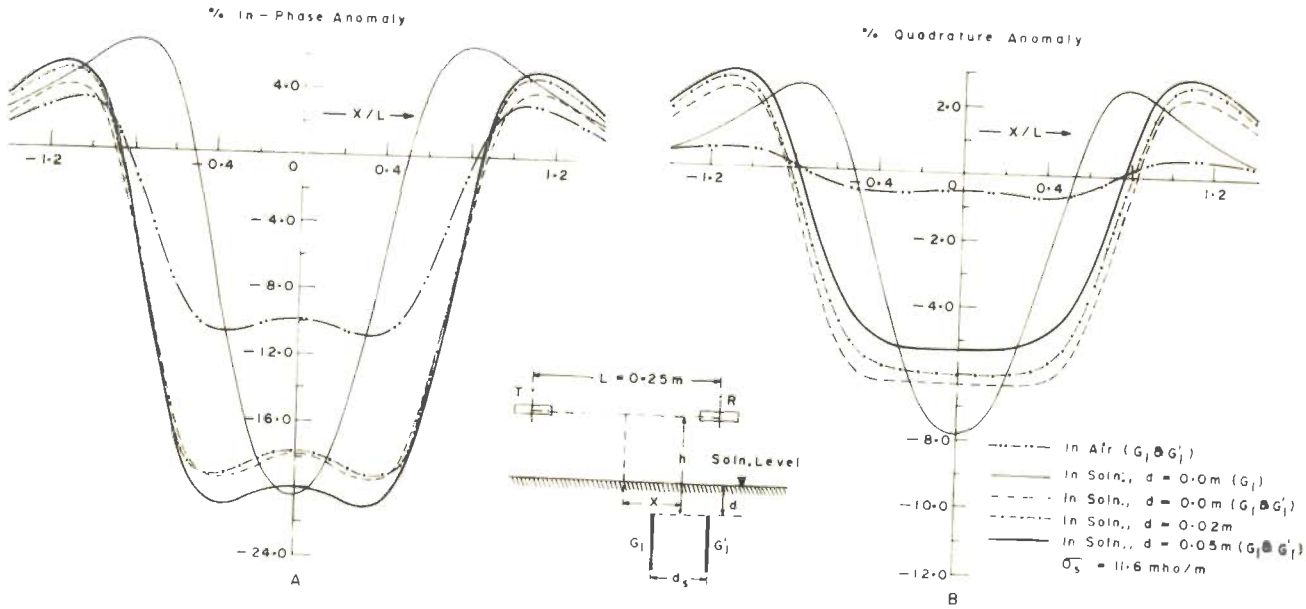


Fig 5-10a ANOMALY PROFILES OVER TWO EQUAL AND PARALLEL GRAPHITE SHEETS WITH VARIATION OF DEPTH OF BURIAL ( $h/L=0.4$ )

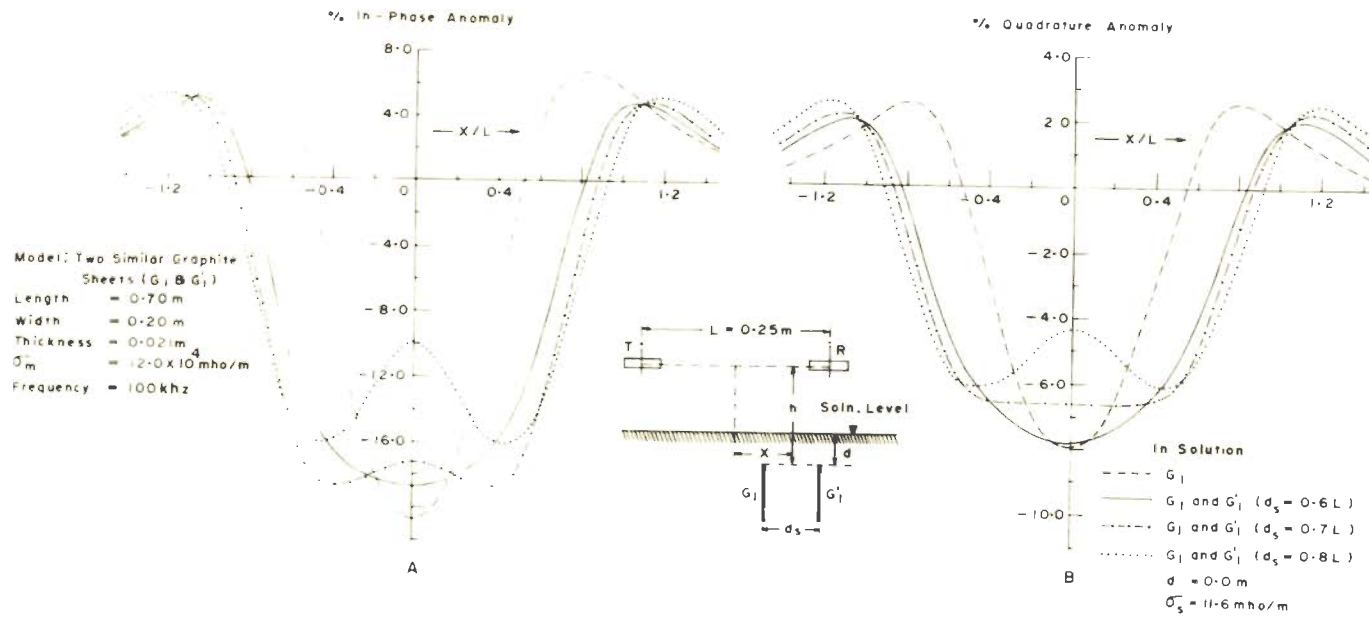


Fig. 5-10b ANOMALY PROFILES OVER TWO EQUAL AND PARALLEL GRAPHITE SHEETS WITH VARIATION OF THE HORIZONTAL SEPARATION ( $d_s$ ) BETWEEN THEM AT  $h/L = 0.4$

system is obtainable through a superposition of anomalies due to individual sheets until they are very close to produce an appreciable inductive interaction between them. The inductive interaction and hence the spatial relationship between the anomaly vectors of the individual sheets would depend upon the relative positioning of the transmitting and receiving coils and the sheets themselves. When the sheets are so close that there is very slight resolution, the superposition of individual profiles shows that the peak-to-peak excursion of the combined anomaly may even be smaller than the individual ones (as observed, for example, when  $d_s = 0.8L$  and  $h/L = 0.4$  in the case of the above sheets). This may be inferred as a destructive interaction between the two bodies.

In the present case as the separation between the sheets exceeds  $d_s = 0.6L$ , the resolution as well as the values of both the peaks increase, though they may still remain smaller than the individual responses, and the central positive going peak also increases. The latter even crosses the zero line and becomes greater than the extreme positive peaks as shown by the curves  $I_1$  and  $Q_1$  in figure 5.8 (a). Thus, it is predominantly a geometrical effect which determines the response characteristics of the two-body system as the distance between them is varied until the inductive interaction is not pronounced.

The vicinity of another conductor near a target even when there is little inductive interaction between them would, thus, introduce an additional ambiguity in the interpretation of e.m. survey data. The error in the interpretation might be significant even for such separations as make the individual anomalies appear resolved and it would probably further accentuate when the resolution ceases. As seen above, in the latter situation a single peak in the anomaly profile may be observed at a place below which there might not be any conductor. This may naturally mislead the borehole locations.

When the sheets are immersed in a salt solution ( $\sigma_s = 11.6$  mho/m), keeping other parameters constant, the peak-to-peak excursions for both the Ip and Qr profiles of the double sheet system, for  $d_s = 0.6L$ , are found to be nearly the same as those for a single sheet (figure 5.10a). Also, as in the case of  $\sigma_s = 0$ , no resolution is found to occur at this separation and it appears only for  $d_s \geq 0.7L$  (figure 5.10b). As the depth of burial of the sheets is increased the resolution between the sheets is found to decrease only slightly (figure 5.10a).

### 5.3.2 Unequal sheets

Observations were also made over two unequal graphite sheets (0.56m x 0.15m x 0.013m and 0.56m x 0.10m x 0.013m) to represent an arbitrary geological situation.

The width of one of the sheets is one and a half times that of the other. As before, the response measurements were made for different values of horizontal separation between them ( $1.6L \geq d_s \geq 0.2L$ ). Two transverse dispositions were considered viz (i) the top edges were in the same horizontal plane and (ii) the lower edges were in the same horizontal plane. Figures 5.11 and 5.12 show the corresponding anomaly profiles.

For both the transverse configurations, and a horizontal separation of  $1.6L$  between them, the sheets are well resolved and the outer peaks are nearly equal to those produced by the individual sheets. The central positive peak, however, is much greater than the positive peak of the either. Thus, the maximum excursion between the central positive and the adjoining negative peaks is comparatively greater than that between the latter and the end peaks (figures 5.11 and 5.12). The two sheets are, thus, favourably disposed and may be detected more easily than if they were situated away from each other with no inductive interaction between them. As the horizontal distance between them is reduced, all the peaks diminish. Though the two sheets continue to be resolved, yet they are comparatively less detectable due to the reduction of the peak amplitudes. The central peak becomes smaller than the end peaks as  $d_s$  is reduced to  $L$ . At  $d_s = 0.6L$  no resolution is noticeable between the two sheets, a

phenomenon similar to that in the case of equal sheets. At this separation the sheet-pair behaves like a single inclined sheet causing an apparent masking of one sheet by the other. If the sheets are situated even nearer, say  $d_s = 0.2L$ , the peak-to-peak value further increases and the form of the anomaly profile is similar to that for  $d_s = 0.6L$ . The peak obtained for the composite system at  $d_s = 0.2L$  is greater than the single peaks of anomalies of the individual sheets.

It, thus, appears that the most favourable disposition of such twin unequal bodies, corresponds to a distance between them such that there is a constructive inductive interaction between them thereby enhancing the central peak and still retaining the resolution. In the field this has to be attained by varying  $L$  and  $h$ .

### 5.3.3 Models of other shapes

The response of two closely placed cylinders of equal lengths (0.80m) and diameters (0.053m) with their axes perpendicular to the profile traverse has also been investigated. Figure 5.13 shows anomaly profiles at (a)  $h/L = 0.3$  and (b)  $h/L = 0.4$ , respectively, for  $d_s$  lying between  $0.6L$  and  $1.0L$ . In this case also the resultant profiles may be approximated by the superposition of the individual profiles (cf. Section 5.3.1). At  $h/L = 0.6$ , the cylinders are clearly

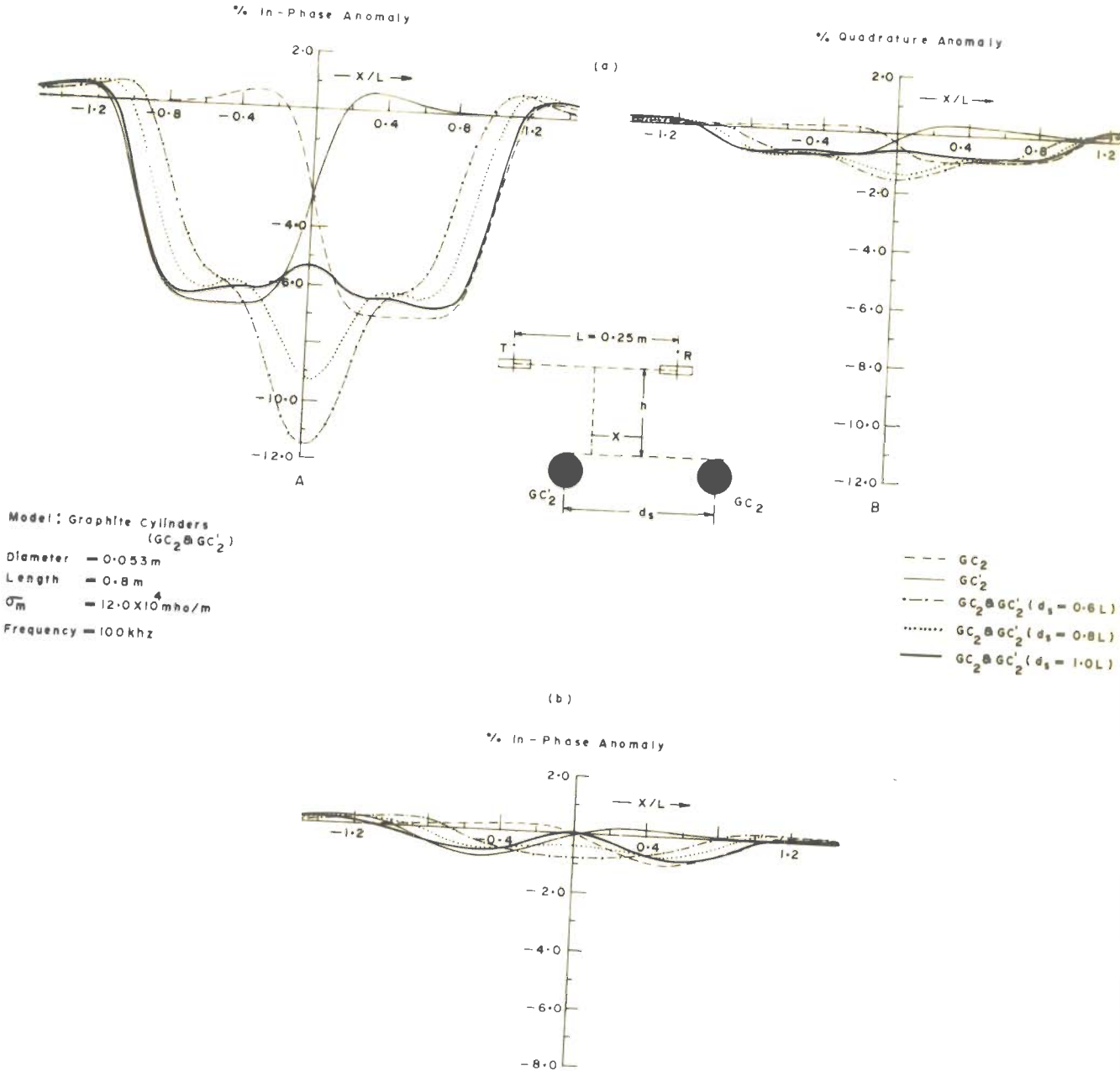


Fig. 5-13 ANOMALY PROFILES OVER TWO EQUAL AND PARALLEL GRAPHITE CYLINDERS WITH VARIATION OF THE HORIZONTAL SEPARATION ( $d_s$ ) BETWEEN THEM AT (a)  $h/L = 0.3$  AND (b)  $h/L = 0.6$



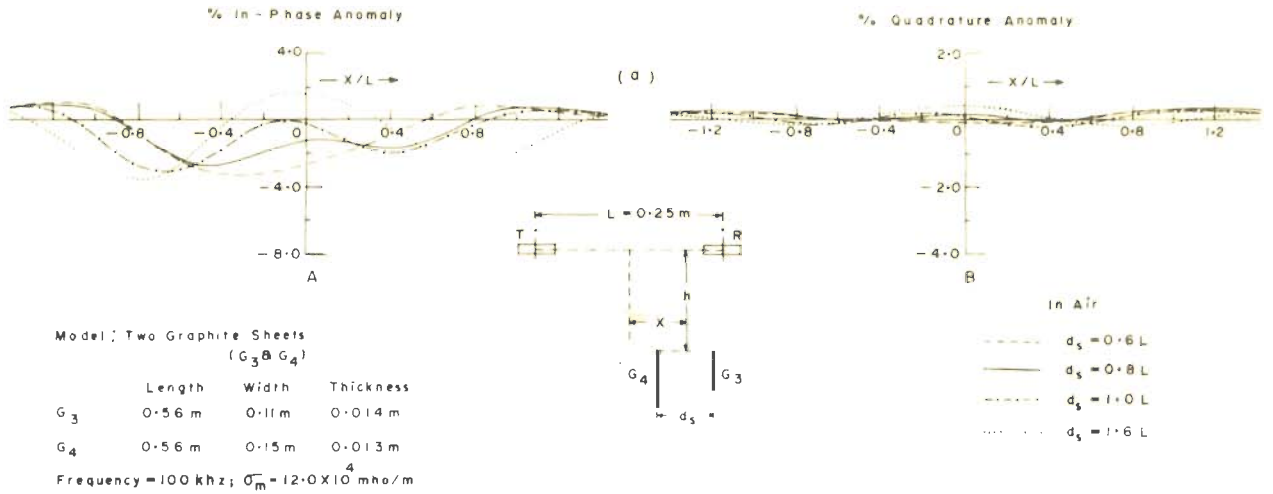


Fig. 5-11 ANOMALY PROFILES OVER TWO UNEQUAL AND PARALLEL GRAPHITE SHEETS WITH VARIATION OF  $d_s$  (WHEN THE TOP SURFACES ARE IN SAME LEVEL) AT (a)  $h/L = 0.6$  AND (b)  $h/L = 0.4$

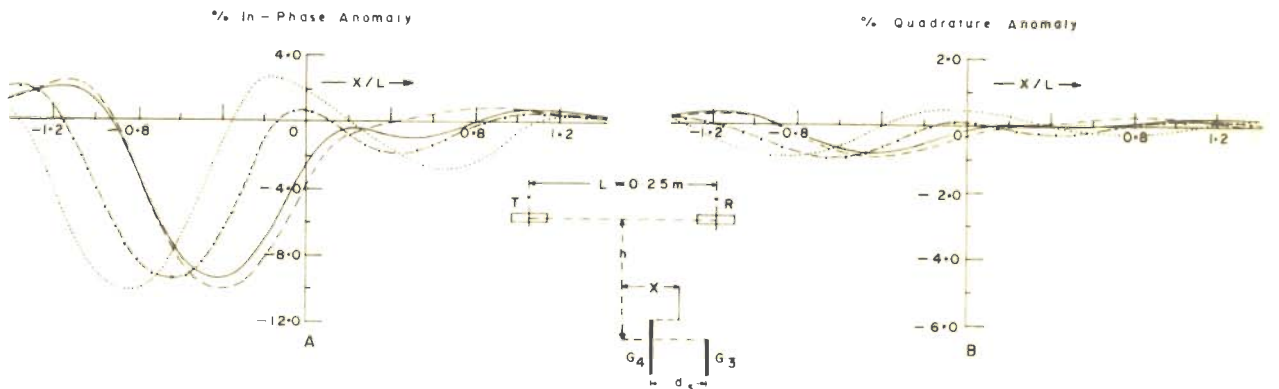


Fig. 5-12 ANOMALY PROFILES OVER TWO UNEQUAL AND PARALLEL GRAPHITE SHEETS WITH VARIATION OF  $d_s$  (WHEN THE LOWER SURFACES ARE IN SAME LEVEL) AT  $h/L = 0.6$

resolved, as seen from the  $I_p$  profile, for  $d_s = L$  (the  $Q_r$  component at this height being negligibly small), the resolution is reduced for  $d_s = 0.8L$ , and for  $d_s = 0.6L$  the cylinders are not resolved at all. Of course, a depression in the middle of the profile (cf. figure 5.8) may indicate the presence of two bodies at low heights ( $h/L = 0.3$ ). Since  $d_s$  is the distance between vertical sections through the axes of the cylinders, the minimum lateral distance between them is still less because of the large diameters of the cylinders. Thus, the resolution in this case can be expected only for larger separations than that for thin sheet like bodies.

Two aluminium spheres of diameters 0.12m and 0.10m were also studied. In case when the line joining their centres is parallel to the profile they are not resolved even at  $d_s = 0.8L$  ( $h/L = 0.3$  or  $0.4$ ) (figure 5.14) in the sense that there is no central positive hump noticeable. However, the assymetry in the anomaly profiles due to difference in the sphere sizes indicates the presence of two bodies. For  $d_s = 0.6L$ , the response of the twin spheres has the appearance of that due to a single body and in this case the single negative peak is less than that obtained by superposing the two. A clear resolution is seen for  $d_s = L$  and as for other models the peak-to-peak values are smaller than the corresponding values for the individual spheres.

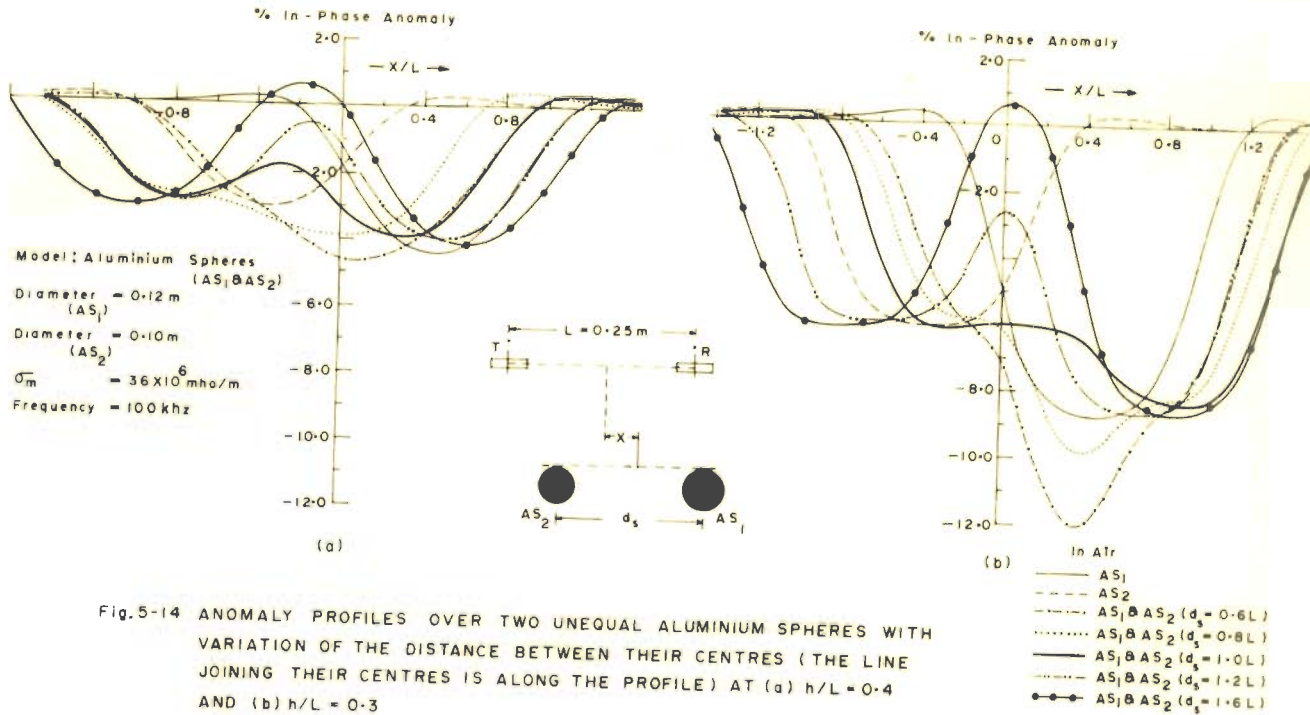


Fig.5-14 ANOMALY PROFILES OVER TWO UNEQUAL ALUMINIUM SPHERES WITH VARIATION OF THE DISTANCE BETWEEN THEIR CENTRES (THE LINE JOINING THEIR CENTRES IS ALONG THE PROFILE) AT (a)  $h/L = 0.4$  AND (b)  $h/L = 0.3$

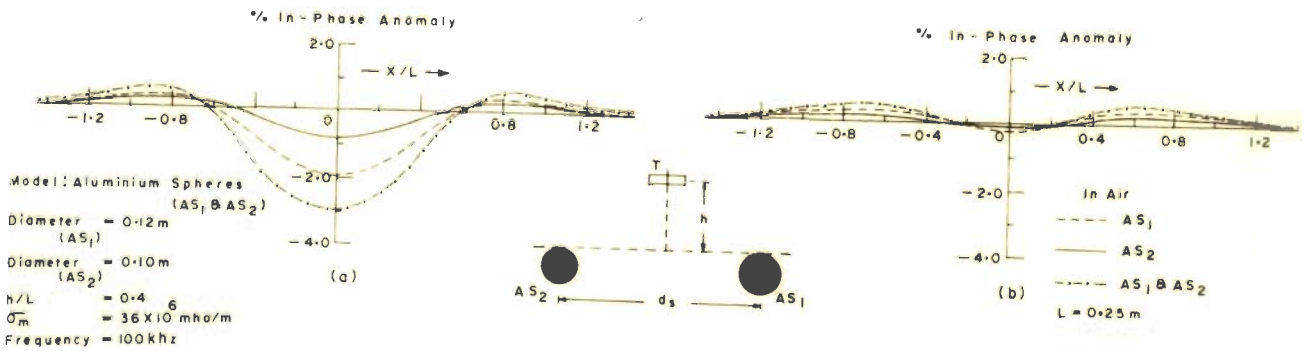


Fig. 5 - 15 ANOMALY PROFILES OVER TWO UNEQUAL ALUMINIUM SPHERES (THE LINE JOINING THEIR CENTRES IS ORTHOGONAL TO THE PROFILE) FOR (a)  $d_s = 0.6L$  AND (b)  $d_s = 1.0L$

An interesting observation has been made in the case when the horizontal line joining the centres of the sphere is perpendicular to the profile direction. Here we find that the sum of the individual responses of the two spheres is exactly the same as the combined response of the two (figure 5.15).

The above observations on twin conductors will be further complicated if the number of bodies in a group is more than two. Evolution of a different approach for the interpretation of data in such cases appears to be imperative.

## CHAPTER VI

### CONCLUSIONS AND PLANS FOR FURTHER STUDY

#### 6.1 Main Results and Inferences

The aforementioned theoretical analyses and the experimental observations shed light on some of the inherent difficulties in arriving at an unambiguous interpretation of the induction prospecting data. These are quite serious when an ore-body is found to be associated with a disseminated mineralised halo, a partially conducting hostrock, and/or an overburden. In such cases the electromagnetic response of a target is markedly modified if there is a conductive contact between the target and its surrounding medium. But if the two are insulated from each other, the modification of the response is not appreciable unless the conductivity of the surrounding medium and/or overburden happens to be quite high. Apart from conducting surrounding medium, the neighbouring conducting bodies, if present, also affect the e.m. response of a target. The nature and magnitude of their interaction depends upon electrical parameters and relative disposition of these closely spaced bodies. The salient findings of the present work are summarised below.

### 6.1.1 Analytical studies

Since the response of a conducting system is an effect of the currents induced in it, the latter may be regarded as a more basic physical entity. A detailed analysis of the induced currents in a spherical model covered by a concentric shell is found to provide valuable physical insight and information about the nature of the influence of a conducting cover. The spatial variation of the current density inside the sphere as well as in the shell has been studied for representative combinations of the conductivities of the covering shell and the sphere, thickness of the shell, and a number of frequencies within which the quasi-static limit holds.

The influence of a conducting cover comprises:

- (i) the skin-effect which reduces the amplitude of the current density inside the sphere for any induction number of the shell and
- (ii) the rotation of the current density vector towards the in-phase axis as the induction number of the shell increases.

An apparent increase of the in-phase component of the induced currents in the core is caused by the cover due to the second factor. The interaction between the shell and sphere is not limited only to the reduction of

the current density in the latter with increase in the induction number of the former but the reverse may also hold. Thus, a reduction in the amplitude of the current density within the shell is observed with increasing conductivity of the core. The redistribution of the induced currents between the constituents of a composite system when the induction number of the either changes, obviously introduces an ambiguity in the interpretation.

The multi-frequency analysis of the induced currents exhibits the existence of a frequency-band of the energising field for which the current density inside the sphere attains maxima. This frequency band is characterised mainly by the electrical parameters of the sphere. Another frequency band exists for the current maxima within the shell also. This phenomenon, similar to a resonance effect, may give a clue for the suitability and hence the desirability of a particular frequency band for which the target may produce a maximum response.

The effect of inhomogeneity in the core conductivity has also been analysed. At low frequencies the reduction of the induced currents due to skin effect is found to be compensated by a linear increase of conductivity from the surface towards the interior of the sphere.

A resonance-like phenomenon is observed in the scattered field (by a similar spherical model) also. Thus, two distinct peaks characterising the two layers of model are noticeable from a plot of the quadrature component versus the frequency of energisation. The first peak at a lower frequency is due to the inner core implying an almost transparency of the shell, while the second peak is due to the shell. The layering is reflected in the in-phase component also, in the form of an inflexion when the less conducting shell starts showing up with the increase in the frequency of energisation. The value of the in-phase and quadrature components of the total response at higher frequencies will, thus, be mainly dependent on the shell parameters.

The variation of the total response of the system with increase in the induction number ( $\alpha_1$ ) of the sphere has also been studied for different values of the shell induction number ( $\alpha_2$ ). For small values of  $\alpha_2$ , the in-phase component of the response increases with increase in  $\alpha_1$  and settles as usual to a saturation level. The trend, however, becomes quite different for greater values of  $\alpha_2$  and a reduction is found to occur in the in-phase component as  $\alpha_1$  increases. This gives rise to an apparent paradox that the in-phase component of a given conducting system is greater than that of another having the same dimensions but containing a core of higher conductivity.



From the profiles of  $H_Z$ ,  $H_Z^{r_1}$  and  $H_Z - H_Z^{r_2}$ , as defined in Section 2.4, it is found that for certain combinations of the sphere and shell parameters,  $H_Z$  may be smaller than  $H_Z^{r_2}$ . This phenomenon is similar to that described in the previous paragraph. The profile of  $H_Z - H_Z^{r_2}$  has, thus, an opposite sign (hence an inverted appearance) relative to that of  $H_Z$  or  $H_Z^{r_1}$ . If the frequency is further increased, the sign is again reversed.

A greater response (particularly the in-phase component) of a less conducting body as compared to that of a composite system having a core of higher conductivity is attributable to the relative magnitudes and phases of the induced currents in the core and the shell on which depends the values of  $H_Z - H_Z^{r_2}$ . Thus, the reduction of the in-phase component of the response with increase in the conductivity of the core may be explained on the phenomenological reasoning that contribution due to the shell for these conditions is greater than and out of phase with that due to the core.

Though the spherical model studied theoretically has an idealised geometry, yet similar features of the response variation are observed during experimental investigations over bodies of other shapes as well, including those having planar boundaries.

The formulation and derivation of analytical expression for the response of an ideally conducting horizontal half-plane, embedded in a partially conducting half-space underneath an overburden, has been made using the Wiener-Hopf technique. The method of experimental simulation, however, provides a much more potential contrivance to study such a model or even other complicated ones simulating more realistic geological situations.

#### 6.1.2 Scale-model experiments

Investigations on models of different geometries and conductivities having a conductive and/or an inductive interaction with the surrounding medium of finite conductivity have also been carried out. In the case of the former, an important feature is the deformation and redistribution of the current lines at the conductivity-discontinuity between the target and the surrounding medium. The target of higher conductivity draws additional currents from the less conducting surrounding medium causing an enhancement of the target response as measured through a T001 L100 R001 prospecting system. The enhancement, which has been termed as Slichter effect, is quite significant in the case of elongated bodies but is relatively inappreciable for such models as have spherical shape and smaller extent orthogonal to the profile. The study has been extended to situations when the surrounding medium and/or overburden are not in conductive

contact with the target. The response-enhancement in this case is no more noticeable and there is, in general, an inductive shielding of the target by the surrounding medium.

Thus, a dependence of the nature of variation of the anomaly on the type of contact with the surrounding medium, conductivity and thickness of the overburden, and also on the shape of the target adds to the complications in the interpretation of the induction prospecting data.

The inductive interaction between closely spaced ore-bodies, which are known to occur commonly, have also been investigated. It is found that when the bodies are separated by distances at which their individual anomalies are resolved, the combined anomaly profile may be obtained, to a fair degree of correctness, by a simple geometrical superposition of the individual profiles. However, if the distances between the adjacent bodies is so small as to cause an appreciable inductive coupling between them, a single peak is observed. In these circumstances, sometimes the collective response is found to be even less than the response of the either. For still closer distances between the bodies, a pronounced depression in the negative peak is noticed. The anomaly profiles over two close vertical unequal sheets appears like that due to a single inclined body. In such

situations the job of a prospecting geophysicist to recommend the drill-holes becomes very difficult.

The present analysis, thus, identifies some of the significant factors which should be taken into account while interpreting the induction prospecting data.

## 6.2 Limitations and Extensions of the Present Study

Notwithstanding detailed investigations over a large number of model set-ups, whose results are presented here, significant gaps remain to be filled before an exhaustive ready-to-use set of rules could be evolved for the interpretation of the induction prospecting data in conducting terrains. Some of the programs which could not be completed because of practical difficulties are being planned now to make a further advance in this direction. These include:

- (i) Preparation of anomaly index diagrams for different values of  $\sigma_s$  (corresponding to those existing for  $\sigma_s = 0$ ) and depths of burial of the target using sheets of graphite, stainless steel etc. simulating some more representative geologic situations
- (ii) Measurement of the deformation of the field or current lines in a conducting medium

caused by the introduction of a higher conducting target for different depths of burial

- (iii) Study of the influence of a conductive contact between the top of the target and overburden choosing larger conductivities and greater thicknesses of the latter for smaller values of  $\frac{h-d}{L}$  than heretofore tried in order to have a greater pertinence with the ground prospecting
- (iv) Study of the effect of a conducting surrounding medium over discs of various diameters and thicknesses in contrast to spherical models of the same diameters
- (v) Study of the effect of overburden having a fluctuating thickness
- (vi) Simulation of induction logging systems
- (vii) Non-linear modeling employing permeable targets
- (viii) Analog modeling using computers with a view to develop some direct interpretation techniques

(ix) Model studies using transients.

Work on some of the above problems is already  
in progress.

## REFERENCES

- Ament, W.S., 1954, Application of a Wiener-Hopf technique to certain diffraction problems: NRL Rep. No.4334, p.23.
- Ashour, A.A., 1950, Induction of electric currents in a uniform circular disk: Quart. Jour. Mech. Appl. Math., v.3, p.119-128.
- Ashour, A.A., 1965, Electromagnetic induction in finite thin sheets: Quart. Jour. Mech. Appl. Math., v.18, Pt.1, p.73-86.
- Barakat, R., 1963, Diffraction of plane waves by an elliptic cylinder: Jour. Acoust. Soc. Am., v.35, p.1990-1996.
- Belluigi, A., 1956, Determination of the electrical conductivity of the ground by the known distribution of surface potentials: Gerl. Beitr. Geophys., v.65, p.171-184.
- Bhattacharya, P.K. and Sinha, A.K., 1965, Response of a spherical conductor to an oscillating magnetic dipole and its use in geophysical prospecting: Jour. Sci. Engg. Res., Indian Instt. of Tech., Kharagpur, Pt.1, v.9, p.51-62.
- Bödvarsson, G., 1966, Direct interpretation methods in applied geophysics: Geoexploration, v.4, p.113-138.
- Bosschart, R.A., 1964, Analytical interpretation of fixed source electromagnetic prospecting data: Ph.D. thesis, Univ. of Delft.
- Bosschart, R.A., 1967, Ground Electromagnetic Methods: in Mining and Groundwater Geophysics/1967, Econ. Geol. Report No.26, Geol. Sur. Can., p.67-80.
- Bouwkamp, C.J., 1954, Diffraction theory: Rep. Progr. Phys., v.17, p.35-100.

- Boyd, D. and Roberts, B.C., 1961, Model experiments and survey results from a wing-tip-mounted electromagnetic prospecting systems: *Geophys. Prosp.*, v.9, p.411-420.
- Braekken, H., 1961, Deep ore exploration by electrical methods: *Geophys. Prosp.*, v.9, p.144-162.
- Brekhovskikh, L.M., 1960, *Waves in Layered Media*; New York, Academic Press, p.561.
- Bruckshaw, J. McG., 1936, Experiments on conducting laminae in periodic magnetic fields: *Proc. Phys. Soc. London*, v.48, p.63-74.
- Buckingham, E., 1914, On physically similar systems: Illustrations of the use of dimensional equations: *Phys. Rev.*, v.4, p.345-376.
- Burrows, K., 1957, An investigation into the interpretation of airborne electromagnetic data by means of scale model experiments: M.Sc. thesis, Univ. of Manchester.
- Carlson, J.F. and Heins, A.E., 1947, The reflection of an electromagnetic plane wave by an infinite set of plates, I: *Quart. Appl. Math.*, v.4, p.313-329.
- Chetaev, D.N., 1966, A new method for the solution of problems in the electrodynamics of anisotropic media: *Bull. (Izv.) Acad. Sci., USSR, Phys. Solid Earth*, No.4, p.233-236.
- Chu, T.S. and Karp, S.N., 1964, The field of a dipole above an infinite corrugated plane: *Quart. Appl. Math.*, v.21, p. 257-268.
- Clark, A.R. and Mungal, A.G., 1951, Scale model experiments in electromagnetic methods of geophysical exploration: *Can. Jour. Phys.*, v.29, p.285-293.
- Clemmow, P.C., 1959, Infinite integral transforms in diffraction theory: *IRE Trans. Ant. and Prop.*,



v.AP-7, p.S7-S11.

- Clemmow, P.C. and Weston, V.H., 1961, Diffraction of a plane wave by an almost circular cylinder: Proc. Roy. Soc., A, v.264, p.246-268.
- Coggon, J.H., 1971, Electromagnetic and electrical modeling by the finite element method: Geophysics, v.36, p.132-155.
- Consbruch, C.V., 1963, Elektromagnetische induktion im Zylinder raemlich - variabler Leitfaehigkeit: Ph.D. thesis, Ludwig - Maximilians - Universitaet, Munich.
- Davydov, V.M., 1969, Build-up of an electromagnetic field in the presence of an anisotropic layer: Bull. (Izv.) Acad. Sci., USSR, Phys. Solid Earth, No.4, p.238-244.
- Debye, P., 1909, Der Lichtdruck auf kugeln von beliebigem Material: Ann. Phys., v.30, p.57.
- Dmitriev, V.I., 1959, The effect of inhomogeneities in the earth on the field of a rectilinear, infinitely long cable: Bull. (Izv.) Acad. Sci., USSR, Geophys. Ser., No.4, p.435-437.
- Dmitriev, V.I., 1960, A solution of a basic problem in the theory of the induction method of electromagnetic surveying: Bull. (Izv.) Acad. Sci., USSR, Geophys. Ser., No.8, p.748-753.
- Dmitriev, V.I., 1969, Approximate boundary conditions at a thin inhomogeneous layer in electrical exploration problems: Bull. (Izv.) Acad. Sci., USSR, Phys. Solid Earth, No.12, p.757-758.
- Dolan, W., 1960, A versatile approach to electromagnetic scale modeling: Paper presented at the S.E.G. Meeting, Galveston, Texas.
- Dosso, H.W., 1966a, A plane-wave analogue model for studying electromagnetic variations: Can. Jour.

- Phys., v.44, p.67-80.
- Dosso, H.W., 1966b, A multilayer conducting earth in the field of plane waves: *Can. Jour. Phys.*, v.44, p. 81-89.
- Dosso, H.W., 1966c, Analogue model measurements for electromagnetic variations near vertical faults and dykes: *Can. Jour. Phys.*, v.3, p.287-303.
- Douloff, A.A., 1960, The response of a conducting disc in a dipolar magnetic field: M.A. thesis, University of Toronto.
- Douloff, A.A., 1961, The response of a disc in a dipole field: *Geophysics*, v.26, p.452-464.
- Dýakonov, B.P., 1957, A cylinder in the field of a point source of electric current: *Bull. (Izv.) Acad. Sci. USSR, Geophys. Ser.*, No.1, p.135-140.
- Dýakonov, B.P., 1959, The diffraction of electromagnetic waves by a circular cylinder in a homogeneous half-space: *Bull. (Izv.) Acad. Sci., USSR, Geophys. Ser.*, No.9, p.950-955.
- Erdélyi, A., Magnus, W., Oberhettinger, F., and Tricomi, F.G., 1954, *Tables of integral transforms*: New York, McGraw-Hill, v.1, p.391.
- Faldus, K., Peter, V., Praus, O., and Tobyasova, M., 1963, A study on the electromagnetic field of a magnetic vertical dipole on the model of homogeneous half-space with a spherical cavity: *Stud. Geophys. Geodet.*, v.7, p.372-395.
- Faraday, M., 1832, *Experimental researches in electricity*-Second series: *Phil. Trans. Roy. Soc.*, v.122, p.163-194.
- Fraser, D.C., 1966, Rotary field electromagnetic prospecting: Ph.D. thesis, Univ. of California, Berkeley.

- Friedlander, F.G., 1951, On the half-plane diffraction problem: *Quart. Jour. Mech. Appl. Math.*, v.4, Pt.3, p.344-357.
- Frischknecht, F.C. and Mangan, G.B., 1960, Preliminary report on electromagnetic model studies: U.S.G.S. Open File Report.
- Fuller, B.D., 1971, Electromagnetic response of a conductive sphere surrounded by a conductive shell: *Geophysics*, v.36, p.9-24.
- Gaur, V.K., 1959, Model experiments simulating conditions encountered in airborne electromagnetic prospecting: Ph.D. thesis, Univ. of London, London.
- Gaur, V.K., 1963, Electromagnetic model experiments simulating an airborne method of prospecting: *Bull. NGRI*, v.1, p.167-174.
- Gaur, V.K., Verma, O.P., and Gupta, C.P., 1972, Enhancement of electromagnetic anomalies by a conducting overburden: *Geophys. Prosp.*, v.20, p.580-604.
- Germey, K., 1964, Die Beugung einer ebenen elektromagnetischen Welle an zwei parallelen unendlich langen idealleitenden Zylindern von elliptischem Querschnitt: *Ann. Physik*, v.13, p.237-251.
- Grant, F.S. and West, G.F., 1965, Interpretation Theory in Applied Geophysics: New York, McGraw-Hill Book Co. Inc., p.584.
- Gupta, C.P., Raval, U. and Negi, J.G., 1973, Induced current distribution in a conductive two-layer spherical body: *Geophysics*, v.38 (In press).
- Gupta Sarma, D. and Maru, V.M., 1971, A study of some effects of a conducting host rock with a new modelling apparatus: *Geophysics*, v.36, p.166-183.
- Hedström, E.H. and Parasnis, D.S., 1958, Some model experiments relating to electromagnetic prospecting with special reference to air-borne work: *Geophys. Prosp.*, v.6, p.322-341.

- Heins, A.E., 1948, The radiation and transmission properties of a pair of semi-infinite parallel plates: Quart. Appl. Math., v.6, p.157-166 and p.215-220.
- Heins, A.E., 1956, The scope and limitations of the method of Wiener and Hopf: Comm. Pure Appl. Math., v.9, p.447-466.
- Heins, A.E. and Wiener, N., 1946, A generalization of the Wiener-Hopf integral equation: Proc. Nat. Acad. Sci., v.32, p.98-101.
- Hill, D.A. and Wait, J.R., 1972, Electromagnetic scattering of a small spherical obstacle near the ground: Can. Jour. Phys., v.50, p.237-243.
- Hohmann, G.W., 1971, Electromagnetic scattering by conductors in the earth near a line source of current: Geophysics, v.36, p.101-131.
- Hood, P. and Ward, S.H., 1969, Low-frequency Airborne Electromagnetic Methods, in Airborne Geophysical Methods: Adv. Geophys., New York, Academic Press, v.13, p.41-79.
- Horiuchi, K., 1957, Electromagnetic fields due to current flowing parallel to interface of two different media: Jour. Phys. Soc. Jap., v.12, p.170-176.
- Jones, D.S., 1953, Diffraction by a thick semi-infinite plate: Proc. Roy. Soc., A, v.217, p.153-175.
- Jones, F.W. and Price, A.T., 1971, Geomagnetic effect of sloping and shelving discontinuities of earth conductivity: Geophysics, v.36, p.58-66.
- Keller, G.V. and Frischknecht, F.C., 1966, Electrical Methods in Geophysical Prospecting: Oxford, Pergamon Press, p.517.
- Kertz, W., 1960, Leitungs fähiger Zylinder im transversalen magnetischen Wechselfeld: Gerl. Beitr. Geophys., v.69, p.4-28.

- Koefoed, O. and Kegge, G., 1968, The electrical current pattern induced by an oscillating magnetic dipole in a semi-infinite thin plate of infinitesimal resistivity: *Geophys. Prosp.*, v.16, p.144-158.
- Koiter, W.T., 1954, Approximate solution of Wiener-Hopf type integral equations with applications: *Proc. Koninkl. Nederl. Akad. Van Wetenschappen, Ser. B*, v.57, p.558-579.
- Lahiri, B.N. and Price, A.T., 1939, Electromagnetic induction in non-uniform conductors and the determination of the conductivity of the earth from the terrestrial magnetic variations: *Phil. Trans. Roy. Soc., Ser. A*, v.237, p.509-540.
- Lamb (Jr.), G.L., 1959, Diffraction of a plane sound wave by a semi-infinite thin elastic plate: *Jour. Acous. Soc. Am.*, v.31, p.929-935.
- Lamontagne, Y., 1970, Model studies of the turam electromagnetic method: M.A. Sc. thesis, Univ. of Toronto.
- Lamontagne, Y. and West, G.F., 1971, EM response of a rectangular thin plate: *Geophysics*, v.36, p.1204-1222.
- Latter, R., 1958, Approximate solutions for a class of integral equations: *Quart. Appl. Math.*, v.16, p.21-31.
- Levine, H. and Schwinger, J.S., 1948, On the radiation of sound from an unflanged circular pipe: *Phys. Rev.*, v.73, p.383-406.
- Lowrie, W. and West, G.F., 1965, The effect of conducting overburden on electromagnetic prospecting measurements: *Geophysics*, v.30, p.624-632.
- March, H.W., 1953, The field of a magnetic dipole in the presence of a conducting sphere: *Geophysics*, v.18, p.671-684.

- Martin, L., 1960, Field outside a conducting strip in the presence of a magnetic dipole: M.A. thesis, Univ. of Toronto.
- Meyer, J., 1963, Elektromagnetische induktion in einem leitenden homogenen Zylinder durch aussere magnetische und elektrische wechselfelder miteilungen aus dem: Mitl. Max-plank Instt., Aeronomie, v.13, p.1-67.
- Mihram, G.A., 1972, The modeling process: IEEE Trans. on Systems, Man, Cybernetics, v.SMC-2, p.621-629.
- Molotschnow, G. and Janovsky, B., 1959, Model experiments with low frequency electromagnetic field: Freiburger Forschungsh., v.60, p.17-29.
- Nair, M.R., Biswas, S.K. and Mazumdar, K., 1968, Experimental studies on the electromagnetic response of tilted conducting half-planes to a horizontal-loop prospecting system: Geoexploration, v.6, p.207-244.
- Negi, J.G., 1962a, Studies on the electromagnetic field response of some geological inhomogeneities: Ph.D. thesis, Indian Instt. of Tech., Kharagpur.
- Negi, J.G., 1962b, Inhomogeneous cylindrical ore body in presence of a time varying magnetic field: Geophysics, v.27, p.386-392.
- Negi, J.G., 1962c, Diffraction of electromagnetic waves by an inhomogeneous sphere: Geophysics, v.27, p.480-492.
- Negi, J.G., 1967, Electromagnetic screening due to a disseminated spherical zone over a conducting sphere: Geophysics, v.32, p.69-87.
- Negi, J.G. and Gupta, C.P., 1968, Models in applied Geoelectromagnetics: Earth-Sci. Rev., v.4, p.219-241.
- Negi, J.G. and Raval, U., 1969, Negative electromagnetic

- screening by a cylindrical conducting cover:  
Geophysics, v.34, p.944-957.
- Negi, J.G., Gupta, C.P., and Raval, U., 1972a, Induction anomaly due to an elongated covered ore-zone excited by a long current carrying cable: Geoph. Prosp., v.20, p.193-211.
- Negi, J.G., Gupta, C.P., and Raval, U., 1972b, Turam response of a permeable inhomogeneous cylindrical conductor surrounded by a thin shell: Pure Appl. Geophys., v.97, p.137-145.
- Negi, J.G., Gupta, C.P., and Raval, U., 1973, Electromagnetic response of a permeable inhomogeneous conducting sphere: Geoexploration, v.11, p.1-20.
- Negi, J.G. and Saraf, P.D., 1973, Effects of anisotropy on quasi-static fields of a vertical electric dipole buried in a layered anisotropic earth: Radio Sci., v.8, p.155
- Nikitina, V.N., 1956, Anomalies in electromagnetic fields over cylindrical inhomogeneities: Trans: (Trudy) Instt. Geophys. Acad. Sci., USSR, No.32, p.159.
- Nikitina, V.N., 1960, The calculation of a variable electromagnetic field over a sloping vein: Bull. (Izv.) Acad. Sci., USSR, Geophys. Ser., No.3, p.328-334.
- Noble, B., 1958, Methods based on the Wiener-Hopf technique for the solution of partial differential equations: New York, Pergamon Press, p.246.
- Parasnis, D.S., 1966, Electromagnetic prospecting - CW. Techniques: Geoexploration, v.4, p.177-208.
- Parasnis, D.S., 1970a, Mining Geophysics: Amsterdam, Elsevier Publishing Co., p.356.
- Parasnis, D.S., 1970b, An elegant, universal nomenclature for electromagnetic moving source-receiver dipole configurations: Geophys. Prosp., v.18, p.88-102.

- Parasnis, D.S., 1971, Analysis of some multi-frequency, multi-separation electromagnetic surveys: Geophys. Prosp., v.15, p.163-179.
- Parasnis, D.S., 1973, Personal Communication.
- Parry J.R., 1965, A theoretical and experimental investigation of finite thin dykes in a uniform electromagnetic field: M.S. thesis, Univ. of California, Berkeley.
- Parry, J.R., and Ward, S.H., 1971, Electromagnetic scattering from cylinders of arbitrary cross-section in a conductive half-space: Geophysics, v.36, p.67-100.
- Paterson, N.R., 1967, Exploration for Massive Sulphides in the Canadian Shield: Mining and Groundwater Geophysics/1967, p.275-289.
- Poddar, M. and Bhattacharya, P.K., 1966, On the response of conducting plates to an inducing dipolar field (model studies): Geoexploration, v.4, p.93-105.
- Praus, O., 1966, The field of the plane electromagnetic wave at the surface of two layered anisotropic earth: Stud. Geophys. Geodet., v.10, p.460-466.
- Price, A.T., 1949, The induction of electric currents in non-uniform thin sheets and shells: Quart. Jour. Mech. Appl. Math., v.3, p.385-410.
- Pris, G.V., 1965, Electromagnetic field of a horizontal circular loop antenna placed above a conducting half-space: Bull. (Izv.) Acad. Sci., USSR, Phys. Solid Earth. No.4, p.263-267.
- Ranasinghe, V. V.C., 1962, Inductive interaction between nearby conducting bodies in a time varying magnetic field: M.A. thesis, Univ. of Toronto, Toronto.
- Rao, K.N.N., Gupta, C.P., and Raval, U., 1973, Electromagnetic response resolution in time-domain for a



covered spherical conductor: Geophys. Res. Bull.,  
v. , p.

- Rauch, L.M., 1953, Studies in Radar Cross-sections - IX, Willow Run Research Centre: Univ. of Michigan Press.
- Raval, U., 1972, Study of electromagnetic diffraction by some conducting structures with special reference to perturbation in shape, non-uniform conductivity and dissipative surrounding medium: Ph.D. thesis, Jiwaji University, Gwalior.
- Raval, U. and Gupta, C.P., 1971a, Electromagnetic scattering due to deformed inhomogeneous bodies (Part I: Sphere): Pure Appl. Geophys., v.87, p.134-145.
- Raval, U. and Gupta, C.P., 1971b, Electromagnetic scattering due to deformed inhomogeneous bodies (Part II: Cylinder): Pure Appl. Geophys., v.87, p.146-154.
- Rikitake, T., 1961, The effect of ocean on rapid geomagnetic changes: Geophys. Jour.R.A.S., v.5, p.1-15.
- Roy, A., 1970, On the effect of overburden on electromagnetic anomalies - a review: Geophysics, v.34, p.646-659.
- Satpathy, B.N., 1971, Induced currents in a conducting sphere placed in a field of an oscillating magnetic dipole: Pure Appl. Geophys., v.90, p.163-168.
- Schaub, Yu.B., 1963, Estimated capability of a type of inductive prospecting by airplane: Bull. (Izv.) Acad. Sci., USSR, Geophys. Ser., No.7, p.649-652.
- Schaub, Yu.B., 1965, Use of the non-linear conductivity effect in rocks for electrical prospecting: Bull. (Izv.) Acad. Sci., USSR, Phy. Solid Earth, No.6, p.409-412.
- Schultz, E.V., 1950, Scattering by a prolate spheroid: Engg. Res. Instt., Univ. of Michigan, Ann. Arbour.

- Seigel, K.M., Alperin, H.A., Bonkowski, R.R., Crispin, J.W., Maffett, A.L., Schensted, C.E. and Schensted, I.V., 1953, Studies in Radar Cross-Section - VIII: Willow Run Research Centre, Univ. of Michigan Press.
- Senior, T.B.A., 1952, Diffraction by a semi-infinite metallic sheet: Proc. Roy. Soc. A, v.213, p.436-458.
- Sinclair, G., 1948, Theory of models of electromagnetic systems: Proc. I.R.E., v.36, p.1364-1370.
- Slichter, L.B., 1932, The observed and theoretical response of conducting spheres: Am. Instt. Mining Metal. Petro. Engr. Trans., v.97, p.443-459.
- Slichter, L.B., 1951, An electromagnetic interpretation problem in geophysics: Geophysics, v.16, p.431-449.
- Slichter, L.B., 1959, Some aspects, mainly geophysical, of mineral exploration in Natural Resources: New York, McGraw-Hill Book Co. Inc., p.368-412.
- Slichter, L.B. and Knopoff, L., 1959, Field of an alternating magnetic dipole on the surface of a layered earth: Geophysics, v.24, p.77-88.
- Smythe, W.R., 1968, Static and Dynamic Electricity (3rd Ed.): New York, McGraw-Hill Book Co. Inc., p.628.
- Strangway, D.W., 1966a, Electromagnetic scale modeling in Methods and Techniques in Geophysics: New York, Interscience Publishers, v.2, p.1-31.
- Strangway, D.W., 1966b, Electromagnetic parameters of some sulphide ore bodies in Mining Geophysics: Tulsa, Society of Exploration Geophysicists, v.1, p.227-242.
- Stratton, J.A., 1941, Electromagnetic Theory: New York, McGraw-Hill Book Co. Inc., v.2, p.615.
- Svetov, B.S., 1960, Certain results of model investigations according to the inductive method: Bull. (Izv.) Acad. Sci., USSR, Geophys. Ser., No.1, p. 71-78.

- Swift (Jr.), C.M., 1971, Theoretical magnetotelluric and turam response from two-dimensional inhomogeneities: *Geophysics*, v.36, p.38-52.
- Tesche, F.R., 1951, Instrumentation of electromagnetic modelling and applications to electromagnetic prospecting: Ph.D. thesis, Univ. of California, Los Angeles.
- Tikhonov, A.N. and Shakhshvarov, D.N., 1956, Method for calculating electromagnetic fields produced by an alternating current in stratified media: *Bull. (Izv.) Acad. Sci., USSR, Geophys. Ser., No.3.*
- Tikhonov, A.N. and Shakhshvarov, D.N., 1959, The electromagnetic field produced by a dipole at points in distant zones: *Bull. (Izv.) Acad. Sci., USSR, Geophys. Ser., No.7, p.672-677.*
- Tikhonov, A.N. and Shakhshvarov, D.N., 1961, On the non-uniform asymptotic behaviour of dipole-excited electromagnetic fields in layered media: *Bull. (Izv.) Acad. Sci., USSR, Geophys. Ser., No.1, p.65-66.*
- Tikhonov, A.N., Shakhshvarov, D.N. and Rybakova, E.V., 1959, The properties of the electromagnetic field of a dipole activated in a layer lying on an insulation: *Bull. (Izv.) Acad. Sci., USSR, Geophys. Ser., No.11, p.1173-1174.*
- Tornqvist, G., 1958, Some practical results of airborne electromagnetic prospecting in Sweden: *Geophys. Prosp., v.6, p.112-126.*
- Van'yan, L.L., 1963a, The electromagnetic field of a harmonic dipole grounded at the surface of a multi-layered, anisotropic medium: *Bull. (Izv.) Acad. Sci., USSR, Geophys. Ser., No.8, p.740-741.*

- Vanyan, L.L., 1963b, Build-up of an electromagnetic field in an anisotropic layer: Bull. (Izv.) Acad. Sci., USSR, Geophys. Ser., No.10, p.924-928.
- Velikin, A.B. and Bulgakov, J.I., 1967, Transient method of electrical prospecting (one loop version): Intern. Sem. on Geophys. Methods, Moscow.
- Verma, O.P., 1972, Electromagnetic model experiments simulating conditions encountered in geophysical prospecting: Ph.D. thesis, Univ. of Roorkee, Roorkee.
- Vozoff, K., 1971, The effect of overburden on vertical component anomalies in AFMAG and VLF exploration: A computer model study: Geophysics, v.36, p.53-57.
- Wait, J.R., 1951, A conducting sphere in a time varying magnetic field: Geophysics, v.16, p.666-672.
- Wait, J.R., 1952, The cylindrical ore-body in the presence of a cable carrying an oscillating current: Geophysics, v.17, p.378-386.
- Wait, J.R., 1953a, A conducting permeable sphere in the presence of a coil carrying an oscillating current: Can. Jour. Phys., v.31, p.670-678.
- Wait, J.R., 1953b, Induction by a horizontal oscillating magnetic dipole over a conducting homogeneous earth: Trans. Am. Geophys. Un., v.34, p.185-188.
- Wait, J.R., 1959, On the electromagnetic response of an imperfectly conducting thin dyke: Geophysics, v.24, p.167-171.
- Wait, J.R., 1960, Some solutions for electromagnetic problems involving spheroidal, spherical and cylindrical bodies: Jour. Res. Nat. Bur. Stand., v.64B, p.15-32.

- Wait, J.R., 1962, *Electromagnetic Waves in Stratified Media*: Oxford, Pergamon Press, p.372.
- Wait, J.R., 1969, Electromagnetic induction in a solid conducting sphere enclosed by a thin conducting spherical shell: *Geophysics*, v.34, p.753-759.
- Wollaston, C., 1881, Discussion of Adams, 1881 on earth currents: *Jour. Soc. Teleg. Eng. Electr.*, v.10, p.50-56.
- Ward, S.H., 1952, A theoretical and experimental study of the electromagnetic method of geophysical prospecting: Ph.D. thesis, Univ. of Toronto, Toronto.
- Ward, S.H., 1959, Unique determination of conductivity, susceptibility, size, and depth in multifrequency electromagnetic exploration: *Geophysics*, v.24, p.531-546.
- Ward, S.H., 1967, *The Electromagnetic Method*, in *Mining Geophysics*; Tulsa, Society of Exploration Geophysicists, v.2, p.224-372.
- Ward, S.H., 1971, Foreword and introduction: *Geophysics*, v.36, p.1-8.
- Weinstein, L.A., 1969, *The Theory of Diffraction and the Factorization Method*: Boulder, Golem Press.
- West, G.F., 1960, Quantitative interpretation of electromagnetic prospecting measurements: Ph.D. thesis, Univ. of Toronto, Ontario.
- Wesley, J.P., 1958a, Response of dyke to oscillating dipole: *Geophysics*, v.23, p.128-133.
- Wesley, J.P., 1958b, Response of a thin dyke to oscillating dipole: *Geophysics*, v.23, p.134-143.
- Wiener, N. and Hopf, E., 1931, *Über eine Klasse singularer Integralgleichungen*: *Sitz. Berlin Akad. Wiss.*, p.696-706.

- Williams, W.E., 1954, Diffraction by two parallel planes of finite length: Proc. Camb. Phil. Soc., v.50, p.309-318.
- Wu, Tai Te and Wu, Tai Tsun, 1963, Iterative solutions of Wiener-Hopf integral equations: Quart. Appl. Math., v.20, p.341-352.
- Zakharov, V.KH., 1963, Modeling of dipole electromagnetic prospecting: Leningr. Gorn Instt. Zap., v.46, p.105-110.
- Zakharov, V.KH., 1964, The interpretation of anomalies of electromagnetic dipole profiling taken above solids of revolution (spheres, cylinders): Bull. (Izv.) Acad. Sci., USSR, Geophys. Ser., No.4, p.339-342.
- Zakharov, E.V. and Il'in, I.V., 1970, Integral representations of electromagnetic fields in stratified media: Bull. (Izv.) Acad. Sci., USSR, Phys. of Solid Earth, No.8, p.495-499.

## CAPTIONS FOR FIGURES

CHAPTER I	page
Fig. 1-1 Anomaly index diagram for a vertical thin sheet in air (After Strangway, 1966b).	13
Fig. 1-2 A generalised geological situation of occurrence of a mineralised ore body.	20
CHAPTER II	
Fig. 2-1 An inhomogeneous covered sphere in a uniform alternating magnetic field.	27
Fig. 2-2 The (a) amplitude and (b) phase of the normalised induced current density in the sphere and the shell varying with the distance from the centre for different frequencies.	27
Fig. 2-3 The argand diagrams of the normalised current density at different depths for (a) an uncovered sphere and (b) a covered sphere for different frequencies.	39
Fig. 2-4 The in-phase and quadrature components of the normalised current density for different frequencies.	39
Fig. 2-5 The amplitude of the normalised current density in the sphere and the shell versus frequency.	41
Fig. 2-6 The influence of changing the conductivity	41

- of the sphere on the induced current density for  $10^3$  hz. The amplitude as well as the in-phase and quadrature components have been plotted.
- Fig. 2-7 The effect of inhomogeneity in the core conductivity on the (a) amplitude and (b) phase of the current density for  $10^2$  hz. 41
- Fig. 2-8 The effect of inhomogeneity in the conductivity of the sphere on the amplitude of the current density for (a)  $10^3$  hz and (b)  $10^4$  hz. 44
- Fig. 2-9 The argand diagrams of the normalised current density on the surface of the sphere showing effects of varying the conductivity and the thickness of the shell for (a)  $10^3$  hz and (b)  $10^4$  hz. 44
- Fig. 2-10 A covered sphere in a radial dipolar field. 48
- Fig. 2-11 Anomaly index diagram of the response factor  $X_n$  for  $n=1, 2$  and  $3$ . 48
- Fig. 2-12 Anomaly index diagram of the response factor  $X_1$  for different conductivities of the shell over a nonpermeable sphere. 48
- Fig. 2-13 Anomaly index diagrams of the response factor  $X_1$  for different conductivities of the shell over a permeable sphere. 57
- Fig. 2-14 Multifrequency anomaly index diagrams of 57



the response factor  $X_1$  for different (a) thicknesses and (b) conductivities of the shell.

- Fig. 2-15 Profiles of  $H_Z^{r_1}$  and  $H_Z$  over a covered sphere for different frequencies ( $h/L = 0.3$ ;  $\sigma_{O_2} = 1.0$  mho/m). 61
- Fig. 2-16 Profiles of  $H_Z^{r_1}$  and  $H_Z - H_Z^{r_2}$  over a covered sphere for different frequencies ( $h/L = 0.3$ ;  $\sigma_{O_2} = 1.0$  mho/m). 61
- Fig. 2-17 Profiles of  $H_Z^{r_1}$  and  $H_Z$  over a covered sphere for different frequencies ( $h/L = 0.4$ ;  $\sigma_{O_2} = 1.0$  mho/m). 62
- Fig. 2-18 Profiles of  $H_Z^{r_1}$  and  $H_Z - H_Z^{r_2}$  over a covered sphere for different frequencies ( $h/L = 0.4$ ;  $\sigma_{O_2} = 1.0$  mho/m). 62
- Fig. 2-19 Profiles of  $H_Z^{r_1}$  and  $H_Z - H_Z^{r_2}$  showing the transition when  $H_Z^{r_2}$  becomes greater than  $H_Z$  at (a)  $h/L = 0.3$  and (b)  $h/L = 0.4$  ( $\sigma_{O_2} = 1.0$  mho/m). 63
- Fig. 2-20 Profiles of  $H_Z^{r_1}$  and  $H_Z$  over a covered sphere for different frequencies ( $h/L = 0.3$ ;  $\sigma_{O_2} = 0.1$  mho/m). 64
- Fig. 2-21 Profiles of  $H_Z^{r_1}$  and  $H_Z - H_Z^{r_2}$  over a covered sphere for different frequencies ( $h/L = 0.3$ ;  $\sigma_{O_2} = 0.1$  mho/m) 64
- Fig. 2-22 Profiles of  $H_Z^{r_1}$  and  $H_Z$  over a covered sphere for different frequencies ( $h/L = 0.4$ ; 65

$$\sigma_{O_2} = 0.1 \text{ mho/m}).$$

Fig. 2-23 Profiles of  $H_z^{r_1}$  and  $H_z - H_z^{r_2}$  over a covered sphere for different frequencies (h/L = 0.4;  $\sigma_{O_2} = 0.1 \text{ mho/m}$ ). 65

Fig. 2-24 An ideally conducting horizontal half-plane embedded in a half-space underlying an overburden. 72

### CHAPTER III

- Fig. 3-1 Block diagram of the Transmitter unit. 94
- Fig. 3-2 A view of the (a) transmitting and (b) receiving coils 96
- Fig. 3-3 Block diagram of the Receiver unit. 99
- Fig. 3-4 (a) A view of the transmitter, the receiver and the recorder systems. 103  
(b) A view of the T-R carriage and the fiducial markings. 104  
(c) A view of the model-tank. 105  
(d) A view of tray simulating an overburden. 106
- Fig. 3-5 An illustration of anomaly reckoning. 109
- Fig. 3-6 Anomaly profiles over a horizontal graphite sheet illustrating the difficulty in reckoning the peak-to-peak excursions for such models. 111

## CHAPTER IV

- Fig. 4-1 Anomaly profiles over a copper wire 119  
(dia. 0.0021 m) for different depths of burial.
- Fig. 4-2 Anomaly profiles over a copper wire 119  
(dia. 0.0009 m) for different depths of burial.
- Fig. 4-3 In-phase and Quadrature components of the 120  
anomaly versus the depth of burial for copper  
wires.
- Fig. 4-4 Induction index ( $I_i$ ) versus the depth of 120  
burial for horizontal copper wires.
- Fig. 4-5 Anomaly index diagram for horizontal 120  
copper wires (d varying).
- Fig. 4-6 Anomaly profiles over a horizontal gra- 123  
phite cylinder (length 0.4 m, dia. 0.053 m)  
for different depths of burial.
- Fig. 4-7 Anomaly profiles over a horizontal gra- 123  
phite cylinder (length 0.8 m, dia. 0.053 m)  
for different depths of burial.
- Fig. 4-8 Anomaly profiles over a horizontal gra- 124  
phite cylinder (length 0.51 m, dia. 0.051 m)  
for different depths of burial.
- Fig. 4-9 Anomaly profiles over a horizontal 124  
graphite cylinder (length 0.56 m, dia. 0.075 m)  
for different depths of burial.
- Fig. 4-10 Anomaly index diagrams for horizontal 126  
graphite cylinders (d varying). The first point

	page
of each curve corresponds to the case when the model is in air and the last point to $d=0.0$ m	126
Fig. 4-11 Induction index ( $I_i$ ) versus depth of burial for horizontal graphite cylinders.	126
Fig. 4-12 Enhancement ratios (a) $I_s/I_a$ and (b) $Q_s/Q_a$ versus the length of horizontal graphite cylinders.	126
Fig. 4-13 Anomaly profiles over a graphite sphere (dia. 0.10 m) for different depths of burial.	134
Fig. 4-14 Anomaly profiles over a graphite sphere (dia. 0.12 m) for different depths of burial.	134
Fig. 4-15 Anomaly profiles over a graphite sphere (dia. 0.13 m) for different depths of burial.	134
Fig. 4-16 Anomaly profiles over an aluminium sphere (dia. 0.12 m) for different depths of burial.	135
Fig. 4-17 Anomaly profiles over an aluminium sphere (dia. 0.10 m) for different depths of burial.	135
Fig. 4-18 Anomaly profiles over a graphite sphere (dia. 0.12 m) for $L = 0.15$ m.	137
Fig. 4-19 Anomaly profiles for a graphite sphere (dia. 0.12 m) for different frequencies of energisation.	137
Fig. 4-20 Anomaly profiles over a graphite sphere (dia. 0.12 m) for different conductivities of the surrounding medium.	137

	page
Fig. 4-21 Anomaly profiles over a short thick graphite cylinder ( $GB_1$ ) (length 0.13 m, dia. 0.14 m) for different depths of burial when (a) $h/L = 0.2$ , (b) $h/L = 0.3$ and (c) $h/L = 0.4$ .	140- 142
Fig. 4-22 Anomaly profiles over a short thick graphite cylinder ( $GB_2$ ) (length 0.15 m, dia. 0.16 m) for different depths of burial when (a) $h/L = 0.2$ , (b) $h/L = 0.3$ and (c) $h/L = 0.4$ .	140- 142
Fig. 4-23 Anomaly index diagrams for graphite cylinders (a) $GB_1$ and (b) $GB_2$ .	143
Fig. 4-24 Enhancement ratios (a) $I_s/I_a$ and (b) $Q_s/Q_a$ versus depth of burial for a graphite cylinder ( $GB_1$ ).	143
Fig. 4-25 Enhancement ratios (a) $I_s/I_a$ and (b) $Q_s/Q_a$ versus depth of burial for a graphite cylinder ( $GB_2$ ).	145
Fig. 4-26 Induction index ( $I_i$ ) versus depth of burial for graphite cylinders (a) $GB_1$ (b) $GB_2$ .	145
Fig. 4-27 Anomaly profiles over a vertical graphite sheet ( $G_1$ ) (0.70 m x 0.20 m x 0.021 m) for different conductivities of the surrounding medium ( $h/L = 0.5$ ).	148
Fig. 4-28 Anomaly profiles over a vertical graphite sheet ( $G_1$ ) for different conductivities of the surrounding medium ( $h/L = 0.375$ ).	148

	page
Fig. 4-29 Anomaly profiles over a vertical graphite sheet ( $G_1$ ) in air for different frequencies.	149
Fig. 4-30 Anomaly profiles over a vertical graphite sheet ( $G_1$ ) in a conducting solution ( $\sigma_s = 10.1$ mho/m, $d = 0.03$ m) for different frequencies.	149
Fig. 4-31 Anomaly profiles over a vertical graphite sheet ( $G_1$ ) in a conducting solution ( $\sigma_s = 3.3$ mho/m, $d = 0.03$ m) for different frequencies.	149
Fig. 4-32 Anomaly index diagrams for a vertical graphite sheet ( $G_1$ ) (a) $d = 0.0$ m and (b) $d = 0.03$ m for 100 khz.	150
Fig. 4-33 Anomaly index diagrams for a vertical sheet ( $G_1$ ) (a) $d = 0.0$ m and (b) $d = 0.03$ m for 50 khz.	150
Fig. 4-34 Enhancement ratios ( $I_s/I_a$ and $Q_s/Q_a$ ) versus conductivity ratio ( $\sigma_s/\sigma_m$ ) at (a) $h/L = 0.5$ and (b) $h/L = 0.375$ for a vertical graphite sheet ( $G_1$ ).	152
Fig. 4-35 Enhancement ratios (a) $I_s/I_a$ and (b) $Q_s/Q_a$ versus depth of burial for a vertical graphite sheet ( $G_1$ ).	152
Fig. 4-36 Induction index ( $I_1$ ) versus conductivity ratio ( $\sigma_s/\sigma_m$ ) for a vertical graphite sheet	153

( $G_1$ ) for different depths of burial at (a)  
 $h/L = 0.375$  and (b)  $h/L = 0.5$ .

- Fig. 4-37 Induction index ( $I_1$ ) versus conductivity ratio ( $\sigma_s/\sigma_m$ ) for a vertical graphite sheet ( $G_1$ ) for different frequencies at (a)  $h/L = 0.375$  and (b)  $h/L = 0.5$ . 153
- Fig. 4-38 Anomaly profiles over a vertical graphite sheet ( $G_1$ ) for different depths of burial ( $h/L = 0.5$ ). 156
- Fig. 4-39 Anomaly profiles over a vertical graphite sheet ( $G_1$ ) for different depths of burial ( $h/L = 0.4$ ). 156
- Fig. 4-40 Anomaly index diagram for a vertical graphite sheet ( $G_1$ ) for different depths of burial ( $L = 0.25$  m). 157
- Fig. 4-41 Enhancement ratios (a)  $I_s/I_a$  and (b)  $Q_s/Q_a$  versus depth of burial for a vertical graphite sheet ( $G_1$ ) ( $L = 0.25$  m). 157
- Fig. 4-42 Anomaly profiles over a vertical stainless steel sheet ( $SS_1$ ) (1.02m x 0.41m x .00049m) for different depths of burial ( $h/L = 0.6$ ). 159
- Fig. 4-43 Anomaly profiles over a vertical stainless steel sheet ( $SS_1$ ) for different depths of burial ( $h/L = 0.4$ ). 159
- Fig. 4-44 Anomaly profiles over a vertical stain- 160

	page
less steel sheet ( $SS_2$ ) (1.02mx0.41mx0.00019m) for different depths of burial ( $h/L = 0.6$ ).	
Fig.4-45 Anomaly profiles over a vertical stain- less steel sheet ( $SS_2$ ) for different depths of burial ( $h/L = 0.4$ ).	160
Fig.4-46 Anomaly index diagram for a vertical stainless steel sheet ( $SS_1$ ) for different depths of burial.	161
Fig.4-47 Anomaly index diagram for a vertical stainless steel sheet ( $SS_2$ ) for different depths of burial.	161
Fig.4-48 Induction index ( $I_i$ ) versus the depth of burial for a vertical stainless steel sheet ( $SS_1$ ).	161
Fig.4-49 Induction index ( $I_i$ ) versus the depth of burial for a vertical stainless steel sheet ( $SS_2$ ).	161
Fig.4-50 Enhancement ratios (a) $I_s/I_a$ and (b) $Q_s/Q_a$ versus depth of burial for a vertical stainless steel sheet ( $SS_1$ ).	162
Fig.4-51 Enhancement ratios (a) $I_s/I_a$ and (b) $Q_s/Q_a$ versus depth of burial for a vertical stainless steel sheet ( $SS_2$ ).	162
Fig.4-52 Anomaly profiles over a vertical stain- less steel sheet ( $SS_1$ ) for different conducti- vities of the surrounding medium ( $d = 0.01$ m and $h/L = 0.5$ ).	164



	page
Fig.4-53 Anomaly profiles over a vertical stainless steel sheet ( $SS_1$ ) for different conductivities of the surrounding medium ( $d = 0.01$ m and $h/L = 0.375$ ).	164
Fig.4-54 Anomaly profiles over a vertical stainless steel sheet ( $SS_1$ ) for different depths of burial ( $h/L = 0.375$ ).	165
Fig.4-55 Anomaly profiles over a vertical stainless steel sheet ( $SS_1$ ) for different frequencies ( $h/L = 0.375$ ).	165
Fig.4-56 Anomaly index diagrams for a vertical stainless steel sheet ( $SS_1$ ) for different conductivities of the surrounding medium at (a) $d = 0.0$ m and (b) $d = 0.03$ m for 100 khz.	166
Fig.4-57 Anomaly index diagrams for a vertical stainless steel sheet ( $SS_1$ ) for different conductivities of the surrounding medium at (a) $d = 0.0$ m and (b) $d = 0.03$ m for 50 khz.	166
Fig.4-58 Enhancement ratios ( $I_s/I_a$ and $Q_s/Q_a$ ) versus the conductivity ratio ( $\sigma_s/\sigma_m$ ) for a vertical stainless steel sheet ( $SS_1$ ) for (a) 100 khz and (b) 50 khz.	167
Fig.4-59 Induction index ( $I_i$ ) versus the conductivity ratio ( $\sigma_s/\sigma_m$ ) for a vertical stainless steel sheet ( $SS_1$ ) for (a) 100 khz and (b) 50 khz.	167
Fig.4-60 Anomaly profiles over a copper sheet	168

(CS<sub>1</sub>) (1.04m x 0.35m x 0.0017m) for different depths of burial ( $h/L = 0.6$ ).

- Fig. 4-61 Anomaly profiles over a copper sheet (CS<sub>1</sub>) for different depths of burial ( $h/L = 0.4$ ). 168
- Fig. 4-62 (a) Anomaly index diagram and (b) Induction index ( $I_i$ ) versus depth of burial for a vertical copper sheet (CS<sub>1</sub>). 169
- Fig. 4-63 Enhancement ratios (a)  $I_s/I_a$  and (b)  $Q_s/Q_a$  versus depth of burial for a vertical copper sheet (CS<sub>1</sub>). 169
- Fig. 4-64 Anomaly profiles over a perspex sheet (PS<sub>1</sub>) (1.04m x 0.35m x 0.0069m) for different depths of burial ( $h/L = 0.3$ ). 171
- Fig. 4-65 Anomaly profiles over a perspex sheet (PS<sub>1</sub>) for different depths of burial ( $h/L = 0.2$ ). 171
- Fig. 4-66 Anomaly profiles over a perspex sheet (PS<sub>2</sub>) (0.92m x 0.35m x 0.0016m) for different depths of burial ( $h/L = 0.3$ ). 172
- Fig. 4-67 Anomaly profiles over a perspex sheet (PS<sub>2</sub>) for different depths of burial ( $h/L = 0.2$ ). 172
- Fig. 4-68 Anomaly index diagram for perspex sheet (PS<sub>1</sub>) for different depths of burial. 173
- Fig. 4-69 Anomaly index diagram for a perspex sheet (PS<sub>2</sub>) for different depths of burial. 173
- Fig. 4-70 Induction index ( $I_i$ ) versus depth of burial for a perspex sheet (PS<sub>1</sub>). 173

- Fig. 4-71 Induction index ( $I_i$ ) versus depth of burial for a perspex sheet ( $PS_2$ ). 173
- Fig. 4-72 Anomaly profiles over a horizontal graphite sheet ( $G_2$ ) (0.70m x 0.20m x 0.009m) for different depths of burial at (a)  $h/L = 0.5$  and (b)  $h/L = 0.4$  ( $\sigma_s = 10.1$  mho/m). 176
- Fig. 4-73 Anomaly profiles over a horizontal graphite sheet ( $G_2$ ) for different depths of burial at (a)  $h/L = 0.5$  and (b)  $h/L = 0.4$  ( $\sigma_s = 7.3$  mho/m). 180
- Fig. 4-74 Anomaly profiles over a horizontal graphite sheet ( $G_2$ ) for different depths of burial at (a)  $h/L = 0.5$  and (b)  $h/L = 0.4$  ( $\sigma_s = 4.4$  mho/m). 181
- Fig. 4-75 Anomaly profiles over a horizontal graphite sheet ( $G_2$ ) for different conductivities of the surrounding medium at (a)  $h/L = 0.5$  and (b)  $h/L = 0.4$  ( $d = 0.01$  m). 182
- Fig. 4-76 Anomaly profiles over a horizontal graphite sheet ( $G_1$ ) for different depths of burial at (a)  $h/L = 0.5$  and (b)  $h/L = 0.4$  ( $\sigma_s = 10.1$  mho/m). 183
- Fig. 4-77 Anomaly profiles over a horizontal graphite sheet ( $G_1$ ) for different conductivities of the surrounding when (a)  $d = -0.021$  m, and (b)  $d = 0.0$  m ( $h/L = 0.375$ ). 184

Fig. 4-78 Anomaly profiles over a horizontal  
graphite sheet ( $G_1$ ) for different frequencies  
at (a)  $d = - 0.021$  m and (b)  $d = 0.01$  m  
( $\sigma_s = 10.1$  mho/m). 185

CHAPTER V

Fig. 5-1 Anomaly profiles over an aluminium sphere ( $AS_2$ ) of dia. 0.10 m in a container at  
(a)  $h/L = 0.3$  and (b)  $h/L = 0.2$  for different  
depths of burial. 191

Fig. 5-2 Anomaly profiles over a graphite sphere ( $GS_1$ ) of dia. 0.10 m in a container at  
(a)  $h/L = 0.3$  and (b)  $h/L = 0.2$  for different  
depths of burial. 191

Fig. 5-3 Anomaly profiles over a vertical gra-  
phite sheet ( $G_1$ ) for different overburden  
thicknesses ( $d_b$ ) when the surrounding medium  
is non-conducting for (a) 100 khz and  
(b) 50 khz. 193

Fig. 5-4 Anomaly profiles over a horizontal  
graphite sheet ( $G_1$ ) for different overburden  
thicknesses ( $d_b$ ) when the surrounding medium  
is non-conducting for (a) 100 khz and  
(b) 50 khz. 194

Fig. 5-5 Anomaly profiles over a vertical graphite  
sheet ( $G_1$ ) for different overburden thicknesses  
( $d_b$ ) when the surrounding medium is a conducting 196

solution for (a) 100 khz and (b) 50 khz.

- Fig. 5-6 Anomaly profiles over a horizontal graphite sheet ( $G_1$ ) for different overburden thicknesses ( $d_b$ ) when the surrounding medium is a conducting solution for (a) 100 khz and (b) 50 khz. 197
- Fig. 5-7 Anomaly profiles over a graphite sheet ( $G_1$ ) held in a conducting solution and overlain by an aluminium foil when the sheet is (a) horizontal and (b) vertical. 199
- Fig. 5-8 Anomaly profiles over two equal and parallel graphite sheets ( $G_1$  and  $G_1'$ ) with variation of the horizontal separation ( $d_s$ ) between them at (a)  $h/L = 0.4$  and (b)  $h/L = 0.2$ . 202
- Fig. 5-9 Anomaly profiles over two equal and parallel graphite sheets ( $G_1$  and  $G_1'$ ) with variation of  $h/L$  for  $d_s = 0.7L$ . 203
- Fig. 5-10 Anomaly profiles over two equal and parallel graphite sheets ( $G_1$  and  $G_1'$ ) with variation of (a) depth of burial and (b) horizontal separation ( $d_s$ ) between them at  $h/L = 0.4$ . 203 and 204
- Fig. 5-11 Anomaly profiles over two unequal and parallel graphite sheets ( $G_3$  and  $G_4$ ) with variation of  $d_s$  (when the top surfaces are in the same level) at (a)  $h/L = 0.6$  and (b)  $h/L = 0.4$ . 208

- Fig. 5-12 Anomaly profiles over two unequal and 208  
parallel graphite sheets ( $G_3$  and  $G_4$ ) with  
variation of  $d_s$  (when the lower surfaces are  
in the same level) at  $h/L = 0.6$ .
- Fig. 5-13 Anomaly profiles over two equal and 210  
parallel graphite cylinders ( $GC_2$  and  $GC'_2$ )  
with variation of the horizontal separation  
( $d_s$ ) between them at (a)  $h/L = 0.3$  and  
(b)  $h/L = 0.6$ .
- Fig. 5-14 Anomaly profiles over two unequal 212  
aluminium spheres ( $AS_1$  and  $AS_2$ ) with varia-  
tion of the distance between their centres  
and the line joining their centres along the  
profile at (a)  $h/L = 0.4$  and (b)  $h/L = 0.3$ .
- Fig. 5-15 Anomaly profiles over two unequal 212  
aluminium spheres ( $AS_1$  and  $AS_2$ ) with the  
line joining their centres orthogonal to  
the profile for (a)  $d_s = 0.6L$  and (b)  $d_s = 1.0L$